Dipole Bands in ^{195}Bi and ^{197}Bi Nuclei

Given Kearabilwe Mabala

A thesis submitted in fulfilment of the requirements
for the degree of Doctor of Philosophy
in the Department of Physics
University of Cape Town
March 2003

Acknowledgements

Go leboga ga se tiro e e potlana, mme go matshwanedi gore ke riana. I wish to express my sincere gratitude to the following[1] for making the realization of this thesis possible:

- Prof. John F. Sharpey-Schafer$^{\alpha}$, supervisor, with a prolific scientific and social character which attracted many of us to iThemba LABS. Special thanks to you Prof., – "the seeds that you sow shall blossom";
- Dr. Elena Gueorguieva-Lawrie$^{\alpha}$, supervisor, for her willingness to guide, support and being very patient with me. I owe you so much that it is difficult to express my sincere gratitude in any other way – ke lebogela kemo nokeng mma;
- Dr. Roger Fearick$^{\beta}$, supervisor, for the guidance and support throughout the duration of the project;
- Dr. J. J. Lawrie$^{\alpha}$ for allowing me to pursue this reseach in the Physics group and for helping with setting up of the AFRODITE electronics;
- the director (J. F. S-S) of iThemba LABS and members of its Program Advisory Committee (PAC) for allocation of beam-time to this project;
- Cyclotron Group: Dr. Lowry Conradie$^{\alpha}$, Deon de Villiers$^{\alpha}$, Dirk Fourie$^{\alpha}$, Willem van Heerden$^{\alpha,\delta}$, Ben Greyling$^{\alpha}$, and all other members for delivering a reliable ^{20}Ne and ^{22}Ne beams onto target;
- Drs. Simon Mullins$^{\alpha}$, Richard Newman$^{\alpha}$ for their invaluable help and increasing the flow of the thesis by proof reading it. S. M, I hope you will soon join me again at SOWETO – this time for umqombothi!!
- Prof. Ramon Wyss$^{\epsilon}$, for his theoretical input and explanation of the questions related to this work;

[1] α: iThemba LABS; β: University of Cape Town; δ: Presently at Riyadh, Saudi Arabia; ϵ: Kungl Tekniska Högskolan, Sweden; ψ: University of Witwatersrand.

- Dr. Ricky Smit[α], for providing the sustanance!! Ke lebogela setlhako se o se nkapoletseng mo nakong e e maleba;
- Dr. John Pilcher[α] and Sean Murray[α,β] for their help whenever I had computer related problems;
- Dr. Siegie Förtsch[α], Mr. Franz Gonglach[α] and all the postgraduates[α] within the Physics Group;
- Dr. Surjit Mukherjee[α], Marco Benatar[α,β] and Ian Korir[ψ] for showing me that there is more to life than physics;
- All those who assisted during many weekends of data acquisition;
- The staff[α] le ditsala tsa me tsotlhe ka go lekana;
- The University of Cape Town (UCT), the National Research Foundation (NRF) and iThemba LABS for funding I received;
- Batsadi ba me – Khumoeng, Bokhabe, Mma-Bodiya, Zacharia, Magonki, Pontsho le Tsabeng. Bo nnake – Medupe, Mmasetlhabi, Thebe, Dosie, Tsholofelo le Kwesi. Botlhe ba lesika, for their loving support throughout the duration of this project;
- Mmamecha le Ipeleng – a special thank you! for your loving support, patience and understanding throughout the duration of this project;
- Last but not least, the acknowledgements would be incomplete without thanking all my ancestors.

This work is dedicated to my late grandfather Joseph Ditlhobolo Lebeloane. "Ke Mokaa, mmina tlou wa ga Segabutlane, motho yo o sue o Lebeloane. Yo o rileng a kgotswa a kgogogela...Ga tsoga mauweuwe a dithole ga sia banna le basadi, motho a betwa ke mosokwane lephakela".

Kearabilwe Mabala, *March 2003*

Dipole Bands in ^{195}Bi and ^{197}Bi Nuclei

Given Kearabilwe Mabala

iThemba LABS, P. O. Box 722, Somerset West, 7129, South Africa

e-mail: mabala@tlabs.ac.za

Abstract

High-spin states in ^{195}Bi and ^{197}Bi have been populated using the ^{181}Ta(^{20}Ne,6n) and ^{181}Ta(^{22}Ne,6n) reactions respectively, both at a beam energy of 125 MeV. The γ-γ coincidence data associated with the above reactions were measured on separate experiments employing the AFRODITE array, which at that time consisted of 7 Clover and 8 Low Energy Photon Spectrometer (LEPS) detectors at iThemba Laboratory for Accelerator Based Sciences (iThemba LABS).

The spectroscopic analysis of the ^{195}Bi and ^{197}Bi data sets involved the following measuments: γ-γ coincidence relationship, Directional Correlation of Oriented (DCO) states, Linear Polarisation, γ Intensity and Recoil Shadow Anisotropy Method (RSAM) lifetime measurements. One dipole band was found in each of the ^{195}Bi and ^{197}Bi nuclei. The dipole band in ^{197}Bi was linked to the low lying states and its excitation energy, spin and parity, $\frac{37}{2}^{+}$, were determined. This is the first known and the only dipole band in any of the Bi isotopes with measured spin and parity. Another band consisting of M1 and E2 cross-over transitions was found above the $(\frac{13}{2}^{+})$ level in ^{195}Bi. This is the first observation, that such a band is found at such a low spin, suggesting that shape coexistence between spherical and deformed shapes occurs at very low spins.

Furthermore, the properties of the dipole bands in ^{195,197}Bi such as the dynamic moments of inertia, spin and parity of the bandhead lead to the assignment of the $\pi i_{\frac{13}{2}} h^2_{\frac{9}{2}} \otimes \nu i^2_{\frac{13}{2}}$ configuration to these bands. The $\pi i_{\frac{13}{2}}$ configuration was assigned to Band 1 in ^{195}Bi, supported by the results of Total Routhian Surface and the Cranked Shell Model calculations and the $\frac{B(M1)}{B(E2)}$ ratios.

The Total Routhian Surface (TRS) model for the dipole bands in ^{195,197}Bi predicts deformation, $\beta_2 = 0.17$ much larger than that employed by the Tilted Axis Cranking (TAC) model for the Pb nuclei, ($\beta_2 = 0.1$). However, the larger deformation is in conformity with the one recently measured for the 11^{-} isomers in ^{194,196}Pb [Vyv02, Vyv02a] and the one earlier predicted for the dipole bands in the

light Pb isotopes [Ben89, Cla93].

Therefore, it would be very interesting to further study the relative contribution of the collective rotation and shears mechanism for the dipole bands associated with larger deformations.

Contents

List of Figures

List of Tables

Chapter 1

Introduction

Atomic nuclei in the neutron deficient Pb and Bi region, with $192 \leq A \leq 203$, are known to possess a variety of co-existing shapes. The Bi nuclei ($Z = 83$) are situated just above the $Z = 82$ magic gap and are characterized by single-particle excitations associated with spherical shapes at low spins ($J < \approx 15$), and superdeformed (SD) bands as a result of collective rotation of prolate deformed shapes at higher spins.

Studies of the neutron deficient lead nuclei at high spins first revealed the existence of regular cascades of magnetic dipole (M1) γ-ray transitions. These M1 cascades appeared to be associated with collective rotation since they generally follow the $J(J+1)$ rule. Furthermore, collective rotational bands were known for the oblate deformed Tl isotopes [Fir96] built on the $\pi h_{\frac{9}{2}}$, $K = \frac{9}{2}$ configuration. However, since the nuclear deformation in the Pb isotopes in the spin regime where the M1 cascades are found is expected to be small, a mechanism other than collective (electric) rotation has to be responsible for the observations. One such proposed mechanism arising from the Tilted Axis Cranking (TAC) model described in Chapter 2 [Fra93] is that of magnetic rotation and the shears mechanism [Fra93]. This model considers rotation around the total angular momentum axis, called shears mechanism. It is usually stated that in Pb isotopes this mechanism is dominant and the contribution of the collective rotation of the slightly deformed core is negligible.

Recently the deformation of the 11^- isomers (built on the same high-K pro-

ton configuration as the M1 bands) in ^{194,196}Pb were measured as $\beta_2 = 0.21$ (4) [Vyv02] and $\beta_2 = 0.156$ (28) [Vyv02a], which is much larger than the deformation used with the TAC model for the Pb nuclei, ($\beta_2 = 0.10$). Accepting nuclear deformation this large, may lead to a dominant contribution of the collective rotation and might re-open questions about the mechanism that generates these bands.

It is known that the high-K protons are the ones that drive the nuclear shape towards small oblate deformation. Thus, the thesis presents a γ-ray spectroscopic study of ^{195}Bi and ^{197}Bi nuclei, searching for M1 bands that contain three deformation driving protons. We consider the fact that if such bands exist, then they may correspond to nuclear deformations even larger than that of the Pb isotopes. Prior to the present work, studies were conducted on the two nuclei which led to the discovery of single-particle low-lying γ-ray sequences associated with ^{195}Bi [Lön86] and ^{197}Bi [Cha86]. Subsequent studies involved, among others, investigation of superdeformation (SD) in $^{195-197}$Bi nuclei [Cla95, Cla96] and extension of the ^{197}Bi level scheme up to $\approx$ 4.025 MeV [Zho95]. The proposed spins and parities for ^{195}Bi level scheme (known only up to $\approx (2.311 + \Delta)$ MeV) were tentatively assigned [Lön86]. The following three isomeric levels: 32, 80 and 750 ns at 0.888, 2.196 and $(2.311 + \Delta)$ MeV, respectively, were found in ^{195}Bi level scheme [Lön86].

Thus, the rest of the thesis is organised as follows:

Chapter 2 discusses the theoretical nuclear models and properties,

Chapter 3 describes the reaction mechanism in which high-spin states in ^{195,197}Bi were populated and the experimental equipment used,

Chapter 4 outlines the experiments and methods used for data analysis,

Chapter 5 presents the results of the experimental data analysis including the level schemes,

Chapter 6 discusses interpretation of the experimental quantities deduced from the level schemes in relation to the theoretical predictions of the TRS, Cranked Shell Model (CSM) and Tilted Axis Cranking (TAC) models. Configuration assignments for the bands are suggested,

Chapter 7 contains the summary of the work presented in this thesis and conclusion.

Chapter 2

Nuclear Properties and Models

2.1 Nuclear Single-Particle and Structure Models

Quantum mechanical rotation of a perfect sphere shown in Figure 2.1 (a) is not a meaningful concept, since no orientation can be assigned to it. However, the assumption of an axially symmetric spheroidal (deformed) nuclei depicted in Figure 2.1 (b) and (c) allows a possible nuclear rotation about the axis perpendicular to the symmetry axis, that is, y or z axis. Hence, the description of the experimental spectra from the rapidly rotating nuclei [Boh79] is based on the collective type of excitations, while non-collective (single-particle) mode of motion is shown by spherical or near spherical nuclei.

2.1.1 Single-Particle Motion

The single-particle mode of motion is mainly observed in spherical and near spherical nuclei. The angular momentum is generated by the alignment of the nucleons spins along the symmetry axis as shown in Figure 2.2 (b). This mode leads to an irregular level scheme like the one associated with the ^{147}Gd [Häu80] nucleus, for example. The angular momentum vector, j_i for the individual nucleons are summed to produce the total angular momentum

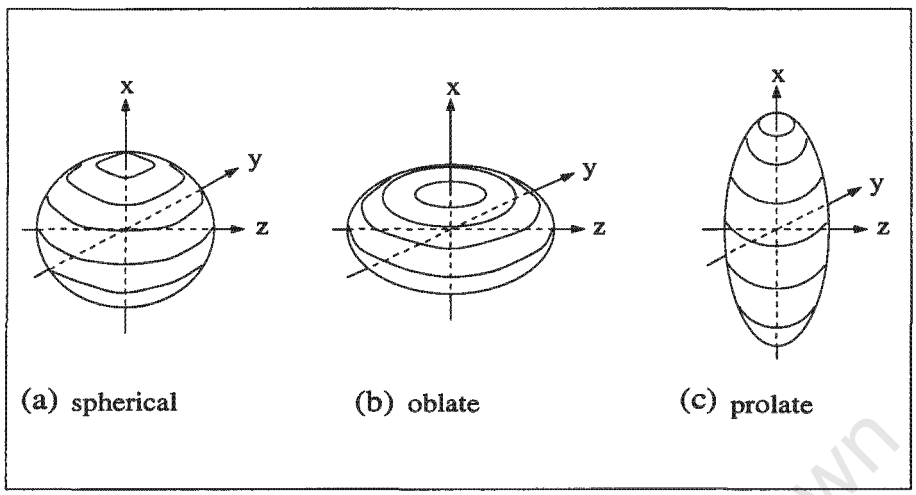

Figure 2.1: *A diagramatic representation of three types of nuclear shape (a) spherical, (b) oblate and (c) prolate. The x-axis denotes the symmetry axis for the oblate and prolate shapes.*

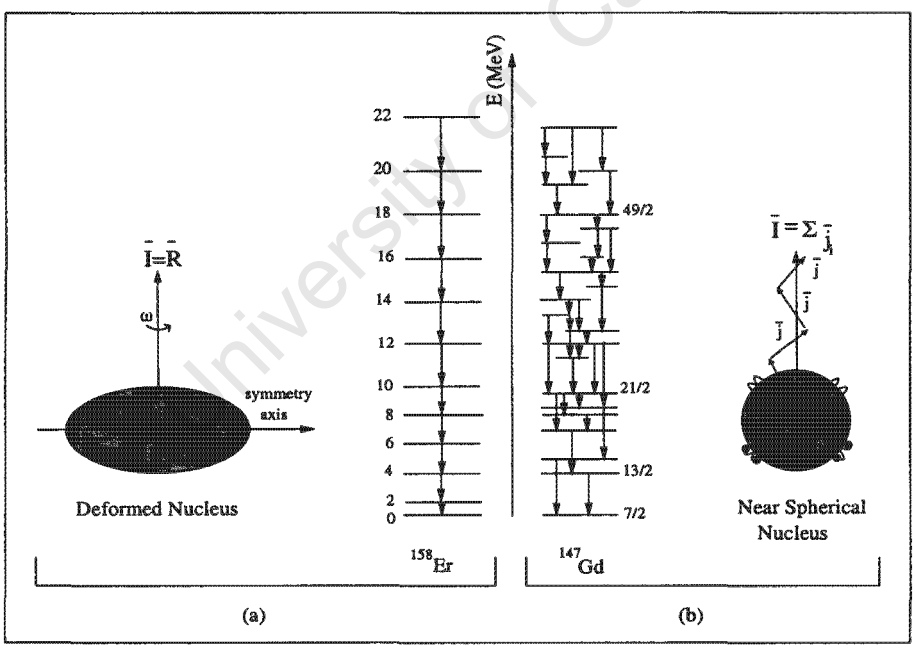

Figure 2.2: *Schematic illustration of the (a) collective motion around the axis perpendicular to the symmetry axis and (b) single-particle motion, generating angular momentum, I, by summing the orbital angular momentum projections onto the symmetry axis.*

vector, $I = \sum j_i$. Even-even nuclei always have a total angular momentum, $I = 0$, at the ground state.

2.1.2 Rotational Motion

In a collective nuclear rotational motion, the nucleons coherently rotate around the axis perpendicular to the symmetry axis, as illustrated in Figure 2.2 (a). This nuclear mode of motion leads to a regular rotational band of levels such as the one observed for the ^{158}Er [Tjø85] nucleus. Hence, the total angular momentum, I of the nucleus is given by the sum of the orbital angular momentum projections on the rotation axis.

In the Particle-Rotor Model (PRM), the system is divided into single-particle motion and a rotating core. Thus, it is convenient to express the nuclear Hamiltonian as:

$$H = H_{int} + H_{rot}, \tag{2.1}$$

where H_{int} is the Hamiltonian associated with the intrinsic motion of the single-particle and H_{rot} the collective rotational Hamiltonian of the nuclear motion, $\frac{\hbar^2}{2\Im}\mathbf{R}^2$.

The total angular momentum, $\mathbf{I}$ of the rotating nucleus consist of two parts. That is, the angular momenta generated by the collective motion, $\mathbf{R}$ and generated by the intrinsic motion of the valence nucleons, $\mathbf{j}$:

$$\mathbf{I} = \mathbf{R} + \mathbf{j}. \tag{2.2}$$

The projections of the angular momenta, $\mathbf{I}$ and $\mathbf{j}$ onto the symmetry axis (conventionally referred to as the 3-axis) are respectively expressed as:

$$I_3 = K \qquad \text{and} \qquad j_3 = \Omega. \tag{2.3}$$

Equation 2.1 takes the form:

$$H = H_{int} + \frac{\hbar^2}{2\Im}\mathbf{R}^2 = H_{int} + \frac{\hbar^2}{2\Im}(\mathbf{I}-\mathbf{j})^2 \tag{2.4}$$

$$= H_{int} + \frac{\hbar^2}{2\Im}\Big(\mathbf{I}^2 + \mathbf{j}^2 - 2(\mathbf{I}\cdot\mathbf{j})\Big). \tag{2.5}$$

The collective rotational Hamiltonian is given by:

$$H = \hbar^2\left(\sum_i \frac{I_i^2}{2\Im_i} + \sum_i \frac{j_i^2}{2\Im_i} - \sum_i \frac{I_i j_i}{\Im_i}\right). \tag{2.6}$$

The first term in equation 2.6 is the overall rotation and the second is a single-particle contribution. The third term provides the particle-rotor coupling in the PRM. There is no collective rotation around the 3-axis, hence, R_3=0. From axial symmetry we have $\Im_1 = \Im_2 = \Im$. Then, the collective Hamiltonian in equation 2.6 is given by:

$$H_{rot} = \frac{\hbar^2}{2\Im}(\mathbf{I}^2 - I_3^2) + \frac{\hbar^2}{2\Im}(j_1^2 + j_2^2) - \frac{\hbar^2}{\Im}(I_1 j_1 + I_2 j_2). \tag{2.7}$$

Employing the ladder operators [Gri95], the last term, called the Coriolis coupling is written as:

$$H_{cor} = -\frac{\hbar^2}{\Im}(I_+ j_- + I_- j_+), \tag{2.8}$$

where $j_+ = j_1 + ij_2$ and $j_- = j_1 - ij_2$. The H_{cor} term couples the single-particle motion with that of the rotating core.
The two most important limiting cases are:

- The Deformation Aligned (DAL) or strong coupling limit, whereby the rotational motion of the core is slow compared to the motion of the particle. The rotational motion has a small influence on the nuclear intrinsic motion.

- The final case is the Rotation Aligned (RAL) or decoupled limit. In this case the rotational frequency is sufficiently high that the Coriolis force is strong enough to align the total angular momentum and the single-particle angular momentum.

The two cases in which **R** and **j** can couple together are diagramatically shown in Figure 2.3 and labelled (a) DAL and (b) RAL.

Deformation Aligned Limit

In the DAL scheme (Figure 2.3 (a)), the valence nucleon angular momentum, j, tends to align with the symmetry (z) axis. DAL is the case for: (a) large deformation β_2, since the level splitting in the Nilsson Hamiltonian is proportional to β_2^2 whereas the rotational constant $\frac{\hbar^2}{2\Im}$ scales as β_2^{-2}; and (b) for low spins I, or for nucleons with small angular momenta j; (c) for large j

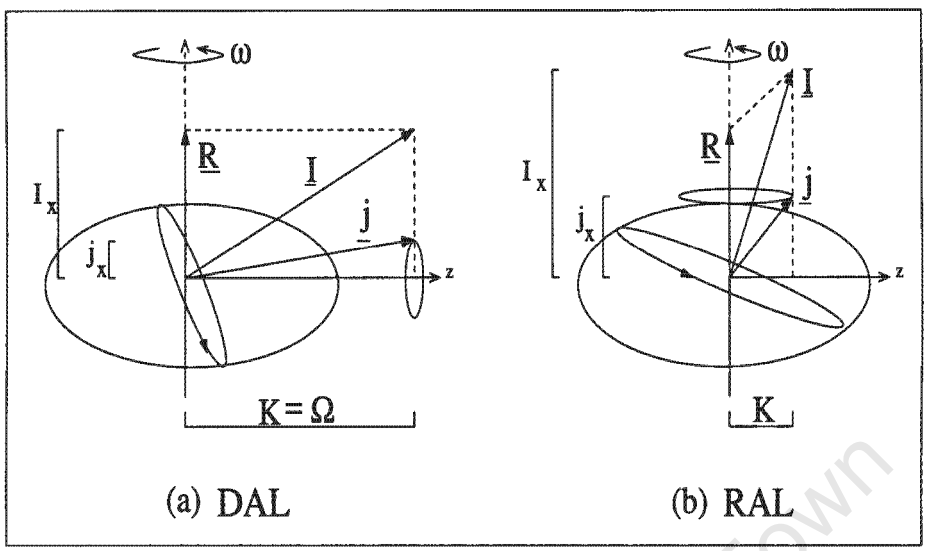

Figure 2.3: *Diagramatic representation of the (a) Deformation Aligned (DAL) and (b) Rotation Aligned (RAL) coupling schemes.*

values DAL can only occur for high Ω orbitals. The total momentum, I and its projection, K on the symmetry axis are conserved quantum numbers:

$$K = \sum_i \Omega_i, \tag{2.9}$$

where Ω is the z-component of the single-particle angular momentum. The corresponding energy spectrum is given by:

$$E_I^K = \frac{\hbar^2}{2\Im}\Big(I(I+1) - K^2\Big), \tag{2.10}$$

with spin sequence ΔI=1:

$$I = K, K+1, K+2, ...$$

for $K \neq \frac{1}{2}$ [Rin80]. The sequence normally decouples into two ΔI=2 bands, characterised by different signature, α (section 2.2.2). For $K = 0$, for example in an even-even nucleus in its ground state equation 2.10 takes the form:

$$E_{rot} = \frac{\hbar^2}{2\Im} I(I+1), \tag{2.11}$$

where I is an even number.

Rotation Aligned Limit

The RAL scheme (Figure 2.3 (b)), is the opposite extreme to the DAL scheme. In this case, the rotational frequency is sufficiently high such that the Coriolis force is strong enough to align the single-particle angular momentum along the rotational axis. This case occurs when the total intrinsic angular momentum, **j** and the total angular momentum, **I** are large. When the intrinsic angular momentum, **j** is aligned with the rotational axis, then the total energy of the nucleus will be minimised.
The spin values and the level energies of the states in a corresponding rotational band are determined by the projection of the single-particle angular momentum on the rotational axis, j_1:

$$I = j_1, j_1 + 2, j_1 + 4, ...$$

and

$$E = \frac{\hbar^2}{2\Im}(I - j_1)(I - j_1 + 1). \tag{2.12}$$

Equation 2.12 states that, the states with complete alignment ($j_1 = j$) have the lowest energy and the band is favoured. The band with less alignment ($j_1 = j - 1$) is termed unfavoured (can be populated in (HI,xnγ) reactions). The spin sequence for the favoured band is :

$$I = j, j + 2, j + 4, ...$$

and for the unfavoured is:

$$I = j - 1, j + 1, j + 3, ...$$

2.1.3 Nuclear Shape Parametrisation

Nuclear shape determines to a large extent the possible nuclear motion modes. Therefore, a convenient shape parametrisation for the nucleus is necessary and can be based on the equation of the surface, expressed by the radius vector, R:

$$R = R(\theta, \phi) \tag{2.13}$$

$$= R_0\left(1 + \sum_{\lambda=0}^{\infty}\sum_{\mu=-\lambda}^{\lambda}\alpha_{\lambda\mu}Y_{\mu\lambda}(\theta, \phi)\right). \tag{2.14}$$

R is defined in spherical coordinates to point from the centre of a nucleus to its surface and $Y_{\mu\lambda}(\theta,\phi)$ are the spherical harmonics[1]. The coefficients, $\alpha_{\lambda\mu}$ describe the changes of the nuclear volume with λ defining the deformation type. Examples illustrating the: $(\lambda = 1)$ dipole, $(\lambda = 2)$ quadrupole, $(\lambda = 3)$ octupole and $(\lambda = 4)$ hexadecapole deformation are shown in Figure 2.4. μ is an integer varying from $-\lambda$ to $+\lambda$. For the axially symmetric nucleus

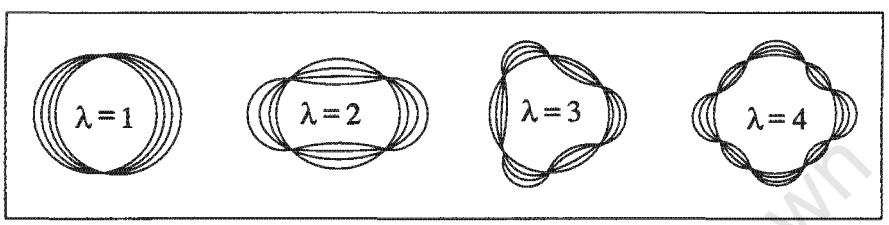

Figure 2.4: *Diagramatic illustration of the multipole deformation for λ =1, 2, 3, and 4.*

with quadrupole deformation, the five:

$$\alpha_{2m} \; : \; \alpha_{21},\; \alpha_{22},\; \alpha_{20},\; \alpha_{2-1},\; \alpha_{2-2}$$

coefficients reduce to only two (α_{20} and $\alpha_{22} = \alpha_{2-2}$). The other ($\alpha_{21} = \alpha_{2-1}$) terms vanish. The coefficients, α_{20} and α_{22} are related to the β_2 and γ parameters according to:

$$\alpha_{20} = \beta_2 cos\gamma \tag{2.15}$$

and

$$\alpha_{22} = \frac{1}{\sqrt{2}}\beta_2 sin\gamma. \tag{2.16}$$

The parameters, β_2 and γ define the extent of quadrupole deformation and deviation from an axially symmetric shape respectively.
The equation for the nuclear surface which involves the β_2 and γ parameters is given by:

$$R(\theta,\phi,\gamma) = R_0\Bigg(1+\beta_2\sqrt{\frac{5}{16\pi}}\Big(cos\gamma(3cos^2\theta-1) + \sqrt{3}sin\gamma sin^2\theta cos2\phi\Big)\Bigg). \tag{2.17}$$

[1]defined as $Y_m^l(\theta,\phi) = P_{lm}(cos\theta)e^{im\phi}$, where P_{lm} is the associated Legendre Polynomial [Arf85].

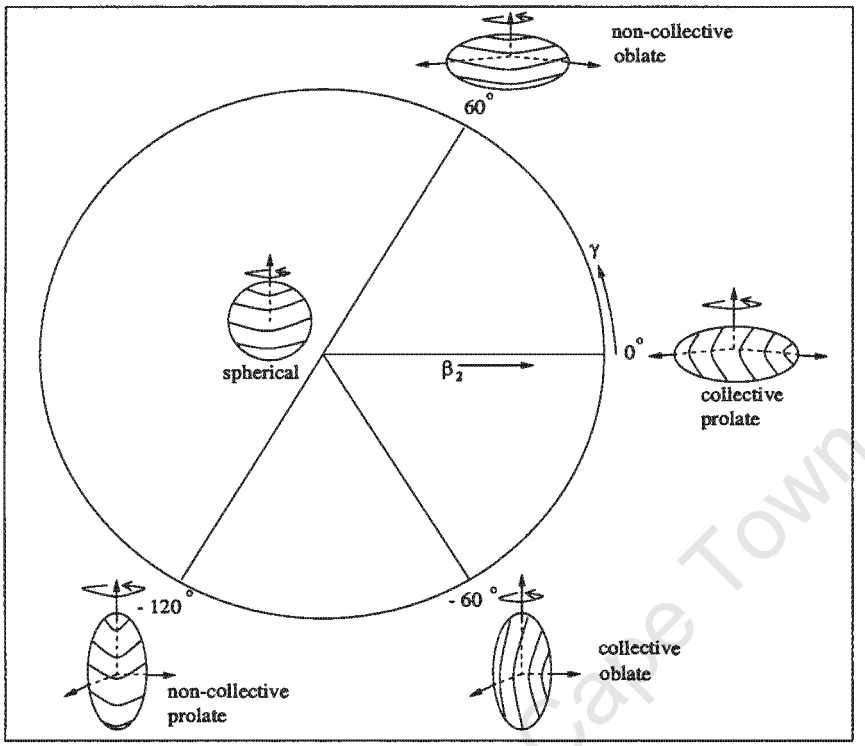

Figure 2.5: *Diagramatic illustration of the Lund convention [And76] for various shapes ($\lambda = 2$) of the rotating nucleus in the (β_2,γ) plane.*

The nuclear shapes which correspond to various (β_2,γ) coordinates for $\lambda = 2$ are diagramatically illustrated in Figure 2.5. The prolate shape corresponds to $\gamma = 0°$ and -120°, while an oblate shape corresponds to $\gamma = 60°$ and -60°. The maximum collectivity is observed for -60° $\leq \gamma \leq$0° while non-collectivity occurs for shapes with γ = -120° and $\gamma = 60°$. In accordance with the Lund convention [And76] rotation occurs around the smallest, the intermediate and the largest axis which correspond to the three 0° $\leq \gamma \leq$ 60°, -60° $\leq \gamma \leq$ 0° and -120° $\leq \gamma \leq$ -60° sectors respectively.

2.1.4 Electromagnetic Moments and Transition Probabilities

De-excitation of the nucleus involves interaction of states, from the initial $|\psi_i\rangle$ to the final $|\psi_f\rangle$ state. The matrix element of the electromagnetic interaction between the two states is non-zero, that is:

$$\langle\psi_i|H'|\psi_f\rangle \neq 0, \tag{2.18}$$

where H' is a small time-dependent perturbation which describes the interaction between the field and the charges. If the interaction is small, first order time-dependent theory can be employed to obtain the transition probability, T_{if} between the initial and final states through Fermi's Golden Rule [Rae86] as:

$$T_{if} = \frac{2\pi}{\hbar}|\langle\psi_i|H'|\psi_f\rangle|^2\rho(E_f). \tag{2.19}$$

$\rho(E_f)$[2] is the density of final states. Equation 2.19 define the probability per unit time of the decay from the initial to the final state associated with the emission of a γ-ray (of energy $E_\gamma = E_i - E_f$).
H' can be written in terms of the electric, (Q_{LM}) and magnetic, (M_{LM}) transition multipole operators:

$$H' = \sum_{LM} a_{LM}Q_{LM} + b_{LM}M_{LM}, \tag{2.20}$$

where

$$Q_{LM} = \int \rho(\mathbf{r})r^L Y_{LM}(\theta,\phi)d\tau \tag{2.21}$$

and

$$M_{LM} = \int \mu(\mathbf{r})\Delta\Big(r^L Y_{LM}(\theta,\phi)\Big)d\tau \tag{2.22}$$

Parity is conserved in electromagnetic transitions. In accordance with parity selection rule, the electric multipole radiation of order L has opposite parity to that of magnetic radiation of the same multipolarity, L and can be deduced from equation 2.21 and 2.22 respectively as:

$$\pi = \begin{cases} (-1)^L & Q_{LM} \\ -(-1)^L = (-1)^{L+1} & M_{LM}, \end{cases} \tag{2.23}$$

so that transitions EL or ML of even parity are:

$$M1, E2, M3, ...$$

and transitions EL or ML of odd parity are:

$$E1, M2, E3, ...$$

[2] $\rho(E_f) \equiv \frac{dN_f}{dE_f}$ where dN_f is the number of final states per interval dE_f lying within the energy band of width $\Delta E = \hbar/t$ about the energy E_f [Mar69].

Table 2.1: *Parity and angular momentum selection rules for γ-ray emission. The Dipole, Quadrupole and Octupole transitions are abbreviated as D-pole, Q-pole and O-pole respectively.*

	even π			odd π		
Multipolarity	D-pole	Q-pole	O-pole	D-pole	Q-pole	O-pole
Type of radiation	M1	E2	M3	E1	M2	E3
$\Delta\pi$	0	0	0	1	1	1
$\|\Delta$ I$\|$	≤ 1	≤ 2	≤ 3	≤ 1	≤ 2	≤ 3

By conservation of angular momentum, the angular momentum carried by a γ-ray is related to the angular momenta (spins) I_i and I_f of the initial and final states. Thus, vectorially we have:

$$\mathbf{L} = \mathbf{I}_i - \mathbf{I}_f, \tag{2.24}$$

which leads to the selection rule that L can have any integer value between the sum and difference of the quantum numbers of the initial and final states:

$$\Delta I \equiv |I_i - I_f| \leq L \leq \sum I \equiv I_i + I_f. \tag{2.25}$$

A summary of the parity and angular momentum selection rules for the lowest Q_{LM} and M_{LM} multipole operators is given in Table 2.1. Examples of (a) Pure M1, (b) Pure E1 and (c) Mixed M1, E2 γ-ray transitions are provided in Figure 2.6 (together with Table 2.1) to illustrate the operation of the momentum and parity selection rules. A general formula which gives the relationship between the transition probability, $T_{if}(\sigma L)$ and the reduced transition probability, $B(\sigma L)$ for a nucleus decaying from state I_i to state I_f separated by γ-ray energy, E_γ is given by:

$$T_{if}(\sigma L) = \frac{8\pi(L+1)}{\hbar L\Big((2L+1)!!\Big)^2}\left(\frac{E_\gamma}{\hbar c}\right)^{(2L+1)} B(\sigma L, I_i \rightarrow I_f), \tag{2.26}$$

where σ denotes the type of radiation (electric or magnetic) and the double factorial [Bur63]:

$$(2L+1)!! = 1.3.5...(2L+1).$$

The reduced transition probabilities for the electric and magnetic case are given by:

$$B(EL, I_i \rightarrow I_f) = \frac{1}{2I_i+1}|\langle f|Q_{LM}|i\rangle|^2 \tag{2.27}$$

and

$$B(ML, I_i \rightarrow I_f) = \frac{1}{2I_i + 1} |\langle f | M_{LM} | i \rangle|^2 \tag{2.28}$$

respectively.

Electric Quadrupole Moments

The reduced transition strength, B(E2) for the collective E2 transitions and the intrinsic quadrupole moment, Q_0 are related by:

$$B(E2) = \frac{5}{16\pi} Q_0^2 \langle IK20 | I - 2K \rangle^2 \quad (eb)^2, \tag{2.29}$$

where

$$Q_0 = \frac{3}{\sqrt{5\pi}} ZR^2 \beta_2. \tag{2.30}$$

β_2 in equation 2.30 is the deformation parameter (discussed in section 2.1.3) and $R \approx 1.23A^{1/3}$ fm is the nuclear radius. For a prolate and oblate deformed nucleus $Q_0 > 0$ and $Q_0 < 0$ respectively, while $Q_0 = 0$ for a spherical case (see Figure 2.1).

Magnetic Dipole Moments

The reduced transition strength, B(M1) for the stretched magnetic dipole (M1) transitions provide information about the currents in the nucleus and it is

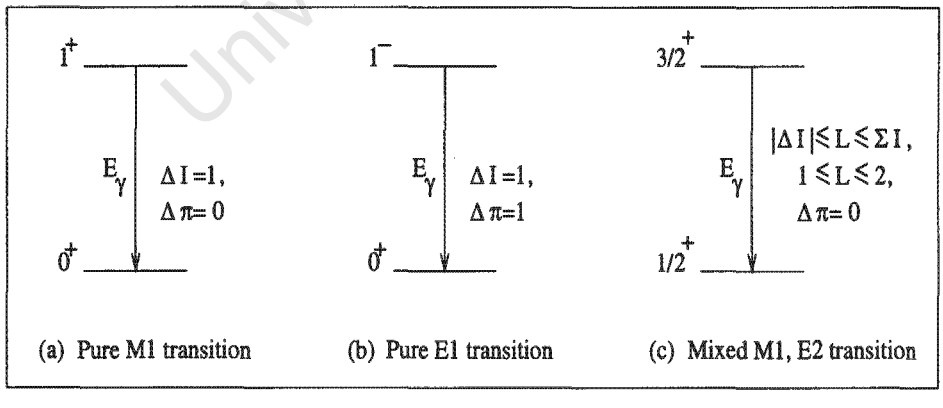

Figure 2.6: *Diagramatic illustrations of application of the momentum and parity selection rules to γ-ray transitions, in order to determine their multipolarities.*

defined in terms of the nuclear g-factors :

$$B(M1) = \frac{3}{4\pi}(g_K - g_R)^2 K^2 \langle IK10|I-1K\rangle^2 \quad \mu_N^2, \tag{2.31}$$

where g_R estimated by:

$$g_R \approx Z/A, \tag{2.32}$$

is the rotational g-factor responsible for the current arising from collective rotation of the core. This in turn gives rise to the magnetic dipole moment:

$$\mu = \mu_N g_R R, \tag{2.33}$$

where $\mu_N = \frac{e\hbar}{2mc}$ is the nuclear magneton. The intrinsic g-factor, g_K describes the currents generated by the orbital motion of the valence nucleons. The total magnetic dipole moment, μ for total angular momentum, $\mathbf{I} = \mathbf{R}+\mathbf{j}$ of the nucleus is given by:

$$\mu = \left(g_R I + (g_K - g_R)\frac{K^2}{I+1}\right) \quad \mu_N. \tag{2.34}$$

2.2 The Cranked Shell Model

Cranking of the nuclear Hamiltonian was first suggested by Inglis [Ing54] in 1954. The Cranked Shell Model (CSM) was further reviewed by Harris [Har65], suggesting a scheme whereby the energies of high-spin rotational bands of deformed nuclei might be obtained by an extension of the CSM. The model is applied to the collective rotational motion. The advantage of the CSM is that, it describes the total angular momentum as the sum of the single-particle angular momenta such that:

$$J_x(\omega) = \sum_{i=1}^{n} j_{xi}, \tag{2.35}$$

where j_x is the projection of the single-particle angular momentum on the rotation axis. It provides a description of a rotating spheroidal nucleus around an (x)-axis perpendicular to the symmetry (z)-axis. Assuming a constant rotational frequency, ω applied to the nuclear potential around the x-axis then the nucleus is referred to as being cranked. Transformation of

coordinates from the laboratory (x,y,z) to those in the rotating (x',y',z') system is given by:

$$x' = x, \tag{2.36}$$

$$y' = ycos\omega t + zsin\omega t, \tag{2.37}$$

$$z' = -ysin\omega t + zcos\omega t. \tag{2.38}$$

The time-dependent Schrödinger equation [deV83]:

$$i\hbar\frac{\partial\psi_{lab}}{\partial t} = H_{lab}\psi_{lab}, \tag{2.39}$$

is transformed from the non-rotating laboratory system to the rotating system by the rotational operator:

$$\Re = e^{-iJ_x\omega t}, \tag{2.40}$$

where $J_x = J_{x'}$ is the x-component of the total angular momentum. The wave-function of the nucleon is given by:

$$\psi_{lab} = \Re\psi_{rot} = e^{-iJ_x\omega t}\psi_{rot}. \tag{2.41}$$

Assuming that the nuclear mean field is not affected by transformation to the rotating frame then:

$$H_{lab} = \Re H_{rot}\Re^{-1}, \tag{2.42}$$

where ψ_{rot} and H_{rot} relates to the rotating system. The Schrödinger equation can now be written as:

$$i\hbar\frac{\partial\Re\psi_{rot}}{\partial t} = \Re H_{rot}\psi_{rot}. \tag{2.43}$$

Substituting equation (2.41) into (2.39) and subsequently taking the time derivative yields:

$$i\hbar\frac{\partial\psi_{rot}}{\partial t} = (H_{rot} - \hbar J_{x'}\omega)\psi_{rot}, \tag{2.44}$$

where

$$H^{\omega} = H_{rot} - \hbar J_{x'}\omega, \tag{2.45}$$

is referred to as the cranking Hamiltonian or Routhian. H_{rot} in equation 2.45 is the single-particle Hamiltonian in the rotating (intrinsic) frame and the

term $-\hbar J_{x'}\omega$ is refered to as the "cranking term". It describes the effects of the centrifugal and Coriolis force on the individual nucleons in the rotating coordinate system. The Coriolis and centrifugal forces tends to align the single-particle angular momenta of the individual nucleons with the rotational x-axis.

2.2.1 Nuclear Spin and Parity

The total angular momentum of a nucleon, j is defined as the coupled sum of the orbital angular momentum, l and spin, s: $j = l + s$. The total angular momentum (or nuclear spin), I of a nucleus is the vector sum of the total angular momenta of all the nucleons. The following rules [Kra88] applies: I is a half integer and I is an integer for odd-A and even-A nuclei respectively. The parity quantum number, π is defined as the eigenvalue of the reflection operator through the origin. If the parity operator $\hat{\pi}$ acts on a wavefunction $\Psi(x)$, such that:

$$\hat{\pi}\Psi(x) = \Psi(-x) = +\Psi(x) \tag{2.46}$$

and

$$\hat{\pi}\Psi(x) = \Psi(-x) = -\Psi(x), \tag{2.47}$$

then it implies that the wavefunctions in equation 2.46 and 2.47 have even (unchanged) and odd (changed by inversion) parities respectively. Parity quantum number is expressed as $\pi = \pm 1$, which are the eigenvalues of the parity operator, $\hat{\pi}$. The parity associated to a single-particle level is determined by its orbital angular momentum as $\pi = (-1)^l$. The total parity of the nucleus is determined by the product of the parities of all occupied levels.
Therefore, knowing the nuclear spin and parity, nuclear states can then be labelled according to the notation: I^{π}.

2.2.2 Signature

The rotation operator, $\Re_x$ which corresponds to a rotation around the x-axis through an angle π is $\Re_x = \Re_{x'}$ given by:

$$\Re_{x'} = e^{-i\pi J_{x'}}. \tag{2.48}$$

Rotation around the x-axis is the only one apart from the parity operator $\hat{\pi}$, which will leave the cranked Hamiltonian, H^{ω} invariant, contrary to similar rotations governed by $\Re_y$ and $\Re_z$ operators around the y and z axes, respectively. The square of the operator $\Re_{x'}$ corresponds to a rotation through angle 2π is given by:

$$\Re_{x'}^2 = (-1)^A. \tag{2.49}$$

The eigenvalues of $\Re_x$ are given by:

$$r = e^{-i\pi\alpha}, \tag{2.50}$$

where both r and α are referred to as signature quantum numbers.
Bohr and Mottelson [Boh75] showed that the signature was related to the total angular momentum, I by:

$$r = (-1)^I. \tag{2.51}$$

Therefore, for even-even nuclei we have:

$$r = +1 \quad (\alpha = 0) \quad I = 0, 2, 4, ..., \tag{2.52}$$

$$r = -1 \quad (\alpha = 1) \quad I = 1, 3, 5, ..., \tag{2.53}$$

while for odd-A nuclei:

$$r = -i \quad (\alpha = +\frac{1}{2}) \quad I = \frac{1}{2}, \frac{5}{2}, \frac{9}{2}, ..., \tag{2.54}$$

$$r = +i \quad (\alpha = -\frac{1}{2}) \quad I = \frac{3}{2}, \frac{7}{2}, \frac{11}{2}, ..., \tag{2.55}$$

The above four relations are expressed by the relation:

$$I = \alpha \ mod \ 2. \tag{2.56}$$

The only good quantum numbers that remain in the rotating nucleus are those of parity (π) and signature (α). Therefore, nuclear states in a rotating nucleus are labelled in terms of parity and signature.

2.3 Comparison of the Theoretical Cranking Model Predictions with the Experiment

In Cranked Shell Model (CSM) all parameters of the nuclear system like energy, angular momentum, etc. are calculated with respect to the rotating coordinate system, fixed with the principle axes of the nucleus, while the experimentally measured values are with respect to the laboratory system. Thus, in order to compare the CSM calculations with the experimental results, a common coordinate system should be used. A method to transform the experimental data from the laboratory coordinate system to the rotating coordinate system is described in the following subsections. In a $\Delta I = 2$ rotational band, the energy of a transition from one energy level to the next is:

$$E_\gamma = E_{rot}(I) - E_{rot}(I-2) = \frac{\hbar^2}{2\Im}(4I-2). \tag{2.57}$$

For such a rotational band, the rotational frequency, ω is defined as:

$$\hbar\omega = \frac{dE}{dI} \cong \frac{E_\gamma}{2}, \tag{2.58}$$

while for a $\Delta I = 1$,

$$\hbar\omega = \frac{dE}{dI} \cong E_\gamma. \tag{2.59}$$

2.3.1 The Routhian

Having obtained the rotational frequency (equation 2.58), the experimental Routhian is determined by transforming the measured excitation energy, E_x into the frame rotating with frequency, ω. The excitation energy in the rotating frame called the Routhian, E' is given by:

$$E' = E_x - \hbar\omega I_x \tag{2.60}$$

where I_x is the projection of the total aligned angular momentum on the rotational axis (x).

Furthermore, we define the experimental single-quasiparticle Routhian, $e'(\omega)$ and the alignment, $i(\omega)$ by subsequently subtracting the energy contribution from the collective rotation:

$$e'(\omega) = E' - E'_{ref} \tag{2.61}$$

and

$$i_x(\omega) = I_x - I_{ref}. \tag{2.62}$$

The ground state rotational band in a (neighbouring) even-even nucleus or its first excited band are usually employed as the reference. The reference functions are parametrised by means of the Harris formulae [Har65] giving:

$$E'_{ref} = -\frac{\omega^2}{2}J_0 - \frac{\omega^4}{4}J_1 + \frac{\hbar^2}{8J_0}, \tag{2.63}$$

where J_0 and J_1 are the Harris parameters of a rotational band with a moment of inertia:

$$\Im = J_0 + J_1\omega^2. \tag{2.64}$$

2.3.2 Nuclear Alignment

The aligned angular momentum, or alignment describes the non-collective part of the nuclear spin, projected on the rotation axis. The experimental alignment, $i_x(\omega)$ was defined by subtracting a reference angular momentum, I_{ref} from the experimental I_x and is given by Equation 2.62. The alignment is related to the Routhian through the expression:

$$i_x(\omega) = -\frac{de'(\omega)}{d\omega}, \tag{2.65}$$

which is important in the assignment of a particular configuration to the structure of the nucleus.

2.3.3 Moments of Inertia

There are three types of moments of inertia which can be defined for nuclear rotation, namely, the:

- static $\Im^{(0)}$,
- kinematic $\Im^{(1)}$ and
- dynamic $\Im^{(2)}$.

The relationship between the static moment of inertia $\Im^{(0)}$, the excitation energy, E and the spin, I in a $K = 0$ rotational band is:

$$E_{rot}(I) = \frac{\hbar^2}{2\Im^{(0)}}I(I+1). \tag{2.66}$$

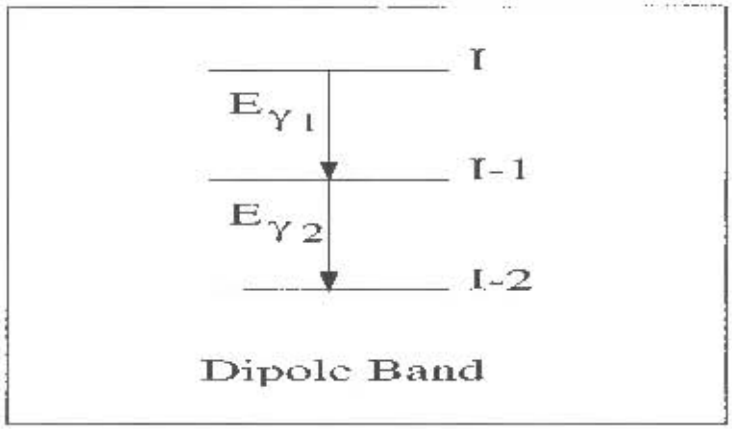

Figure 2.7: *A diagramatic representation of a dipole band.*

The x-component of the total angular momentum projected onto the rotational axis is given by:

$$I_x = \sqrt{I(I+1)}. \tag{2.67}$$

The $\Im^{(0)}$ moment of inertia of a state can be attained by substituting equation (2.67) into (2.66):

$$\Im^{(0)} = \frac{\hbar^2}{2}\left(\frac{E_{rot}}{I_x^2}\right)^{-1} = \frac{\hbar^2}{2}\frac{I_x^2}{E_{rot}}. \tag{2.68}$$

The $\Im^{(1)}$ moment of inertia which provides information about the overall motion of the nucleus as it rotates [Boh81], is defined as:

$$\Im^{(1)} = \frac{\hbar^2}{2}\left(\frac{dE_{rot}}{dI_x^2}\right)^{-1}. \tag{2.69}$$

Since, a γ-ray emitted from a level of spin, I of an even-even nucleus with $K = 0$ has:

$$E_\gamma(I) = E_{rot}(I) - E_{rot}(I-2) \tag{2.70}$$

$$= \frac{\hbar^2}{2\Im^{(0)}}\left(I(I+1) - (I-1)(I-2)\right) \tag{2.71}$$

The $\Im^{(1)}$ moment of inertia is given by:

$$\Im^{(1)} = \frac{\hbar^2}{E_\gamma}(2I_x - 1) \cong \frac{\hbar 2I_x}{E_\gamma} = \hbar\frac{I_x}{\omega}. \tag{2.72}$$

If a dipole band is considered (a sequence of M1 transitions as shown in Figure 2.7), then

$$\Im^{(1)} = \hbar^2 \frac{I_x}{E_\gamma} = \hbar^2 \frac{I_x}{\omega}, \tag{2.73}$$

The $\Im^{(2)}$ moment of inertia [Boh81] reflects how a nucleus responds, if it is subjected to an applied torque. The $\Im^{(2)}$ as a function of I, is defined as:

$$\Im^{(2)} = \frac{\hbar^2}{2} \left(\frac{d^2E}{dI_x^2} \right)^{-1}, \tag{2.74}$$

and thus $\Im^{(1)}$ and $\Im^{(2)}$ moments of inertia are related by:

$$\Im^{(2)} = \Im^{(1)} + \omega \frac{d\Im^{(1)}}{d\omega}. \tag{2.75}$$

The $\Im^{(1)}$ depends on the spin assignment and $\Im^{(2)}$ does not [Shi90]. Therefore, for a rotational band consisting of E2 γ-ray transitions, of energy E_γ, the $\Im^{(2)}$ is:

$$\Im^{(2)} = \frac{4\hbar^2}{\Delta E_\gamma}, \tag{2.76}$$

where ΔE_γ is the energy difference between two consecutive γ-ray transitions within the band. The difference ΔE_γ between consecutive γ-ray transition with energies $E_{\gamma 1}$ and $E_{\gamma 2}$ in a dipole band shown in Figure 2.7 is given by:

$$\Delta E_\gamma = E_{\gamma 1} - E_{\gamma 2} \tag{2.77}$$

$$= (E(I) - E(I-1)) - (E(I-1) \quad E(I-2)). \tag{2.78}$$

Thus,

$$\Im^{(2)} = \frac{\hbar^2}{\Delta E_\gamma}. \tag{2.79}$$

2.4 Total Routhian Surface Calculations

The present work feature the Total Routhian Surface (TRS) calculations by R. Wyss [Wys90, Wys88] which are used in order to predict nuclear deformation. The total Routhian $E^{\omega}_{tot}(Z, N, \hat{\beta})$ of a nucleus (N, Z) in the rotating frame, at a rotational frequency, ω and deformation, $\hat{\beta}$ $(= (\beta_2, \gamma))$ is obtained within the cranked Woods-Saxon Bogolyubov-Strutinsky approach as:

$$E^{\omega}_{tot} = E^{\omega}_{LD}(Z, N, \hat{\beta}) + E^{\omega}_{shell}(Z, N, \hat{\beta}) - E^{\omega}_{pair}(Z, N, \hat{\beta}), \tag{2.80}$$

where $E^{\omega}_{LD}(Z,N,\hat{\beta})$, $E^{\omega}_{shell}(Z,N,\hat{\beta})$ and $E^{\omega}_{pair}(Z,N,\hat{\beta})$ represents the liquid-drop, shell-correction and pairing energies respectively.

Cranking implies that the deformed nucleus rotates around a fixed axis with a given rotational frequency, ω. Thus, the total Routhian is then minimized at a fixed deformation and fixed ω by solving the cranked Hartree-Fock-Bogolyubov equations. The solutions give the angular momentum and energy relative to the non-rotating state with $\omega = 0$.

The deformation parameters, β_2 and γ are transformed into cartesian coordinates, $X = \beta_2 cos(\gamma + 30^{\circ})$ and $Y = \beta_2 sin(\gamma + 30^{\circ})$. The deformation lattice has 9×11 points in the (β_2, γ) plane, starting at $X = 0.05$, $Y = -0.20$ with step length of 0.05. The calculations have been performed for 18 different rotational frequencies, starting at $\hbar\omega = 0.00$ MeV with a step length of 0.05 MeV.

At $\omega = 0$, the pairing gap, Δ_0 is calculated self-consistently at each grid point employing the Bardeen, Cooper and Schrieffer (BCS) method [Bar57] and allowed to decrease with ω in the following way:

$$\Delta_0 = \begin{cases} \Delta_0(1 - \frac{1}{2}(\frac{\omega}{\omega_c})^2) & if \quad \omega \leq \omega_c \\ \Delta_0(\frac{1}{2}(\frac{\omega}{\omega_c})^2) & if \quad \omega > \omega_c, \end{cases} \tag{2.81}$$

where ω_c is defined as the critical frequency at which the pairing gap is reduced to half its original value Δ_0.

Shown in Figure 2.8, is an example of a TRS calculations performed for the $(\pi, \alpha) = (+, \frac{1}{2})$ proton configuration in ^{195}Bi (for experiment I) at a rotational frequency of 0.049 MeV$\hbar^{-1}$. The energy minimum occur with $\beta_2 \approx 0.107$ at $\gamma = -62^{\circ}$, indicating that at this frequency the nucleus is oblate in this configuration.

2.5 Tilted Axis Cranking

Rotation around the axis of rotation perpendicular to the symmetry axis (Principal Axes (PA)) was reviewed [Har65] and described in section 2.2 as Cranking. However, the rotation about the tilted axis (other than the principal axis) has been extensively used to describe the properties of the dipole bands [Fra93]. Schematic illustration of three different types of

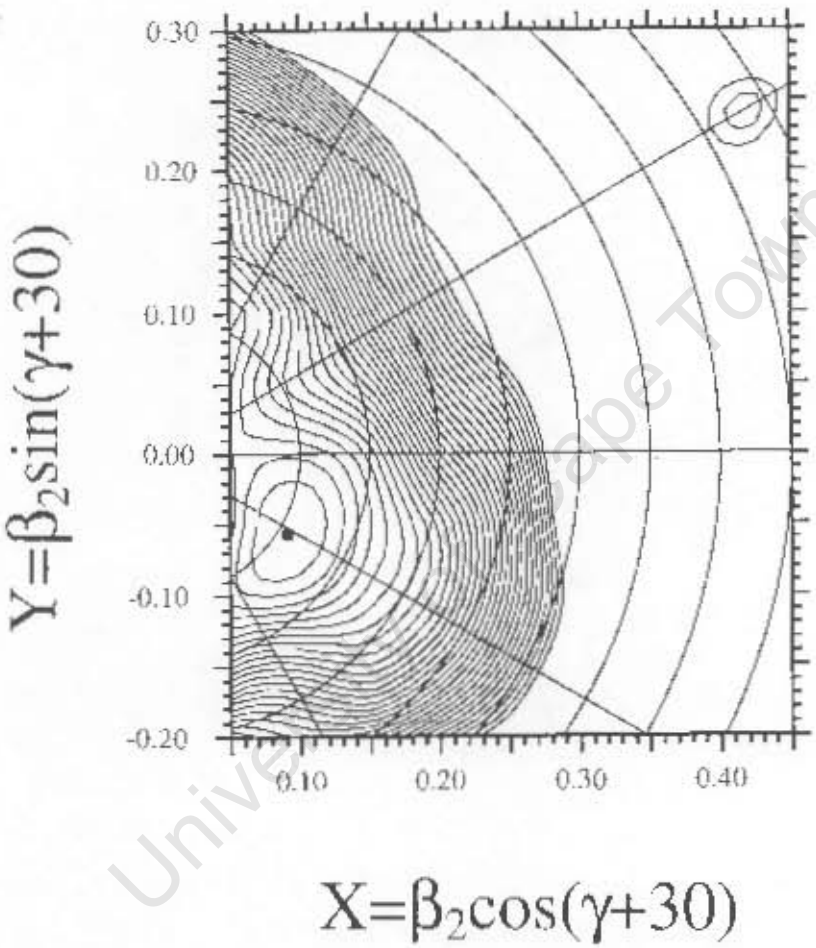

Figure 2.8: *The TRS calculations example for ^{195}Bi in the (β_2,γ) plane, performed at a rotational frequency of 0.049 MeVh^{-1} for the $(\pi,\alpha)-(+,\frac{1}{2})$ configuration.*

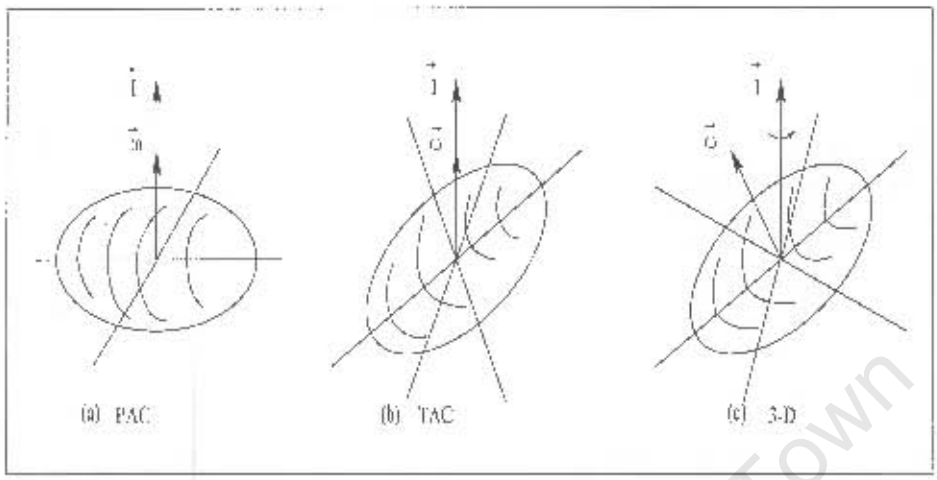

Figure 2.9: *Schematic representation of three types of Cranking, that, is the Principle Axis Cranking (PAC), Tilted Axis Cranking (TAC) and Three Dimensional Cranking (3-D).*

Cranking, that is, the Principle Axis Cranking (PAC), Tilted Axis Cranking (TAC) and the 3-Dimensional (3-D) Cranking [Fra93] are shown in Figure 2.9. PAC is known to be associated with a rotational band composed of one or two signature partner sequences of E2 transitions. The TAC is associated with a $\Delta I = 1$ rotational band of parity π, whose states are directly connected by strong M1 and weak or missing E2 cross-over transitions [Fra93, Fra96, Fra96a, Fra97]. The following reviews [Tho62, Har80, Ker81, Ben93, Fra93, Naz92] among others, have suggested the idea of the three dimensional cranking approach.

The TAC approach is restricted to the case of a uniform rotation about a tilted axis as opposed to the 3-D case. An additional constraint to the TAC case is that, the angular momentum and angular velocity vectors must be parallel. For the parallel geometry the energy is minimal, thus the corresponding configurations can be assigned to the lowest rotational bands. The solutions with precession of the angular velocity vector around the angular momentum have a higher energy and are excluded.

The meanfield Routhians given by:

$$h' = h_{sph} \quad \kappa \sum Q^*_\lambda q_\lambda \quad j_x \omega, \tag{2.82}$$

are used at the onset of the cranking calculations, where j_m is the projection of angular momentum along the tilted axis and h_{sph} the spherical part of the standard Nilsson Hamiltonian plus a monopole pair field [Fra93]. Five components of the quadrupole tensor are found by the self-consistency relations:

$$Q_\lambda - \langle q_\lambda \rangle. \tag{2.83}$$

The PA 1, 2 and 3 are defined as the frame in which:

$$Q'_1 - Q'_{-1} - 0 \qquad \text{and} \qquad Q'_2 = Q'_{-2}. \tag{2.84}$$

The tilting angles, θ and ϕ are used to define the orientation of the PA frame with respect to the tilted axis. In the PA frame, the Hamiltonian, h' can be expressed as:

$$\begin{aligned} h' \quad = \quad & h_{sph} - \hbar\omega_0\beta(\cos\gamma q'_0 - \frac{\sin\gamma}{\sqrt{2}}(q'_2 + q'_{-2})) \\ & -\omega(\sin\theta\cos\phi j'_1 + \sin\theta\sin\phi j'_2 + \cos\theta j'_3). \end{aligned} \tag{2.85}$$

The eigenfunctions of h' are the configurations $|c_i\rangle$ and thus we have:

$$\langle [h', j'_\nu] \rangle = 0. \tag{2.86}$$

Applying equation 2.86 into equation 2.85 then:

$$\langle q'_1 \rangle = \langle q'_{-1} \rangle - \langle q'_2 - q'_{-2} \rangle = 0, \tag{2.87}$$

provided the assumption that J and ω are parallel is valid and three of the above relations in equation 2.83 are satisfied. In order to complete the transformation, the deformation parameters, β and γ, given by the relations below have to be satisfied also:

$$\hbar\omega_0\beta\cos\gamma = \kappa\langle q'_0 \rangle \tag{2.88}$$

and

$$\hbar\omega_0\frac{\sin\gamma}{\sqrt{2}} = -\kappa\langle q'_2 \rangle. \tag{2.89}$$

Therefore, self-consistency is achieved in the following way: The tilting angles, θ and ϕ of the angular momentum with respect to the PA are determined by making ω parallel to J at a fixed β, γ or by minimizing $\langle h' \rangle$.

2.5.1 Magnetic Rotation and Shears Mechanism

Earlier [Boh75] it was thought that rotational cascades are observed only as a result of a substantial nuclear deformation, with a large electric quadrupole moment being measured as opposed to a small electric quadrupole moment in near spherical nuclei. However, magnetic rotation has been proposed as a result from an anisotropic distribution of nucleonic currents. The magnetic character in nuclei is suggested to be generally indicated by the presence of intense stretched magnetic dipole (M1) and very weak or unobservable stretched cross-over electric quadrupole (E2) transitions [Fra96, Fra96a]. In addition, the ratio of the reduced transition probabilities, $\frac{B(M1)}{B(E2)}$ is high, for instance $\approx$ 15-30 $(\mu_N/eb)^2$ for the dipole bands in Pb region, while it is less than 1 $(\mu_N/eb)^2$ for well deformed nuclei [Hug93, Cla94, Fra96, Fra96a, Jen98, Wad98].

At the bandhead of the dipole bands in the Pb nuclei the proton (j_π) and neutron (j_ν) angular momentum vectors are approximately perpendicular to each other. The resultant total angular momentum vector, (J) lies along an axis which is tilted with respect to the symmetry axis through angle, θ as shown in Figure 2.10. Simultaneous alignment of j_π and j_ν (indicated by curved dotted arrows) along the tilted J axis while θ is approximately constant, increases both J (as shown by a dotted arrow along J) and the energy. The almost perpendicular coupling of j_π and j_ν contributes to a large perpendicular component of the magnetic moment vector (μ_{perp}) and thus to large B(M1).

In Figure 2.10, gradual alignment of j_π and j_ν along J causes a rapid decrease (indicated by dotted vectorial lines perpendicular to vector (J)) on μ_{perp}. Generally, the magnetic transition probability, B(M1) is proportional to μ^2_{perp}, hence, B(M1) decreases. This phenomenon is called shears mechanism [Fra93, Mac98, Mac98a, Cla97], since the alignment of the j_π

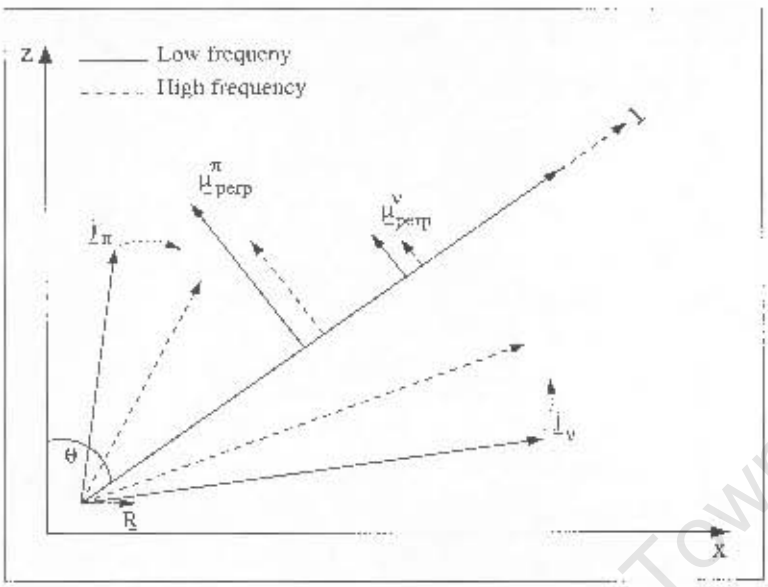

Figure 2.10: *Diagramatic representation of shears mechanism. The proton and neutron angular momentum vectors are represented by j_π and j_ν respectively. Their respective pependicular magnetic moment vector components are labelled by μ^{π}_{perp} and μ^{ν}_{perp}. The total angular momentum vector is represented by J and the angular momentum vector due to collective rotation by R. The solid and dashed arrows show the angular momentum coupling at low and high frequency.*

and j_ν vectors is analogous to closing (indicated by curve dotted arrows in Figure 2.10) the blades of a pair of shears. The work by Clark *et al.* [Cla98a], showed for the first time that the decrease in the B(M1) values with the increasing angular momentum signifies shears mechanism.

In order to have shears mechanism, high-K particle and low-K hole are needed. This can be either high-K proton particle and low-K neutron holes, as in this work, or high-K neutron particle and low-K proton holes, as in the dipole bands in the $A = 110$ region. A number of such bands were found in the mass regions $A = 80$, 130 and 200 [Sch99, Bal94].

The small angular momentum vector (R) is a result of the collective rotation of the weakly deformed core. Regular rotation-like, $J(J-1)$ sequence are predicted, provided j_π and j_ν are sufficiently long.

In electric rotation, the electric quadrupole moment results from an anisotropy

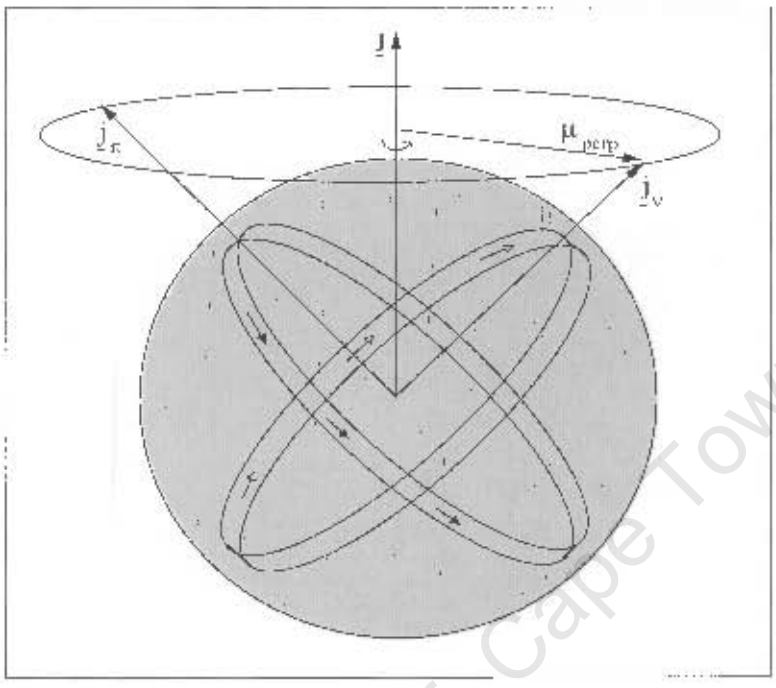

Figure 2.11: *The proton (neutron) current loops represented by filled (unfilled) arrows. The angular momentum vectors, j_π and j_ν are defined with the aid of the current loops. The total angular momentum J is along the axis which the near spherical can rotate. The perpendicular component of the magnetic moment is represented by μ_{perp}.*

in the nuclear charge distribution while in magnetic rotation the magnetic dipole moment results from an anisotropic distribution of nucleonic currents. This leads to a description of magnetic rotation known as the current loop description [Cla98, Wad98] which is shown in Figure 2.11.

An orientation is defined along the total angular momentum vector, J allowing the system to rotate quantum mechanically about the vector J axis. The angular momentum vectors, j_π and j_ν are defined by means of the current loops. The proton and neutron current loops are represented by filled and unfilled arrows respectively. The perpendicular component of the magnetic moment is denoted by μ_{perp} and increases provided the angle between j_π and j_ν vector increases.

2.5.2 Antimagnetic Rotation

Another shears mode referred to as antimagnetic rotation [Cla98] was predicted. This type of rotation occurs provided both blades of the shears (described in section 2.5.1) consist of the same type of particles (that is, either two proton (j_π) or neutron (j_ν) blades) as illustrated in Figure 2.12 (a). For

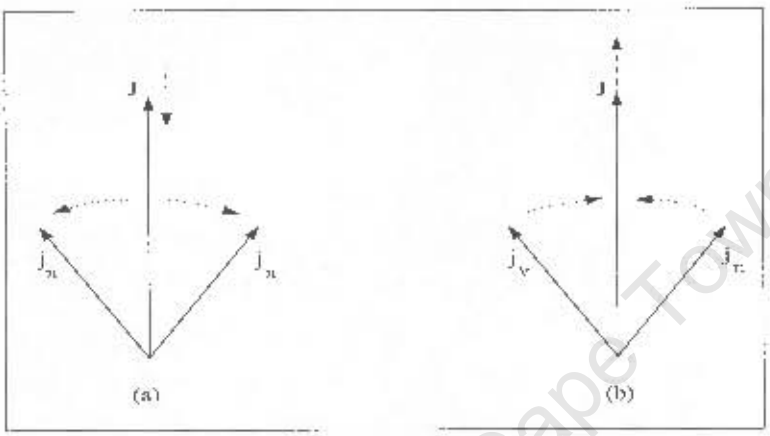

Figure 2.12: *A diagramatic illustration of the modes of rotation, that is, the (a) antimagnetic rotation which occurs if both blades of the shears consist of the same type of particle (that is, either two proton (j_π) or neutron (j_ν) blades) and (b) one which occurs when the blades close with the decrease in excitation energy.*

such a combination, there is no magnetic dipole moment produced since the individual moments are equal and opposite. However, a regular pattern of energy levels is still formed although the decay between these levels is now due to weak electric quadrupole (E2) transitions.

In Figure 2.12 (b), the shears mode is invoked when the blades consist of different type of particles and close (rather than open) with increasing excitation energy. Similarly, a regular pattern of energy levels is formed and strong M1 transitions are observed.

Chapter 3

Experimental Equipment

This chapter provides an overview of the experimental equipment used in this work, in order to study high-spin states. It describes the reaction in which ^{195,197}Bi were populated, subsequently how emitted γ-rays were detected and their energies recorded and what the target requirements were.

3.1 Heavy-Ion Fusion-Evaporation Reactions

There are several detailed reviews [Bas80, Dia80, Eji89, New74] on the formation of excited states in heavy-ion (HI) reactions[1]. In the present work, the ^{181}Ta(^{20}Ne,6n)^{195}Bi and ^{181}Ta(^{22}Ne,6n)^{197}Bi heavy-ion fusion evaporation (HIFE) reactions[2] have been employed. The above reactions involve interaction of the projectile and the target nuclei. A large amount of angular momentum can be imparted upon the target nucleus by the incident projectile. Fusion occurs from the point at which the projectile carrying sufficient energy overcomes the Coulomb barrier that exists between the target and the projectile nuclei. The HIFE process is depicted in Figure 3.1 and described below:

(a) The projectile nucleus is accelerated to an energy that is sufficient to overcome the Coulomb barrier between it and the target nucleus.

[1] (HI) reactions: those with projectile particles involving heavy ions, where a heavy-ion is defined as a nucleus with mass $A \geq 4$ [Sch81].

[2] (HIFE) reactions were first suggested by Niels Bohr in 1936 [Boh36] and later (1963) explored by Morinaga and Gugelot [Mor63].

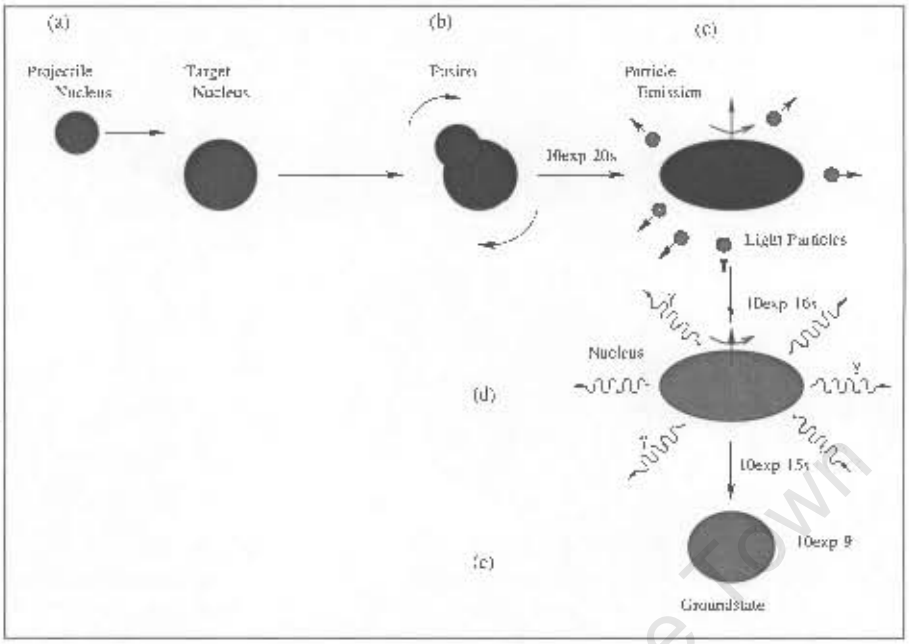

Figure 3.1: *Schematic step-by-step representation of the formation and decay of a compound nucleus through an HIFE reaction.*

(b) The projectile and the target nuclei fuse such that their identity is completely lost [Sch81], to form a highly excited and rapidly rotating compound nucleus.

(c) The compound nucleus initially de-excites through particle emission (of which the majority are neutrons (n), others are protons (p) and α-particles) and most of its excitation energy is removed.

(d) At this stage, the compound nucleus has lost sufficient energy so that its excitation energy lies below the threshold for particle emission ($\lesssim$ 10 MeV) above the yrast line[3] [Gro67]. De-excitation of the residual nucleus continues this time by γ-ray emission which can be categorised into two phases, see Figure 3.2 statistical ("cooling") and discrete ("slowing-down") emission. During the statistical emission, large amounts of energy in the form of E1 γ-rays are carried away, though very little angular momentum is removed from the residual

[3] A sequence of all states that have the lowest energy for a given angular momentum.

nuclei. The discrete emission phase involves the emission of a cascade of γ-rays along the yrast line removing a large amount of angular momentum from the system. Since in this phase the density of states is low, discrete decay sequences can be determined. This phase continues until

(e) the γ decay of residual nucleus terminates at its ground state as shown in Figure 3.1 (e)

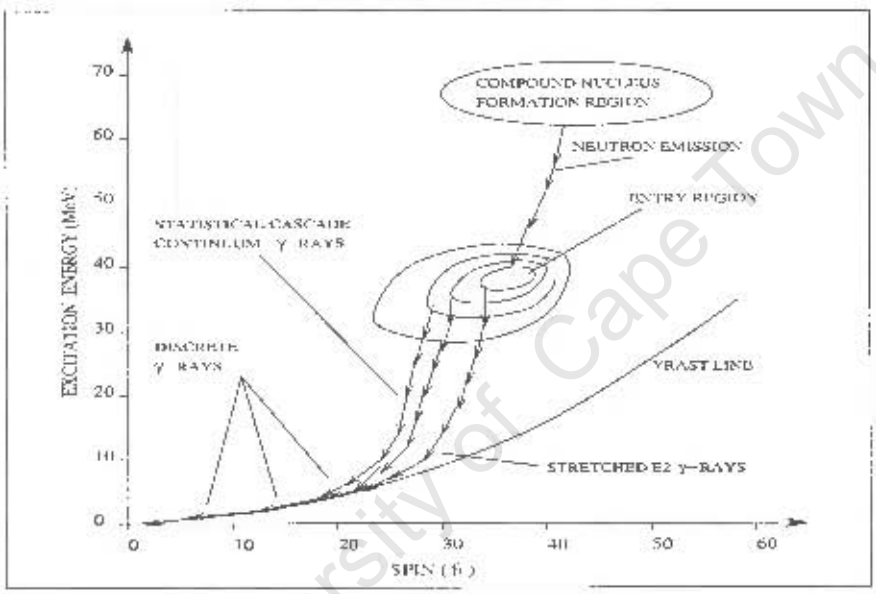

Figure 3.2: *Diagramatic representation of how an excited compound nucleus formed via HIFE decays.*

3.2 Interaction of γ-rays with Matter

In order to measure the energy of the γ-radiation emitted (during the decay of the compound nucleus) discussed in section 3.1, interaction of this radiation with the detector material [Gil95] is necessary. Figure 3.3 summarises the three main interaction processes (discussed below) of γ-rays with matter.

1. **Photoelectric Effect**: The incident photon in Figure 3.3 (a) interacts with an atomic electron (e^-) and all of its energy (E_γ) is absorbed.

The electron is ejected from the atom with the kinetic energy (E_e) given by:

$$E_e = E_\gamma \quad E_b, \tag{3.1}$$

where E_b is the binding energy of the electron. The photoelectric effect is the dominant mode of interaction at low energies (< 200 keV) and falls off rapidly with the increasing energy.

2. **Compton Scattering**: An incident photon with energy E_γ scatters off an electron and part of its energy is transferred to an electron as E_e (Figure 3.3 (b)). The remaining energy, E'_γ is carried away from a secondary photon. From conservation of energy and momentum the relationship between the energies is:

$$E'_\gamma = \frac{E_\gamma}{1 + \frac{E_\gamma}{m_e c^2}(1 - cos\theta)}, \tag{3.2}$$

where $m_e c^2$ ($= 511$ keV) is the energy corresponding to the electron rest mass and θ is the angle through which the γ-ray is scattered. Maximum energy transfer occurs at $\theta = 180°$. This process dominates

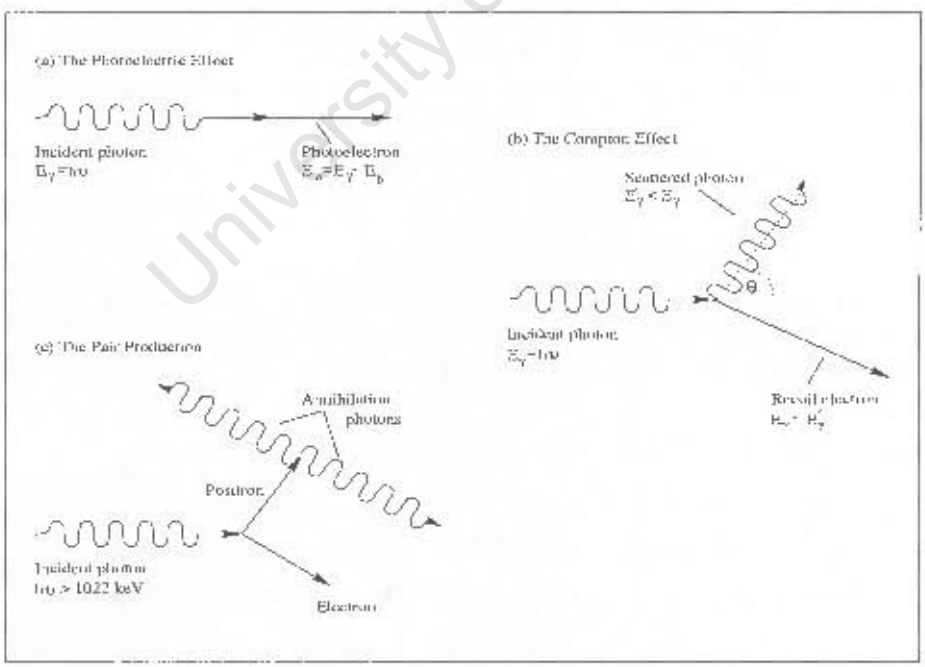

Figure 3.3: *Interaction of γ-rays with matter.*

within the energy range of (200-1000) keV, and decreases slowly as the energy increases.

3. **Pair Production**: This (Figure 3.3 (c)) process occurs only in the vicinity of the Coulombic field of an atom. The "threshold" energy required for the incident γ-ray to produce an electron-positron pair is greater than $2m_ec^2$ (>1022 keV). The excess energy over the "threshold" energy appears as the kinetic energy of an electron and a positron (e^+). Then both the electron and the positron will be slowed down in the adjacent material and the positron will finally react with an electron and annihilate. At very high energies pair production predominates and increases slowly with energy.

These three processes are employed in order to detect γ-rays in the germanium detectors used in AFRODITE array.

3.3 Experimental Equipment

In order to study high-spin states in nuclei, the following equipments are usually used:

- accelerator to produce the desired accelarated projectile particles,
- beam lines to deliver the beam to the target,
- appropriate reactions to produce the nuclei of interest with sufficient reaction rates and
- detectors with high γ-ray efficiency and good resolution.

3.3.1 Plan-view of the facilities at iThemba LABS

iThemba Laboratory for Accelerator Based Sciences (LABS)[4] has two solid-pole injector cyclotrons as shown in Figure 3.4. These are the K = 8 MeV (SPC1) [Dut87] used to accelerate light-ion and the K = 10 MeV (SPC2)

[4]Previously known as the National Accelerator Centre. The new name was officially pronounced by Dr B. S. Ngubane, Minister of Arts, Culture, Science and Technology in the Government Gazzette No. 22860, notice No. 1241, 30 November 2001 (South Africa).

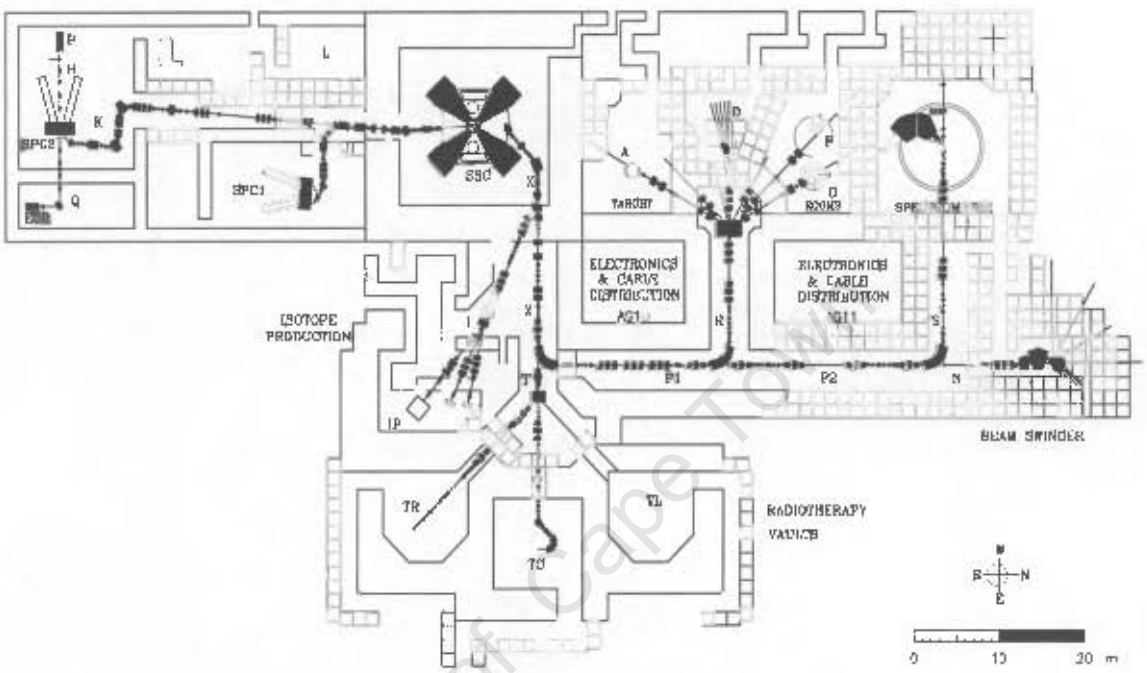

Figure 3.4: *Plan-view of the facilities (see Table 3.1) at iThemba LABS.*

Abbreviation	Name
A	Scattering chamber beam-line
D	Collimated neutron beam facility
ECR	Electron Cyclotron Resonance ion source (at the basement)
F	High-energy γ-ray detectors (AFRODITE array)
G	γ-ray angular correlation table
IP	Isotope production facility
L	Low-energy experimental vault
P	Polarised-ion source (basement)
SPC1	Solid-pole injector cyclotron for light-ions
SPC2	Solid-pole injector cyclotron heavy and polarised ions
SSC	Separated-sector cyclotron
TC	Isocentric neutron therapy
TR	Horizontal proton therapy
TL	Isocentric proton therapy (under development)

Table 3.1: *Abbreviations used on the plan-view in Figure 3.4.*

[Bot87] for heavy-ion and polarised hydrogen ion beams. The K = 200 MeV separated-sector cyclotron (SSC) [Bot87a] (of dimensions: 13.2 m in diameter and 7 m in height) has four sector magnets. The SPC2 in conjunction with the SSC were used to deliver the required ^{20,22}Ne beams both with energies $\approx$ 125 MeV. During both the experiments beams were steered from the SSC along the X, P_1 and R beam-lines (see Figure 3.4) and finally through the F-line to the AFRODITE array (discussed in section 3.3.2) of γ-ray and X-ray detectors shown in Figures 3.6 and 3.13.

3.3.2 AFRODITE Array

AFRODITE, is an acronym derived from AFRican Omnipurpose Detector for Innovative Techniques and Experiments [New98]. It is comprised of two sets of High Purity Germanium (HPGe) detectors, namely, the Low Energy Photon Spectrometers (LEPS) and the Clovers, some of which are shown in Figures 3.6 and 3.13.

The AFRODITE array aluminium frame has a rhombicuboctahedron shape with 18 square and 8 triangular facets. This shape is similar to that of the EXOGAM[5] array for nuclear spectroscopy employing the exotic beams delivered by the Systeme de Production d'Ions Radioactifs et d'Acceleration en Ligne (SPIRAL) facility at the Grand Accelerateur National d'Ions Lourds (GANIL) shown in Figure 3.5. The two square facets at 0° and 180° with respect to the beam direction accomodate the beam pipe (see Figure 3.5 for EXOGAM, Figure 3.6 and 3.13 for AFRODITE). It is worth mentioning that this configuration allows efficient shielding of the detectors from radiation emanating from the scattered beam. The top most square facet (of the AFRODITE) at 90° with respect to the beam direction supports the hydraulic target positioner discussed in section 3.4. The other 15 square facets are used for mounting the detectors as shown in Figure 3.6 and 3.13. The Clover detectors are each housed in a Compton-suppression (shown in Figure 3.6 and Figure 3.10) shield that is made of bismuth germanate $Bi_4Ge_3O_{12}$ (BGO) (section 3.3.3) which is a highly efficient scintillator for the detection of γ-rays [Eml86, Lic84].

[5]taken from: *http://www.ganil.fr/exogam/bibliographic/ng60exogam.doc*

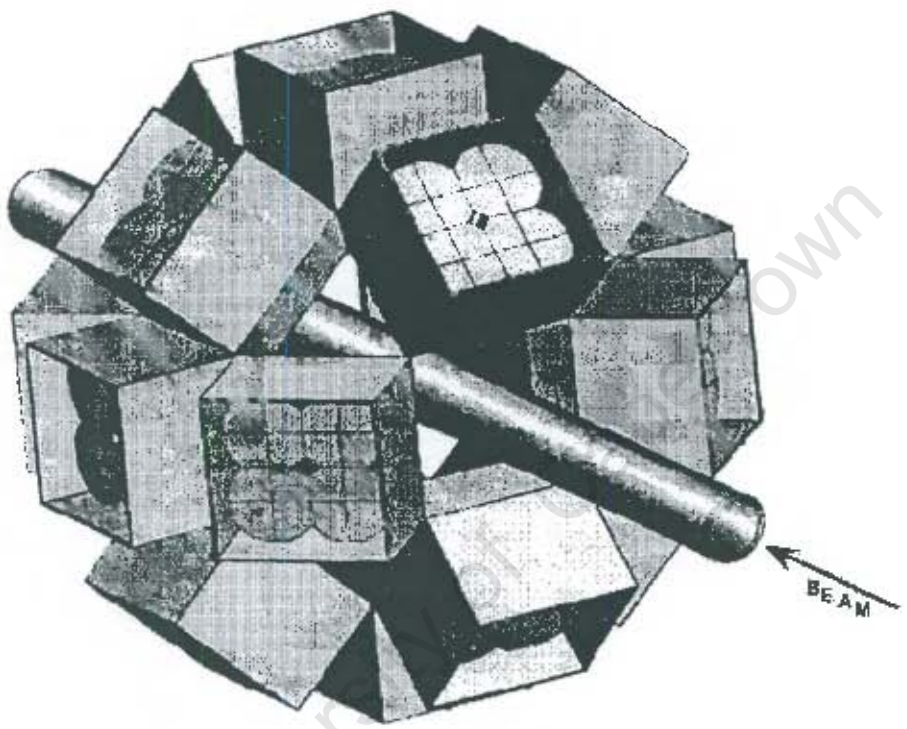

Figure 3.5: *A schematic representation of the EXOGAM, a Ge array for γ-ray spectroscopy at GANIL. The drawing is shown to emphasize the rhombicuboctahedron shape reminiscence of the AFRODITE array. EXOGAM array have three detector rings (like AFRODITE array in Figure 3.7) at 45°, 90° and 135° with respect to the beam direction and accomodate 4, 8 and 4 large segmented Clover detectors respectively (a total of 16 large segmented Clover detectors).*

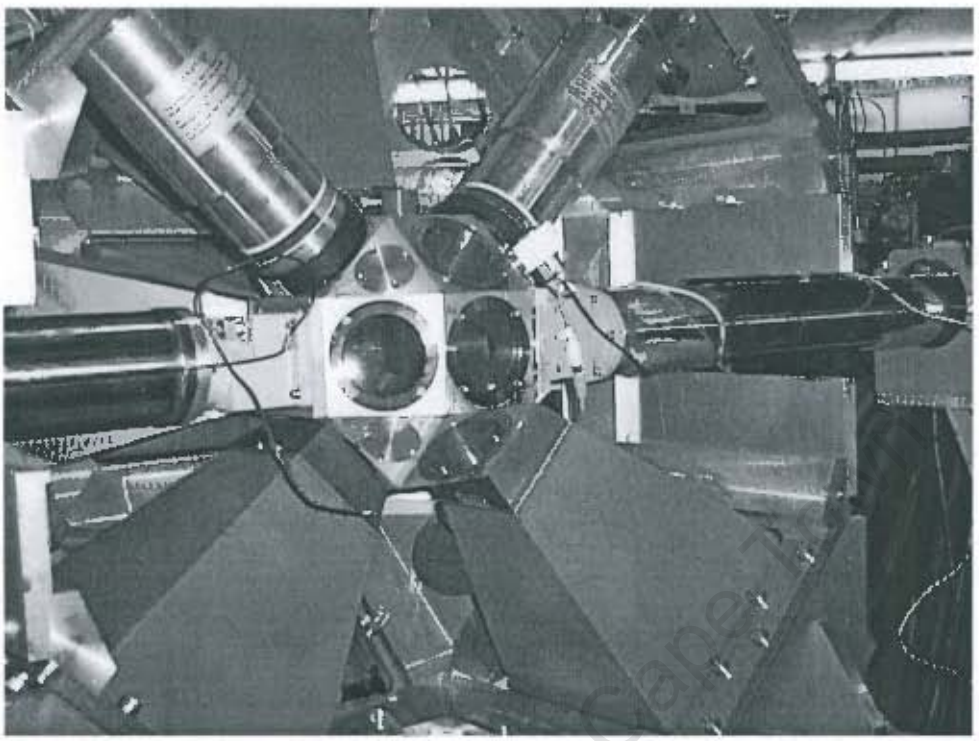

Figure 3.6: *One half of the AFRODITE array with its frame, which supports the LEPS and Clover (housed inside the BGO shield) detectors. The rhombicuboctahedron-shaped target chamber has 16 kapton windows (25 micron thick and 60 mm in diameter) in total. It is supported by the beam pipe (42 mm inside diameter) and the direction of the beam in the figure is from Right to Left (as shown in Figure 3.7).*

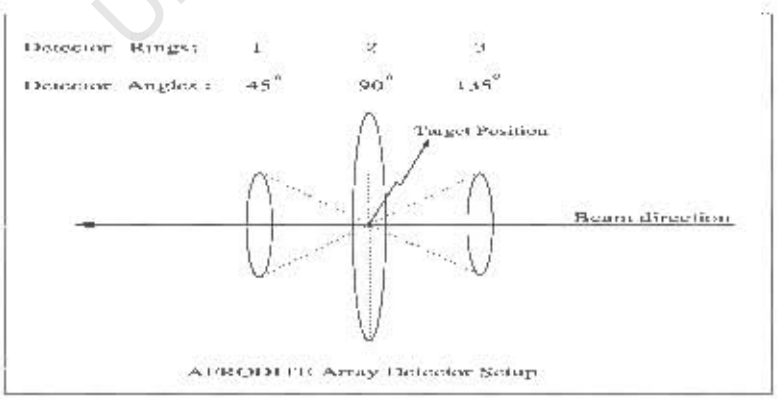

Figure 3.7: *The three AFRODITE array detector rings.*

LEPS and Clovers Detectors

LEPS detectors - consists of a single crystal of p-type HPGe with the dimensions: 10 mm thick and 60 mm in diameter. Each crystal is electrically segmented into four quadrants. The LEPS detectors are more efficient in detecting low energy ($\approx$ 30 – 300 keV) γ-rays. All the 8 LEPS (of which two can be seen in Figure 3.6) were mounted and arranged on the array at different angles: as tabulated in Table 4.1 (with beam direction from Right to Left of the reader on Figure 3.6). The LEPS detector dewars are topped with liquid nitrogen (LN_2) from the storage tank via the couplings (with black insulation around them in Figure 3.13) every 24 hours. Some technical specifications of the AFRODITE array [New98]:

- The distance from crystal surface to the target centre, $D_{tc} = 119\ mm$ for a 4 mm gap between the target chamber and the end-cap.
- The distance from the detector end-cap to the crystal surface, $D_{ec} = 15\ mm$.
- The total opening angle, $T_{ang} = 28.3°$.
- The Solid angle per detector, $S_{ang} = 1.57$ % of 4 π.

Clover detectors - one of which is depicted in Figure 3.8, consist of four n-type coaxial HPGe crystals arranged like a four-leaf Clover with a crystal spacing of about 0.2 mm apart [Jon95] as shown in Figure 3.9. The crystals (70 mm in length, 50 mm in diameter, 36 mm tapering length and 50 mm crystal surface diagonal length) are packed in a common cryostat (shown in Figure 3.8) with a tapered rectangular shape [Bea96, Duc99, Jon95]. The Clover detectors have large efficiency also for higher energy γ-rays. They give increased granularity which results in small Doppler broadening of the peaks and the possibility of add-back (adding the energies of γ-rays deposited in more than one crystal as a result of Compton scattering) which increases the photopeak efficiency. During the experiments Clover detectors were arranged in the manner tabulated in Table 4.1 to the beam direction. The Clover detectors are coupled to an automatic LN_2 filling system which top up the dewars (via the couplings covered with a black insulation in Figure 3.13)

with LN_2 from the storage tank every 12 hours. Some technical specifications of the AFRODITE array [New98]:

- $D_{tc} = 196\ mm$.
- $D_{ec} = 20\ mm$.
- $T_{ang} = 23.2°$.
- $S_{ang} = 1.34$ % of $4\ \pi$ (for a 0.2 mm distance between crystals).

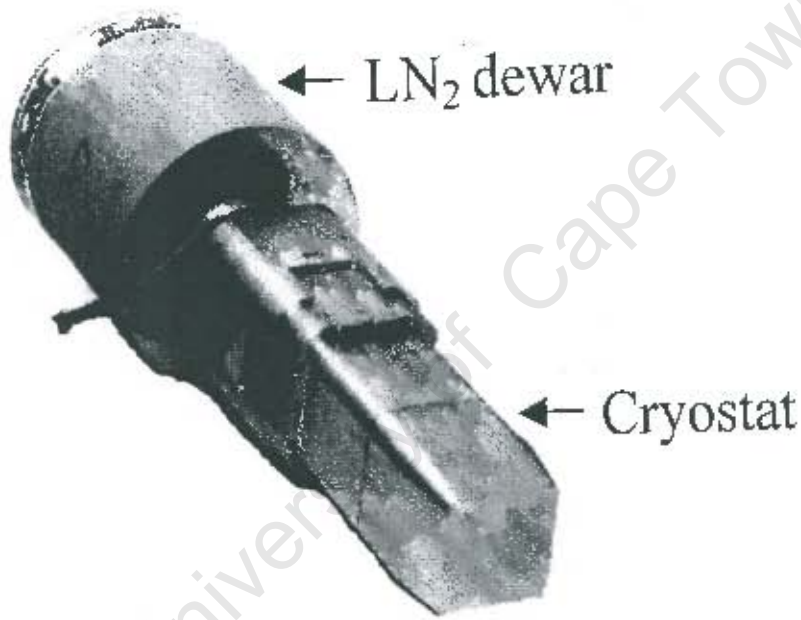

Figure 3.8: *A Clover detector, showing the tapered rectangular cryostat and a cylindrical liquid nitrogen (LN_2) dewar taken from [Duc99].*

3.3.3 Compton Suppression

The BGO ($\approx$ 26 cm in length) Compton suppression shields, one of which is shown in Figure 3.10 are essential in reducing the unwanted γ-ray Compton background. This process is referred to as Compton suppression.

The measurements for the suppressed and unsuppressed spectra were taken with a ^{60}Co radioactive source. The source was mounted on the

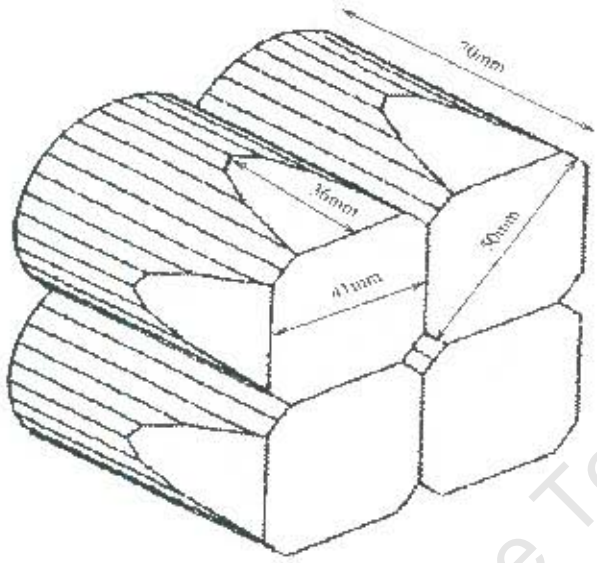

Figure 3.9: *Show how the four-leaf HPGe crystals are crafted and packed together in a Clover detector. This figure is taken from [Jon95].*

Figure 3.10: *A BGO Compton suppression shield taken from [Duc99], showing the tapered heavy metal collimator (with a 35 mm by 35 mm entrance window for γ-rays) at the front end.*

target ladder which was then placed at the target position inside the target chamber. The trigger logic was set to $(\frac{1}{15})$ detectors, that is, whenever one out of fifteen (seven BGO-suppressed Clovers, eight unsuppressed LEPS) detectors fires the event is recorded onto the tape. The constant-fraction discriminator thresholds were set at $\approx$ 40 keV before the experiment using a ^{241}Am radioactive source.

In the suppressed spectrum, the Compton scattered γ-ray events from the germanium crystal are vetoed by the BGO shield. In Figure 3.11 (a) the suppressed spectrum, which is also shown in full scale on the insert, results from the γ-ray events that were not scattered into the BGO shields. The unsuppressed spectrum contains all γ-ray events detected by the Clover detector, irrespective of whether they were scattered into the BGO shields. The unsuppressed and suppressed spectra are normalised such that the number of counts in the photo-peaks recorded are the same.

The background reduction referred to as the Compton-suppression factor (CSF) [Eml86, Lie84, Sha88] is obtained by taking the ratio of the unsuppressed spectrum to the suppressed spectrum. The CSF of about 1.4 over the (300–800) keV energy range is achieved and illustrated in Figure 3.11 (b).

The Peak-to-Total (P/T) ratio is defined as the number of counts in the photo-peak (N_{peak}) to the total number of counts in the spectrum (N_{total}), that is:

$$P/T = \frac{N_{peak}}{N_{total}}. \tag{3.3}$$

For a ^{60}Co source suppressed and unsuppressed spectra depicted in Figure 3.11, the ratios: $P/T = \frac{N_{1173+1332\ keV}}{N_{total\ above\ 100\ keV}} \approx 0.27$ and 0.48 were determined for experiment I respectively. $N_{1173+1332\ keV}$ is the sum of the number of counts in the photo-peaks at 1173 and 1332 keV. While $N_{total\ above\ 100\ keV}$ is the total number of counts in the spectrum above 100 keV. The P/T was previously found for a ^{137}Cs source (with a single photo-peak at 662 keV) suppressed and unsuppressed spectra to be 0.38 and 0.57 respectively (for the sum of 8 Clovers, with all elements considered) [New98].

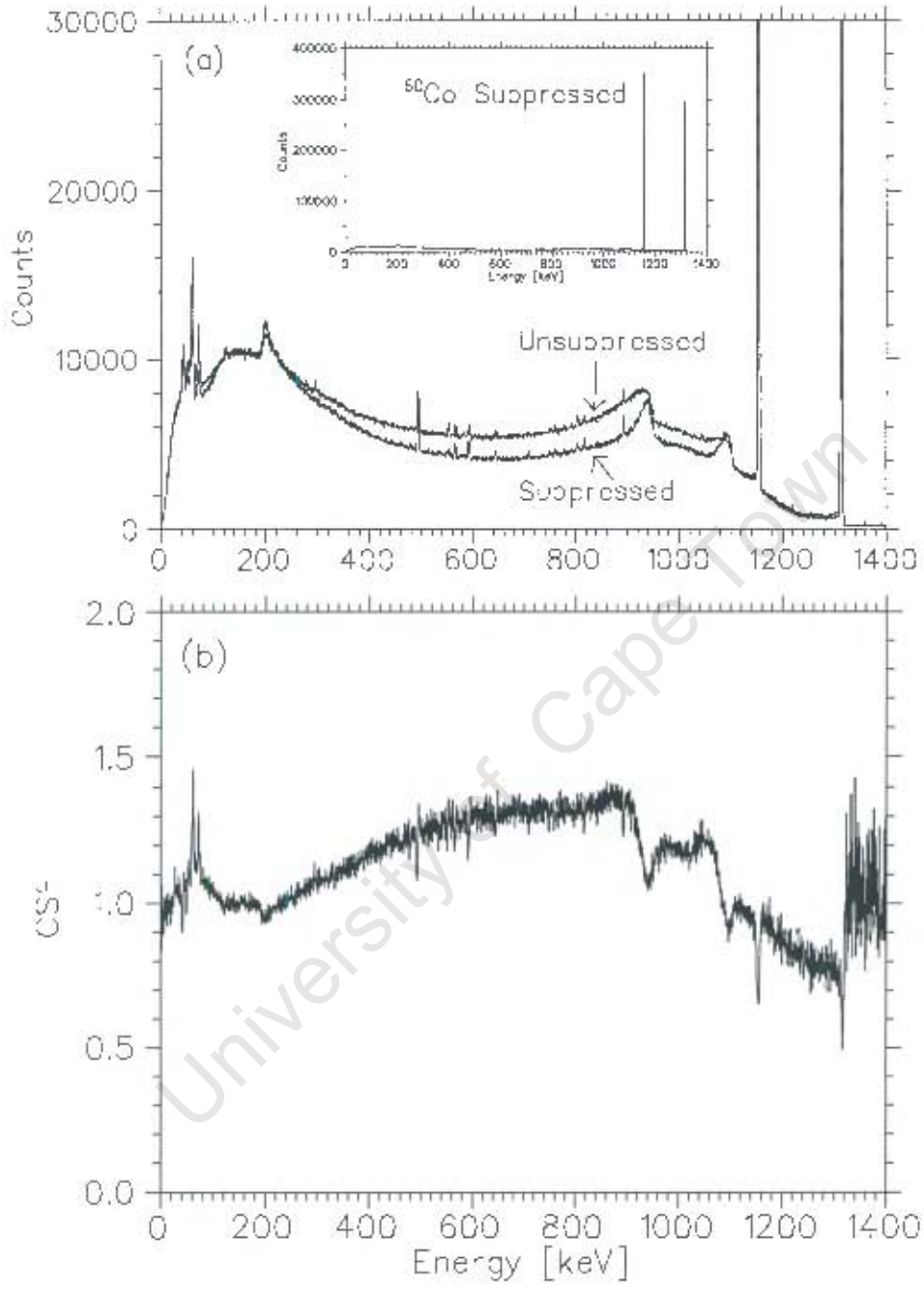

Figure 3.11: *Shows the sum of all Clover elements (a) Compton-suppressed (with a BGO shield to veto the scattered events) and the unsuppressed (without a BGO shield) γ-ray spectra from a ^{60}Co radioative source. The suppressed spectrum is shown on the insert in full scale. (b) Indicates the Compton-suppression factor (CSF) derived from the ratio of the unsuppressed to the suppressed spectra. Both spectra are normalised such that the number of counts in the photo-peaks are the same.*

3.3.4 The Electronics and Data Acquisition System

The standard Nuclear Instrumentation Module (NIM) and Computer Automated Measurement and Control (CAMAC) units were used to set the circuit depicted in Figure 3.12 in the AFRODITE vault marked F in Figure 3.4. The VAX-station 4000-VLC in the vault runs the VMS operating system and the XSYS[6] [Pil92] software package. XSYS software package is employed for various duties before (adjusting the ADC thresholds, zero offsets and setting status words) and during the experiment (data acquisition, monitoring online spectra and event rates).

The electronic circuit diagram depicted in Figure 3.12 consist of two

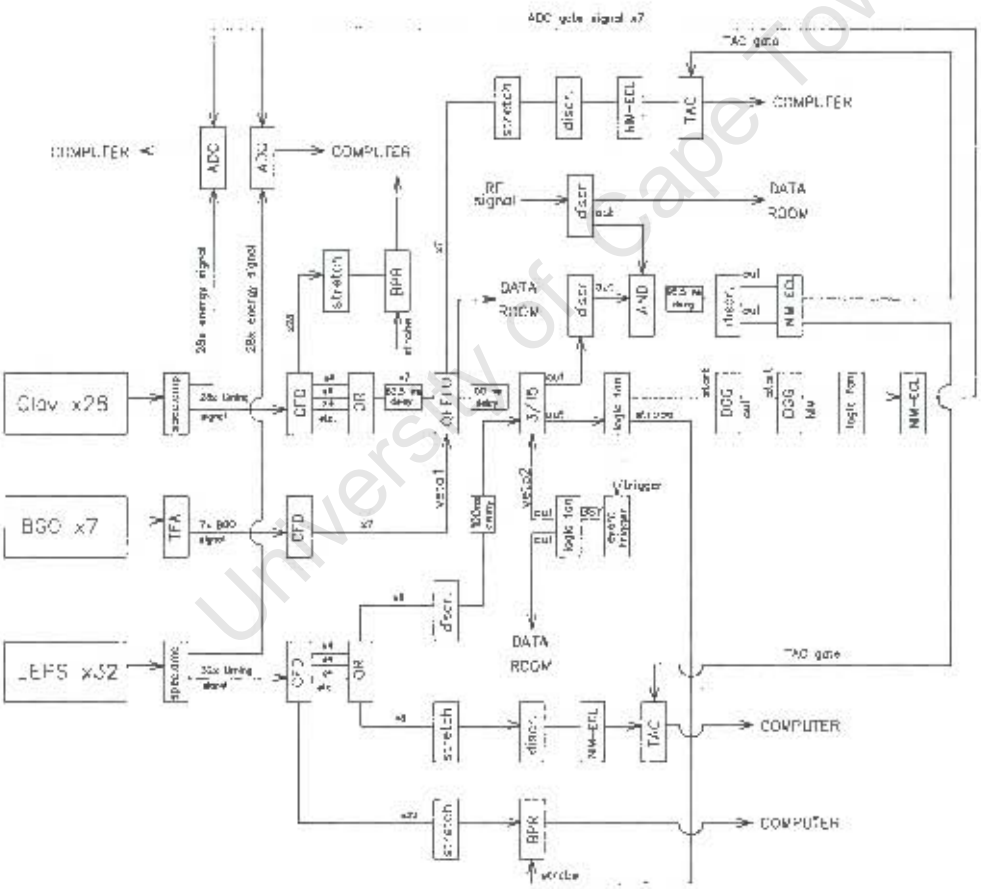

Figure 3.12: *The AFRODITE array electronics [Rou01].*

sub-circuits, namely, an energy and a timing circuit. The details of the

[6] a general purpose data acquisition system, Indiana University report (1985).

Table 3.2: *Electronic modules used for AFRODITE array.*

Module	Model
Analogue-to-Digital Converter (ADC)	Silena 4418/V
Bit Pattern Register (BPR)	(*i*Themba LABS)
Coincidence Unit ($\frac{3}{16}$) coincidence	(*i*Themba LABS)
Constant Fraction Discriminator (CFD)	CAEN N415A or Ortec 934
Discriminator	Phillips 711 or LeCroy 821
Dual Gate Generator (DGG)	LeCroy 222
Event Trigger	(*i*Themba LABS)
Logic Fan-In/Fan-Out (FIFO)	LeCroy 429A
NIM-ECL converter	EDA54 (*i*Themba LABS)
Quad Four-Fold Logic Unit (QFFLU)	Phillips 755
Spectroscopy Amplifier	CAEN N568
Stretcher	(*i*Themba LABS)
Time Amplitude Converter (TAC)	Silena 4418/T
Timing Filter Amplifier (TFA)	Ortec 474

entire circuit with relevant hardware as given in Table 3.2 are discussed in [Rou01]. For the present work, up to 60 electronic signals from 32 Clover, 28 LEPS and 7 BGO detector elements (see Figure 3.13) were processed (see Figure 3.12).

3.4 Target and Beam Requirements

Prior to the experiments (in section 4.1) the target thickness and material were confirmed by performing Particle Induced X-ray Emission (PIXE) analysis [Pro95], at the Materials Research Group at *i*Themba LABS. Thin[7] metallic tantalum (which is 99.988 % ^{181}Ta and only 0.012 % ^{180}Ta) foil targets of $\approx$ 399.6 μg.cm^{-2} and $\approx$ 333.0 μg.cm^{-2} were then employed during the experiment I and experiment II respectively. It is worth mentioning that thin targets were employed in order to avoid Doppler broadening of the peaks.

The target foil (^{181}Ta), aluminium oxide viewer (ruby) and an empty-frame were loaded on the target ladder (of aluminium material) as shown in Fig-

[7] $\leq$ 1000 μg.cm^{-2} [Ada84].

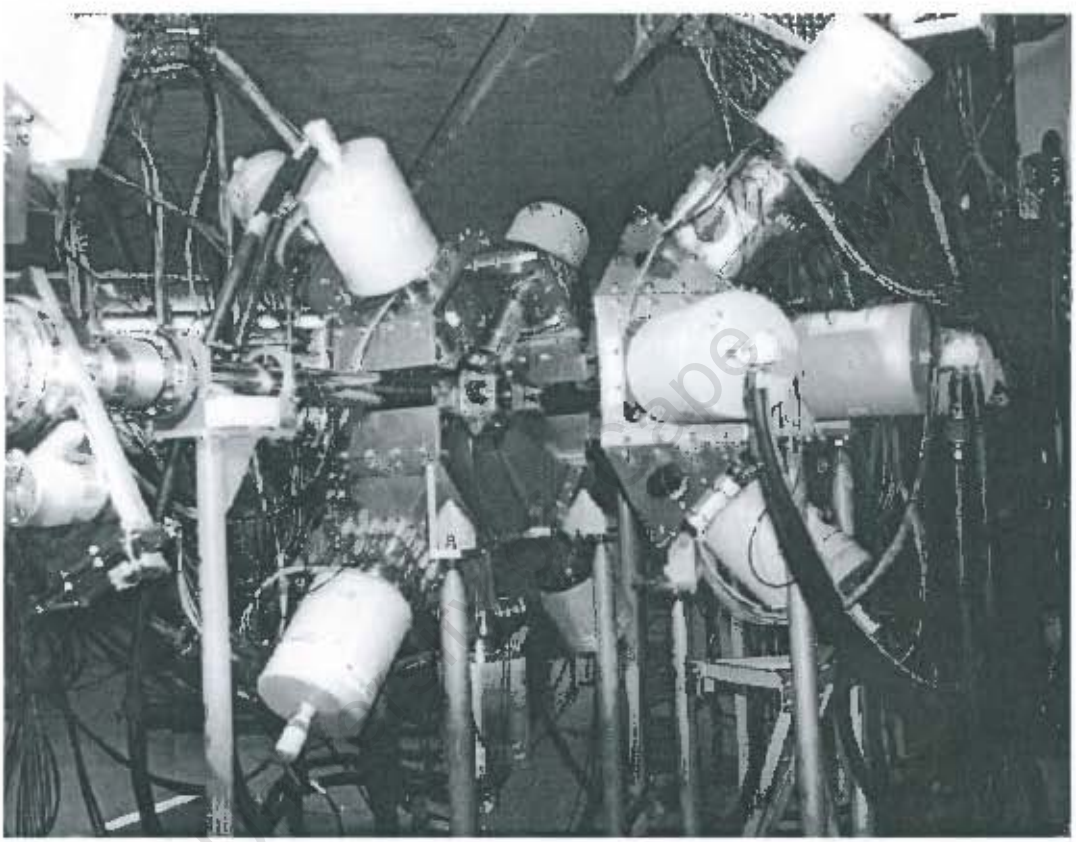

Figure 3.13: *The right and left (pulled back) caps of the AFRODITE aluminium frame respectively. The frame supports the LEPS and Clover (housed inside the BGO shield) detectors. The Liquid Nitrogen (LN_2) couplings to the dewars are shown (with black insulation around them).*

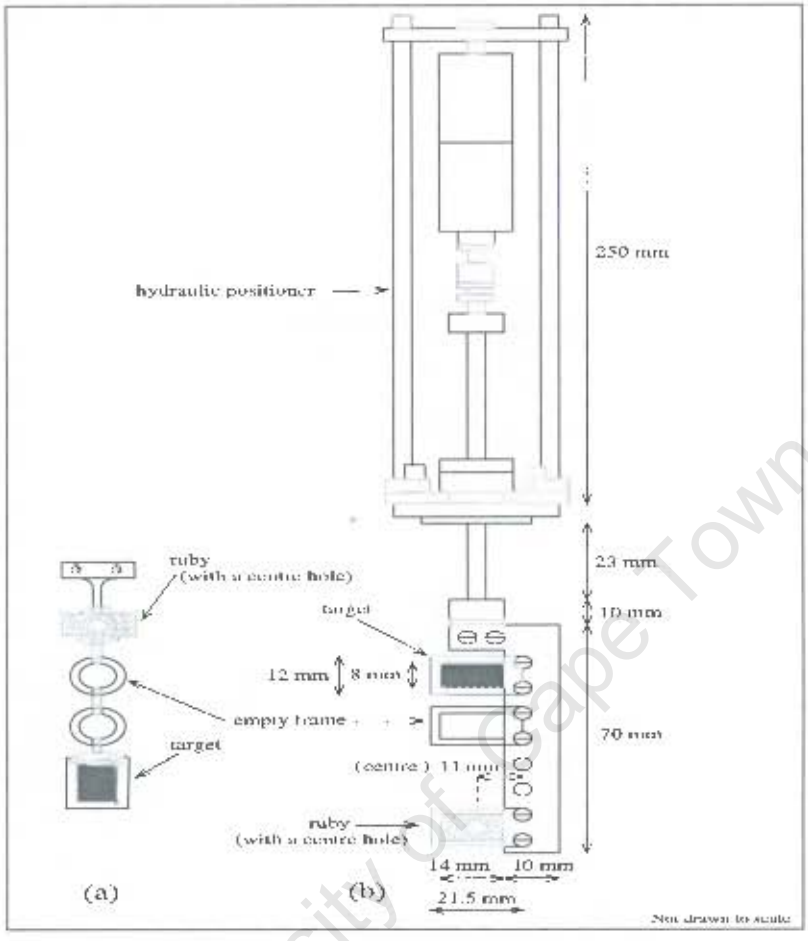

Figure 3.14: *Diagramatic representation of (a) the manually adjusted target ladder used in experiment I and (b) target ladder mounted onto the automatically operated hydraulic positioner used in experiment II.*

ure 3.14 (a) and (b) for experiment I and II respectively. For experiment I the target-ladder in Figure 3.14 (a) was mounted on the manually operated target-ladder holder (not shown on the Figure 3.14) and controlled either up or down in steps of 15 mm from the AFRODITE vault. This involved switching off the beam from the control room in order to get access to the vault. A newly designed target-ladder and a hydraulic positioner shown in Figure 3.14 (b) (which is presently being used in the array) were employed during experiment II. The target-ladder mounted on the hydraulic positioner which can be controlled from the vault or data room via the automatic switch

during beam tuning.

The sixteenth facet (the top one at 90° with respect to the beam direction) of the rhombicuboctahedron-shaped target chamber (in Figure 3.6) is used to support the target holder (Figure 3.14 (a)) or both the target ladder and the hydraulic positioner depicted in Figure 3.14 (b).

The target chamber and the beam line are then evacuated prior to beam tuning. The beam is tuned from the control room by focusing it first through the centre-hole (3 mm in diameter) of the ruby. Fluorescence is observed on the computer monitor via the camera mounted on the target chamber (see Figure 3.6) when the beam interacts with the material of the ruby. The beam is steered and focused to the centre-hole on the ruby (such that no fluorescence is observed) through adjustments to the dipole magnets, quadrupole magnets and the solenoid lenses. Subsequently, the empty-frame is positioned to the beam-spot in order to check the halo[8]. Finally, the ^{181}Ta is positioned at the beam-spot. The beam intensity is further optimised with respect to the counting rate of the detectors. Subsequently data aquisition commences.

It is worth mentioning that the SSC at iThemba LABS is capable of delivering various beams tabulated in Table 3.3 which are used for the following purposes: physics experiments (on weekends), radioisotope production, proton and neutron therapy. In addition, the decision concerning the formation of the ^{195,197}Bi nuclei for the present work involved consideration of the beams available at iThemba LABS.

[8] whether the beam with maximum intensity does not hit the target frame and also to measure the background counting rate.

Table 3.3: *Heavy ion beams delivered by the SSC at iThemba LABS.*

Ion	Charge state	Beam energy (MeV)
$^{1}_{1}$H	1+	66, 200
	2+	32
$^{4}_{2}$He	2+	65, 180, 200
$^{11}_{5}$B	2+	55, 60
$^{12}_{6}$C	3+	58, 150
	4+	100, 150, 180, 200, 230
	5+	300, 320, 360, 380, 400
$^{13}_{6}$C	3+	82
$^{14}_{7}$N	4+	140
	5+	250
	6+	400
$^{16}_{8}$O	3+	100
	5+	200, 250, 300
	6+	400
$^{18}_{8}$O	4+	85, 90, 110
$^{20}_{10}$Ne	4+	110, 115, 120, 125
$^{22}_{10}$Ne	4+	125
$^{24}_{12}$Mg)[a]	5+	
$^{27}_{13}$Al	7+	130, 155
$^{28}_{14}$Si	5+	141
$^{32}_{16}$S)[a]	11+	
	9+	250, 205
$^{40}_{18}$Ar	8+	280, 380
$^{40}_{20}$Ca)[a]	8+	
$^{56}_{26}$Fe)[a]	11+	
$^{64}_{30}$Zn	10+	165, 260
$^{79}_{35}$Br)[a]	14+	
$^{84}_{36}$Kr	13+	420
$^{84}_{36}$Kr	14+	462
	15+	420, 450, 530
$^{121}_{51}$Sb	22+	700
$^{127}_{53}$I	22+	730
$^{129}_{54}$Xe	17+	460
	22+	790
$^{131}_{54}$Xe	16+	350
$^{136}_{54}$Xe	22+	757, 750
$^{184}_{74}$W)[a]	17+	
$^{202}_{80}$Hg)[a]	21+	

)[a] Not sent through the SSC.

Chapter 4

Experiments and Data Analysis Procedure

The coincidence data acquired during the ^{181}Ta+^{20}Ne and ^{181}Ta+^{22}Ne experiments I and II respectively, have been stored as raw pulse heights onto the magnetic Digital Linear Tapes (DLT). At the end of the experiments the tapes are replayed to transform the event data to suitable forms in order to facilitate the analysis procedures.

4.1 The Experiments

The work reported in this thesis is based on the study of the ^{181}Ta(^{20}Ne, $6n$)^{195}Bi (experiment I) and ^{181}Ta(^{22}Ne, $6n$)^{197}Bi (experiment II) HIFE reactions. The excitation functions for these two reactions are presented in Figure 4.1, as predicted by the statistical-model calculations using PACE2 [Gav80, Gav93] code. These predictions were used to select beam energies suitable to conduct the experiment using the above reactions. Fission is predicted to be dominant and was therefore expected to contribute significantly to the background.

Although ^{193}Tl and ^{195}Tl do not appear significantly in the PACE2 calculations (in Figure 4.1) for the ^{181}Ta + ^{20}Ne and ^{181}Ta + ^{22}Ne reactions respectively, a significant population of these isotopes were observed in experiment I and experiment II data probably due to a different reaction

mechanism such as incomplete fusion. The dominant residual nuclei at a beam energy of 125 MeV predicted by the PACE2 calculations for both experimental reaction are given in Table 4.1.

The experimental details are summarised in Table 4.1. Measurements of the

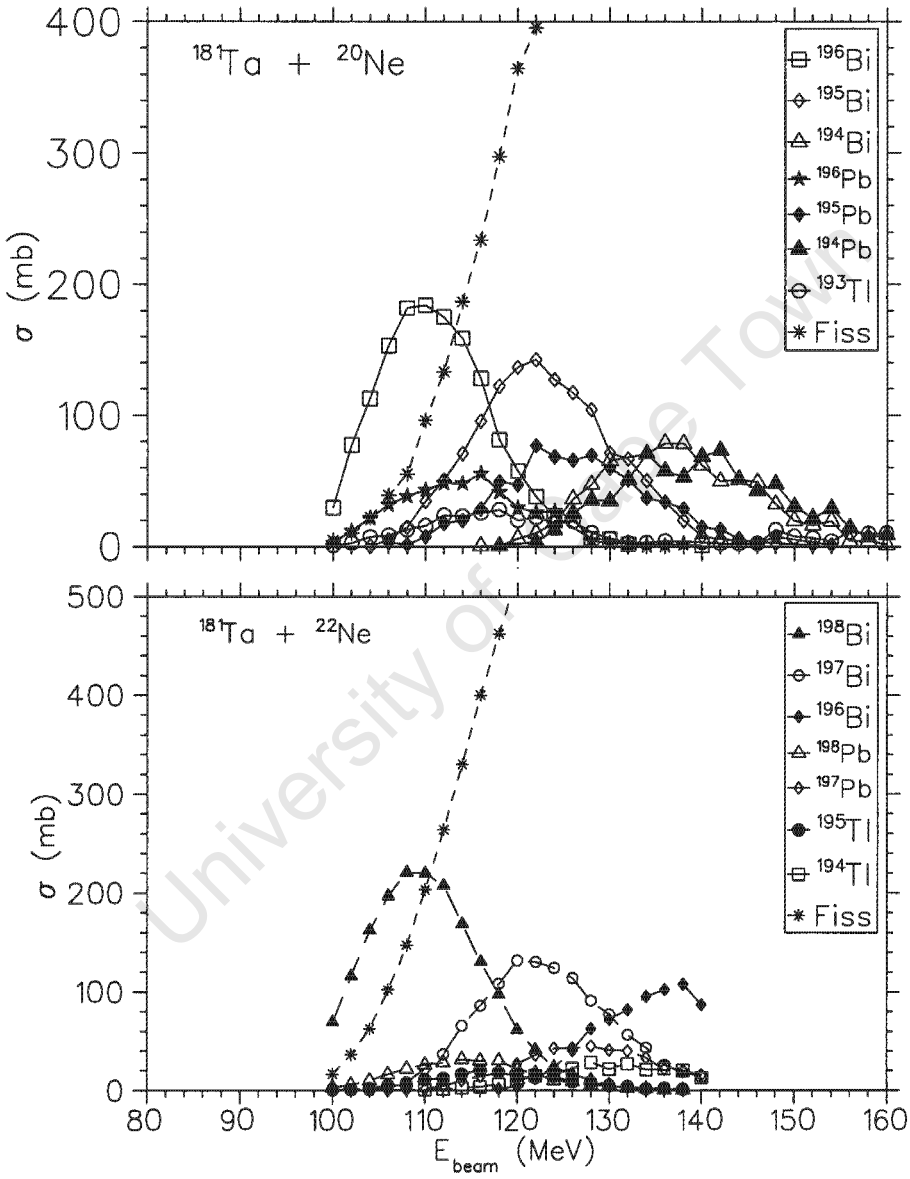

Figure 4.1: *The excitation functions (cross-section σ) predicted by the statistical-model code PACE2 [Gav80, Gav93] following the ^{181}Ta+^{20}Ne and ^{181}Ta+^{22}Ne reactions. A beam energy of about 125 MeV was chosen for both experiments. The curve with stars represent fission in both panels.*

first and second experiment with projectiles ^{20}Ne and ^{22}Ne respectively were both conducted at a beam energy of about 125 MeV. The beam energy was 29 % and 28 % above the Coulomb barrier for first and second experiments respectively. The beam was delivered by the SSC (in section 3.3.1). The beam current for these experiments were varying between 9 and 10 nA for both the ^{181}Ta+^{20}Ne and ^{181}Ta+^{22}Ne reactions. The beam burst separation was 64 and 66 ns for experiment I and II respectively.

Three and four weekends, each of eight shifts (8 hours each) of beam time were allocated[1] for experiment I[2] and II[3] respectively. The trigger logic adopted was $(\frac{3}{15})$ detectors, that is, at least three out of fifteen (seven BGO suppressed Clovers, eight unsuppressed LEPS) detectors had to fire before γ-ray coincidence events were recorded onto tape. About 750×10^6 and 528×10^6 total γ-γ events were recorded (onto the magnetic DLT tapes) for experiment I and II respectively. Only two-thirds of experiment I data were considered for analysis. The reason for that was that, most of the runs in the first weekend data showed a nonlinear behaviour (which was impossible to gainmatch as described in section 4.3) in the low energy region. This was due to an incorrect polarity setting on the amplifiers.

4.2 Energy Calibrations

The energy calibration data were acquired before and after each weekend of the two experiments in singles mode using ^{152}Eu and ^{133}Ba radioactive sources. Prior to these measurements, one specific source per run was mounted on the target ladder which was then placed at the target position inside the target chamber. The energy calibration parameters for both experiments were generated from the source data acquired before each weekend of both experiments.

The centroids of the photopeaks from the source (^{152}Eu and ^{133}Ba) spectra determined using the AUTOCAL-NEW [Law97], a peak-fitting program.

[1] by the iThemba LABS Programme Advisory Commettee (PAC).

[2] performed during weekends from Friday night to Monday morning: 03-06 Dec. 1999, 10-13 Dec. 1999 and 17-20 Dec. 1999.

[3] performed during weekends from Friday night to Monday morning: 22-25 Sept. 2000, 29 Sept.–02 Oct. 2000, 06-09 Oct. 2000 and 13-16 Oct. 2000.

Table 4.1: *Summary of the experimental details.*

Miscellaneous	Experiment I	Experiment II
45° detectors	2 Clovers, 2 LEPS	2 Clovers, 2 LEPS
90° detectors	3 Clovers, 4 LEPS	3 Clovers, 4 LEPS
135° detectors	2 Clovers, 2 LEPS	2 Clovers, 2 LEPS
Total number of BGO's	7	7
target ladder w.r.t the beam axis	22.5°	22.5°
target	^{181}Ta $\approx$ 399.6 μg.cm^{-2}	^{181}Ta $\approx$ 333.0 μg.cm^{-2}
beam	$^{20}_{10}$Ne	$^{22}_{10}$Ne
beam current	(9-10) nA	(9-10) nA
charge state	4 +	4 +
beam-burst separation	63 ns	66 ns
pulse selection	none	none
beam energy, week 1	125.70 MeV	125.15 MeV
beam energy, week 2	126.83 MeV	125.02 MeV
beam energy, week 3	124.40 MeV	125.25 MeV
beam energy, week 4	none	126.21 MeV
recoil velocity (β)	0.0104 (5)	0.0100 (5)
compound system	^{201}Bi	^{203}Bi
dominant residuals at 125 MeV (PACE 2)	^{196}Bi (0.4%), ^{196}Pb (0.4%), ^{195}Bi (8.9%), ^{195}Pb (4.4%), ^{194}Bi (2.2%), ^{194}Pb (1.6%), ^{193}Tl (0.5%).	^{198}Bi (1.7%), ^{198}Pb (0.9%), ^{197}Bi (12.1%), ^{197}Pb (4.6%), ^{196}Bi (4.3%), ^{195}Tl (0.9%), ^{194}Tl (2.4%).
fission at 125 MeV	78.7%	72.2%
event trigger condition	$\geq$ 3	$\geq$ 3
number of events	750$\times$10^6	528$\times$10^6
readout	Ferabus	Ferabus

The program fits a linear function of the form $T_e = aM_e + b$ in order to generate a set of initial linear energy calibration parameters (LECP): a and b, for all elements of the LEPS and Clover detectors used during the experiments. The true γ-ray energy and the measured pulse height are denoted by T_e and M_e, respectively.

4.3 Gaindrift Corrections

The initial LECP (in section 4.2) were then tested by loading them into an XSYS [Gou83, Gou81, Pil92, Pil88] event analysis language (EVAL) code, subsequently sorting[4] all of the in-beam data. This sort was aimed at tracing possible detector (LEPS and Clovers) gaindrifts that might have occurred during the in-beam runs. Major gaindrifts within (1-3) keV range between some of the in-beam runs were observed from spectra generated after sorting. The cause of the gaindrifts between some of the in-beam runs was investigated by Dowie and Mullins [Dow00]. It is likely that temperature fluctuations in the AFRODITE vault affect the amplifiers such that the output signals drift. Therefore, it was necessary to perform the gaindrift corrections as part of data analysis procedure.
The remedial prescription given below was adhered to for the gaindrift corrections:

- The in-beam reference spectra (IRS) (in most cases obtained from the first runs) for the LEPS and Clover elements were chosen either from the runs which were gainmatched or not gaindrifted. In Figure 4.2, a single in-beam gainmatched reference spectrum (IRS) (solid-line) and the in-beam gaindrifted spectrum (IGS) (dashed-line) both extracted from a single run are shown with the 57.53 keV Ta $K_{\beta 1}$ X-ray peak (P_{1l}) and the 1039.5 keV ^{70}Ge peak (P_{1h}) of the IRS chosen as reference peaks.

- The peak-shifts which are the channel differences between the reference peaks (of the IRS) and the shifted peaks (of the IGS) are determined

[4]Sorting the event data from the magnetic DLT tape to the disk through the EVAL computer software program in a more user friendly form.

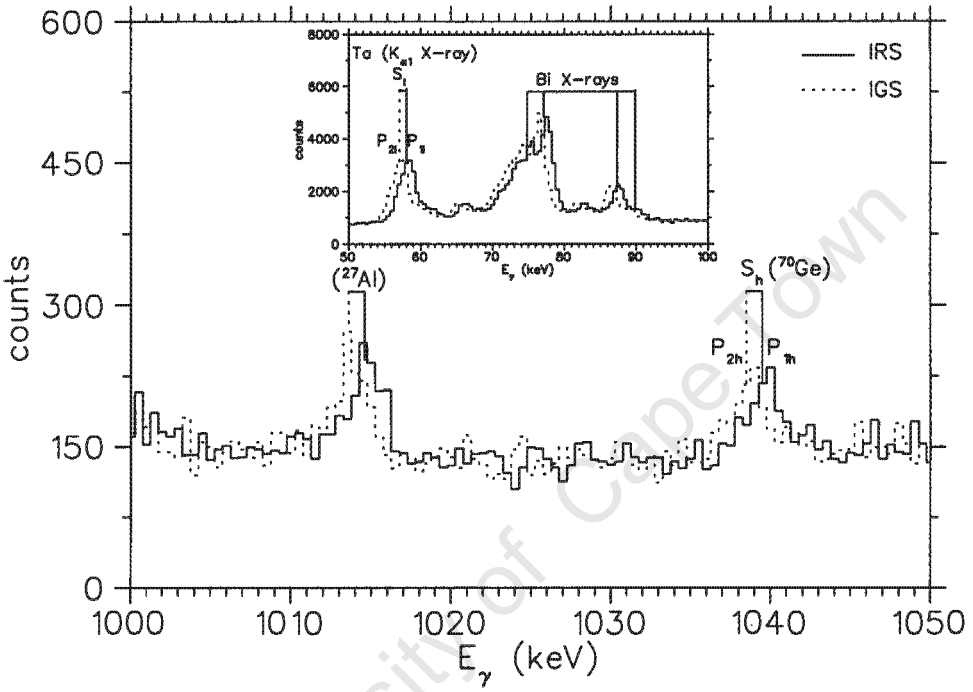

Figure 4.2: *A sample of a gainmatched in-beam reference spectrum (IRS) (solid-line) superimposed with a gaindrifted (IGS) (dashed-line) spectrum of the same Clover element. In this case, a common shift of about* $S_l = S_h = -2\ chn = -1\ keV$ *between the IRS and IGS peaks at the low and high energy regions were observed respectively. The insert depicts a mismatch at the low energy region between IRS and IGS single Clover element spectra. The exact peak-positions associated with the Bi* $K_{\alpha2,\alpha1}$, $K_{\beta1,\beta2}$ *and Ta* $K_{\alpha1}$ *X-rays are indicated by solid lines.*

from $(P_{1l}) - (P_{2l}) = S_l$ and $(P_{1h}) - (P_{2h}) = S_h$, where S_l and S_h are the peak-shifts (in channels) for the peak at the low and high energies respectively.

- The following cases arise:
  If $P_{1l} > P_{2l}$ then $S_l < 0$ and similarly, if $P_{1h} > P_{2h}$ then $S_h < 0$.
  If $P_{1l} < P_{2l}$ then $S_l > 0$ and similarly, if $P_{1h} < P_{2h}$ then $S_h > 0$.

- The final parameter a' (slope or gain) for both LEPS and Clovers were calculated by substituting the initial LECP (from section 4.2), peak positions and the shifts in the equation:

$$a' = \frac{a\,(P_{1h} - P_{1l})}{(P_{1h} + S_h) - (P_{1l} + S_l)}. \tag{4.1}$$

- The final parameter b' (off-set) is given by the equation:

$$b' = D\left(\frac{(P_{1l}S_h - P_{1h}S_l)}{(P_{1h} + S_h) - (P_{1l} + S_l)}\right) + \frac{b\,(P_{1h} - P_{1l})}{(P_{1h} + S_h) - (P_{1l} + S_l)}, \tag{4.2}$$

  where D is the dispersion, which is 0.2 and 0.5 keV/channel for the LEPS and Clovers detectors respectively.

- The data were then sorted for the second time, each run with its own new set of the LECP (a' and b'), and hence these spectra were matched with the IRS, which maintained a good energy resolution.

Therefore, each run had its own correct set of the LECP which were used during the analysis procedures.

4.4 Data Structure

The event-by-event data in XSYS [Gou83, Gou81, Pil92, Pil88] format were sorted into various data structures with the aid of the XSYS Event Analysis Language (EVAL) [Gou83, Gou81] codes. Prior to sorting procedures, the EVAL codes were modified to produce the required data structures as tabulated in Table 4.2 and 4.3. The gates may be set in order to allow selected events to be incremented into the particular data structure generated during sorting.

Table 4.2: *Summary of the data structures for experiment I.*

Experiment I			
Data structure	*Gate(s)*	*Gate(s) position*	*Detectors*
matrix	none	none	7 Clovers
gated matrix	LEPS Bi X-rays	$K_{\alpha 2}$ (374-380) channel)[a] $K_{\alpha 1}$ (381-390) channel)[a]	7 Clovers
DCO matrix	none	none	4 Clovers at 45°; 135° vs 4 Clovers at 45°; 135°
DCO matrix	none	none	4 Clovers at 45°; 135° vs 3 Clovers at 90°
1-dim. spectra, single shadowed, unshadowed	LEPS Bi X-rays	$K_{\alpha 2}$ (374-380) channel)[a] $K_{\alpha 1}$ (381-390) channel)[a]	6 Clover elements at 96° and 84°
1-dim. spectra, doubles in horz. or vert. elements	LEPS Bi X-rays	*ditto*	3 Clovers at 90°
1-dim. spectra, doubles in horz. or vert. elements	none	none	3 Clovers at 90°

)[a] Dispersion for the LEPS and Clovers is 0.2 and 0.5 keV per channel respectively.

Table 4.3: *Summary of the data structures for experiment II.*

Experiment II			
Data structure	*Gate(s)*	*Gate(s) position*	*Detectors*
matrix	none	none	7 Clovers
gated matrix	LEPS Bi X-rays	$K_{\alpha 2}$ (374-380) channel)[a] $K_{\alpha 1}$ (381-390) channel)[a]	7 Clovers
DCO matrix	none	none	4 Clovers at 45°; 135° vs 4 Clovers at 45°; 135°
DCO matrix	none	none	4 Clovers at 45°; 135° vs 3 Clovers at 90°
1-dim. spectra, single shadowed, unshadowed	LEPS Bi X-rays	$K_{\alpha 2}$ (374-380) channel)[a] $K_{\alpha 1}$ (381-390) channel)[a]	6 Clover elements at 96° and 84°
1-dim. spectra, doubles in horz. or vert. elements	LEPS Bi X-rays	*ditto*	3 Clovers at 90°
1-dim. spectra, doubles in horz. or vert. elements	none	none	3 Clovers at 90°

)[a] Dispersion for the LEPS and Clovers is 0.2 and 0.5 keV per channel respectively.

Table 4.4: *X-ray energies for Bi, Tl and Ta.*

X-ray energies (keV))[a]				
Element	$K_{\alpha 2}$	$K_{\alpha 1}$	$K_{\beta 1}$	$K_{\beta 2}$
Bi	74.81	77.11	87.34	89.86
Tl	70.83	72.87	82.58	84.95
Ta	56.28	57.53	65.22	67.01

)[a] taken from [Reu83].

4.5 Doppler-Shift Corrections

The Doppler-shift corrections for the detected γ-rays were necessary for this work since thin ^{181}Ta targets (in section 3.4) were employed in both experiments. Hence, the residual nuclei recoil into vacuum so that the detected γ-rays were subjected to energy shifts according to the equation:

$$E'_{\gamma} = E_{\gamma}(1 + \beta cos\theta), \tag{4.3}$$

where E'_{γ} is the Doppler shifted γ-ray energy, E_{γ} is the unshifted γ-ray energy (detected normal to the recoil nucleus velocity axis) and θ is the angle between the γ-ray and the beam axis.

The Doppler-shifts for the γ-rays emitted by the recoiling ^{195,197}Bi nuclei have been measured for the Clover elements located at 39°, 51°, 129°, and 141°. The recoil velocities were calculated using the above equation and the average $\beta = \frac{v}{c}$, (where v is the velocity of the nucleus and c the speed of light) values obtained were $\beta \approx 1.04 \pm 0.05$ % and $\beta \approx 1.00 \pm 0.05$ % for ^{195}Bi (experiment I) and ^{197}Bi (experiment II) nuclei respectively.

4.6 LEPS Spectra

The individual LEPS spectra were summed to produce the spectra shown in Figure 4.3 for the ^{181}Ta+^{20}Ne and ^{181}Ta+^{22}Ne reactions. Not many peaks apart from the X-rays were observed. Gates on the intense bismuth X-rays were used to construct gated γ-γ matrices and 1-dimensional spectra (see Tables 4.2 and 4.3) in order to preferentially enhance the bismuth γ-ray transitions. During the sorting procedure two gates were set on the Bi $K_{\alpha 2,\alpha 1}$ X-rays (Table 4.4) as illustrated by vertical solid lines on the

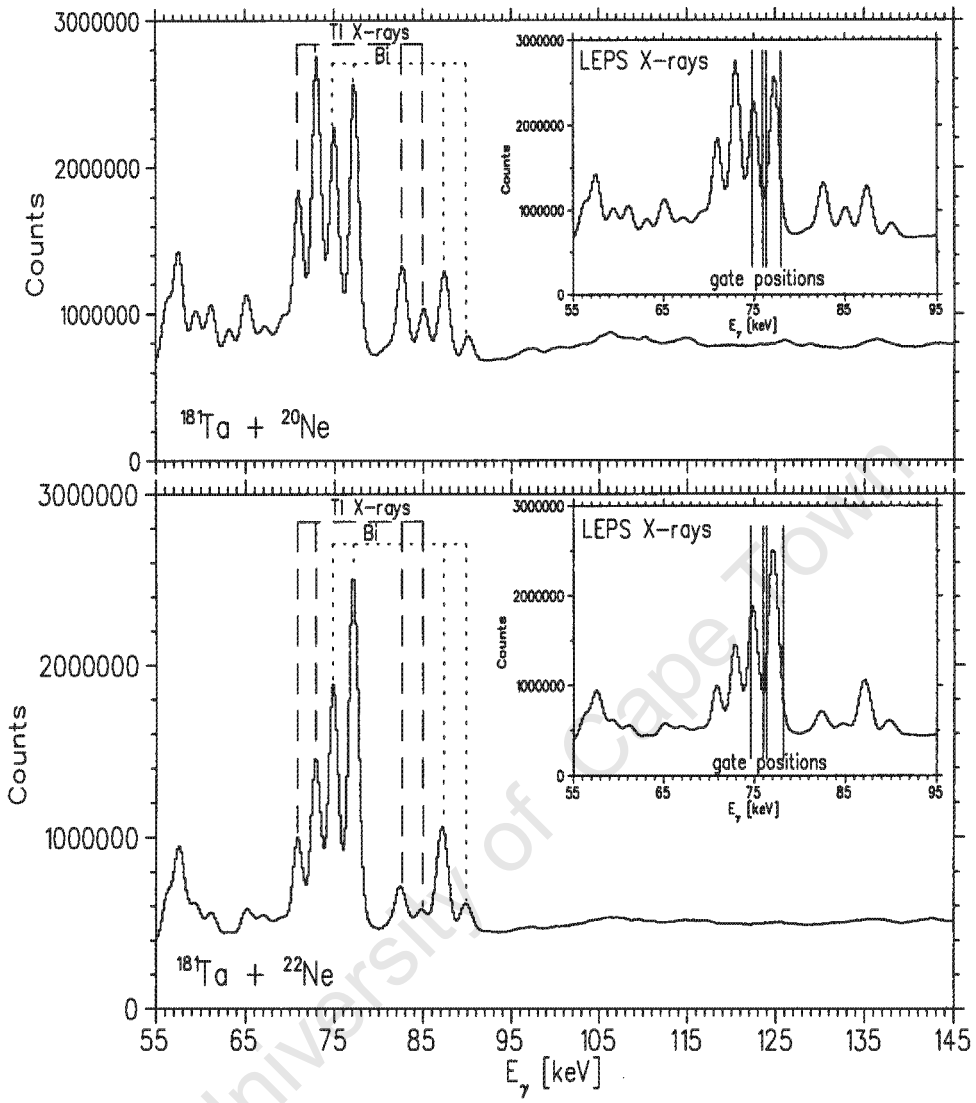

Figure 4.3: *The sum of the LEPS spectra for the first (top panel) and second (bottom panel) experiments. The inserts in both panels show the intense Tl and Bi $K_{\alpha 2,\alpha 1}$ and $K_{\beta 1,\beta 2}$ X-rays observed from the two data sets. The exact positions where the gates were set while sorting the data into gated matrices are shown by the vertical solid lines on both inserts. The Ta X-rays come from the target.*

inserts of Figure 4.3. The requirement adopted was that, at least one of the two X-rays had to be detected by the LEPS detectors for the gated Clover matrix to be incremented.

In Figure 4.3, the observed Tl $K_{\alpha 1}$ and Bi $K_{\alpha 2}$ coincide with Pb $K_{\alpha 2}$ and Pb $K_{\alpha 1}$ X-rays respectively. Furthermore, when gating on the Tl $K_{\alpha 1}$ and Bi $K_{\alpha 2}$ X-rays no contribution of Pb is observed which is not consistent with the results predicted by PACE2 calculation yield for Pb (section 4.1).
The relative yield of the αxn and xn channels were estimated from the intensity of the X-rays observed in the LEPS summed spectra in Figure 4.3 for the ^{181}Ta+^{20}Ne and ^{181}Ta+^{22}Ne reactions. The ratio $\frac{\alpha xn}{xn}$ is about 68 % for the former and 37 % for the latter reactions.

4.7 γ-γ Matrices

The Clover data were sorted into two types of 2-dimensional ($E_{\gamma 1}$;$E_{\gamma 2}$) energy histograms referred to as matrices with the energy of one photon on one axis and the energy of its coincidence partner on the other. That is, the ungated and X-ray gated (as discussed in section 4.6) γ-γ symmetrised matrices with dimensions of (4096 $\times$ 4096) channels, with a dispersion of 0.5 keV per channel. The total projection of the matrix onto one axis is a 1-dimensional γ-ray spectrum of all the counts in the matrix. Figures 4.4 and 4.5 depicts such total projection spectra from the (a) ungated and (b) X-ray gated matrices for the ^{181}Ta+^{20}Ne (experiment I) and ^{181}Ta+^{22}Ne (experiment II) reactions respectively. The gated matrices were constructed as described in section 4.6.

The total number of counts (in the 0 – 3000 channel range) within the total projection of the gated and ungated matrices for experiments I and II, (depicted in Figures 4.4 and 4.5) respectively, were measured and are provided in Table 4.5. The background subtracted total number of counts (P) within the 344 and 311 keV peak region were measured for experiments I and II respectively. The estimate of the total number of background counts (B) beneath the 344 and 311 keV peak region were determined. The peak-to-background (P/B) ratios are calculated for peaks and tabulated in Table 4.5. It can be noted that the P/B is much better for the gated matrix, however, the total number of events in the matrix is much lower.
It is worth mentioning that the LEPS-LEPS and the Clover-LEPS matrices

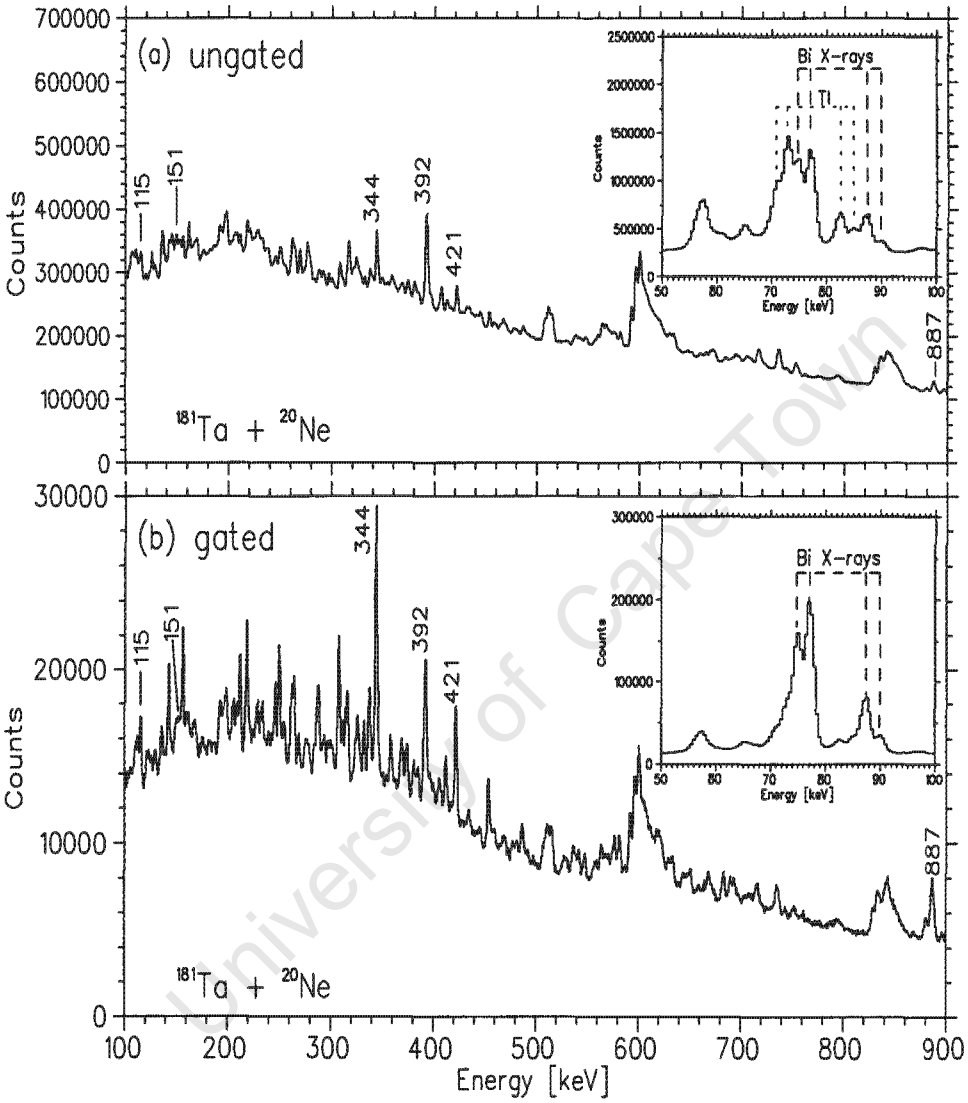

Figure 4.4: *The total projection spectra extracted from the (a) ungated and (b) gated Clover matrices for experiment I. The background is not subtracted in either projection. The known γ-rays of ^{195}Bi [Lön86] are labelled with their energies. The exact positions of the observed X-rays are depicted in the inserts.*

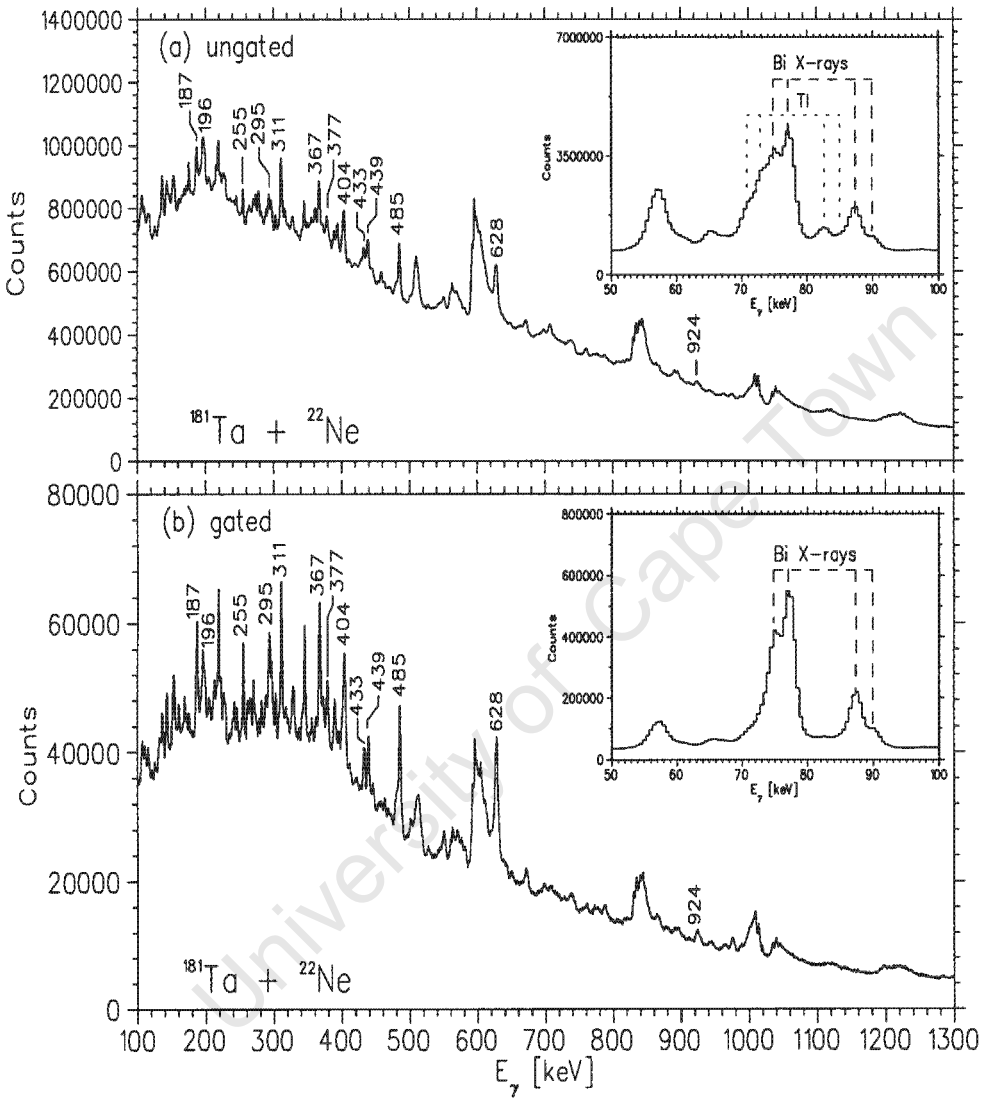

Figure 4.5: *The total projection spectra extracted from the (a) ungated and (b) gated Clover matrices for experiment II. The background is not subtracted in either projection. The known γ-rays of ^{197}Bi [Cha86, Zho95] are labelled with their energies. The exact positions of the observed X-rays are depicted in the inserts.*

Table 4.5: *The total number of counts within the total projection of the gated and ungated matrices and the peak-to-background (P/B) ratio for selected γ-ray peaks for experiments I and II.*

Clover Matrices	Tot. no. of counts within the matrix	P/B (%)
Experiment I		344 keV (685 - 691) channels)[a]
gated	25×10^6	38.2
ungated	512×10^6	18.7
Experiment II		311 keV (618 - 627) channels)[a]
gated	72×10^6	26.5
ungated	1317×10^6	13.8

)[a] Dispersion for the Clovers is 0.5 keV per Channel.

were also created in this work. However, they were not useful since no other peaks apart from the X-rays were observed in the LEPS data.

4.8 Efficiency and Energy Calibration

The efficiency calibration measurements for the AFRODITE (LEPS and Clover) detectors were performed at the end of each experiment with the ^{152}Eu and ^{133}Ba radioactive sources. These sources were mounted on the target ladder (at the target position in Figure 3.14 (a) and (b)), subsequently placed inside the target chamber (in Figure 3.6) at the target position. The trigger logic adopted for these measurements was $(\frac{1}{15})$ detectors.

Separate relative efficiency (ϵ) curves for the 8 LEPS and the 7 Clover detectors are depicted in Figure 4.6. The curves were constructed from the summed singles data for the two types of detectors using the RadWare software Effit-program [Rad95]. The energy calibration parameters necessary to be used in RadWare software ESCL8R-program [Rad95a] were also generated from the source data with ENCAL-program [Rad95] discussed in section 4.2. The efficiency of the LEPS and Clover detectors dropped below 40 keV and 110 keV for LEPS and Clover detectors, respectively, due to absorption and CFD thresholds. The maximum detection efficiency occurs at 40 keV and 110 keV for the LEPS and Clover detectors respectively, and

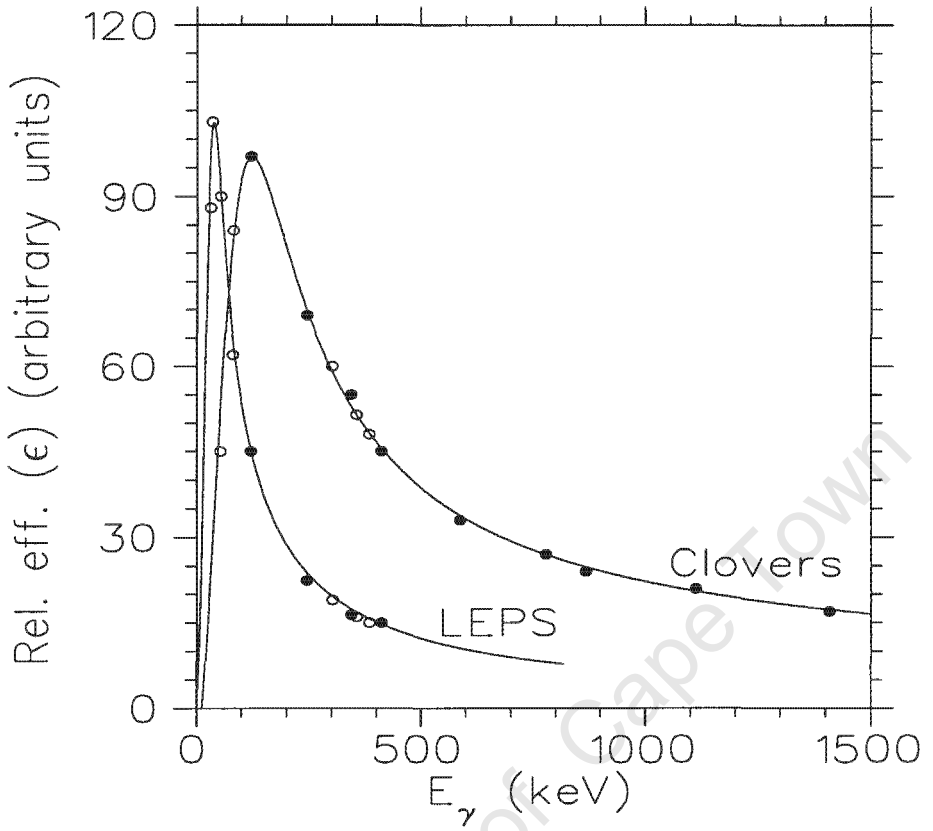

Figure 4.6: *The relative efficiency (ϵ) for the 8 LEPS and 7 Clover detectors measured with the ^{152}Eu (filled-circles) and ^{133}Ba (open-circles) radioactive sources mounted on the target ladder at the target position. The measurements were carried out with the trigger logic set to ($\frac{1}{15}$) detectors (singles mode). The maximum detection efficiency occurs at $\approx$ 40 keV and $\approx$ 110 keV for the LEPS and Clover detectors respectively. The efficiency decreases sharply at lower energy due to γ-ray absorption and the CFD thresholds.*

decreased smoothly as the energy increases. This common behaviour in both types of detectors is caused by the decrease in:

(a) Photoelectric effect and

(b) Compton scattering cross-sections,

with increasing energy of the γ-rays.
The calculated energy and efficiency calibration parameters were provided

to the ESCL8R-program which was used in searching for γ-γ coincidence relationships.

4.9 Construction of the Level Schemes

Construction of the level-scheme involves studying γ-γ coincidence relationships between the detected γ-rays from the background subtracted [Rad95] coincidence spectra (with the aid of the ESCL8R [Rad95a] software program). Following this procedure, several new transitions were placed in the ^{195,197}Bi level schemes. Apart from ^{195,197}Bi γ-rays, several known transitions associated with ^{198}Bi [Zwa00] were observed. A sequence of four new γ-ray transitions was found in experiment II data, however, it could not be associated with a particular nucleus.

4.10 DCO Ratios

In order to determine the multipole order of the γ-ray transitions, two Directional Correlation from Oriented nuclear states (DCO) [Kra73, Dri90] γ-γ matrices were constructed from the Clover detectors, for experiment I and II (summarised in Tables 4.2 and 4.3 respectively). In either experiment, the first matrix consisted of coincidence where both γ-rays were observed at 45° or 135°. The second (asymmetric) matrix consisted of coincidence between γ-rays detected at 45° or 135° (y-axis) and those detected at 90° (x-axis). The same gate on the y-axis was made in both matrices and gated spectra $S(90°)$ and $S(45°; 135°)$ were produced.
The DCO ratios for the γ-rays of interest were determined as:

$$R_{DCO} = \frac{A(45°; 135°)}{A(90°)}, \tag{4.4}$$

where $A(45°; 135°)$ is the area of the peak in $S(45°; 135°)$ and $A(90°)$ is the area of the peak in $S(90°)$.

4.11 Linear Polarisation

The presence of Clover detectors at right angles to the beam direction on the array made it possible for linear polarisation [Fag59, Lit70, But73, Sim83, Sch94, Sch98] measurements to be conducted, in order to determine the parities of the γ-ray transitions associated with the observed structures.
The degree of linear polarisation, P is related to the measured experimental anisotropy, A_p of the γ-rays by:

$$P = \frac{1}{Q(E_\gamma)} A_p, \tag{4.5}$$

where $Q(E_\gamma)$ is the quality factor of the polarimeter which corresponds to the polarisation sensitivity of the detector. The magnetic or electric nature of the transitions are deduced from the sign of the anisotropy, A_p given by:

$$A_p = \frac{N_V - \alpha N_H}{N_V + \alpha N_H}, \tag{4.6}$$

where N_V is the number of γ-rays scattered in a plane perpendicular to the beam direction, N_H the number scattered in the plane parallel to the beam direction and α is the relative efficiency ($= 1.0$ and 1.05 for experiment I and II respectively). Hence, on the basis of the determined linear polarisation anisotropies and the R_{DCO} (section 4.10), γ-ray transitions were assigned the multipolarity, mostly either M1 or E2.
The 1-dimensional γ-ray spectra from the Clover detectors at 90° have been generated for the ungated horizontally (H) and vertically (V) scattered events for experiments I and II (Tables 4.2 and 4.3). Smooth background spectra (with the "*bg*" - automatic background subtraction command) using RadWare software GF2 program [Rad95] were subtracted from the V and H spectra. This was done in order to achieve a flat background in the $V - H$ spectrum. Since the background in the V and H spectra have their maxima in different channels. Their direct subtraction leads to a background with an "S"-shape (for instance positive and negative at the low and high energies respectively). Subsequently, the difference ($V - H$) between the V and H scattered events was also determined. For the gated spectra (Tables 4.2 and 4.3) the H, V and $V - H$ spectra were also generated for both experiments following the same procedure as above and are discussed in sections 5.1.3 and 5.2.3.

4.12 Transition Intensities

The intensity, I_γ of a γ-ray transition is given by:

$$I_\gamma = \frac{S}{\epsilon}, \tag{4.7}$$

where S is the area of the γ-ray transition and ϵ the detector efficiency[5] for the γ-ray. The total intensity, I_t of a transition is given by:

$$I_t = I_\gamma(1+\alpha) = \frac{S}{\epsilon}(1+\alpha), \tag{4.8}$$

where α is the electron conversion coefficient[6] (for example which can either be α(M1) or α(E1) for the M1 or E1 γ-ray transitions respectively).

4.13 RSAM Lifetime Measurements

The Recoil Shadow Anisotropy Method (RSAM) [Gue01] was employed to search for isomeric states with lifetimes in the range of a few nanoseconds. The anisotropy (A_{RSAM}) for the γ-ray transitions were determined by employing:

$$A_{RSAM} = \frac{N_U - \alpha N_S}{N_U + \alpha N_S}, \tag{4.9}$$

where N_U is the number of the γ-rays detected in the unshadowed Clover element (96° with respect to the beam direction), N_S the number detected in the shadowed elements (84° with respect to the beam direction) and α is the relative efficiency. Only single hit events were considered. The three Clover detectors positioned at 90° with respect to the beam direction were considered, since they are the most sensitive to the shadow effect. In addition, there were more Clovers at 90° than at 45° and 135°. The Clover spectra were generated (for experiments I and II) by gating on the $K_{\alpha 1}$ Bi X-rays (Table 4.2 and 4.3) detected with the LEPS detectors. The elemental Clover spectra at 84° and 96° were extracted and separately summed into two Clover spectra at corresponding angles (the two Clover elements are

[5] for the present work, the relative detector efficiency was considered (and discussed in section 4.8).

[6] defined as $\alpha = \frac{I_e}{I_\gamma}$, which gives the probability of electron emission relative to γ emission and ranges from very small (≈ 0) to very large [Kra88].

offset from 90° by about 6°, see Table 4.1).
There is a separate on-going project at iThemba LABS which does not form part of this work, in order to determine the AFRODITE RSAM calibration curve which will be used in measuring lifetimes of the isomers.

Chapter 5

Results of Data Analysis

This chapter presents the experimental results of the γ-γ coincidence relationships, DCO ratios, linear polarisation measurements, transition intensities and the RSAM lifetime measurements for the ^{195,197}Bi nuclei. Furthermore, the results for ^{198}Bi nucleus and the unassigned γ-ray structure observed in our data are discussed.

5.1 ^{195}Bi Level Scheme

The level scheme of ^{195}Bi deduced from the previous study [Lön86] known only up to the $(2311 + \Delta)$ keV state, is shown in Figure 5.1. The 114.6, 150.8, 343.7, 391.7, 421.0 and 886.8 keV transitions associated with the known ^{195}Bi level scheme in Figure 5.1 [Lön86] were observed in the ungated and gated total projection spectra shown in Figure 4.4 of Chapter 4. The intensities of the delayed transitions in these total projections were hindered, since the nuclei recoiled out of focus of the detectors. Our data confirm the previously known ^{195}Bi level scheme [Lön86] and the energies agree well with the previous measurements. However, in our data the known 887.9 keV transition is found a bit less in energy. In the present work, two γ-ray cascades labelled Band 1 and 2 in Figure 5.2 have been found and assigned to ^{195}Bi. This lead to a considerable extension of the level scheme up to the I + 4 state in Band 2, with Band 2 feeding Band 1 at level 2889.0 keV through one or more unobserved transition(s) marked X.

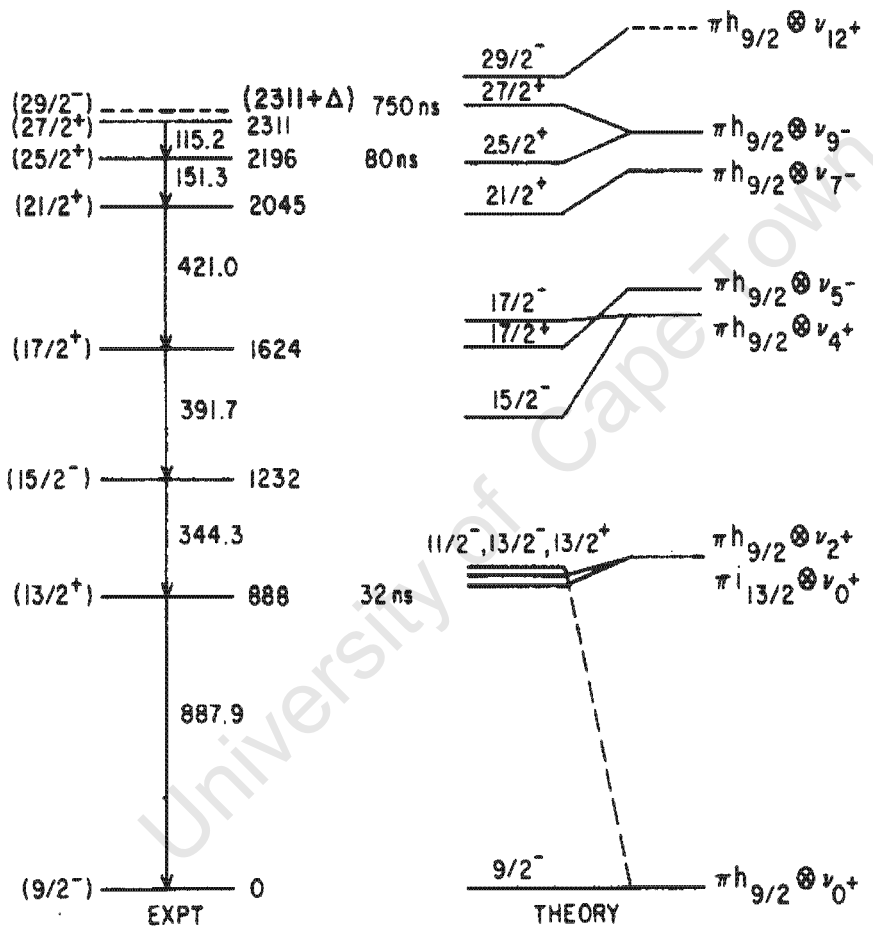

Figure 5.1: *Level scheme of ^{195}Bi taken from [Lön86].*

Figure 5.3 (a) and (b) shows the examples of the background subtracted

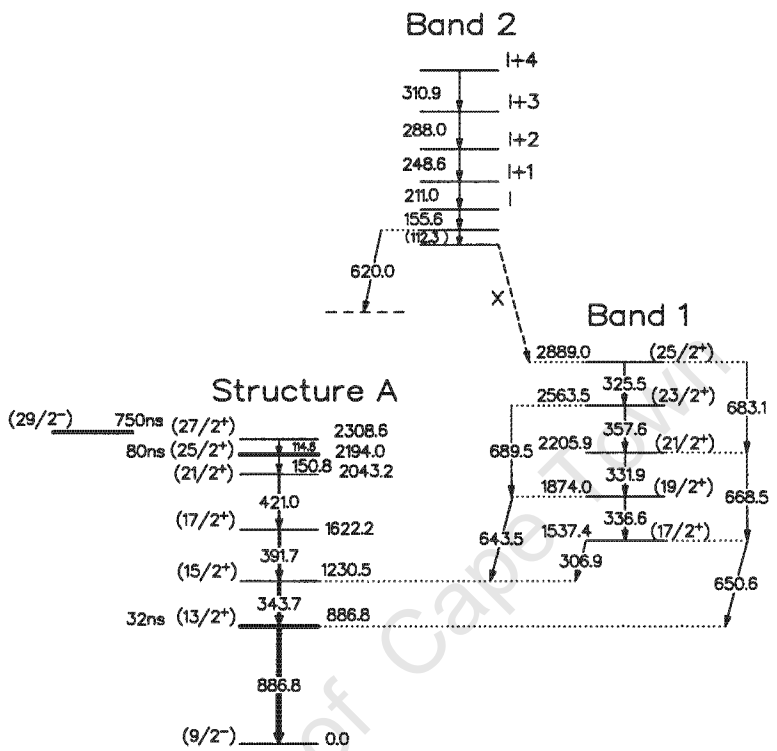

Figure 5.2: *The extended level scheme for ^{195}Bi deduced from the present work (experiment I).*

γ-ray coincidence spectra extracted from the ungated matrix. The gates have been set as indicated by the dashed-lines on the (a) previously known 886.8 keV [Lön86] ground-state and (b) newly observed 306.9 keV Band 1 γ-ray transitions.

The 886.8 keV gate in Figure 5.3 (a) display a coincidence relationship with all (343.7, 391.7, 421.0 keV) previously known transitions above the $(\frac{13}{2}^+)$ (32 ns) isomeric state. The new 306.9 keV Band 1 candidate seen in coincidence with the 886.8 keV was gated as illustrated on Figure 5.3 (b). The 306.9 keV gate unfolded the 155.8, 325.5, 331.9, 336.6, 357.6 keV Band 1 transitions together with the 668.5, 683.1 and 689.5 keV cross-over transitions. However, the 689.5 keV transition is observed weakly in this spectrum. The 155.8 keV transition is in coincidence with itselve. The

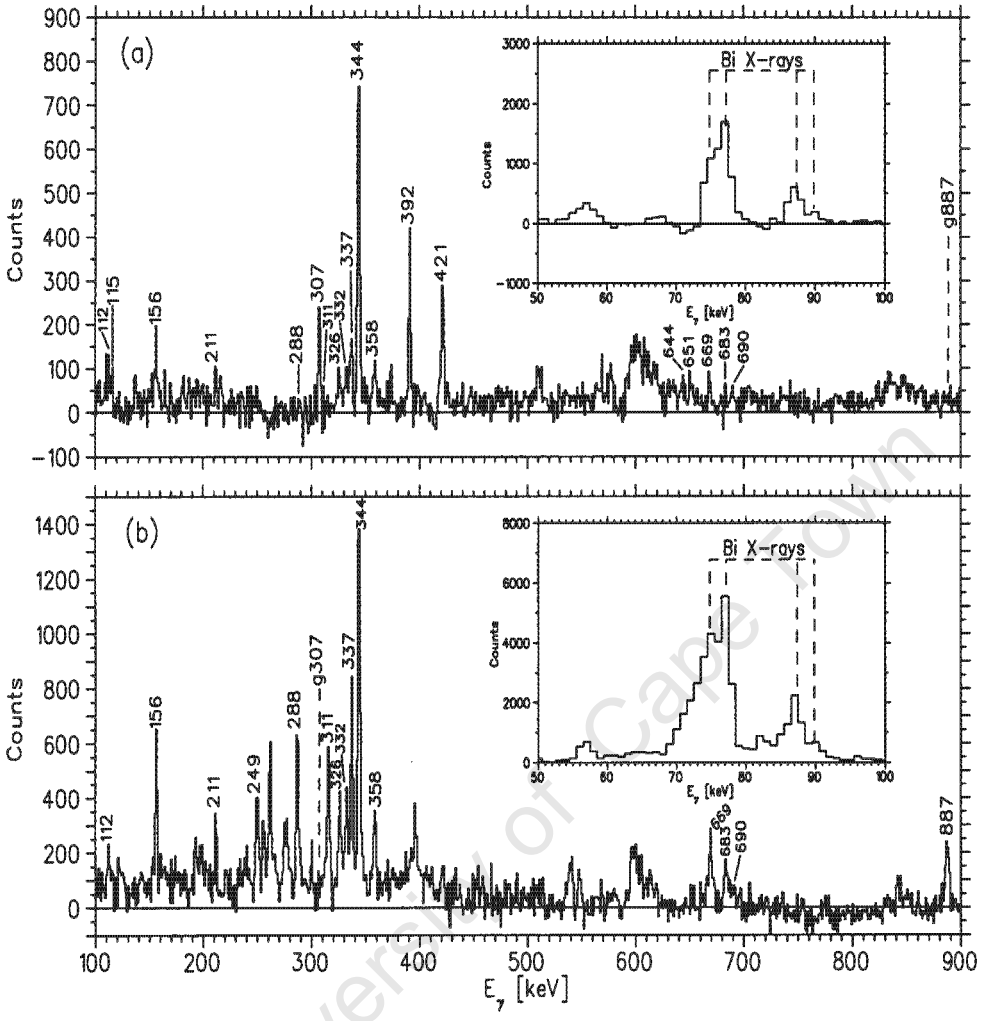

Figure 5.3: *The background subtracted spectra extracted from the ungated matrix and gated on the: (a) 886.8 keV and (b) 306.9 keV γ-ray transitions. The position of the gates are indicated by dashed-lines in both panels. In (a) and (b), the insert show the exact positions of the Bi X-rays observed in the low energy region of the two spectra. The presence of the Bi X-rays and the known yrast transitions in ^{195}Bi within the 306.9 keV gated spectrum confirm that the 306.9 keV transition belongs to ^{195}Bi.*

112.3, 155.6, 211.0, 248.6, 288.0 and 310.9 keV transitions are in coincidence and form a cascade of γ-rays labelled Band 2.

5.1.1 γ-γ coincidences

Dipole Band 1

The γ-ray coincidence spectra for Band 1 representing the sum of single gates set on 306.9, 336.6, 331.9, 357.6 and 325.5 keV transitions are shown in Figure 5.4 for the (a) ungated and (b) gated matrices. The known 886.8 and 343.7 keV γ-ray transitions in Structure A can be clearly seen while the 114.5 and 150.8, 391.7 and 421.0 keV transitions are not observed. The Band 1 E2 cross-over transitions are weakly observed in both spectra.

Band 2

The γ-ray coincidence spectra for Band 2 representing the sum of 310.9, 288.0, 248.6, 211.0 and 112.3 keV gates are shown in Figure 5.5. These spectra have been generated from the (a) ungated and (b) gated matrices. Most of the γ-ray transitions from Band 1 as well as Structure A are observed. Furthermore, the 643.5, 650.6, 668.5, 683.1 and 689.5 keV cross-over γ-ray transitions are weakly seen. No linking transition (denoted by X in Figure 5.2) was found, thus making it impossible to measure the spins, parities and excitation energies of the levels of Band 2.
Figures 5.6 and 5.7 depicts the γ-ray coincidence spectra extracted from the ungated matrix for Band 2. The gates are shown by dashed-lines and the γ-ray transitions are labelled with their respective energies. The 112 keV gate shown in Figures 5.6 (c) is in coincidence with itself. The other γ-rays with energies near 100 keV next to the 112 keV γ-ray are not observed when the same gate is made in the spectrum extracted from the gated matrix.
The decay of Band 2 proceeds:

(i) through the 620 keV transition and

(ii) towards Band 1, populating the $(\frac{25}{2}^+)$ level at 2889.0 keV.

It looks like the decay path through the 620 keV transition ends up on an isomeric level, since no coincidence with low energy transitions are seen (see Figure 5.7 (d)). It was not possible to find the transitions linking the Band 2 with Band 1. Thus, no excitation energy, spin and parities could

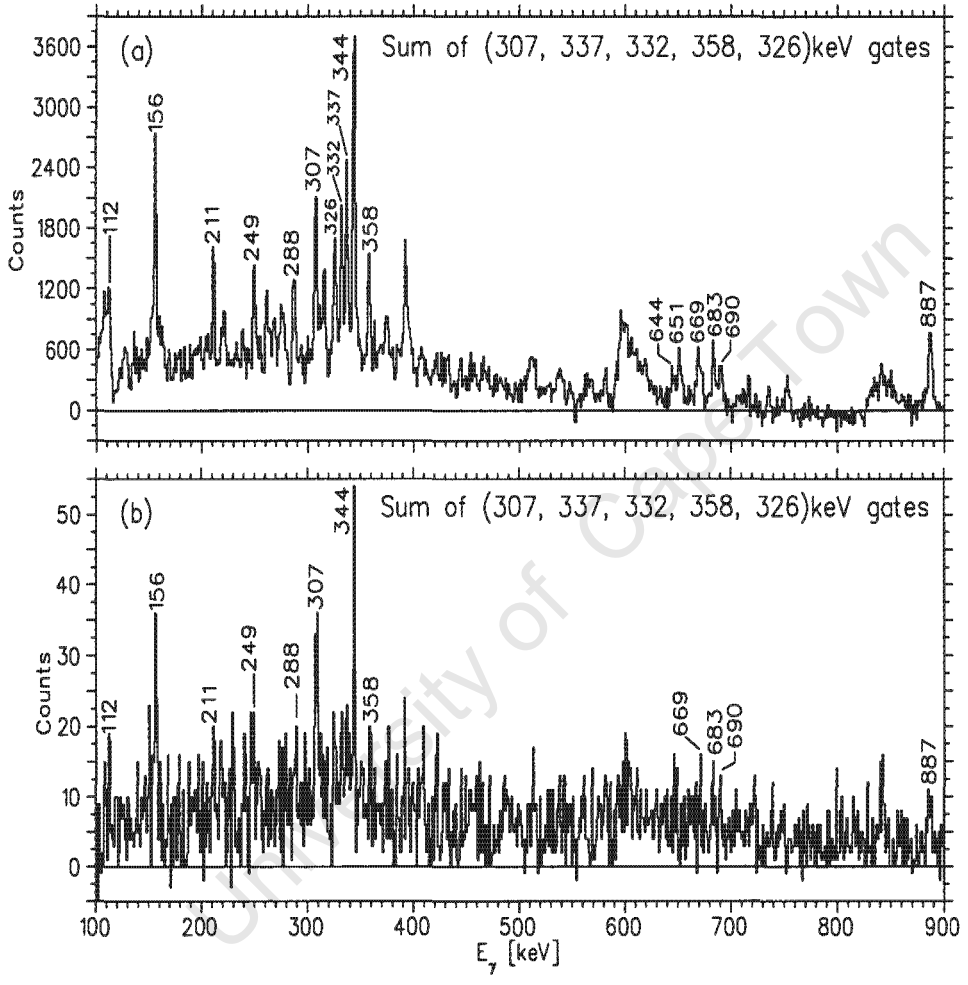

Figure 5.4: *The summed coincidence γ-ray spectra for band 1 in ^{195}Bi. They are generated from the (a) ungated and (b) gated (on the $K_{\alpha 2}$, $K_{\alpha 1}$ Bi X-rays detected with the LEPS detectors) matrices by summing the 306.9, 336.6, 331.9, 357.6 and 325.5 keV gates.*

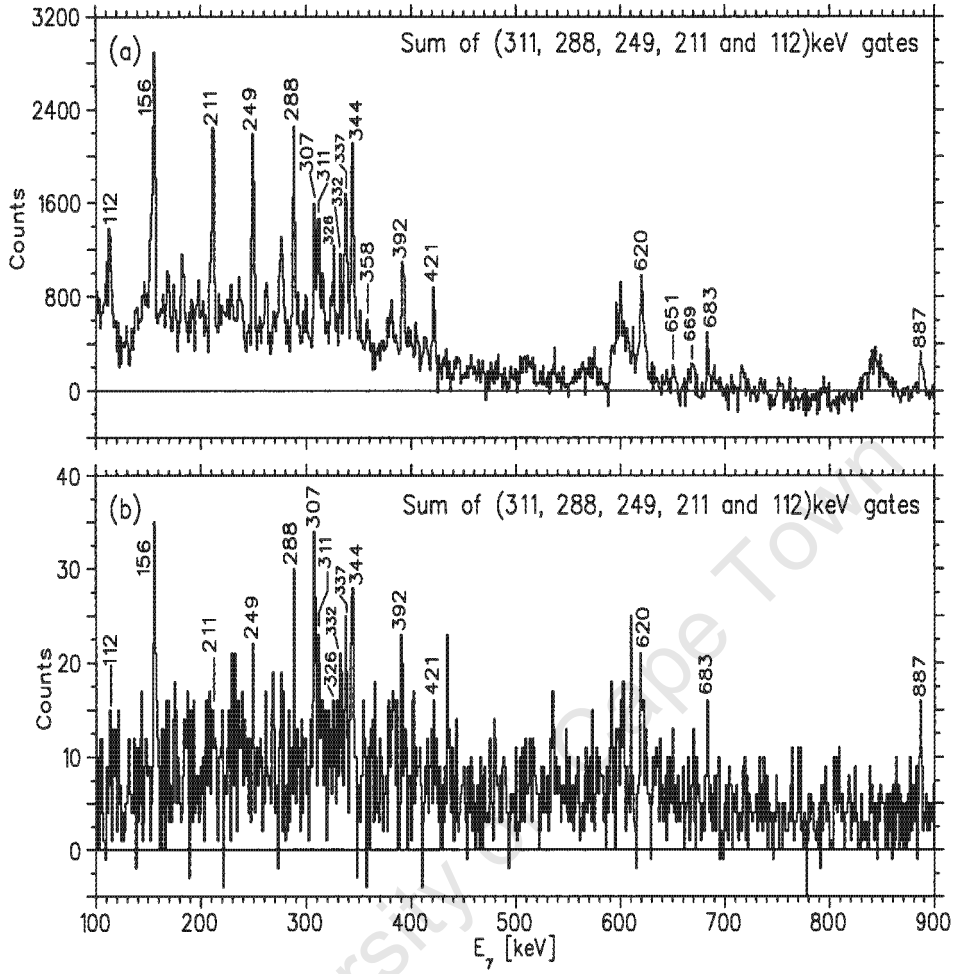

Figure 5.5: *The summed coincidence γ-ray spectra for ^{195}Bi Band 2 gates. These spectra are generated from the (a) ungated and (b) gated (on the $K_{\alpha 2}$, $K_{\alpha 1}$ Bi X-rays detected with the LEPS detectors) matrices by summing the 310.9, 288.0, 248.6, 211.0 and 112.3 keV gates.*

be determined for Band 2. It looks like that one decay path from Band 2 goes to Band 1 and another one goes to the yrast sequence, since we see the coincidence between Band 2 and the 421 and 392 keV transitions.

The second component of the 156 keV doublet was not placed in the level scheme, but it is likely that this transition is included in the decay path connecting Band 2 to Band 1.

A cross-over 650.6 keV, was found in parallel to the new 306.9 keV and

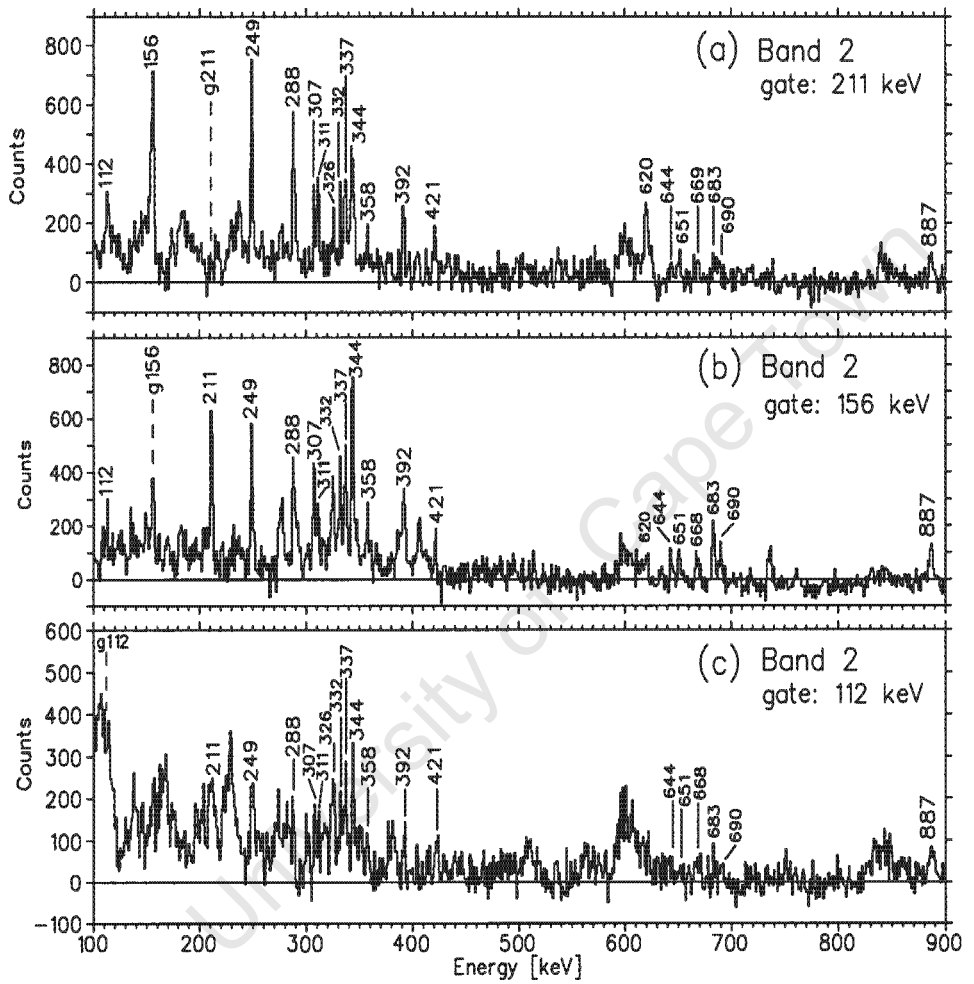

Figure 5.6: *The spectra are extracted from the ungated matrix for Band 2 in ^{195}Bi, gated on the: (a) 211.0, (b) 155.6 and (c) 112.3 keV γ-ray transitions. In all the panels the position of the gates are indicated by the dashed-lines and peaks are labelled with their respective energies.*

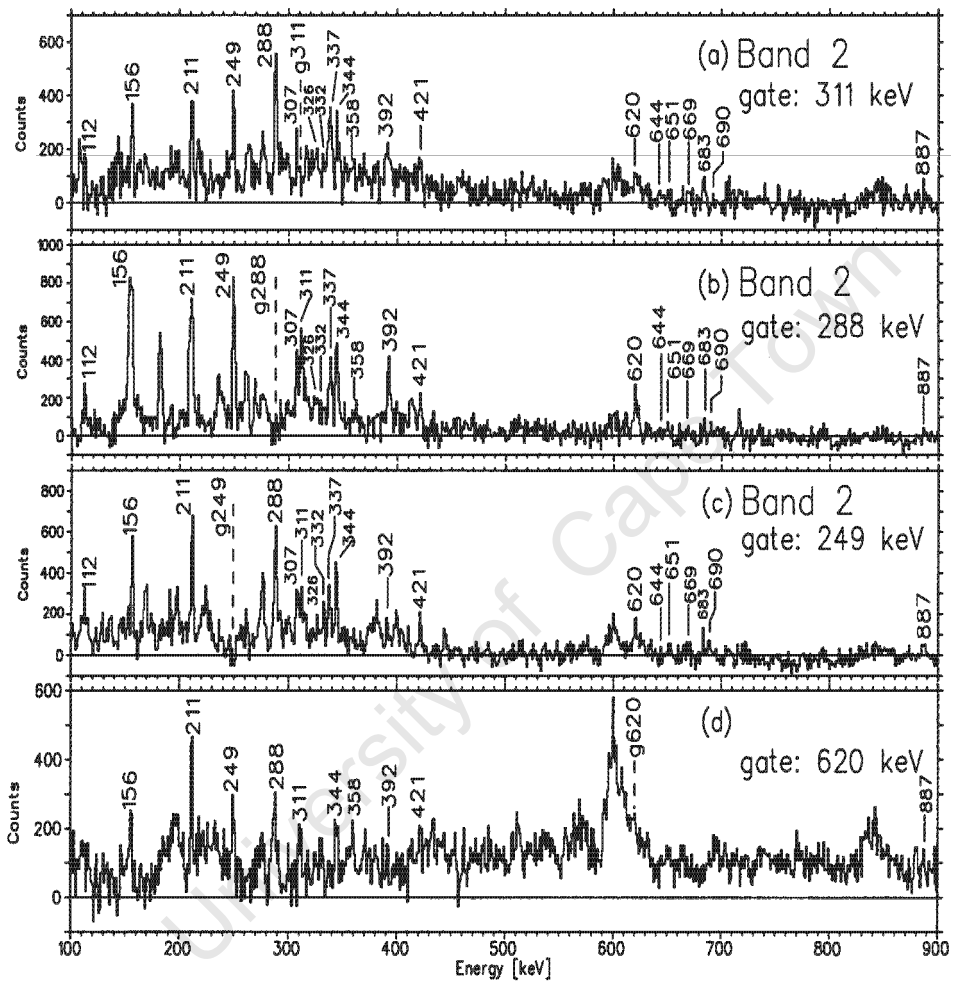

Figure 5.7: *The spectra are extracted from the ungated matrix for Band 2 in ^{195}Bi, gated on the: (a) 310.9, (b) 288.0 and (c) 248.6 and (d) 620 keV γ-ray transitions. In all the panels the position of the gates are indicated by the dashed-lines and peaks are labelled with their respective energies.*

previously known 343.7 keV transitions. Thus, M1 multipolarity was assigned for 343.7 keV transition in contrast to its previous tentative E1 assignment. However, this does not contradict the calculation presented in Figure 5.1, since it considers single-particle excitations in a spherical nucleus. The calculation does not predict the rotational behaviour of the deformed nucleus. Although it is possible that we can have $\Delta I = 0$ and $\Delta I = 2$ for the 650.6 keV $(\frac{13}{2}^{+,-}) \rightarrow (\frac{13}{2}^{+})$ or $(\frac{17}{2}^{+}) \rightarrow (\frac{13}{2}^{+})$ respectively, however, the DCO ratio will be the same. However, the E2 assignment of 650.6 keV is more likely because: (i) we did not observe $\Delta I = 0$ M1, E1 or $\Delta I = 1$ M1 transitions like $(\frac{15}{2}^{+} \rightarrow \frac{15}{2}^{+})$, $(\frac{15}{2}^{+} \rightarrow \frac{15}{2}^{-})$ or $(\frac{15}{2}^{+} \rightarrow \frac{13}{2}^{+})$ respectively which could link Band 1 with Structure A, for instance between the 1874.0 and 886.8 keV, 2205.9 and 1230.5 keV levels and (ii) in this case, the excitation energies of the levels with the same spins of Structure A and Band 1 are close, for instance the $(\frac{17}{2}^{+})$ levels in Structure A and Band 1 are at 1622.2 and 1537.4 keV respectively, which explains the high intensity of Band 1.

5.1.2 ^{195}Bi DCO

Firstly, the R_{DCO} for a number of transitions with known multipolarities in ^{193}Tl [Rev92] were measured. Two coincidence spectra were obtained by gating on the $K_{\alpha 1}$ Tl X-ray (in Table 4.4 of Chapter 4) on the y-axis of the two DCO matrices. Subsequently, subtraction of a background spectrum (created by gating on the background region near the Tl X-ray peak) was performed. The R_{DCO} for a number of known dipole and quadrupole transitions in ^{193}Tl [Rev92] were calculated from these background subtracted spectra. Average R_{DCO} values of 0.69 ± 0.04 and 1.23 ± 0.08 were obtained for the stretched dipole ($\Delta I = 1$) and the stretched quadrupole ($\Delta I = 2$) transitions respectively and are marked by dotted lines in Figure 5.8. The results for the multipole order of the known transitions in ^{193}Tl were in agreement with those reported by Reviol *et al.*, [Rev92].

The γ-ray Clover spectra $S(45°; 135°)$ and $S(90°)$ gated on the $K_{\alpha 1}$ Bi X-ray (in Table 4.4) were generated from the two DCO matrices (Table 4.2). The results of the R_{DCO} determined for the ^{195}Bi transitions are given in

Table 5.1: *The level energies (E_{exc}), initial spins I_i, γ-ray transition energies (E_γ), intensities (I_γ), total intensities (I_t), DCO ratios ($R_{DCO} = \frac{I(45°;135°)}{I(90°)}$), $\frac{B(M1)}{B(E2)}$ ratios and the spin assignments for the ^{195}Bi nuclei.*

E_{exc} (keV)	I_i	E_γ (keV)	I_γ (%)	I_t (%)	R_{DCO}	$\frac{B(M1)}{B(E2)}$ $(\mu_N/eb)^2$	*Assignment*
886.8	$\frac{13}{2}^+$	886.8					$(\frac{13}{2}^+) \rightarrow (\frac{9}{2}^-)$
1230.5	$(\frac{15}{2}^+)$	343.7)[a]	47(3)	82	0.79(6)		$(\frac{15}{2}^+) \rightarrow (\frac{13}{2}^+)$
1537.4	$(\frac{17}{2}^+)$	306.9	15(4)	21	0.77(8)	7.7(12)	$(\frac{17}{2}^+) \rightarrow (\frac{15}{2}^+)$
1537.4	$(\frac{17}{2}^+)$	650.5	17(3)	17	1.05(35)		$(\frac{17}{2}^+) \rightarrow (\frac{13}{2}^+)$
1622.2	$(\frac{17}{2}^+)$	391.7	7(2)	15			$(\frac{17}{2}^+) \rightarrow (\frac{15}{2}^+)$
1874.0	$(\frac{19}{2}^+)$	336.6	24(3)	26	0.71(5)	4.6(9)	$(\frac{19}{2}^+) \rightarrow (\frac{17}{2}^+)$
1874.0	$(\frac{19}{2}^+)$	643.5	21(3)	14	1.16(39)		$(\frac{19}{2}^+) \rightarrow (\frac{15}{2}^+)$
2043.2	$(\frac{21}{2}^+)$	421.0	36(2)	36			$(\frac{21}{2}^+) \rightarrow (\frac{17}{2}^+)$
2194.0	$(\frac{25}{2}^+)$	150.8	)[b]				$(\frac{25}{2}^+) \rightarrow (\frac{21}{2}^+)$
2205.9	$(\frac{21}{2}^+)$	331.9	15 (2)	12	0.63(6)	6.1(11)	$(\frac{21}{2}^+) \rightarrow (\frac{19}{2}^+)$
2205.9	$(\frac{21}{2}^+)$	668.5	11(3)	11	1.72(26)		$(\frac{21}{2}^+) \rightarrow (\frac{17}{2}^+)$
2308.6	$(\frac{27}{2}^+)$	114.6	)[b]				$(\frac{27}{2}^+) \rightarrow (\frac{25}{2}^+)$
2563.5	$(\frac{23}{2}^+)$	357.6	14(2)	10	0.53(7)	3.3(9)	$(\frac{23}{2}^+) \rightarrow (\frac{21}{2}^+)$
2563.5	$\frac{23}{2}^+$	689.5	9(2)	9	1.44(15)		$\frac{23}{2}^+ \rightarrow \frac{19}{2}^+$
2889.0	$(\frac{25}{2}^+)$	325.5	10(2)	11	0.66(10)	3.5(8)	$(\frac{25}{2}^+) \rightarrow (\frac{23}{2}^+)$
2889.0	$(\frac{25}{2}^+)$	683.1	8(2)	8	1.47(21)		$(\frac{25}{2}^+) \rightarrow (\frac{21}{2}^+)$
		620.0	5(2)	14			
		112.3	10(2)		0.67(16)	)[c]	)[c]
	I	155.6)[a]	17 (2)	58	0.66(8)	)[c]	Band 2
	$I+1$	211.0	13 (2)	23	0.55(8)	)[c]	Band 2
	$I+2$	248.6	14 (2)	21	0.55(8)	)[c]	Band 2
	$I+3$	288.0	13 (2)	17	0.48(7)	)[c]	Band 2
	$I+4$	310.9	7 (1)	8	0.53(14)	)[c]	Band 2

)[a] Measurement for the unresolved peak.

)[b] Could not be determined due to lack of enough statistics.

)[c] Could not be determined - linking transitions not found.

Table 5.1 and depicted in Figure 5.8. The R_{DCO} for the ^{195}Bi transitions indicates that the structure shown in Figure 5.2 includes a sequence of stretched dipoles with associated stretched quadrupole "cross-over" transitions (Band 1) which are fed on top by a cascade (Band 2) of stretched dipole transitions. The dashed-lines in Figure 5.8 indicates the average R_{DCO} values determined for the stretched dipole and the stretched quadrupole transitions and are 0.63 ± 0.04 and 1.37 ± 0.08 respectively.

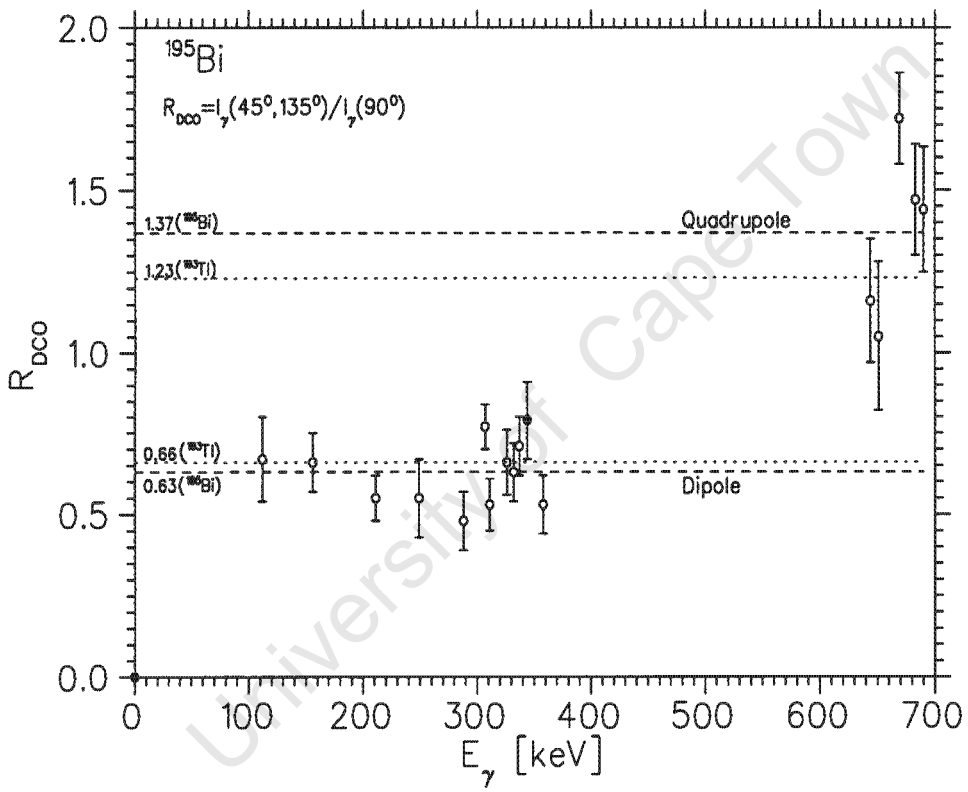

Figure 5.8: *The DCO ratios (R_{DCO}) for the γ-ray transitions from the two new (open-circles) structures associated with the ^{195}Bi nucleus together with a previously known (filled-circle) transition. The dashed-lines correspond to the average R_{DCO} values obtained for the new stretched dipole (0.63 ± 0.04) and the stretched quadrupole (1.37 ± 0.08) transitions. The dotted-lines correspond to the average R_{DCO} values determined from the selected ^{193}Tl [Rev92] γ-ray transitions.*

5.1.3 Linear Polarisation Measurements for ^{195}Bi

The data set of Experiment I had insufficient statistics to infer the electric or magnetic character for the γ-ray transitions. Thus, we could not measure parities neither for the known γ-ray transitions close to the ground-state nor those for Bands 1 and 2 in ^{195}Bi (Figure 5.2). Clearly, the V-H spectra shown in Figure 5.9 gated on the Bi X-rays and in Figure 5.10 ungated (Tables 4.2 and 4.3) are of no use in determining the magnetic or electric character of the transitions labelled with their energies in the H and V - Clover sum spectra.

5.1.4 Transition Intensities and $\frac{B(M1)}{B(E2)}$ ratios for ^{195}Bi

The relative total transition intensities for Band 2 (Figure 5.11) were studied in order to infer the character of the transitions. The γ-ray coincidence spectrum gated on the top most 310.9 keV transition of Band 2 was generated from the ungated matrix. Subsequently, the relative gamma intensities for the 156, 211, 249 and 288 keV lines were determined. The relative total intensities were obtained when the areas of the peaks were corrected for the detector relative efficiency (assuming a 5 % uncertainty) and internal electron conversion. Assuming M1 and E1 multipolarity respectively the γ-ray transition intensities were normalised to that of 288.0 keV transition and shown in Figure 5.11. The points within the rectangles represent the 155.8 keV transition observed as a doublet in the spectrum depicted in Figure 5.6 (middle panel).

Figure 5.11 shows the relative total transition intensities for these transitions. In the absence of decays out of the band, gating on the transition lying at the top of the band ensures a constant total intensity down the cascade. Though this was not found to be so for either the M1 or E1 case, the assignment of magnetic dipole character to the transitions of Band 2 is favoured, because it gives approximately constant intensity.

The 887 keV $((\frac{13}{2}^+) \rightarrow (\frac{9}{2}^-))$ coincidence gate was used, in order to measure

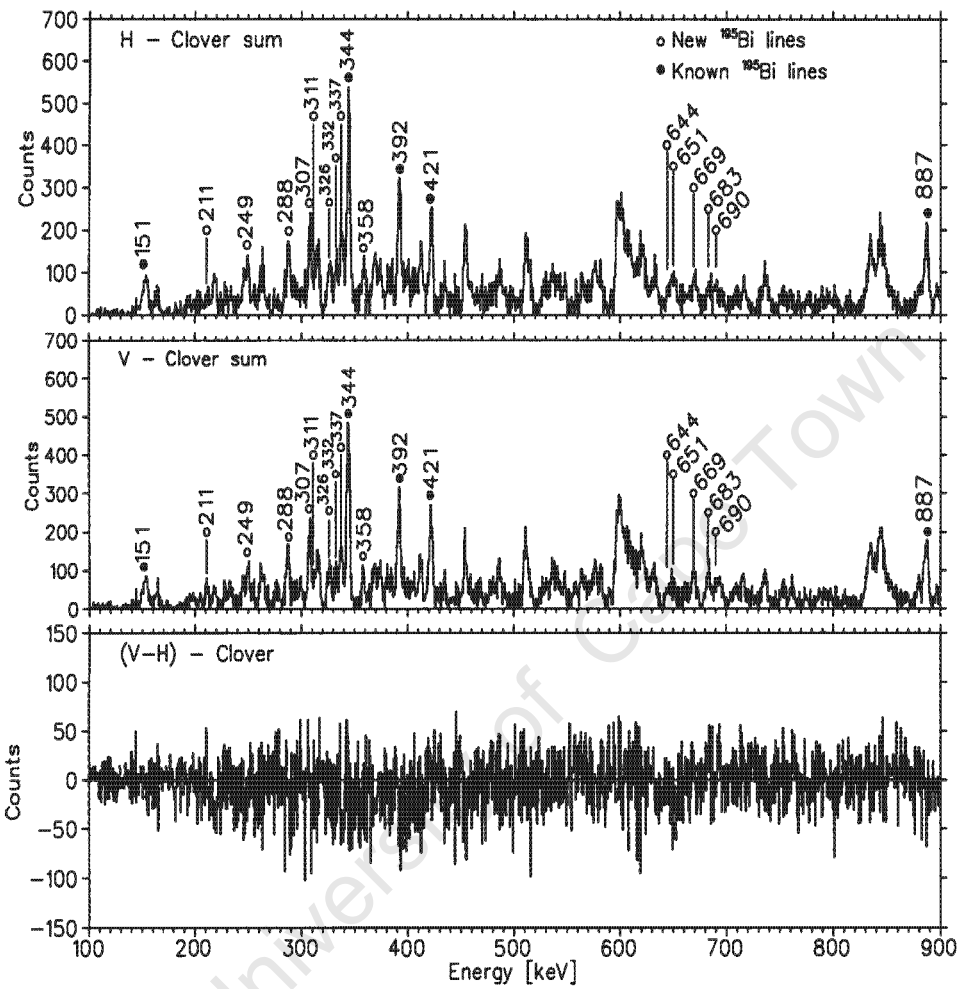

Figure 5.9: *The top and the middle panels depicts the Bi X-ray gated (Table 4.2) and background subtracted double-hit-events spectra of the horizontal (H) and vertical (V) scattered events extracted from Clover detectors at 90° respectively. The bottom panel displays the difference spectrum, which had insufficient counts to allow the electric or magnetic character of the γ-ray transitions to be determined. In both the top and middle panels the open and filled-circles represent the γ-rays from Bands 1, 2 and the ground-state band, respectively.*

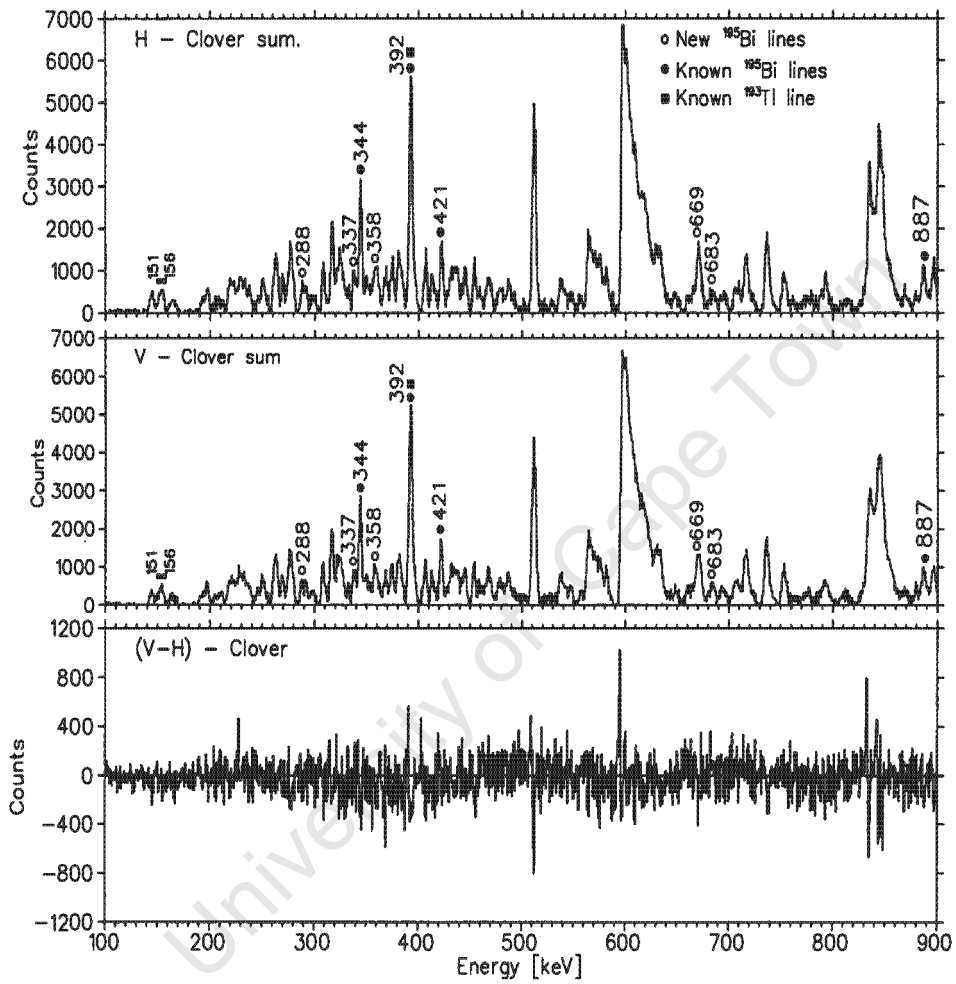

Figure 5.10: *The top and the middle panels depict background subtracted double-hit-events spectra of the horizontal (H) and vertical (V) scattered events extracted from Clover detectors at 90° respectively. The bottom panel displays the difference spectrum which has insufficient counts to allow the determination of the electric or magnetic character for the ^{195}Bi γ-ray transitions. In both the top and middle panels the open and filled-circles represent the γ-rays from Bands 1, 2 and the ground-state band, respectively.*

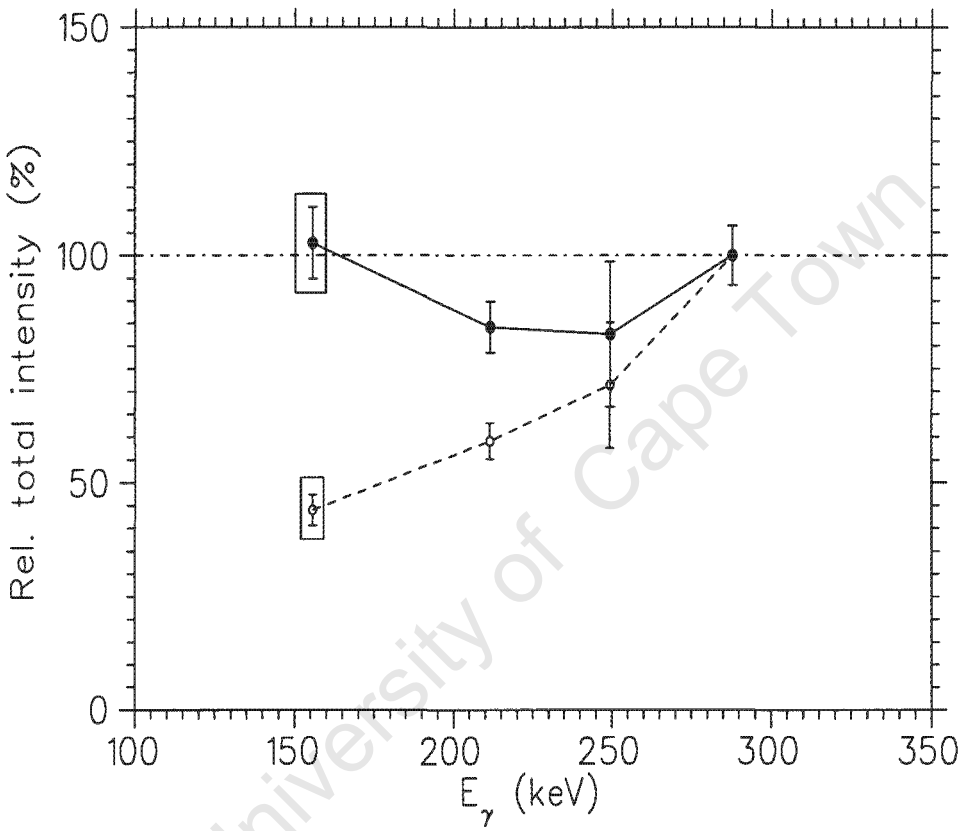

Figure 5.11: *Relative total transition intensities for Band 2 in ^{195}Bi assuming M1 (filled-circles) and E1 (open-circles) multipolarity. The gate was set on the 310.9 keV transition situated at the top of Band 2. The points within the rectangles indicate the 155.8 keV transition which is observed as a doublet. The dashed-dot line highlights the 100 % relative intensity mark.*

the relative intensities of the transitions in ^{195}Bi from structure A (below the $(\frac{21}{2}^+)$ level) and Band 1.

The relative intensities for the transitions within Band 2 were measured from 344 keV coincidence gated spectrum. From this 344 keV coincidence gate we extracted the relative intensities of the 156, 211, 249 and 288 keV transitions of Band 2. The intensities of the top most 311 and the lowest 112 keV transitions of Band 2 could not be determined due to insufficient counts in this gate. However, the 211 and 326 keV coincidence gated spectra were used in extracting the intensities for the 311 and 112 keV transitions respectively and were afterwards approximately normalised. The 156 keV transition is a doublet and its total intensity is included in Table 5.1.

Only one part of the intensity of Band 2 goes towards Band 1. In order to obtain the total intensity of Band 2 the relative intensities of the different decay paths were estimated. From the spectrum gated on 249 keV transition it was found that the relative intensity of 620 keV transition is $\approx$ 6.6 units, the total intensity in Band 1 is $\approx$ 7.0 units, while the total intensity inside Band 2 (measured for 211 keV transition) is $\approx$ 15.4 units. Thus, it is likely that below 211 keV transition, the intensity of Band 2 splits into two approximately equal parts, one going towards Band 1, the other one passing through 620 keV transition and probably ending up on an isomeric level. No evidence is found for other decay paths. Thus, the intensities of the transitions of Band 2, found from 344 keV gate were doubled in order to account for the intensity passing through 620 keV transition. The results obtained for the intensities of the γ-rays in ^{195}Bi are listed in Table 5.1.

The $\frac{B(M1)}{B(E2)}$ ratios were measured for the transitions in Band 1. The branching ratio for each level was accurately measured gating on the transition just above it. The results for the $\frac{B(M1)}{B(E2)}$ ratios are listed in Table 5.1.

5.1.5 RSAM Lifetime Measurements for ^{195}Bi

The previously known (filled-circles) transitions in Figure 5.13 from Structure A (in Figure 5.2) all lie below the known isomeric states [Lön86]. That is, the 114.6 keV transition below the 750 ns isomer at 2308.6 keV level. The 150.8, 343.7, 391.7 and 421.0 keV transitions lie below the 80 ns isomer

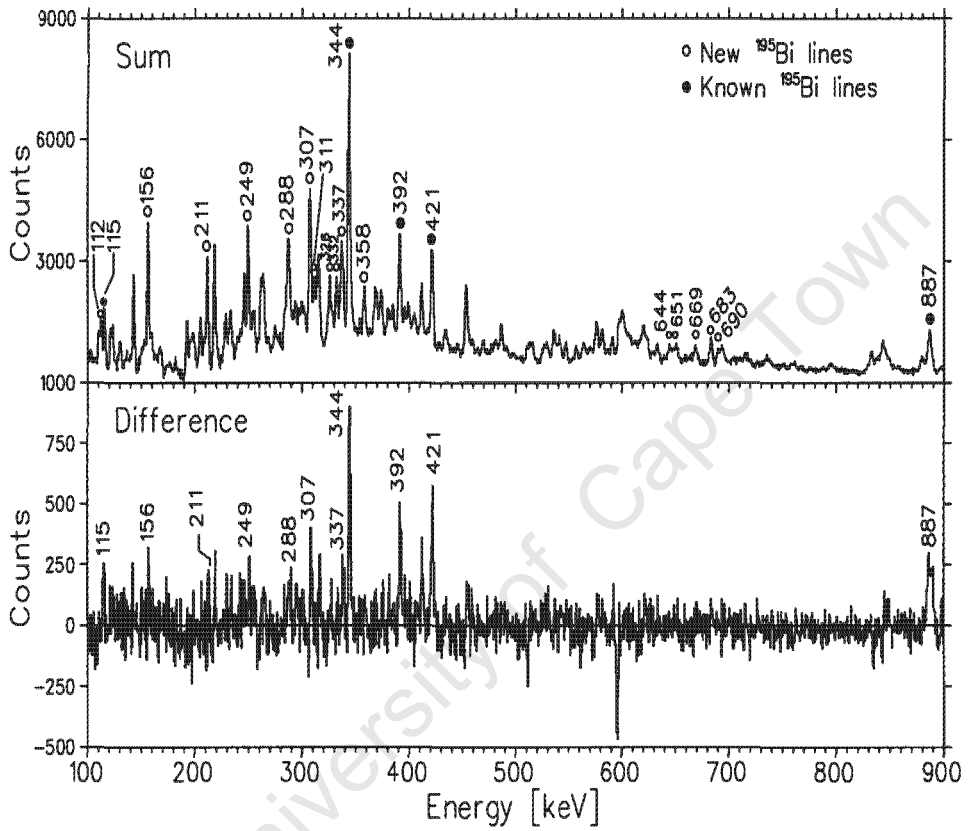

Figure 5.12: *The sum (difference) spectrum gated on the $K_{\alpha 1}$ and $K_{\alpha 2}$ Bi X-rays (Table 4.4) detected by the LEPS detectors generated for the $N_U + \alpha N_S$ ($N_U - \alpha N_S$) of the γ-rays detected by the Clover detectors at 96° (N_U) and 86° (N_S). The γ-ray transitions marked with filled-circles and open-circles highlights the known (delayed) and the new (prompt) ^{195}Bi transitions.*

Table 5.2: *The energies (E_γ) and the anisotropies (A_{RSAM}) for the γ-ray transitions in ^{195}Bi.*

E_γ (keV)	$\frac{N_{II}-\alpha N_S}{N_{II}+\alpha N_S}$ (%))[a]
112.3	)[b]
114.6	16
150.8	)[b]
155.6)[c]	4
211.0	3
248.6	6
288.0	3
306.9	3
310.9	4
325.5	4
331.9	3
336.6	4
343.7	9
357.6	4
391.7	12
421.0	16
643.5	)[b]
650.6	)[b]
668.5	8
683.1	7
689.5	)[b]
886.8	25

)[a] $\alpha = 1.05$, error bars were estimated to ≈ 4 % (see text).

)[b] Could not be determined due to lack of enough statistics.

)[c] Measurement for the unresolved peak doublet.

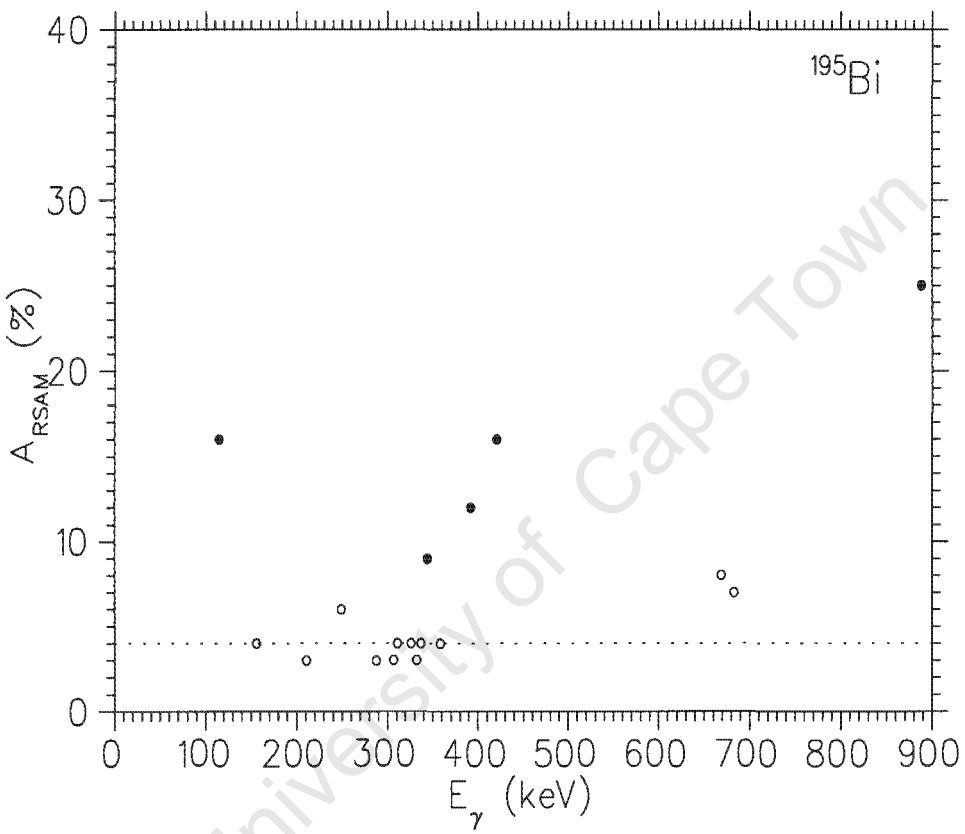

Figure 5.13: *The γ-ray anisotropies (A_{RSAM}) extracted from the Clover sum ($N_U + \alpha N_S$) and difference ($N_U - \alpha N_S$) spectra gated on the $K_{\alpha 1}$ and $K_{\alpha 2}$ Bi X-rays (Table 4.4) detected by the LEPS detectors. The open-circles (closed-circles) depict the new (old) transitions found in ^{195}Bi for Band 1 and 2. A dotted-line marks the 4 % anisotropy line.*

at 2194.0 keV level while the 886.8 keV transition is situated below the 32 ns isomer at 886.8 keV level. The intensities of these delayed transitions are hindered since the nuclei recoil out of the focus of the detectors. The anisotropies for the ^{195}Bi transitions were measured and listed in Table 5.2. The Clover sum ($N_U + \alpha N_S$) and the difference (N_U - αN_S) spectra have been generated and shown in Figure 5.12. The relative efficiency was measured as: $\alpha = 1.05$ and has been used in generating these spectra. Table 5.2 lists the energies (E_γ) and the measured anisotropies (A_{RSAM}) of γ-ray transitions associated with the ^{195}Bi nuclei.

Firstly, we estimated the error bars on the measured anisotropy. Thus, the anisotropy for few prompt peaks, that is, transitions which do not appear in the difference spectrum as peaks was measured. The anisotropy for such transitions is $\leq$ 4 %, which was accepted as the error bars on the anisotropy in general for experiment I. The transitions which are known to be delayed show peaks in the difference spectrum and have large anisotropy (in Table 5.2) which confirm their delayed nature. In Figure 5.13 the A_{RSAM} for the known delayed transitions fall within 9 – 25 % range. The A_{RSAM} values for most of the Band 1 and 2 (Figure 5.2) γ-ray are below 6 % and are considered therefore, to be prompt. Therefore, on the basis of these results there is no evidence of the existence of nanosecond isomeric states in the two new bands.

5.2 ^{197}Bi Level Scheme

The previous level scheme of ^{197}Bi [Zho95] known only up to 4.025 MeV is shown in Figure 5.14. The low-lying states (below 4.025 MeV level) in the ^{197}Bi level scheme arise entirely from the single-particle excitations. However, a band labelled Band 1 in Figure 5.15 has been found and assigned to ^{197}Bi in the present work. The discussion of the ^{197}Bi level scheme shown in Figure 5.15 is divided into several parts which presents the analysis performed on the γ-γ coincidence relationships, DCO ratios, polarisation measurements and the nanosecond isomer search.

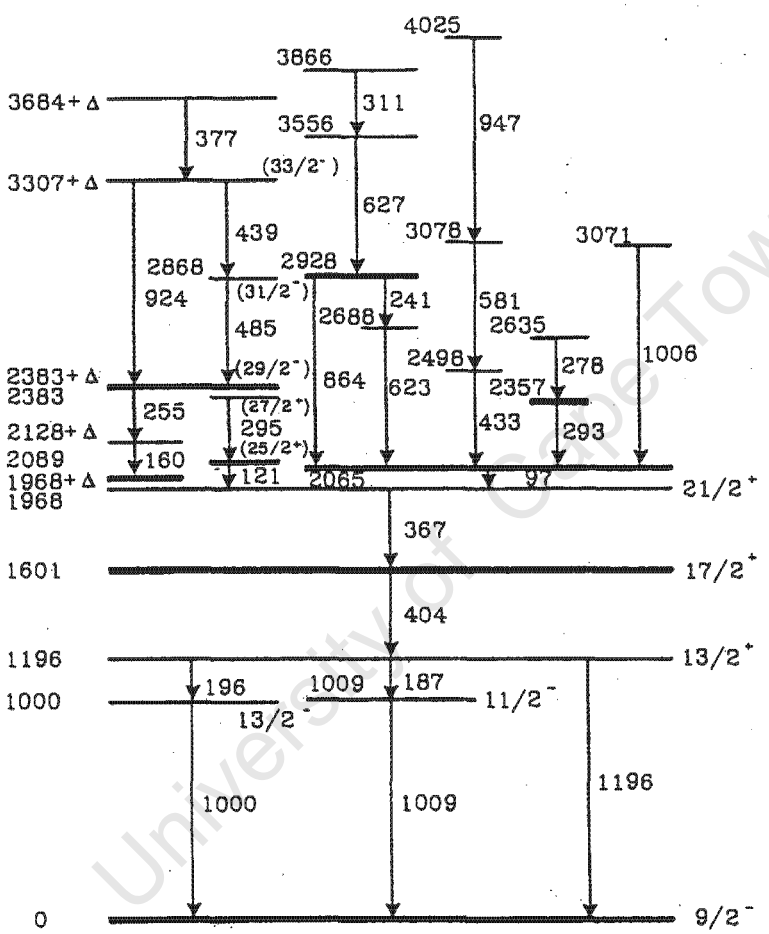

Figure 5.14: *The known level scheme of ^{197}Bi taken from [Zho95].*

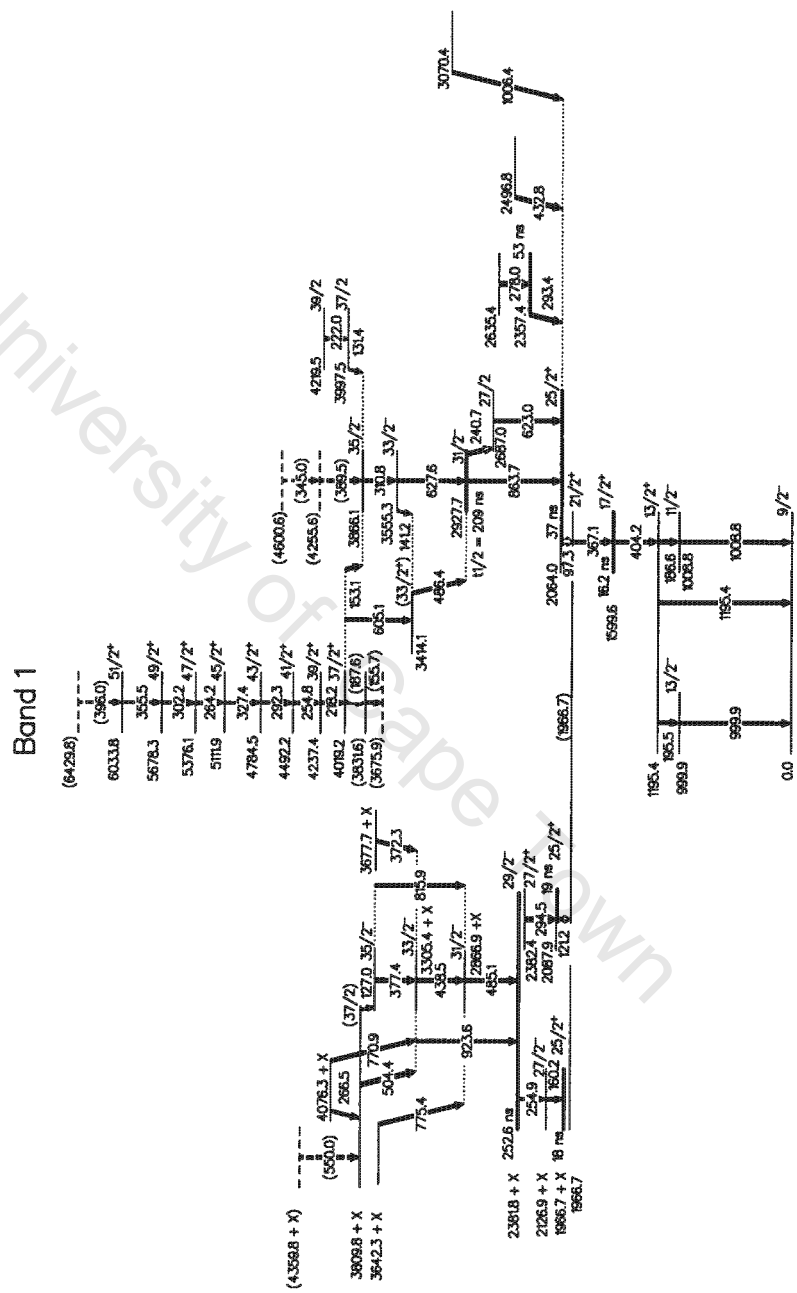

Figure 5.15: *The level scheme of ^{197}Bi deduced from the present work.*

5.2.1 γ-γ coincidences

The discussion is divided into three parts, that is, the:

- low lying levels,
- levels above the $\frac{29}{2}^-$ isomer and
- levels above the $\frac{25}{2}^+$ isomer.

Low lying levels

Isomers with long lifetimes made it difficult to establish γ-ray coincidences. No new levels were found in this part of the level scheme. However, our analysis confirmed the previously suggested level scheme [Zho95].

The 999.9, 1008.8, 1195.4 keV coincidence gates

In the present work the γ-γ coincidence relationship analysis did not confirm a coincidence between 97.3 and 294.5 keV transitions as reported by Chapuran et al., [Cha86]. However, it supports the order of the transitions in the ^{197}Bi level scheme by Zhou et al., [Zho95], shown in Figure 5.14. The 999.9, 1008.8, 1195.4 keV gates are shown in Figure 5.16 (a), (b) and (c) respectively. No new lines are seen in these gates. These gates indicate the ordering of the transitions with regard to their intensities down the cascade. The 999.9, 1008.8 and 1195.4 keV transitions are observed in the coincidence spectra gated on the 404.2 and 367.1 keV transitions depicted in Figure 5.18.

Levels above the $\frac{29}{2}^-$ isomer at 2381.8 + X keV

Few new levels were deduced from this work and those known were confirmed.

The 485.1, 550.0 and 377.4 keV coincidence gates

The 485.1 keV coincidence gate in Figure 5.17 (a) revealed eight new transitions (775.4, 504.4, 266.5, 372.3, 550.0, 770.9, and 127.0, 815.9 keV) together with the known (377.4, 438.5 and 404.2 ($\frac{17}{2}^+ \rightarrow \frac{13}{2}^+$) keV) transitions

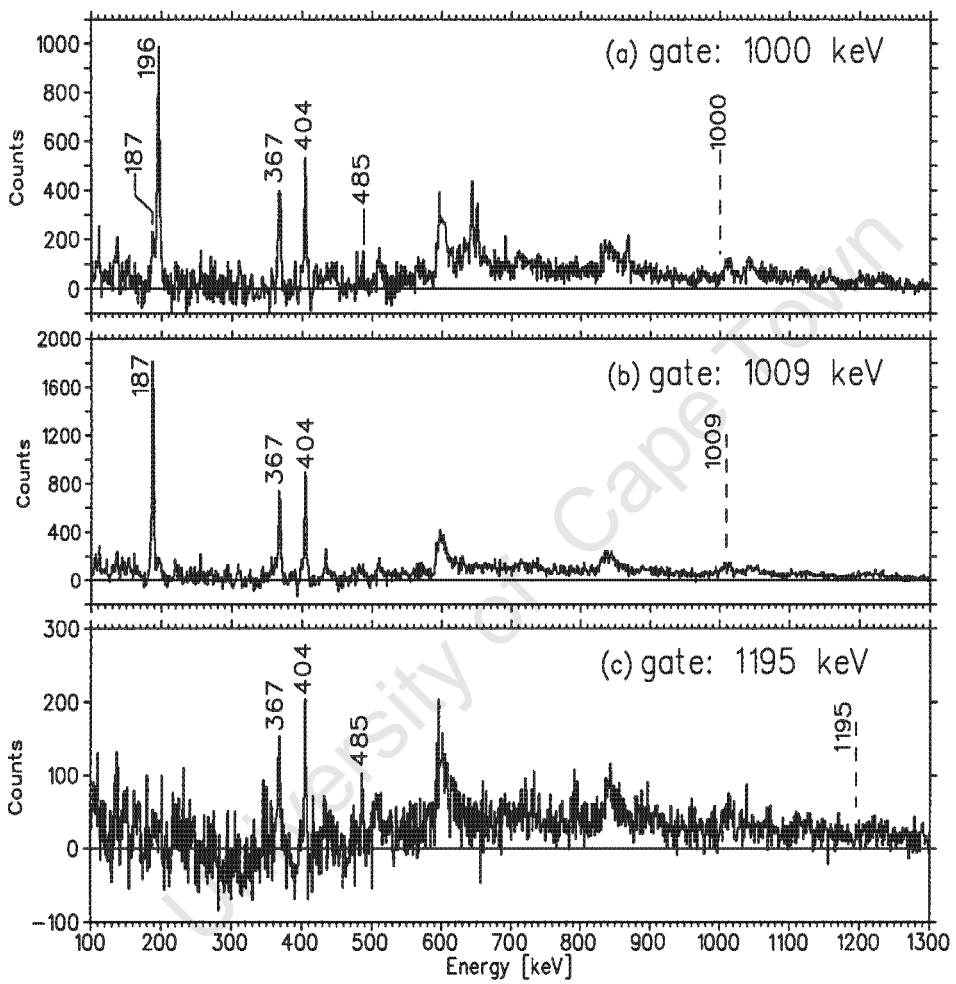

Figure 5.16: *The ^{197}Bi coincidence γ-ray spectra generated from the ungated γ-γ matrix by gating on the (a) 999.9, (b) 1008.8 and (c) 1195.4 keV transitions.*

associated with the ^{197}Bi nucleus. The 550 keV coincidence gate in Figure 5.17 (c) shows that it is self-coincident. This is an indicative of the existence of another 550 keV transition in ^{197}Bi which is not placed yet in the level scheme. It is also in coincidence with the lower-lying (186.6, 195.5, 367.1, 377.4, 438.5, 404.2 and 923.6 keV) ^{197}Bi transitions. The 266.5, 372.3 and 770.9 keV transitions in the 485.1 keV coincidence gate shown in Figure 5.17 (a) are weaker and close to less intense transitions. The 377.4 keV coincidence gated in Figure 5.17 (b) yields three (127.0, 266.5 and 550.0 keV) new transitions in ^{197}Bi. The 330, 345 and 630 keV transitions observed within the gate belong to ^{198}Bi nucleus. The 404.2, 438.5, 485.5 and 923.6 keV transitions below the $\frac{33}{2}^-$ at (3305.4 + X) keV level are observed.

Levels above the $\frac{25}{2}^+$ isomer at 2064.0 keV

All the transitions above the $\frac{31}{2}^-$ isomer at 2927.7 keV are new, apart from the 628 and 311 keV transitions. The γ-ray coincidence spectra extracted from the gated and ungated γ-γ matrix (see Table 4.3 in Chapter 4) gated on various transitions above the $\frac{25}{2}^+$ at 2064.0 keV showing these new transitions are discussed. Furthermore, summed coincidence spectra produced by gating on new transitions from Band 1 are also discussed.

The 628 keV coincidence gate

The intensities of all of the low-lying transitions are hindered by the existence of the 209, 37 and 16.2 ns isomers at 2927.7, 2064.0 and 1599.6 keV respectively. Some low-lying 999.9, 1008.8, 97.3, 623.0 and 863.7 keV transitions are not seen in the 628 keV gated spectrum, while other previously known low-lying (195.5, 367.1 and 404.2 keV) transitions [Zho95, Cha86] can be observed in Figure 5.18 (b). The 389.5 and 345.0 keV transitions placed above the 3866.1 keV level are tentative, and are thus bracketed. These transitions, together with the 131.4 keV line are seen in coincidence with the 628 keV transition in Figure 5.19.

The new (218.2, 254.8, 292.3, 327.4, 264.2, 302.2, 355.5 and 396.0 keV) transitions which constitute Band 1 in Figure 5.15 are in coincidence with the

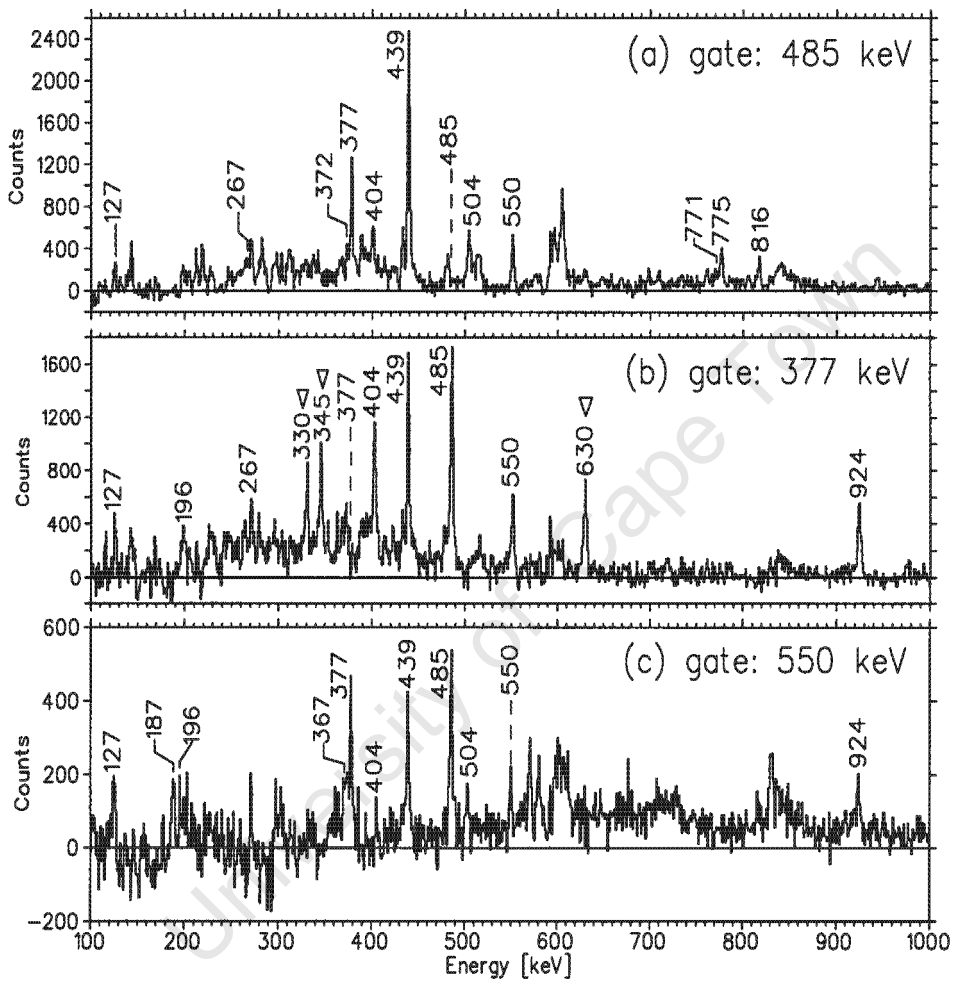

Figure 5.17: *The ^{197}Bi coincidence γ-ray spectra generated from the ungated γ-γ matrix by gating on the (a) 485.1, (b) 377.4 and (c) 550.0 keV transitions. In (b), the energies for the γ-ray transitions observed in ^{198}Bi are indicated by the arrows.*

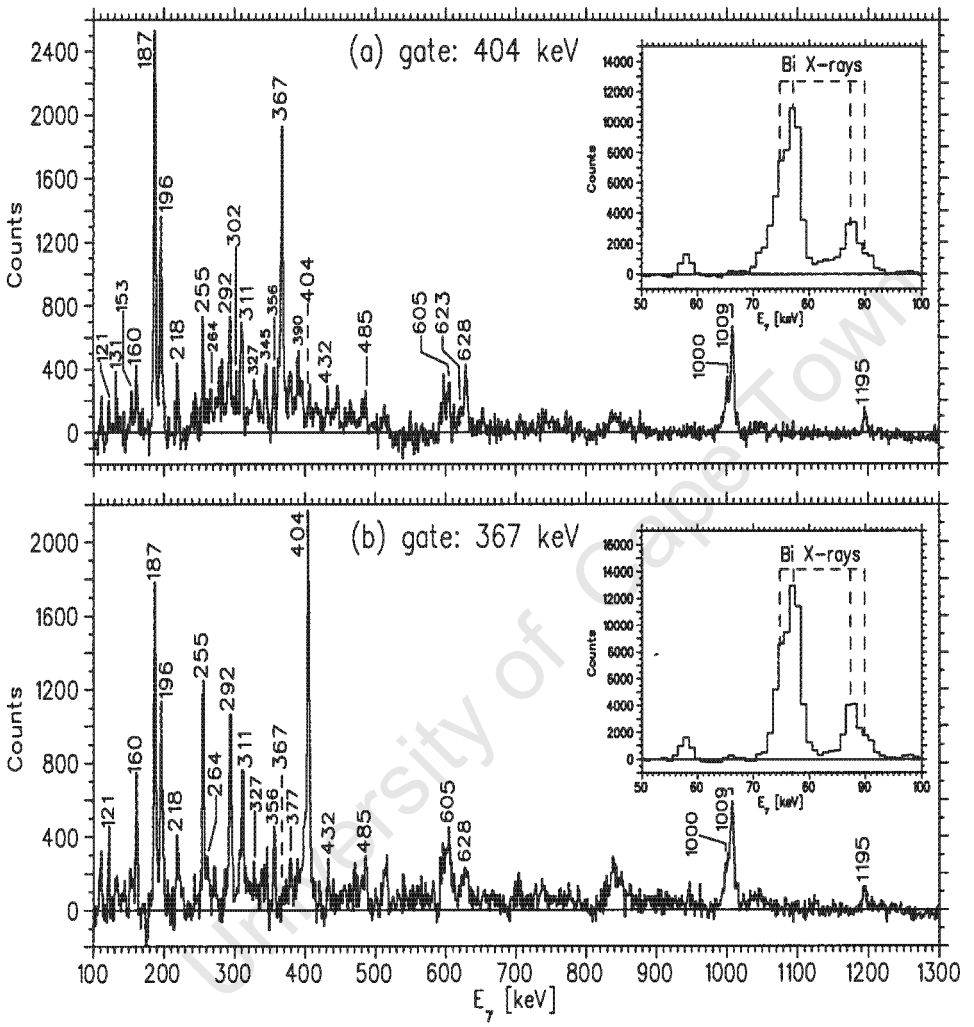

Figure 5.18: *The ^{197}Bi spectra extracted from the ungated matrix, gated on the: (a) 404.2 and (b) 367.1 keV γ-ray transitions. The position of the gates are indicated by dashed-lines in both panels. In (a) and (b), the insert show the exact positions of the Bi X-rays observed in the low energy region of the two spectra.*

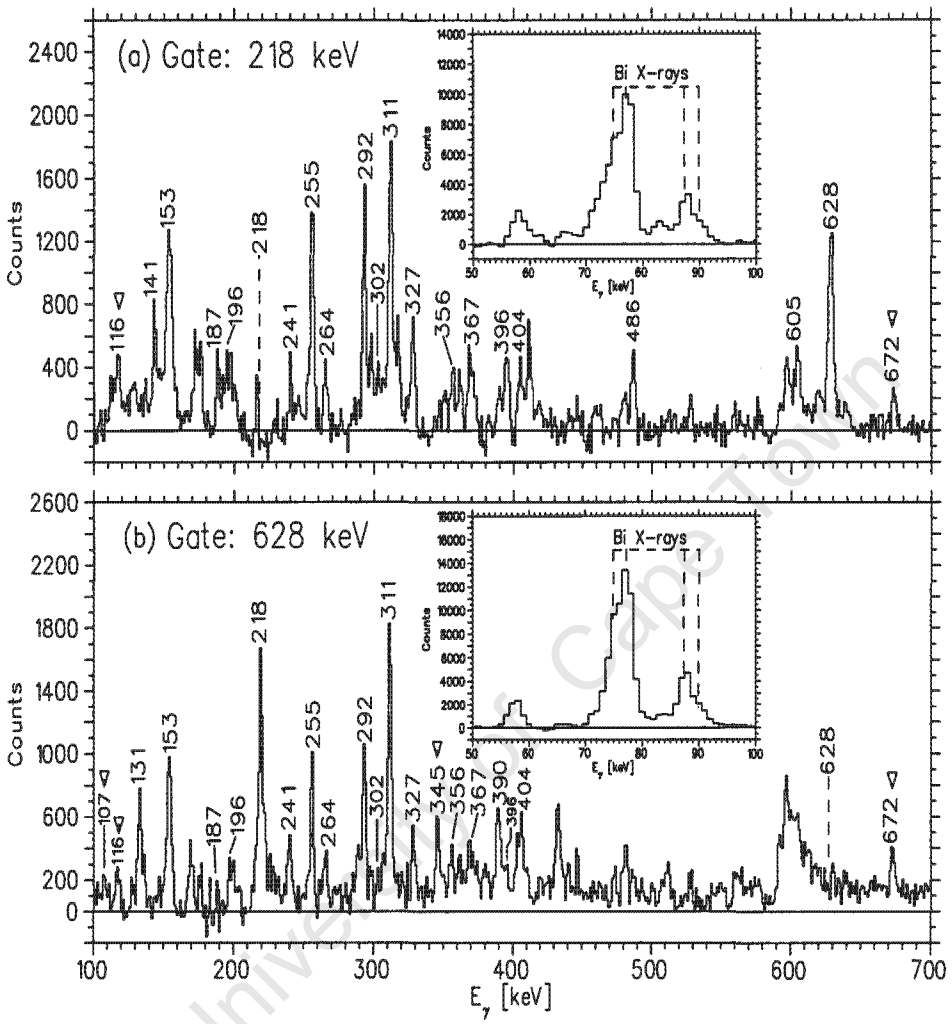

Figure 5.19: *The background subtracted spectra extracted from the ungated matrix, gated on the: (a) 218.2 and (b) 627.6 keV γ-ray transitions. The position of the gates are indicated by dashed-lines in both panels. In (a) and (b), the insert show the exact positions of the Bi X-rays observed in the low energy region of the two spectra. The presence of the Bi X-rays, 311 and 628 keV transitions in the 218.2 keV coincidence gate emphasise that the newly observed 218.2 keV transition belong to ^{197}Bi. The γ-ray transitions marked with arrows belong to ^{198}Bi.*

311 and 627.6 keV transitions (in Figure 5.19 (b)) and are therefore placed in ^{197}Bi. The 302.2 and 396.0 keV transitions are weak in the 627.6 keV gate, but their placement is confirmed by gating on transitions belonging to Band 1. The 628 keV gate yields also some transitions in ^{198}Bi, but the relative transition intensities of these transitions with respect to those of ^{197}Bi are relatively low. Therefore, in the following study when we measure the DCO ratio and linear polarisation for the 628 keV γ-ray, we consider the obtained results as applicable to the 628 keV transition in ^{197}Bi.

The 222, 131 and 311 keV coincidence gates

The 222, 131 and 311 keV γ-ray coincidence spectra extracted from the ungated $\gamma-\gamma$ matrix are shown in Figures 5.20 (a), (b) and (c) respectively. A coincidence relationship between the new 222 and 131 keV transition and the known transitions below the $\frac{35}{2}^-$ level at 3866.1 keV is observed. The 311 keV γ-ray coincidence spectrum extracted from the (d) gated matrix show that it is in coincidence with the Band 1 (218, 255, 292, 327, 264 keV) transitions and also in coincidence with the transitions of ^{197}Bi. Comparing the spectra in Figure 5.20 (c) and (d) one can see that many strong peaks from the former spectrum do not appear anymore in the latter one, indicating that they belong to a Tl nucleus.

Gates on Band 1 transitions

The coincidence spectra in Figure 5.21 (a) and (c) are gated on the 396.0 and the 302 keV transitions respectively. The 396.0 keV transitions is in coincidence with the low-lying 186.6, 195.5, 367.6 and 404.2 keV transitions and the 311 and 627.6 keV. The 302.2 keV gate yields some (186.6, 404.2 and 627.6 keV) low-lying transitions. Band 1 transitions are in coincidence with themselves and with with the low-lying 186.6, 195.5, 367.1 and 404.2 keV transitions as well as the 311 and 628 keV transitions as shown in Figure 5.21, 5.22 and 5.19 (a). Thus Band 1 was assigned to ^{197}Bi. In Figure 5.19 (a) seven new (254.8, 292.3, 327.4, 264.2, 302.2, 355.5 and 396.0 keV) transitions are revealed and placed in Band 1 (above the $\frac{37}{2}^+$ at 4019.2 keV level). The new 605.1, 486.4, 153.1, and 141.2 keV transitions are seen in coincidence

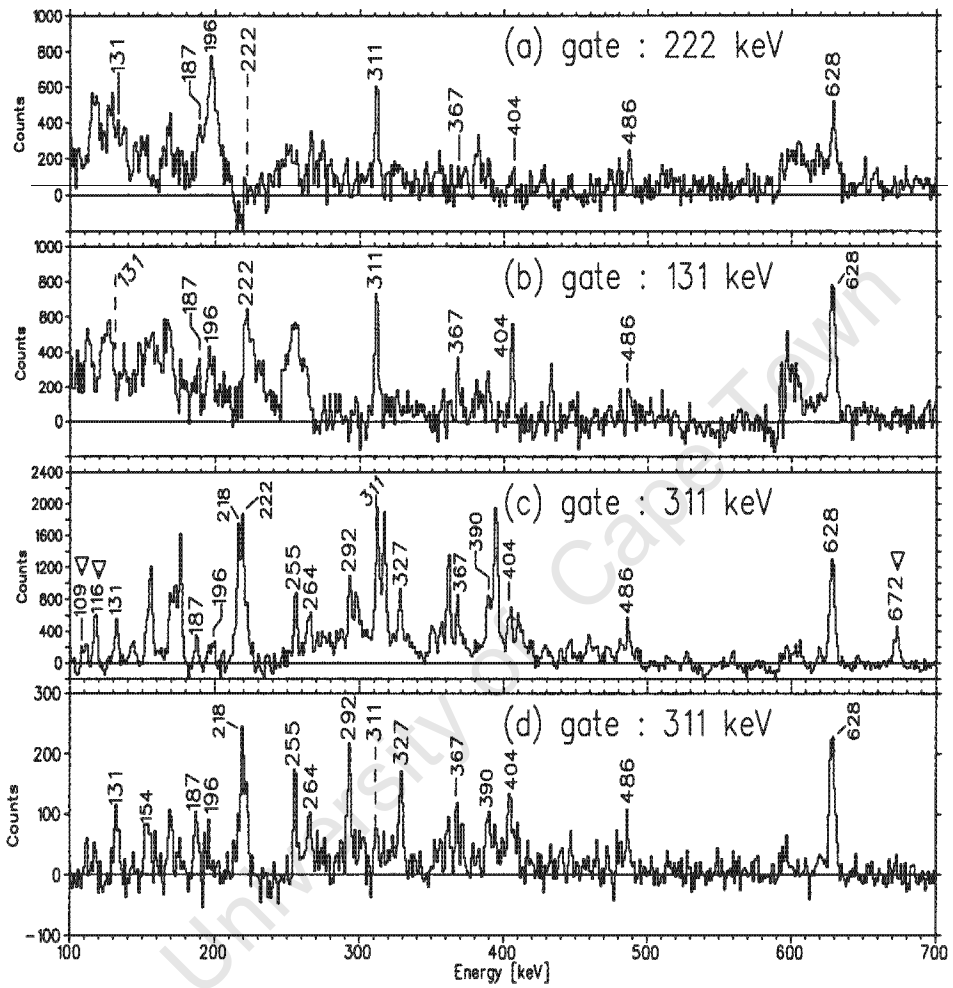

Figure 5.20: *The ^{197}Bi coincidence γ-ray spectra generated from the ungated γ-γ matrix by gating on the (a) 222.0, (b) 131.4 and (c) 310.8 keV transitions. The γ-ray spectrum (d) gated on the 310.8 keV transition was extracted from the gated γ-γ matrix. The arrows in panel (c) indicates the ^{198}Bi γ-ray transitions.*

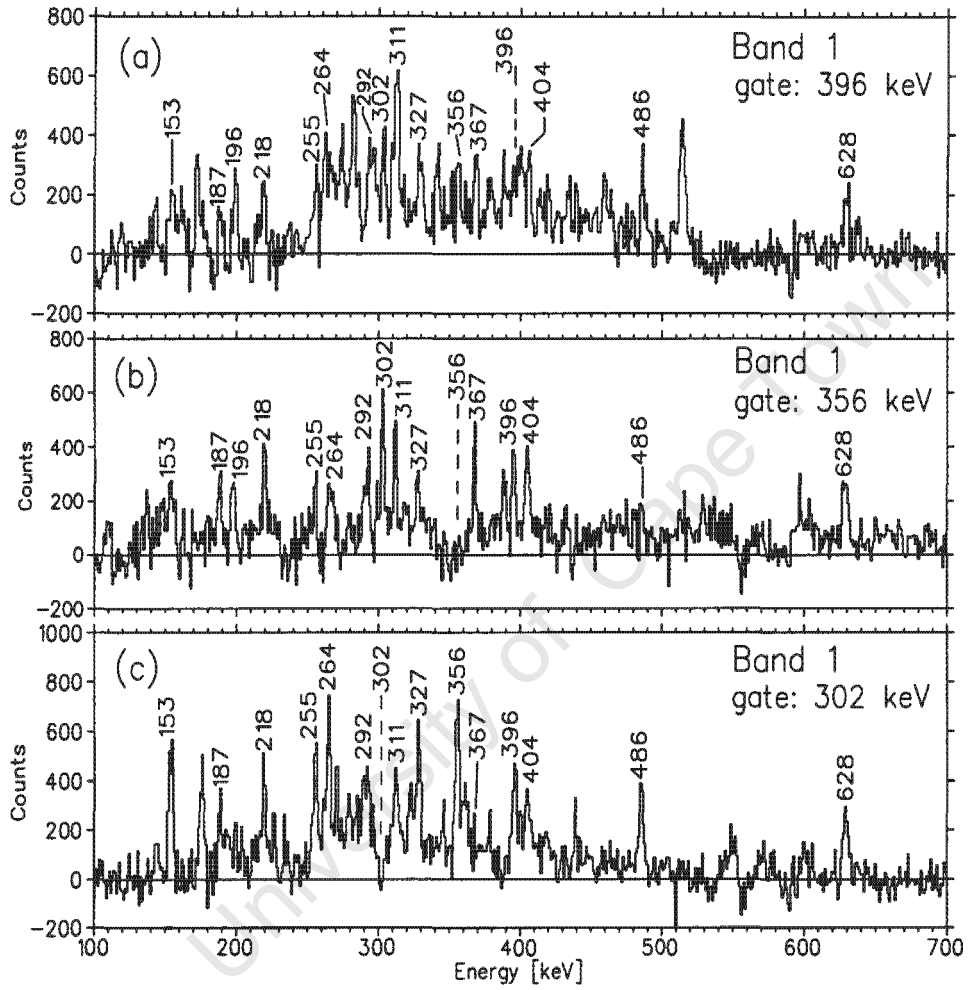

Figure 5.21: *The γ-ray coincidence spectra generated from the ungated matrix, gated on the (a) 396.0 keV, (b) 355.5 keV and (c) 302.2 keV γ-ray transitions of Band 1. In all panels, the position of the gates are indicated by the dashed-lines and the γ-ray peaks are labelled with their respective energies.*

with the 218 keV gate.

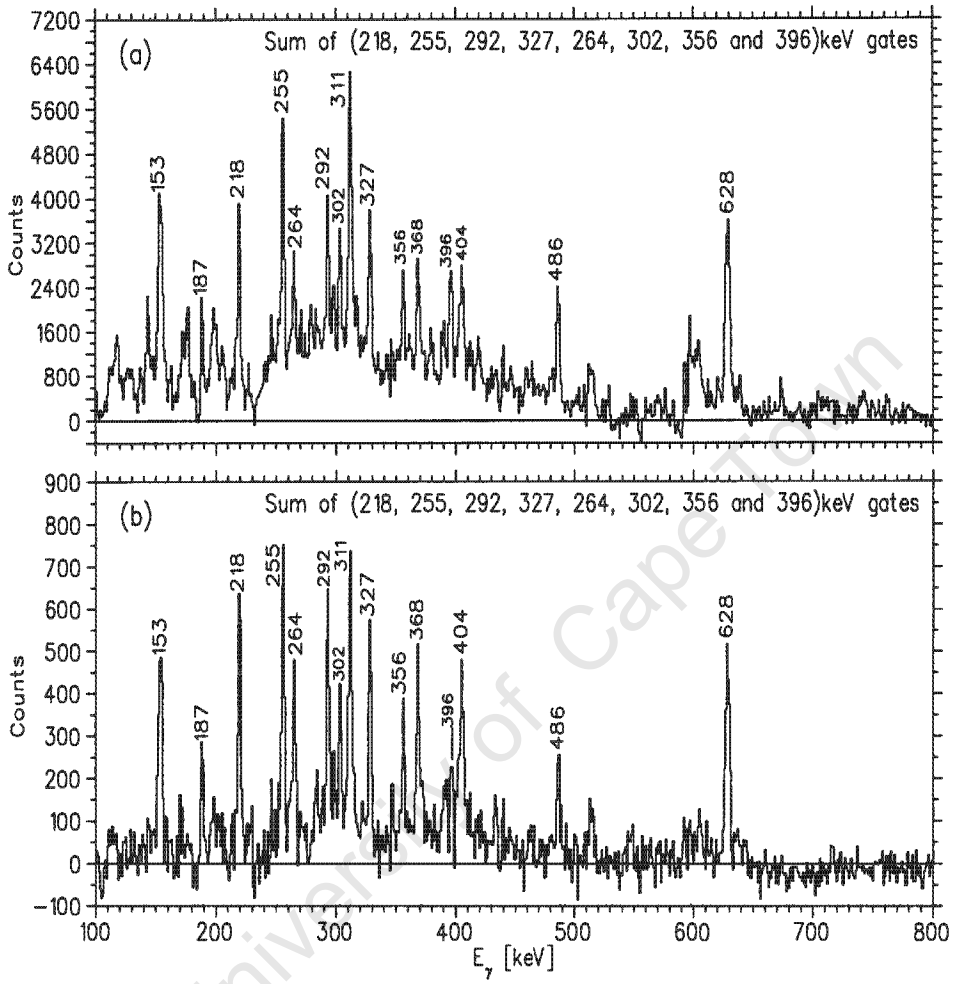

Figure 5.22: *The summed coincidence γ-ray spectra for Band 1 in ^{197}Bi. These spectra are generated from the (a) ungated and (b) gated (on the $K_{\alpha 2}$, $K_{\alpha 1}$ Bi X-rays detected with the LEPS detectors) matrices by summing the 218.2, 254.8, 292.3, 327.4, 264.2, 302.2, 355.5 and 396.0 keV gates.*

5.2.2 ^{197}Bi DCO

A similar procedure to the one followed in section 5.1.2 was adhered to, in performing the R_{DCO} measurements for experiment II. The γ-ray Clover spectra gated on the $K_{\alpha 1}$ Bi X-ray on the y-axis of the DCO matrices were

Table 5.3: *The level energies (E_{exc}), initial spins I_i, γ-ray transition energies (E_γ), intensities (I_γ), total intensities (I_t), DCO ratios ($R_{DCO} = \frac{I(45°;135°)}{I(90°)}$), polarisation anisotropy ($A_p = \frac{N_V - \alpha N_H}{N_V + \alpha N_H}$), $\frac{B(M1)}{B(E2)}$ ratios and the spin assignments for the ^{197}Bi nuclei.*

E_{exc} (keV)	I_i	E_γ (keV)	I_γ (%)	I_t (%)	R_{DCO}	A_p	$\frac{B(M1)}{B(E2)}$ $(\mu_N/eb)^2$	Assignment
999.9	$\frac{13}{2}^-$	999.9			)[a]	)[a]		$\frac{13}{2}^- \rightarrow \frac{9}{2}^-$
1008.8	$\frac{11}{2}^-$	1008.8			)[a]	)[a]		$\frac{11}{2}^- \rightarrow \frac{9}{2}^-$
1195.4	$\frac{13}{2}^+$	1195.4			)[a]	)[a]		$\frac{13}{2}^+ \rightarrow \frac{9}{2}^-$
1195.4	$\frac{13}{2}^+$	186.6			0.74(8)	)[a]		$\frac{13}{2}^+ \rightarrow \frac{11}{2}^-$
1195.4	$\frac{13}{2}^+$	195.5			0.70(14)	)[a]		$\frac{13}{2}^+ \rightarrow \frac{13}{2}^-$
1599.6	$\frac{17}{2}^+$	404.2			1.17(9)	)[a]		$\rightarrow \frac{13}{2}^+$
1966.7	$\frac{21}{2}^+$	367.1			0.88(7)	+0.06(1)		$\frac{21}{2}^+ \rightarrow \frac{17}{2}^+$
2064.0	$\frac{25}{2}^+$	97.3			1.24(28)	)[a]		$\frac{25}{2}^+ \rightarrow \frac{21}{2}^+$
2087.9	$\frac{25}{2}^+$	121.2						$\frac{25}{2}^+ \rightarrow \frac{21}{2}^+$
2126.9 + X	$\frac{27}{2}^-$	160.2			0.77(16)			$\frac{27}{2}^- \rightarrow \frac{25}{2}^+$
2357.4		293.4)[b]			0.55(9)	)[a]		
2382.4	$\frac{27}{2}^+$	294.5)[b]			0.63(10)	)[a]		$\frac{27}{2}^+ \rightarrow \frac{25}{2}^+$
2381.8 + X	$\frac{29}{2}^-$	254.9				)[a]		$\frac{29}{2}^- \rightarrow \frac{27}{2}^-$
2496.8		432.8			0.65(15)	)[a]		
2635.4		278.0			)[a]	)[a]		)[a]
2687.0	$\frac{27}{2}^a$	623.0			)[a]	)[a]		$\frac{27}{2}^a \rightarrow \frac{25}{2}^+$
2866.9 + X		485.1)[b]			0.54(9)	-0.04(4)		$\frac{31}{2}^- \rightarrow \frac{29}{2}^-$
2927.7	$\frac{31}{2}^-$	240.7			0.47(31)			$\frac{31}{2}^- \rightarrow \frac{27}{2}^a$
2927.7	$\frac{31}{2}^-$	863.7			)[a]	)[a]		$\frac{31}{2}^- \rightarrow \frac{25}{2}^+$
3070.4		1006.4			)[a]	)[a]		$\rightarrow \frac{25}{2}^+$
3305.4 + X	$\frac{33}{2}^-$	438.5			0.54(14)	-0.02(1)		$\frac{33}{2}^- \rightarrow \frac{31}{2}^-$
3305.4 + X	$\frac{33}{2}^-$	923.6			1.11(25)	+0.26(2)		$\frac{33}{2}^- \rightarrow \frac{29}{2}^-$
3414.1	$(\frac{33}{2}^+)$	486.4)[b]			0.54(9)	)[a]		$(\frac{33}{2}^+) \rightarrow \frac{31}{2}^-$
3555.3	$\frac{33}{2}^-$	627.6)[b]			0.54(7)	-0.03(1)		$\frac{33}{2}^- \rightarrow \frac{31}{2}^-$
3555.3	$\frac{33}{2}^-$	141.2			)[a]	)[a]		$\frac{33}{2}^- \rightarrow (\frac{33}{2}^+)$
3642.3 + X		775.4			)[a]	)[a]		$\rightarrow \frac{31}{2}^-$
3677.7 + X		372.3			)[a]	)[a]		$\rightarrow \frac{33}{2}^-$
3682.8 + X	$\frac{35}{2}^-$	377.4			0.55(14)	)[a]		$\frac{35}{2}^- \rightarrow \frac{33}{2}^-$
3682.8 + X		815.9			)[a]	)[a]		$\frac{35}{2}^- \rightarrow \frac{31}{2}^-$
3809.8 + X	$(\frac{37}{2}^a)$	127.0		)[a]	0.63(19)			$(\frac{37}{2}^a) \rightarrow \frac{35}{2}^-$
3809.8 + X	$(\frac{37}{2}^a)$	504.4			)[a]	)[a]		$(\frac{37}{2}^a) \rightarrow \frac{33}{2}^-$
(3831.6)		(155.7))[c]			)[a]	)[a]		
3866.1	$\frac{35}{2}^-$	310.8	70(4)	100	0.49(10)	-0.06(1)		$\frac{35}{2}^- \rightarrow \frac{33}{2}^-$
3997.5	$\frac{37}{2}^a$	131.4		)[a]		0.55(25)		$\frac{37}{2}^a \rightarrow \frac{35}{2}^-$

...continues from Table 5.3.

E_{exc} (keV)	I_i	E_γ (keV)	I_γ (%)	I_t (%)	R_{DCO}	A_p	$\frac{B(M1)}{B(E2)}$ $(\mu_N/eb)^2$	*Assignment*
4019.8	$\frac{37}{2}^+$	153.7	38(6)	44	0.56(22)	)[a]		$\frac{37}{2}^+ \rightarrow \frac{35}{2}^-$
4019.8	$\frac{37}{2}^+$	(187.6))[c]				)[a]		$\frac{37}{2}^+ \rightarrow$
4019.8	$\frac{37}{2}^+$	605.7	44(6)	44	)[a]	)[a]		$\frac{37}{2}^+ \rightarrow (\frac{33}{2}^+)$
4076.3 + X		266.5			)[a]	)[a]		$\rightarrow (\frac{37}{2}^a)$
4076.3 + X		770.9			)[a]	)[a]		$\rightarrow \frac{33}{2}^-$
4219.5	$\frac{39}{2}^a$	222.0		)[a]	0.66(14)	)[a]		$\frac{39}{2}^a \rightarrow \frac{37}{2}^a$
4237.4	$\frac{39}{2}^+$	218.2)[B1]	26(8)	58	0.54(6)	)[a]		$\frac{39}{2}^+ \rightarrow \frac{37}{2}^+$
(4255.6)		(389.5))[b,c]			0.58(12)	)[a]		$(\frac{53}{2}^+) \rightarrow \frac{51}{2}^+$
(4359.8 + X)		(550.0))[c]			0.64(18)	)[a]		$\rightarrow (\frac{37}{2}^a)$
4492.2	$\frac{41}{2}^+$	254.8)[B1]	20(8)	35	0.64(7)	)[a]	$\geq$ 18.4	$\frac{41}{2}^+ \rightarrow \frac{39}{2}^+$
(4600.6)	$(\frac{39}{2}^a)$	(345.0))[b,c]			)[a]	)[a]		$(\frac{39}{2}^a) \rightarrow (\frac{37}{2}^a)$
4784.5	$\frac{43}{2}^+$	292.3)[B1]	18(9)	28	0.59(9)	)[a]	$\geq$ 12.3	$\frac{43}{2}^+ \rightarrow \frac{41}{2}^+$
5111.9	$\frac{45}{2}^+$	327.4)[B1]	14(10)	20	0.47(17)	-0.05(2)	$\geq$ 13.8	$\frac{45}{2}^+ \rightarrow \frac{43}{2}^+$
5376.1	$\frac{47}{2}^+$	264.2)[B1]	0.5(17)	9	0.46(18)	)[a]	$\geq$ 30.3	$\frac{47}{2}^+ \rightarrow \frac{45}{2}^+$
5678.3	$\frac{49}{2}^+$	302.2)[B1]	0.3(13)	4	0.52(16)	)[a]	$\geq$ 9.3	$\frac{49}{2}^+ \rightarrow \frac{47}{2}^+$
6033.8	$\frac{51}{2}^+$	355.5)[B1]	0.2(13)	3	0.49(23)	)[a]		$\frac{51}{2}^+ \rightarrow \frac{49}{2}^+$
(6429.8)	$(\frac{37}{2}^a)$	(396.0))[c,B1]			)[a]	)[a]		$\rightarrow \frac{51}{2}^+$

$\alpha = 1.05$

[a] Could not be determined due to lack of enough statistics.

[b] Measurement for the unresolved doublet.

[c] Tentative.

[B1] Band 1.

generated.

The R_{DCO} of the previously known E1 (160.2, 186.6 and 195.5 keV), M1 (254.8, 294.5, 438.5 and 485.1 keV) and the E2 (97.3, 367.1, 404.2 and 923.6 keV) transitions in ^{197}Bi [Cha86, Zho95] were determined and are marked with filled-circles and the doublets with stars in Figure 5.23. The R_{DCO} of these transitions are consistent with the previously suggested multipolarities [Cha86, Zho95].

The average R_{DCO} for the known M1 (224.8, 294.5, 438.5 and 485.1 keV) and E1 (160.2, 186.6 and 195.5 keV) transitions in ^{197}Bi [Cha86, Zho95] was determined as 0.65 $\pm$ 0.09 while for the E2 (97.3, 404.2, 923.6 and 367.1 keV) transitions was 1.10 $\pm$ 0.09. These average values are marked by the dashed-lines in Figure 5.23 for ^{197}Bi and the insert of this figure for ^{198}Bi (discussed in section 5.3.1).

The multipolarity for the known 310.9, 432.8 and 627.6 keV transitions marked with empty-squares in Figure 5.23 were not determined previously [Zho95]. However, the present work revealed that they are dipole in character. The new (131.4, 153.1, 218.2, 222.0, 240.7, 264.2, 302.2, 327.4, 355.5, 389.5 and 550.0 keV) transitions (marked with empty-circles in Figure 5.23) were found to be dipole in character. The R_{DCO} (Table 5.3) for the known 97.3 keV ($\frac{25}{2}^+ \rightarrow \frac{21}{2}^+$) transition found in this work confirm the quadrupole nature previously determined by [Cha86].

The R_{DCO} measurements were made cumbersome by the presence of the doublets (transitions which are close to each other in energy). For instance, in order to measure the R_{DCO} for the 292.3 keV ($\frac{43}{2}^+ \rightarrow \frac{41}{2}^+$) line without bringing in the 293.4 keV transition at 2064.0 keV level, the coincidence spectra gated on the intense 310.8 keV ($\frac{35}{2}^- \rightarrow \frac{33}{2}^-$) transition was generated. The R_{DCO} for the 131.4, 222.0, 254.8 and 292.3 keV were determined from this coincidence gated spectra and are given in Table 5.3. Similar values for the R_{DCO} for the 292.3 keV ($\frac{43}{2}^+ \rightarrow \frac{41}{2}^+$) and 254.8 keV ($\frac{41}{2}^+ \rightarrow \frac{39}{2}^+$) transitions were found gating on the 218.2 keV ($\frac{39}{2}^+ \rightarrow \frac{37}{2}^+$) transition. The R_{DCO} for these four new transitions are close to the average value for the dipoles.

The R_{DCO} for the total peak, 293 keV when gated on the X-rays was measured to be $\approx$ 0.55 (0.09). This is consistent with the previously suggested

dipole nature of the 294.5 keV ($\frac{27}{2}^+ \rightarrow \frac{25}{2}^+$). The coincidence spectra gated on the 222.0 keV transition were used to extract the R_{DCO} for the new 486.4 keV ($(\frac{33}{2}^+) \rightarrow \frac{31}{2}^-$) transition which is close in energy to the known 485.1 keV ($\frac{31}{2}^- \rightarrow \frac{29}{2}^-$) transition. The R_{DCO} found for the 486.4 keV transition suggest a dipole nature for this transition.

Two ways were employed to measure the R_{DCO} for the known 367.1 keV ($\frac{21}{2}^+ \rightarrow \frac{17}{2}^+$) transition previously assigned an E2 multipolarity. Firstly, the R_{DCO} was measured from the $K_{\alpha 1}$ Bi X-ray gated coincidence spectra and found to be 0.88 ± 0.07, which is a bit low for a quadrupole transition. Subsequently, a similar R_{DCO} (0.88 ± 0.07) was obtained, when a sum of spectra gated on the 195.5 keV ($\frac{13}{2}^+ \rightarrow \frac{13}{2}^-$) and 186.6 keV ($\frac{13}{2}^+ \rightarrow \frac{11}{2}^-$) transitions were used. Thus, the R_{DCO} of 367.4 keV measured from the present work lies in between the average values for the dipoles and quadrupoles (see Figure 5.23).

5.2.3 Linear Polarisation Measurements for ^{197}Bi

Measurements to determine the sign of the A_p were performed for the ungated and gated Clover spectra depicted in Figures 5.24 and 5.25 respectively. The signs for the A_p in Table 5.3 for the known (367.1, 438.5, 485.1 and 923.6) transitions are in agreement with the multipolarities suggested in the previous [Zho95] study. In the present work the A_p (Table 5.3) for the 310.9 and 627.6 keV transitions were determined for the first time showing magnetic nature.

5.2.4 Transition Intensities for ^{197}Bi

Due to the presence of the isomers in the level scheme ^{197}Bi [Cha86, Zho95], it was rather cumbersome to determine the intensities for all transitions displayed in Figure 5.15. However, the gamma intensities and total intensities (corrected for internal electron conversion) for the transitions above the $\frac{31}{2}^-$ isomer were determined, normalised to the 310.8 keV ($\frac{35}{2}^- \rightarrow \frac{33}{2}^-$) transition intensity and listed in Table 5.1. The gamma intensities for the 153.1, 218.2 and 310.8 keV transitions were extracted from the ungated γ-ray coincidence spectrum. The spectra gated on the 153.1 keV ($\frac{37}{2}^+ \rightarrow \frac{35}{2}^-$) and 327.4 keV

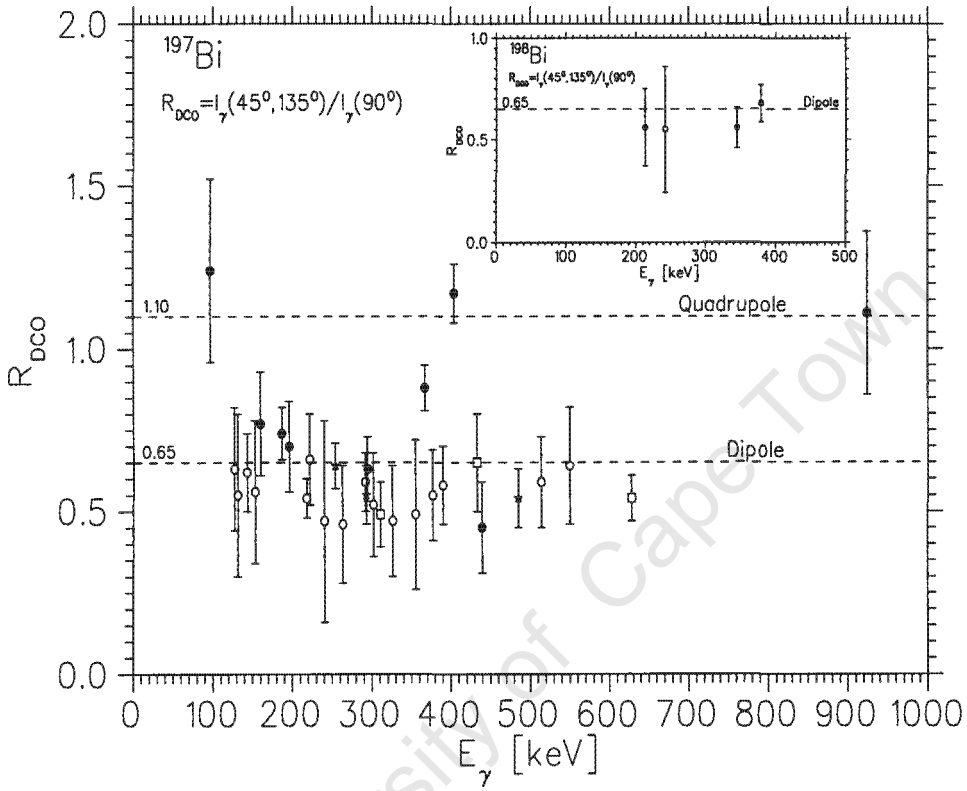

Figure 5.23: *The DCO ratios (R_{DCO}) for the new (open-circles) and the known (filled-circles) γ-ray transitions in ^{197}Bi [Cha86, Zho95] and ^{198}Bi [Zho96, Zwa00] (insert). The stars represent the doublets while the empty-squares mark the known transitions which their multipolarities were not determined in the earlier studies [Zho95, Lön86]. The dashed-lines (also in the insert) correspond to the average R_{DCO} values obtained using the known stretched dipole (0.65 ± 0.09) and the stretched quadrupole (1.10 ± 0.17) transitions. All the new transitions are found to be dipole in nature. A good reproduction of the previously measured dipole and quadrupole transitions is obtained in both cases.*

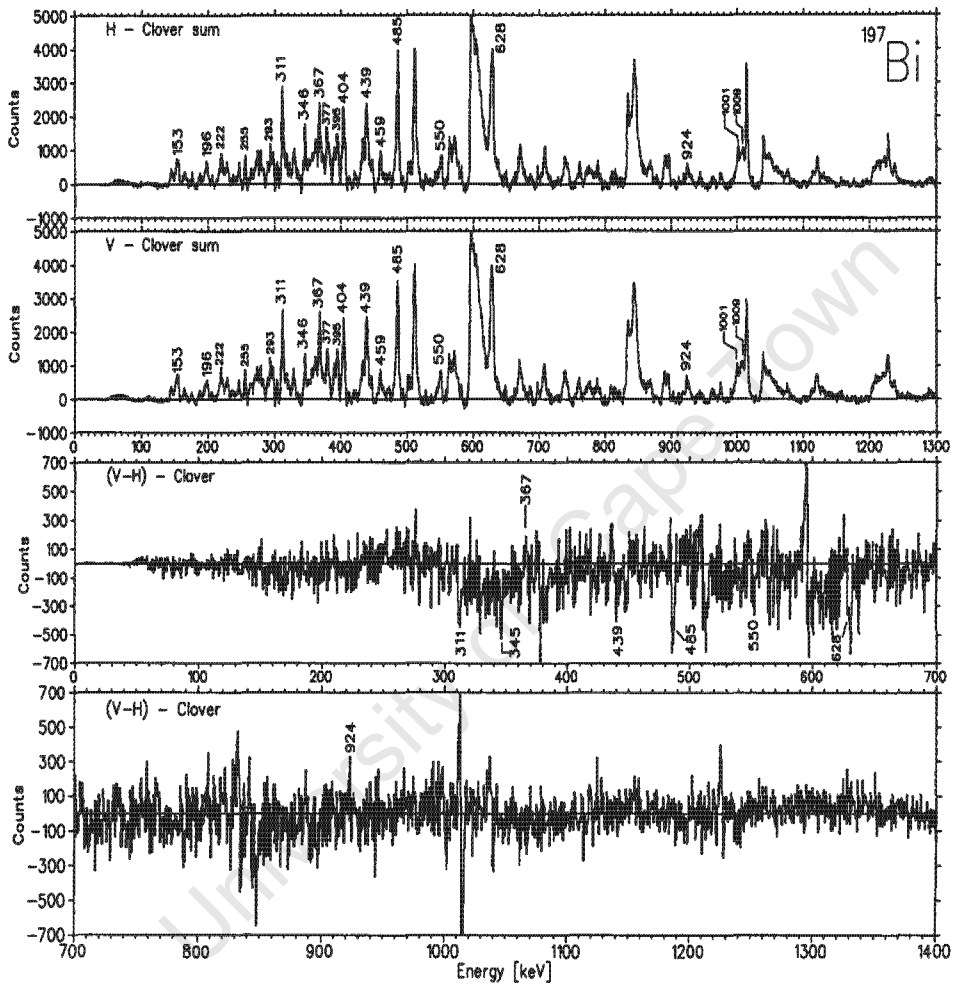

Figure 5.24: *The ungated and background subtracted double-hit-events spectra of the horizontally (H) and vertically (V) scattered γ-rays detected. The difference (V-H) spectrum display the sign of the anisotropy. In particular the magnetic nature of 310.8 and 627.6 transitions can be seen.*

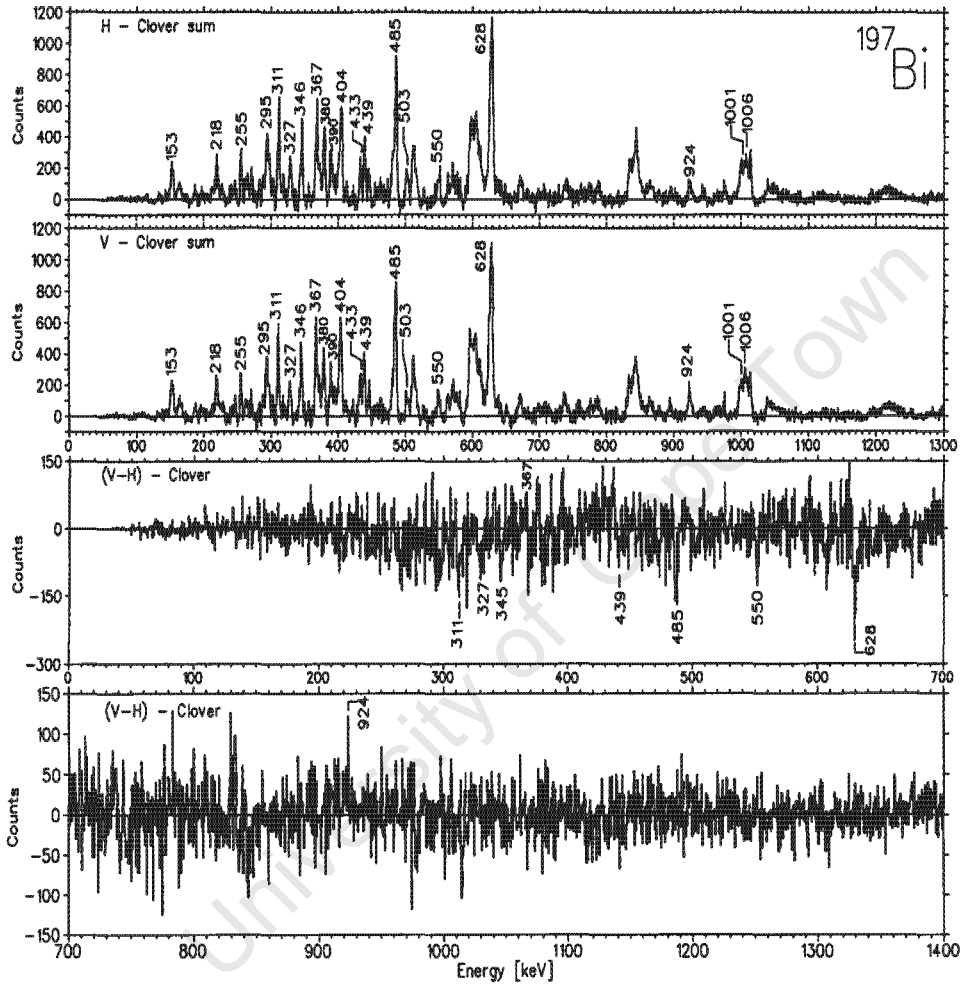

Figure 5.25: *The gated and background subtracted double-hit-events spectra of the horizontally (H) and vertically (V) scattered γ-rays, detected. The difference (V-H) spectrum display the sign of the anisotropy. In particular, the magnetic nature of the newly found 310.8 and 627.6 keV transitions can be seen.*

($\frac{45}{2}^+ \rightarrow \frac{43}{2}^+$) transitions and extracted from the ungated matrix were used to measure the gamma intensities for the 254.8 keV ($\frac{41}{2}^+ \rightarrow \frac{39}{2}^+$) and the 355.5 keV ($\frac{51}{2}^+ \rightarrow \frac{49}{2}^+$) transitions respectively.
Furthermore, a coincidence spectrum gated on the 218.2 keV ($\frac{39}{2}^+ \rightarrow \frac{37}{2}^+$) transition was employed in determining the intensities of the 264.2 ($\frac{47}{2}^+ \rightarrow \frac{45}{2}^+$), 292.3 ($\frac{43}{2}^+ \rightarrow \frac{41}{2}^+$), 302.2 ($\frac{49}{2}^+ \rightarrow \frac{47}{2}^+$) and 327.4 ($\frac{45}{2}^+ \rightarrow \frac{43}{2}^+$). Measuring the branching ratios of the 153 and 605 keV transitions from the spectrum gated on 218 keV transition and correcting for detector relative efficiency, internal electron conversion and the "true" intensity of the 153 keV γ-ray the total intensity of the 605.1 keV transition was found.

5.2.5 RSAM Lifetime Measurements for ^{197,198}Bi

The A_{RSAM} measurements for experiment II were conducted in a procedure reminiscent to that discussed in section 5.1.5. The relative efficiency: $\alpha = 0.91$ was measured and employed to generate the spectra depicted in Figure 5.26. Table 5.4 lists the γ-ray energies (E_γ) and the anisotropies (A_{RSAM}) for most of the transitions in ^{197}Bi. Figure 5.27 highlights the distribution of the γ-ray A_{RSAM}.
Only the known delayed (97.3, 160.2, 186.6, 195.5, 293.4, 367.1, 404.2 and 999.9 keV) transitions appear in the difference spectrum and have large A_{RSAM} values (Table 5.4) in agreement with the previous studies [Cha86, Zho95]. The measured A_{RSAM} are displayed in Figure 5.27. Only the known delayed (97.3, 160.2, 186.6, 195.5, 293.4, 367.1, 404.2 and 999.9 keV) transitions appear in the difference spectrum and have large A_{RSAM} values (Table 5.4) in agreement with the previous studies [Cha86, Zho95]. The measured A_{RSAM} are displayed in Figure 5.27 with the error bars estimated within 4 %. The new transitions, shown by open circles, together with the known (310.8, 438.5 and 485.1 keV) transitions shown by solid-dots are prompt because such peaks do not appear in the difference spectrum. The anisotropy for some of the γ-rays associated with the ^{198}Bi nucleus is listed in Table 5.4 and displayed in Figure 5.27. The results show that 242 keV and 672 keV transitions are prompt and delayed respectively and corroborates the previous studies [Zwa00, Zho96]. The 143 keV transition, a member of

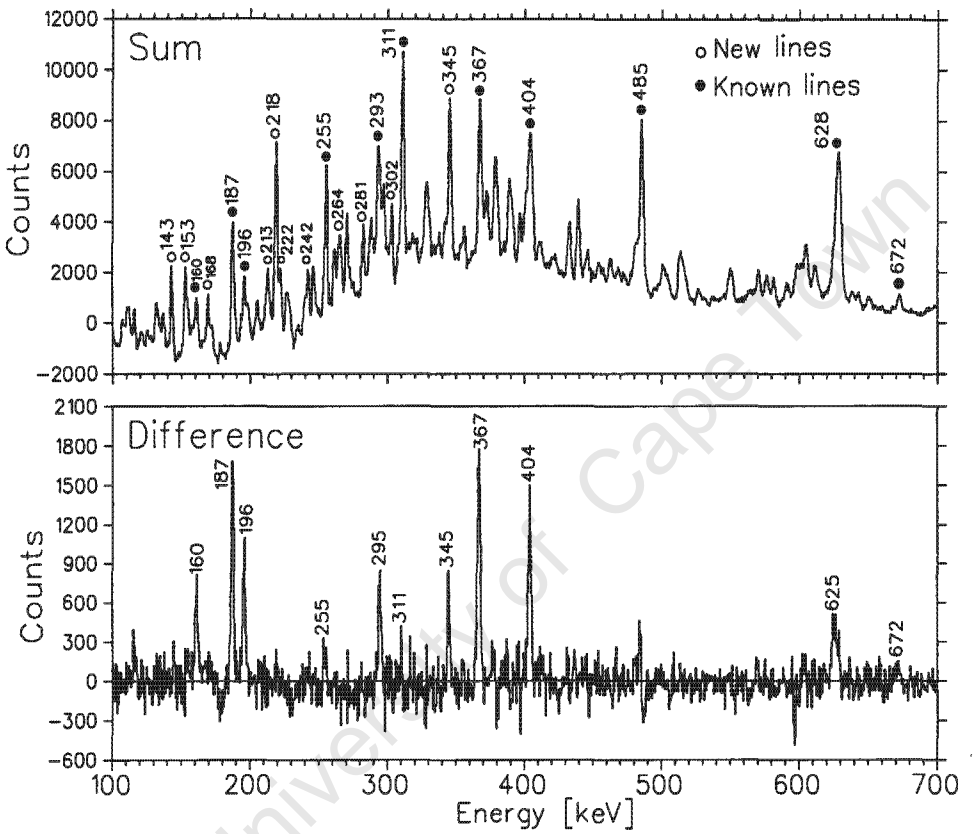

Figure 5.26: *The sum (difference) spectrum gated on the $K_{\alpha 1}$ and $K_{\alpha 2}$ Bi X-rays (Table 4.4) detected by the LEPS detectors generated for the N_U + αN_S (N_U - αN_S) of the γ-rays detected by the Clover detectors at 96° (N_U) and 86° (N_S). The γ-ray transitions marked with filled-circles and open circles highlight the known and the new ^{197,198}Bi transitions respectively.*

Table 5.4: *The γ-ray transition energies (E_γ) and anisotropies (A_{RSAM}) for the ^{197,198}Bi nuclei measured in the Bi X-ray gated spectra.*

E_γ (keV)	$\frac{N_U - \alpha N_S}{N_U + \alpha N_S}$ (%))[a]
97.3	12
142.8)[c]	2
153.1	2
160.2	29
186.6	25
195.5	15
218.2	3
242.1)[d]	6
254.8)[b]	7
293.4)[b]	17
310.8	4
345.0)[b]	16
367.1	28
404.2	20
432.8	10
438.5	8
485.1	5
627)[b]	10
672.0)[d]	15
999.9	15

)[a] $\alpha = 0.91$

)[b] Measurement for the unresolved peak

)[c] γ-ray transition in coincidence with members of the unassigned sequence (in section 5.4)

)[d] γ-ray transitions associated with the ^{198}Bi nucleus.

)[e] error bars are within 4 %

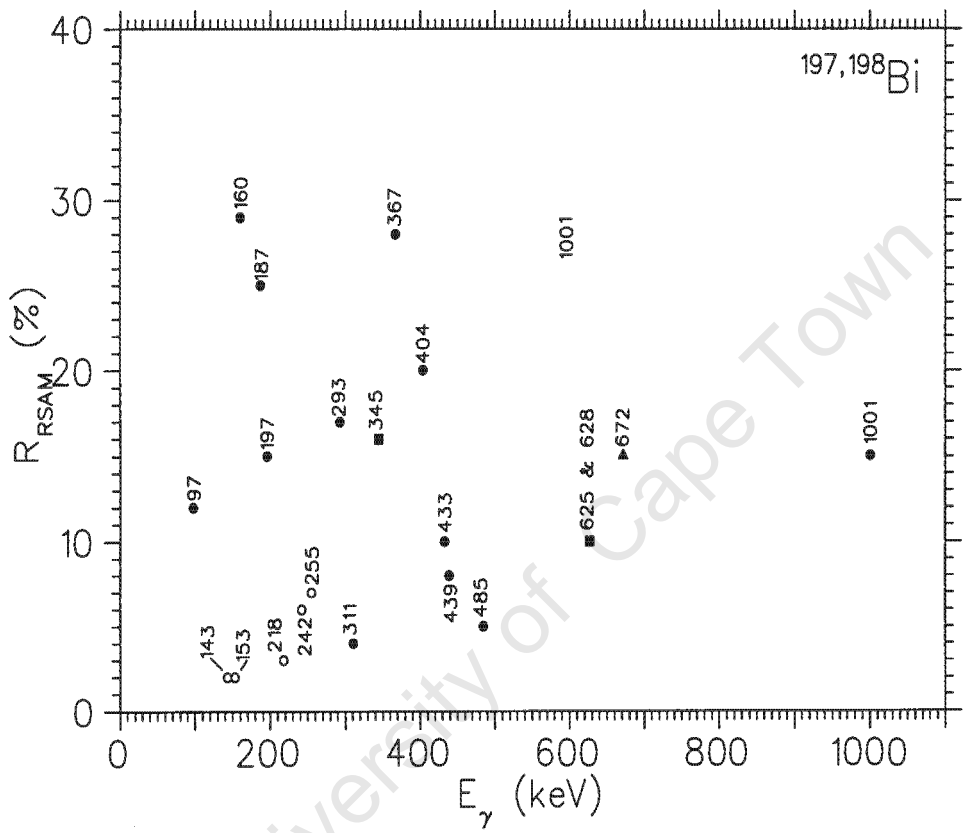

Figure 5.27: *The γ-ray anisotropies (A_{RSAM}) extracted from the Clover spectra gated on the $K_{\alpha 1}$ and $K_{\alpha 2}$ Bi X-rays (Table 4.4) detected by the LEPS detectors. The filled-circles and triangle represents the known ^{197}Bi and ^{198}Bi transitions respectively. The, open-circles (except the 242 keV transition in ^{198}Bi [Zwa00]) depicts the new transitions in ^{197}Bi. The filled-squares indicates the known doublets in both ^{197}Bi [Zho95] and ^{198}Bi [Zho96]. Error bars are within 4 %.*

the unassigned sequence in section 5.4 has been observed as prompt.
The 628 keV line in this spectrum has contributions from the 627.6 keV transition in ^{197}Bi and from the delayed 625 keV transition in ^{198}Bi. Thus, it is a bit cumbersome to determine where the 627.6 keV γ-ray is prompt or not. Some other weak transitions have relatively large A_{RSAM}, but do show peaks in the difference spectrum and are thus considered not delayed. In summary, no evidence for new isomers was found in our data.

5.3 ^{198}Bi Level Scheme

The first observation of excited states in the nucleus ^{198}Bi was made by X. H. Zhou, et al., [Zho96] and they deduced the level scheme shown in Figure 5.28. Three dipole bands associated with ^{198}Bi were found in a later work by Zwartz et al., and reported [Zwa00]. One of these three dipole bands was observed in our experiment II data. This band is labelled D in Figure 5.32 and consists of seven γ-ray transitions. A cascade of γ-rays labelled A, B, C and D above the 1877 keV (5^+) isomeric (8.0 ns) state in ^{198}Bi [Zho96] was observed in the present work as shown in the figure and is in conformity with the previous work [Zho96, Zwa00].

Figure 5.29 display the γ-ray coincidence spectra generated from the ungated γ-γ matrix gated on the (a) 345.1 and (b) 213 keV transitions. In both panel (a) and (b), the known γ-ray transitions associated with ^{198}Bi in coincidence with the gates are labelled with their respective energies and marked with arrows. The ^{197}Bi transitions observed in the (a) 345.1 keV coincidence gate, the low-lying 404.2, 367.1 and possibly 627.6 keV transitions, are very weak, showing that the main component of 345 keV line come from ^{198}Bi. Furthermore, the 379, 372 keV gates shown in Figure 5.30 and the summed coincidence γ-ray spectra for Band D in Figure 5.31 clearly confirm the presence of the known ^{198}Bi transitions in experiment II data. The 116, 107, 672 and 990 keV transitions which lie below the the 15^+ isomeric state at the 1877 keV level [Zho96] in ^{198}Bi were also observed. These were the only transitions observed below the 15^+ (8.0 ns) isomeric state in coincidence with the 345.1 keV transition.

A portion of the ^{198}Bi level scheme (in Figure 5.32) was constructed from

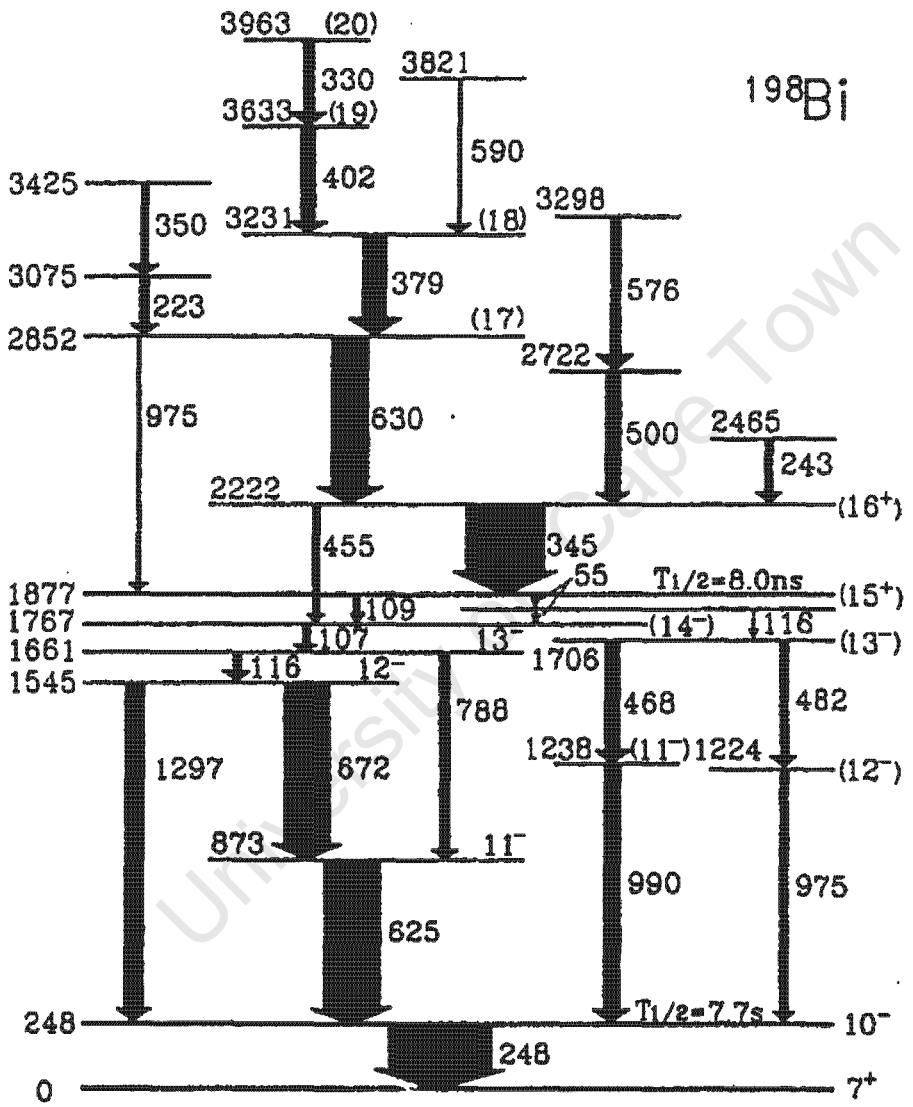

Figure 5.28: *The known level scheme of ^{198}Bi taken from [Zho96].*

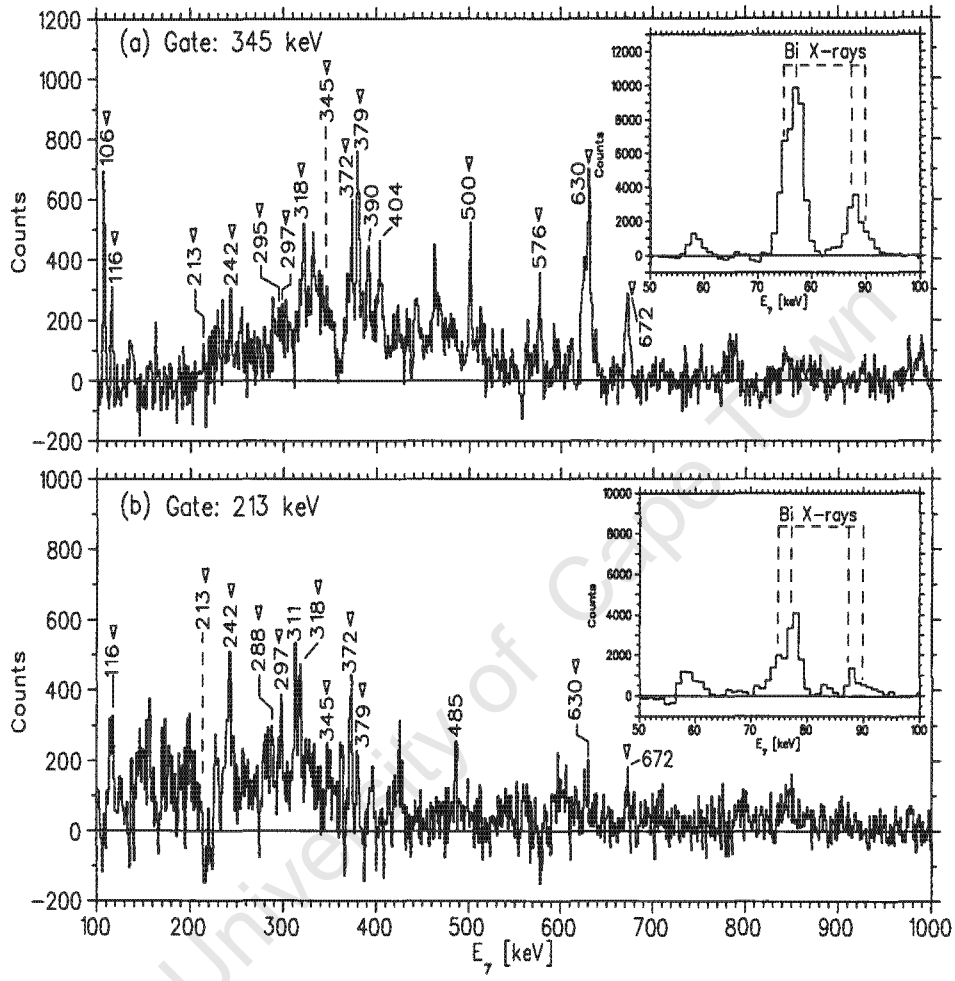

Figure 5.29: *The γ-ray coincidence spectra gated on the (a) 345 keV and (b) 213 keV transitions. All the γ-rays seen in coincidence with the gate in both panels are labeled with their respective energies. Those marked with arrows represent the known transitions above and below the 15^+ isomeric state in ^{198}Bi [Zho96]. The inserts show the exact positions of the Bi X-rays (as in Table 4.4).*

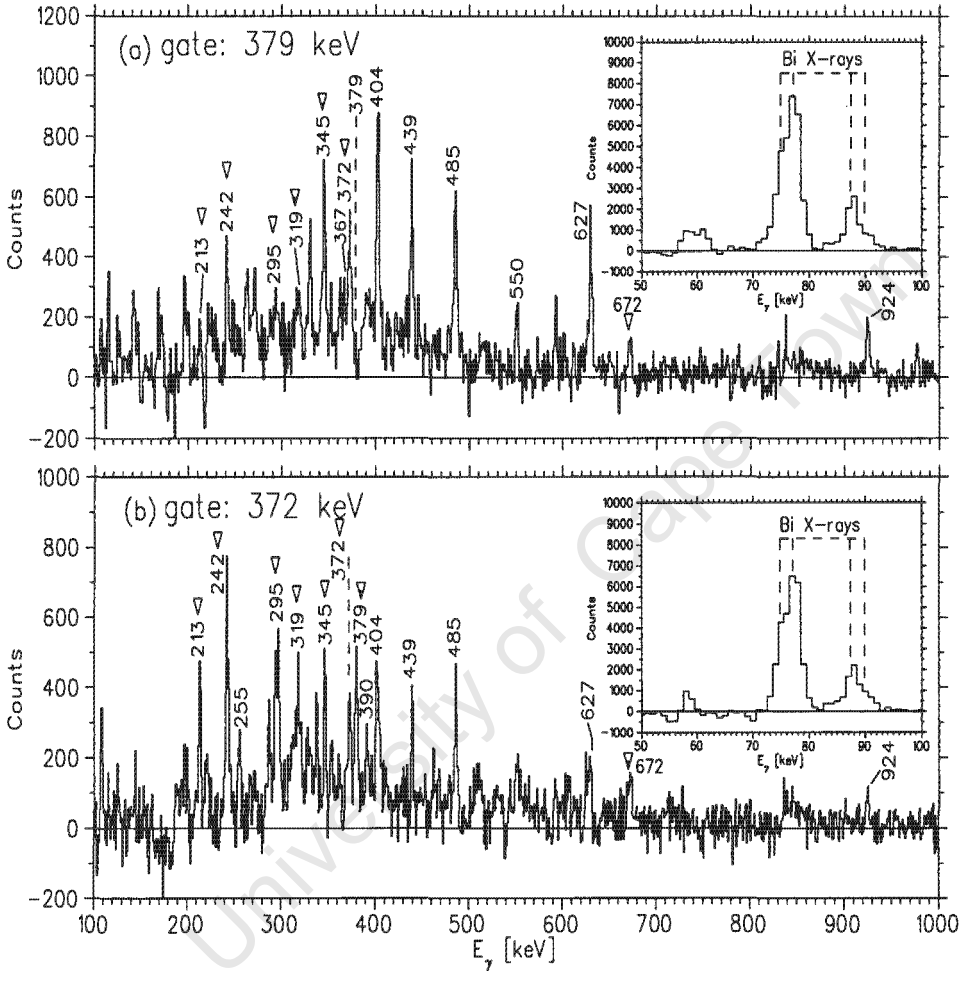

Figure 5.30: *The γ-ray coincidence spectra gated on the (a) 379 keV and (b) 372 keV transitions. All the γ-rays seen in coincidence with the gate in both panels are labeled with their respective energies. Those marked with arrows represent the known transitions above and below the 15^+ isomeric state. The inserts show the exact positions of the Bi X-rays (as in Table 4.4).*

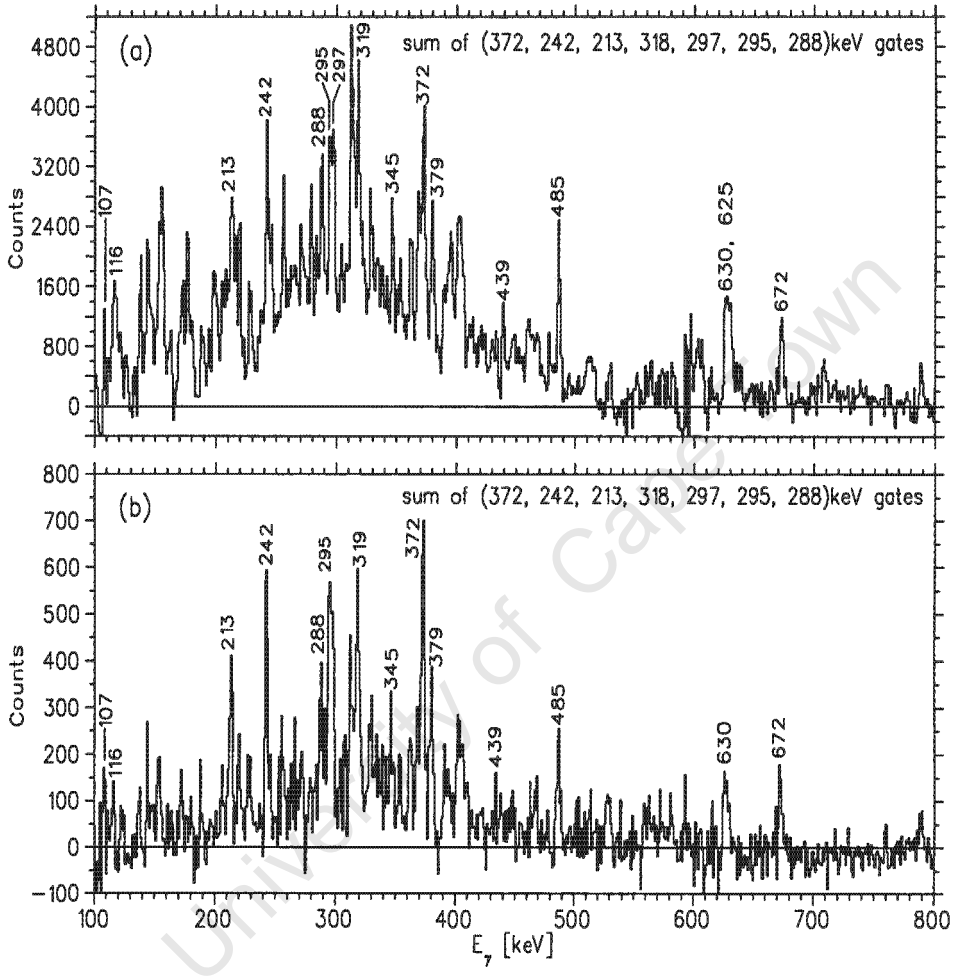

Figure 5.31: *The summed coincidence γ-ray spectra for Band D in ^{198}Bi (Figure 5.32). These spectra are generated from the (a) ungated and (b) gated (on the $K_{\alpha 2}$, $K_{\alpha 1}$ Bi X-rays detected with the LEPS detectors) matrices by summing the 372, 213, 242, 295, 297, 319, 345 and 379 keV gates.*

the γ-ray transitions observed above the 15^+ isomeric state. It confirms the known ^{198}Bi level scheme (Figure 5.28). Attempts were made to find the linking transition(s) between structure D and the transitions above the 15^+ isomeric state (8.0 ns). However, the low statistics in our data did not allow to unfold a decay path between these structures (Figure 5.32). For instance spectra gated on 345 and 213 keV are displayed in Figure 5.29

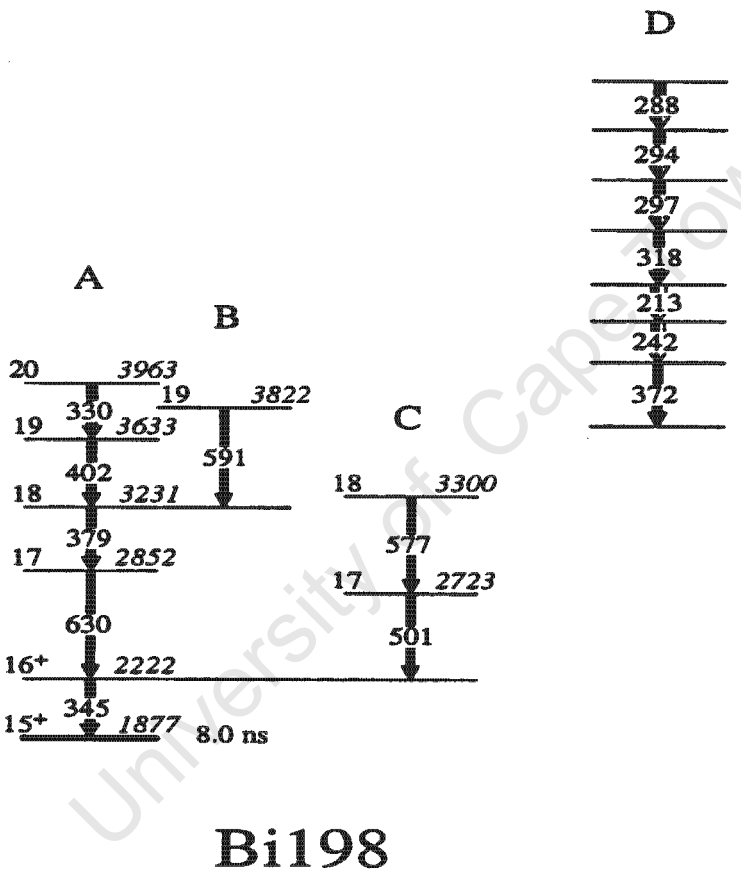

Figure 5.32: *Partial ^{198}Bi level scheme observed from experiment II data.*

5.3.1 ^{198}Bi DCO

The γ-ray transitions associated with the ^{198}Bi [Zho96, Zwa00] nucleus have been observed in the experiment II data. These transitions are listed in Table 5.5 with their energies and where possible the corresponding R_{DCO}. The insert of Figure 5.23 depicts the R_{DCO} for four (212.6, 345.1 and

Table 5.5: *The γ-ray transition energies (E_γ), DCO ratios (R_{DCO}) and the multipolarities for ^{198}Bi [Zho96].*

E_γ (keV)	$R_{DCO} = \frac{A(45°;135°)}{A(90°)}$	*Multipolarity*
212.6	0.56(19)	dipole
242.1	0.55(31)	dipole
287.5	0.56(19)	dipole
294.5	0.55(31)	dipole
297.0	)[a]	)[a]
318.0	)[a]	)[a]
330.4	)[a]	)[a]
345.1)[b]	0.56(10)	dipole
371.8	)[a]	)[a]
378.9	0.68(9)	dipole
402.4	)[a]	)[a]
500.5	)[a]	)[a]
576.5	)[a]	)[a]
592.1	)[a]	)[a]
630.0	)[a]	)[a]

[a] Could not be determined due to lack of enough statistics.

[b] Unseparated doublet - measurement for the total peak.

378.9 keV) transitions. The 212.6, 242.1, 345.1 and 378.9 keV transitions represented by filled circles show a dipole character, thus consistent with the previous results [Zho96, Zwa00]. The R_{DCO} for the 242.1 keV transition shown by an open circle was found for the first time in the present work and clearly indicates the dipole nature of the transition.

5.3.2 Linear Polarisation Measurements for ^{198}Bi

There were no transitions from ^{198}Bi for which it was possible to measure the sign of polarisation anisotropy, due to very low statistics.

5.3.3 RSAM Lifetime Measurements for ^{198}Bi

As shown before in the Figure 5.27 we did observe the known delayed transitions of ^{198}Bi in the difference spectrum. Considerable anisotropy was found for the 345 keV transition, showing its delayed nature. The 345 keV transition in ^{198}Bi is very strong while it is very weak if it at all exists in

^{197}Bi, as seen in Figure 5.29 (a). Thus, there is no doubt that when gating on the Bi X-rays the 345 keV peak belongs to ^{198}Bi. This suggests that the (16^+) level at 2222 keV is a new nanosecond isomer. In order to measure its lifetime, the difference and sum spectra gated on 630 keV transition have to be generated. However, the statistics in these gated spectra were not sufficient to allow such measurements to be performed. Since no new transitions were found in ^{198}Bi and also that this channel is relatively weak, no γ-intensity measurements were done. Intensity balance measurements were however done for the (16^+) level in ^{198}Bi, by gating on the 379 keV and comparing the intensities of the 630 and 345 keV transitions. Similar intensities have been found. Thus, the intensity measurements do not show an isomer, while it can be observed with RSAM. Indeed, this method is much more sensitive to isomeric levels than the intensity balances.

5.4 Unassigned γ-ray sequence

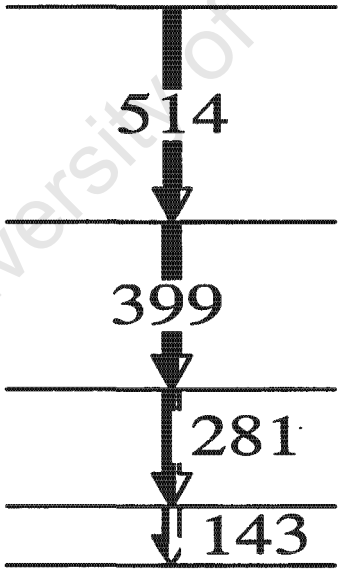

Figure 5.33: *A sequence of four γ-ray transitions found in the experiment II data.*

Four (142.8, 281.1, 399.4 and 513.6 keV) γ-ray transitions in coincidence with each other were found in the experiment II data. The coincidence

Table 5.6: *The γ-ray transition energy (E_γ), DCO ratios (R_{DCO}) and the multipolarity of the unassigned γ-ray sequence (in section 5.4).*

E_γ (keV)	$R_{DCO} = \frac{I(45°;135°)}{I(90°)}$	*Multipolarity*
142.8	0.62(12)	dipole
281.1	0.59(26)	dipole
399.4	0.69(18)	dipole
513.6	0.59(14)	dipole

[a] Could not be determined due to lack of enough statistics.

structure of these transitions is depicted in Figure 5.33. The transitions show a coincidence relationship with a 485 and a 367 keV transition, but not with the other low lying ^{197}Bi transitions as shown in Figure 5.34. Therefore, the structure (in Figure 5.33) could not be assigned unambiguously to either ^{196}Bi, ^{197}Bi or ^{198}Bi nuclei. However, it might be lying above the $\frac{31}{2}^-$(2920 keV) level in ^{197}Bi.

The DCO analysis showed that the 142.8, 281.1, 399.4 and 513.6 keV transitions are dipole in nature. The summed 142.8, 399.4 and 513.6 keV (142.8, 281.1 and 513.6 keV) coincidence γ-ray spectra generated from the DCO matrices were used to determine the DCO ratio tabulated in Table 5.6 for the 281.1 keV (399.4 keV) transition.

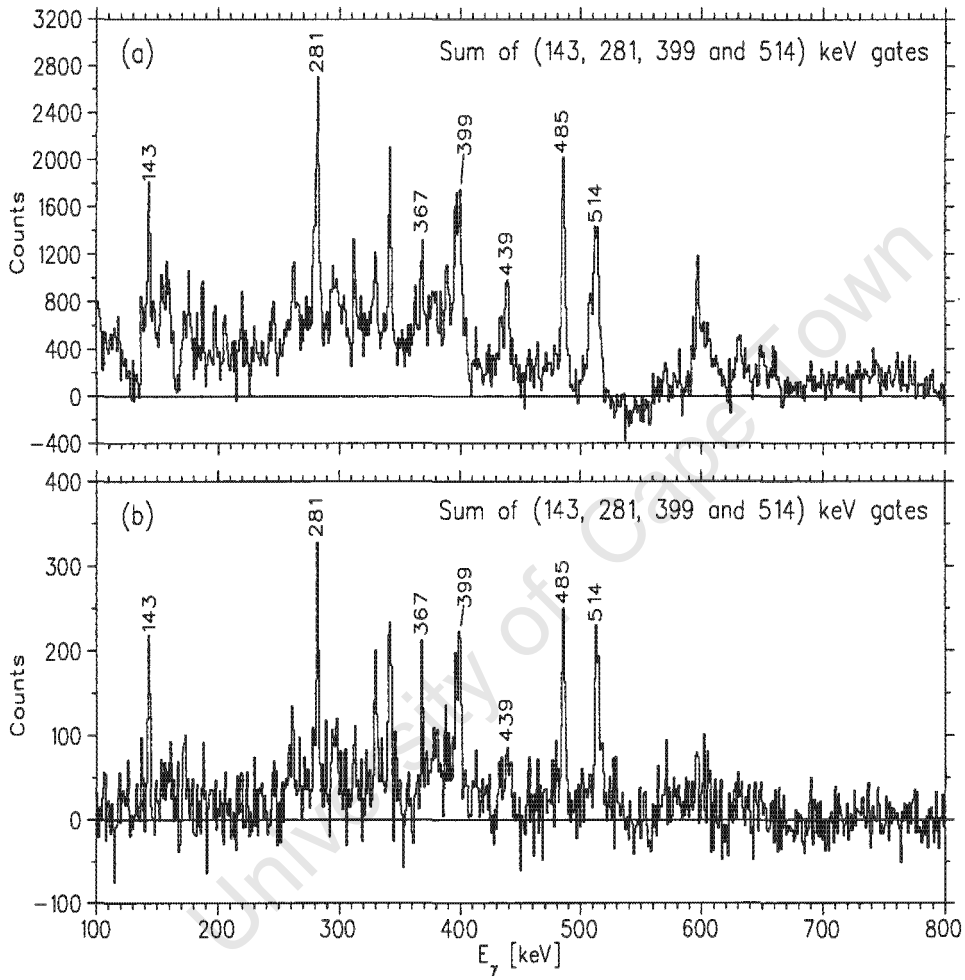

Figure 5.34: *The summed coincidence γ-ray spectra for the unassigned γ-ray sequence. These spectra are generated from the (a) ungated and (b) gated (on the $K_{\alpha 2}$, $K_{\alpha 1}$ Bi X-rays detected with the LEPS detectors) matrices by summing the 143, 218, 399 and 514 keV gates.*

Chapter 6

Discussion

Interpretation of the experimental results in relation to the theoretical predictions of Total Routhian Surface (TRS) calculations, the Cranked Shell Model (CSM) and the Tilted Axis Cranking (TAC) model are discussed in the present chapter.

6.1 Introduction – Dipole Bands

Dipole bands have been discovered at high excitation energies in the near spherical $^{192-201}$Pb and $^{198-202}$Bi nuclei [Plo93, Dag93, Dag94, Hug93, Fan91, Van86, Cla94, Cla93, Por94, Bal92, Bal92a, Duc96, Cla92, Cla92a, Kac02, Sin02, Kuh92, Gör01]. They exhibit several common features:

(i) The bands consist of M1 transitions and are regular (that is, follow the $I(I+1)$ rule);

(ii) No or weak E2 cross-over transitions were observed for these bands;

(iii) The $\frac{B(M1)}{B(E2)}$ ratios are large ($\approx 20-40\ (\mu_N/eb)^2$);

(iv) The dynamic moments of inertia, $\Im^{(2)}$ are small and vary between 10–30 $\hbar^2$/MeV;

(v) No or very small signature splitting is observed for the dipole bands;

(vi) Transitions connecting some of these bands with the low-lying states were not identified in many Pb and Bi nuclei. Thus, their excitation

energies, spins and parities were not known and therefore, made it cumbersome for precise identification of configurations involved in these bands. As a result, interpretation of the structures were on the basis of analysis of the $\frac{B(M1)}{B(E2)}$ branching ratios, mixing ratios derived from the DCO and lifetime measurements. The γ-ray transitions linking some of the bands to the low-lying states have been found for $^{193-198}$Pb [Duc96, Gör01, Kac02, Sin02, Por94].

The dipole bands have been assigned with a high-K proton configuration and associated with small oblate nuclear deformation. These bands have been first interpreted with the aid of the Total Routhian Surface (TRS) and Cranked Shell Model (CSM) calculations assuming collective rotation of an oblate core. Within these models, the dipole bands were interpreted as strongly coupled bands or high-K bands. Later the structures have been interpreted in the framework of Tilted Axis Cranking (TAC) model [Fra93] suggesting a gradual alignment of the proton and neutron spins into the direction of the total angular momentum. This behaviour is dubbed the "shears mechanism" since it resembles the closing of a pair of shears. Within this formalism, magnetic rotation has been suggested for the dipole bands [Fra97].

In this chapter a discussion on the new dipole bands we found in ^{195}Bi and ^{197}Bi nuclei will be presented. This is the first time M1 dipole bands have been observed in these nuclei.

6.2 Band 1 in ^{197}Bi

It is expected that Band 1 like all the dipole bands in this mass region is built on high-K proton and low-K neutron states. Since the excitation energy is consistent with 4 quasiparticle excitations, it is suggested that Band 1 includes three proton and two neutron configurations. In the Pb isotopes, the configuration suggested for the most intense dipole bands involve high-K $\pi i_{\frac{9}{2}}[505]\frac{9}{2}^-$ and $\pi h_{\frac{13}{2}}[606]\frac{13}{2}^+$ orbitals with $K = 11^-$. In the heavier Bi nuclei, configurations involving the same $\pi[505]\frac{9}{2}^-$ and $\pi[606]\frac{13}{2}^+$ orbitals, with a third proton in the $s_{\frac{1}{2}}$ orbital were assigned resulting in a $\pi(h_{\frac{9}{2}}\ i_{\frac{13}{2}}\ s_{\frac{1}{2}})$

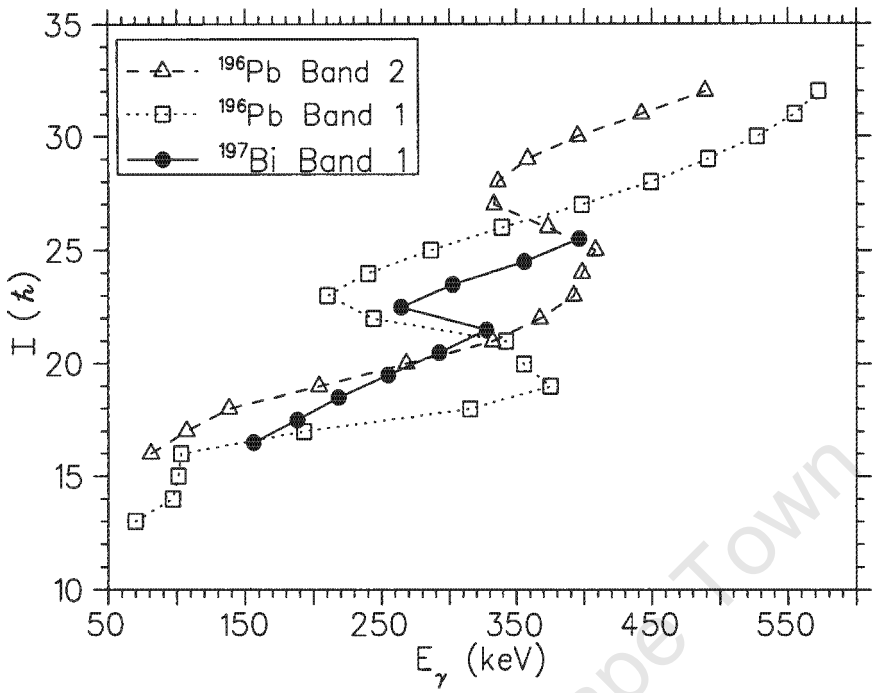

Figure 6.1: *Spin as a function of γ-ray energy for the dipole transitions of Bands 1, 2 in ^{196}Pb [Sin02] and a new Band 1 in ^{197}Bi.*

configuration [Cla93a, Dag94]. The $s_{\frac{1}{2}}$ proton configuration was suggested for the third proton, because the $\Im^{(2)}$ for the dipole bands in Pb were similar to those in these Bi and also because it is known that adding a particle in a normal parity orbital does not change the properties of the band. We also compared the properties of the Band 1 in ^{197}Bi with the two most intense bands in ^{196}Pb assigned to $\pi(h_{\frac{9}{2}}\ i_{\frac{13}{2}}) \otimes \nu(i_{\frac{13}{2}})^2$ for Band 2 and $\pi(h_{\frac{9}{2}}\ i_{\frac{13}{2}}) \otimes \nu(i_{\frac{13}{2}})\nu j$ for Band 1, where $j = p_{\frac{3}{2}}, f_{\frac{5}{2}}$... respectively.
Comparison of the spin, I as a function of γ-ray energy, E_γ for the dipole transitions of Bands 1, 2 in ^{196}Pb [Sin02] and the new Band 1 in ^{197}Bi is shown in Figure 6.1. A much steeper increase in spin with respect to γ-ray energy is observed for Band 1 in ^{197}Bi as compared to Band 1 and 2 in ^{196}Pb. This means that the dynamic moment of inertia of the Band 1 in ^{197}Bi is much larger than those in ^{196}Pb. This can be seen in Figure 6.2, where the $\Im^{(2)}$ are displayed. The $\Im^{(2)}$ observed for Band 1 in ^{197}Bi is almost twice that of Band 1 and 2 in ^{196}Pb before the backbend. It is known that the $\Im^{(2)}$ is

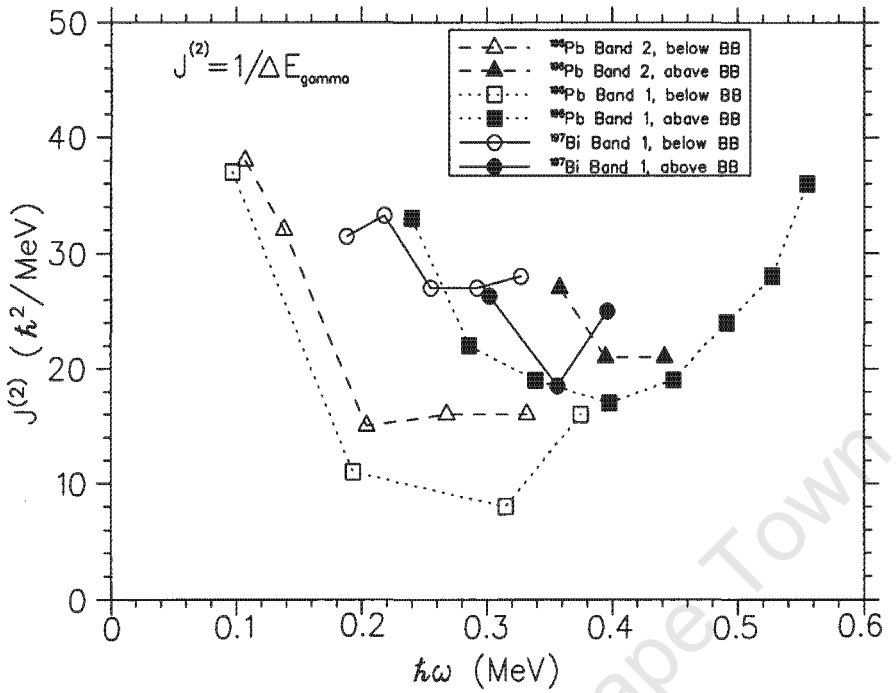

Figure 6.2: *Plots for the dynamic moment of inertia $J^{(2)}$ (denoted by $\Im^{(2)}$ in the text) for the bands in ^{197}Bi and ^{196}Pb [Sin02] nuclei as a function of the rotational frequency. Abbreviation BB in the legend refers to a backbend.*

very sensitive to the proton and neutron configurations. It is expected that such big differences in $\Im^{(2)}$ can be caused only by involving an intruder orbital in the configuration of the band in ^{197}Bi. Since the only other available intruder orbital close to the Fermi level is high-K $\pi h_{\frac{9}{2}}[514]\frac{7}{2}^-$, we suggest that the third proton is occupying the intruder high-K $\pi h_{\frac{9}{2}}[514]\frac{7}{2}^-$ orbital. Shown in Figure 6.3 are the single-particle levels calculated using a Woods-Saxon potential, for neutrons and protons as a function of β_2.

The high-K proton configuration of the dipole bands in this mass region is supported by the large values of $\frac{B(M1)}{B(E2)}$ ratios. In ^{197}Bi, since E2 cross-over transitions were not observed for Band 1 the lower limits for the $\frac{B(M1)}{B(E2)}$ values were obtained and are tabulated in Table 5.3 of Chapter 5. The values are greater than 9 $(\mu_N)^2/(eb)^2$ which supports the involvement of high-K proton orbitals.

In earlier studies, it was observed that the ground bands in even Hg and the

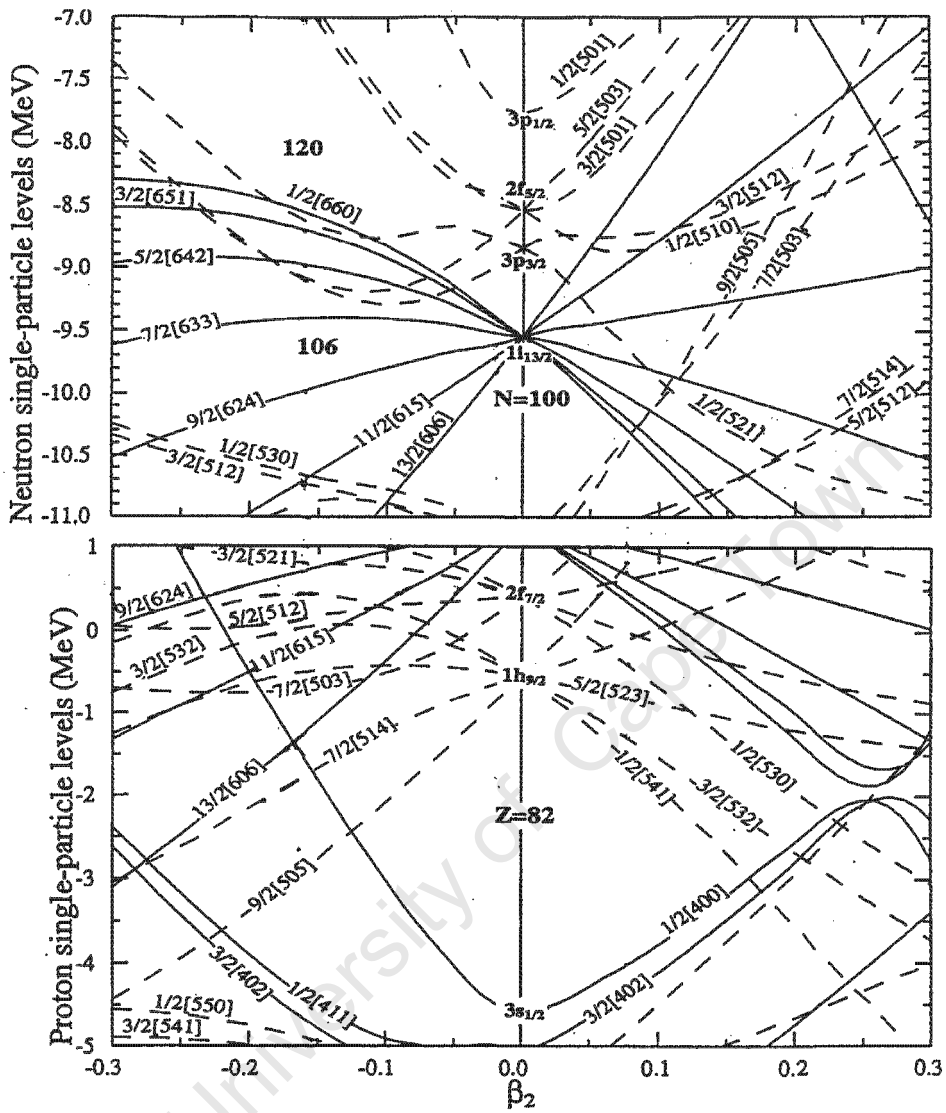

Figure 6.3: *Single-particle levels calculated using a Woods-Saxon potential, for neutrons (upper panel) and protons (lower panel). Orbitals are labelled with Nilsson asymptotic quantum numbers. Solid (dashed) lines denote orbitals of positive (negative) parity.*

dipole bands in Pb bands exhibit similar behaviour of the projection of the angular momentum along the rotational axis, I_x as a function of rotational frequency, $\hbar\omega$ [Duc96, Gör01, Hüb86]. Thus, it was suggested that the Pb have similar small oblate deformation like Hg and that the dipole bands in

Pb are generated by collective rotation of the core while the high-K protons act like spectators. In order to investigate whether similar considerations hold for ^{197}Bi and ^{196}Pb dipole bands, I_x as a function of $\hbar\omega$ curves were generated as depicted in Figure 6.4 for the new Band 1 in ^{197}Bi and Bands 1 and 2 in ^{196}Pb [Sin02]. $K = 11$ and $K = 14.5$ values were used for ^{196}Pb and ^{197}Bi bands during construction of the plots respectively. The following Harris parameters were used (initially used for the Hg core [Hüb86] and later for some dipole bands in Pb [Plo93, Moo95]) as reference: $J_0 = 8\ \hbar^2/\text{MeV}$, $J_1 = 40\ \hbar^4/\text{MeV}^3$. We also used these Harris parameters in our case. The

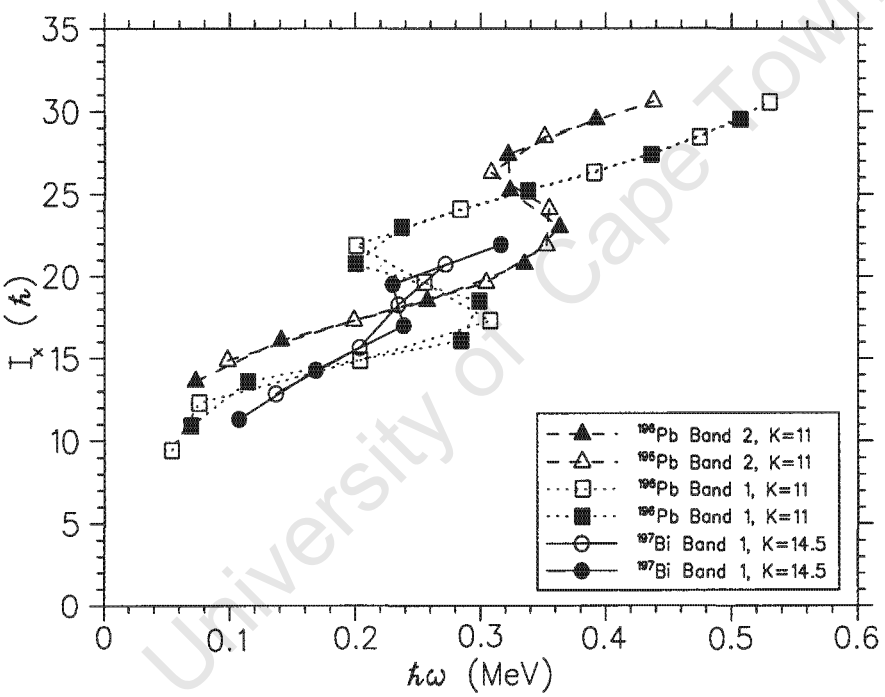

Figure 6.4: *Angular momentum, I_x along the rotational axis as a function of the rotational frequency, $\hbar\omega$ for Band 1 in ^{197}Bi and Bands 1 and 2 ^{196}Pb [Sin02]. The curves were generated for $K = 11$ and $K = 14.5$ in the case of bands in ^{196}Pb and ^{197}Bi respectively.*

steepness of ^{197}Bi curve is again much larger than that of Pb. This implies that either we do not have similar nuclear deformation or the consideration of dipole bands generated as a result of a collective rotation with the high-K protons acting as spectators is not applicable in this case.

In order to measure signature splitting in the new Band 1 in ^{197}Bi, the experimental routhians, é as a function of the rotational frequency, $\hbar\omega$ were plotted together with those for Bands 1 and 2 in ^{196}Pb [Sin02], as shown in Figure 6.5. $K = 11$ and $K = 14.5$ values were used to generate the plots

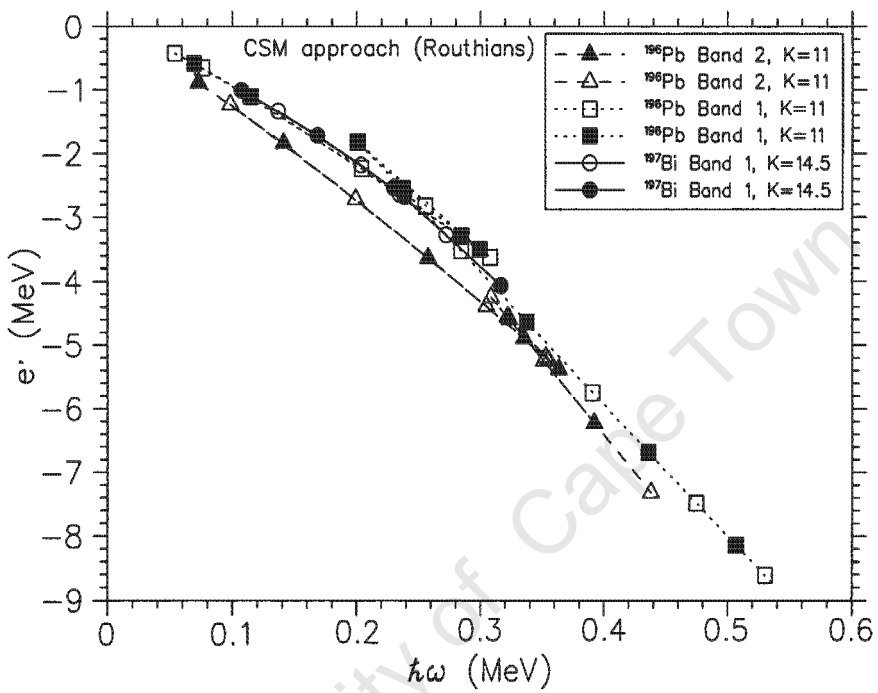

Figure 6.5: *The experimental routhians extracted from the bands in ^{197}Bi and ^{196}Pb [Sin02] nuclei as a function of the rotational frequency. The plots were generated for $K = 11$ and $K = 14.5$ values and the following Harris parameters were used as reference: $J_0 = 8\ \hbar^2/MeV$, $J_1 = 40\ \hbar^4/MeV^3$ [Hüb86, Plo93, Moo95].*

for ^{196}Pb and ^{197}Bi respectively. No signature splitting was observed for Band 1 in ^{197}Bi, which is an indication of a configuration involving high-K orbitals.

An irregularity is observed for Band 1 in ^{197}Bi at about 0.3 MeV (see Figure 6.1). However, the curve of the angular momentum as a function of rotational frequency exhibits a very small gain in angular momentum of $\approx 2\ \hbar$. This gain is too small compared to what is expected for CD or BC alignment in this mass region. For instance, we observe a backbend in both

Bands 1 and 2 of ^{196}Pb (see Figure 6.1) with a CD crossing for Band 2 at $\approx$ 0.34 MeV (see Figure 6.5) with a gain in angular momentum of $\approx$ 8 $\hbar$, and a BC crossing for Band 1 at $\approx$ 0.24 MeV (see Figure 6.5) with a gain in angular momentum of $\approx$ 10 $\hbar$. Therefore, in ^{197}Bi band, the irregularity at $\approx$ 0.3 MeV is not likely to be an alignment of CD or BC neutrons. Further studies are needed in order to address the question about the nature of these irregularity.

It is known that the high-K $\pi[606]\frac{13}{2}^+$ and $\pi[505]\frac{9}{2}^-$ intruder orbitals are deformation-driving. Thus, involving a third high-K deformation-driving orbital might result in larger nuclear deformation than this in the ^{196}Pb isotone. Hence, in order to estimate the deformation corresponding to the newly found Band 1 in ^{197}Bi, TRS calculations were performed. Figure 6.6 shows the results of such calculations performed for $(\pi, \alpha) = (+, +\frac{1}{2})$ configuration at a rotational frequency, $\omega = 0.282$ MeV$\hbar^{-1}$. Four energy minima which correspond to spherical, superdeformed, non-collective oblate and collective oblate deformation develop along the (β_2, γ) plane and their corresponding values are summarised in Table 6.1. Considering the collective oblate minimum revealed by the calculation, it is rather difficult to determine whether the minimum corresponds to a proton configuration with $K = 14.5$ or to a different configuration, because TRS gives only the projection of the spin on the rotational axis. However, we can find more information by considering the non-collective oblate minimum [Wys02]. For this minimum, the spin, $I_p = 14.01$ given by TRS is the projection of the proton angular momentum on the symmetry axis of an oblate nucleus and thus, this minimum should correspond to the nuclear deformation generated by the three high-K $\pi i_{\frac{13}{2}} h_{\frac{9}{2}}^2$ [Wys02]. Considering this minimum, it is not possible to estimate any changes to the deformation which might be involved by the alignment of the neutron pair along the collective rotational axis. However, it is expected that the neutron orbitals lying close to the Fermi level for these nuclei are not deformation-driving, and thus will not lead to changes of the nuclear deformation. The results of TRS calculation thus, predict that the nuclear deformation is $\beta_2 = 0.171$.

In Pb isotopes, the most yrast dipole bands include neutron excitations such as $\nu(i_{\frac{13}{2}})^2$ or $\nu i_{\frac{13}{2}} \nu j$ where $(j = p_{\frac{3}{2}}, f_{\frac{5}{2}}...)$. Figure 6.7 shows the two

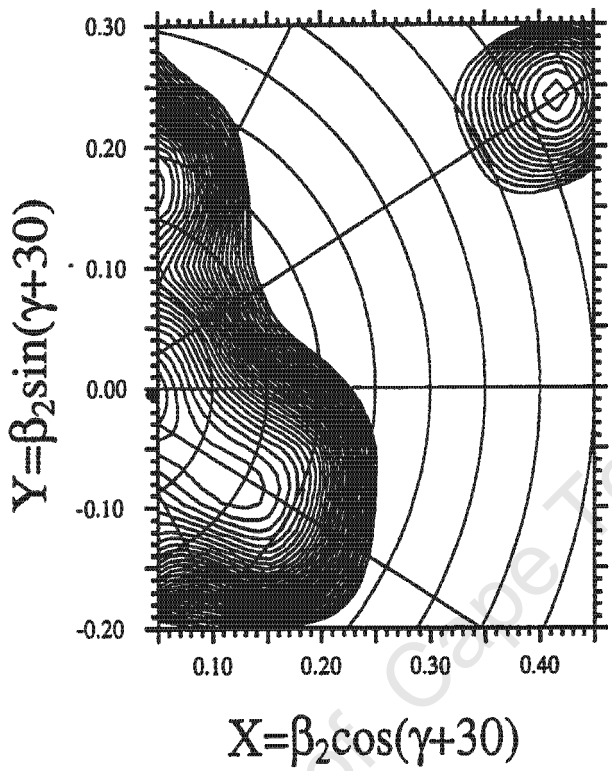

Figure 6.6: *TRS calculation for ^{197}Bi in the (β_2, γ) plane, performed at a rotational frequency of 0.282 $MeV\hbar^{-1}$ for the $(\pi, \alpha) = (+, +\frac{1}{2})$, configuration.*

Table 6.1: *Deformation parameters of the ^{197}Bi nucleus calculated from TRS. The values correspond to rotational frequency, $\hbar\omega = 0.282$ MeV for the $(\pi, \alpha) = (+, +\frac{1}{2})$ configuration.*

Shape	β_2	γ	I_p	I_n
Spherical	0.044	-35.7°	5.67	12.59
Non collective oblate/Triaxial	0.171	> 44.2°	14.01	2.14
Collective oblate	0.142	-64.0°	1.64	15.76
Superdeformed	0.481	0.2°	12.10	19.43

possible configurations for Band 1 in ^{197}Bi, $\pi i_{\frac{13}{2}} h_{\frac{9}{2}}^2 \otimes \nu i_{\frac{13}{2}}^2$ resulting in a bandhead spin of $I \approx \frac{37}{2}^+$ and $\pi i_{\frac{13}{2}} h_{\frac{9}{2}}^2 \otimes \nu i_{\frac{13}{2}} \nu j$ corresponding to $I \approx \frac{33}{2}^-$. Since our experimental data favours the first case, the configuration $\pi(i_{\frac{13}{2}}\ (h_{\frac{9}{2}})^2) \otimes \nu(i_{\frac{13}{2}})^2$ is suggested for Band 1 in ^{197}Bi.

We expect that at higher spins a CD band crossing will occur corresponding

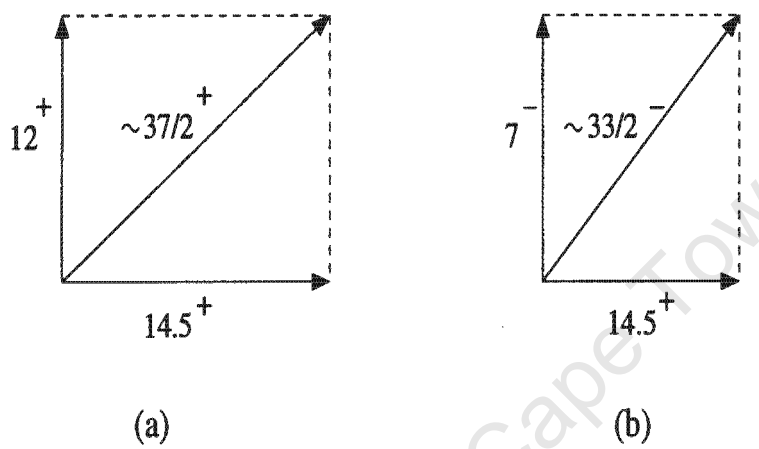

Figure 6.7: *The bandhead spin obtained by the coupling of* $\pi(i_{\frac{13}{2}}\ (h_{\frac{9}{2}})^2)$ *to (a)* $\nu(i_{\frac{13}{2}})^2$ *and (b)* $\nu i_{\frac{13}{2}}\ \nu j$.

to the alignment of a second pair $i_{\frac{13}{2}}$ neutrons along the axis of collective rotation. Studies with a larger array might be needed in order to observe this band crossing.

Although CSM calculations might not be suitable for describing dipole bands since they assume collective rotation, we performed such calculations in order to search for a possible explanation of the irregularity, observed at $\hbar\omega = 0.3$ MeV for Band 1 in ^{197}Bi. Deformation of $\beta_2 = 0.17$ and an axial symmetry, γ = -60° were used in the CSM calculation for Band 1 in ^{197}Bi. The hexadecupole parameter, β_4 was set to zero for the calculations. Thus, plotted in Figure 6.8 are the predicted Wood-Saxon quasi-particle energies in the rotating frame or Routhians, as a function of rotational frequency, $\hbar\omega$. The convention for labelling the orbitals in Figures 6.8 is summarised in Table 6.2. In the top panel of Figure 6.8, it can be seen that closest to the Fermi level, proton routhians originate from the $\pi h_{\frac{9}{2}}[514]\frac{7}{2}$, $\pi h_{\frac{9}{2}}[505]\frac{9}{2}$ and $\pi i_{\frac{13}{2}}[606]\frac{13}{2}$ orbitals. This is consistent with their involvement in the

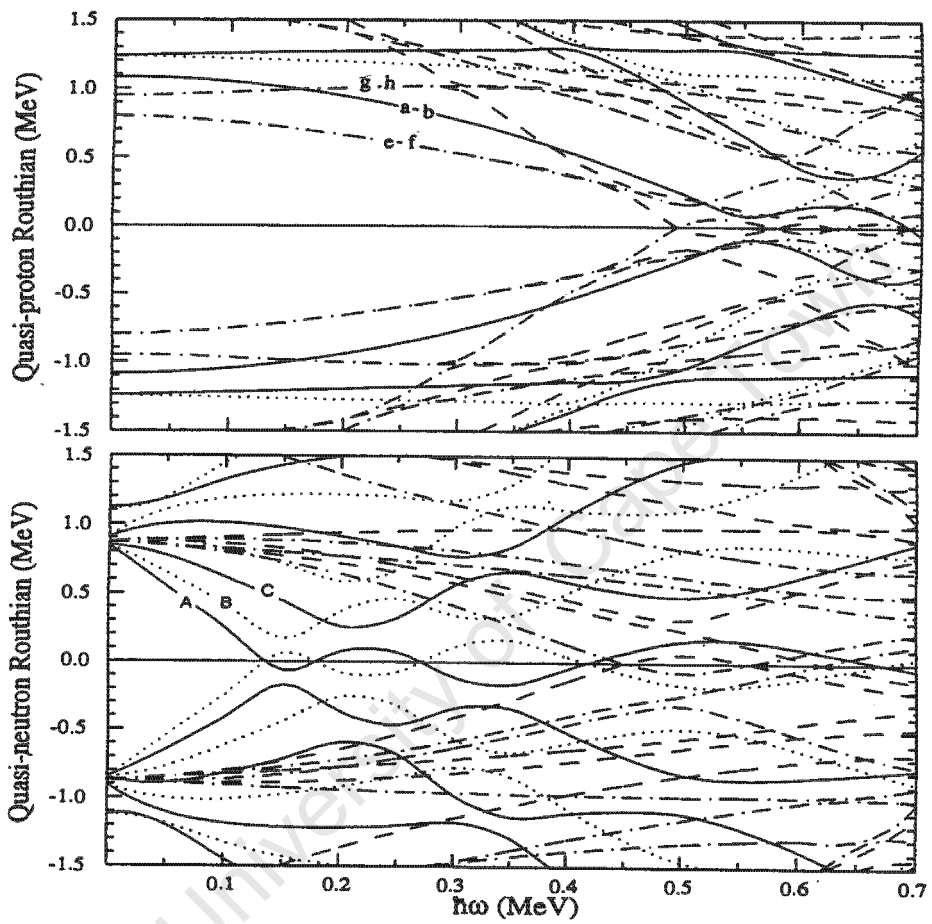

Figure 6.8: *The Wood-Saxon quasi-proton (quasi-neutron) routhian diagram for ^{197}Bi in the top (bottom) panel, performed at a deformation of $\beta_2 = 0.170$, $\beta_4 = 0.0$ and an axial symmetry, $\gamma = -60°$. Solid lines represent $(\pi, \alpha) = (+,+\frac{1}{2})$, dotted $(+,-\frac{1}{2})$, dash-dotted $(-,+\frac{1}{2})$ and dashed $(-,-\frac{1}{2})$.*

Table 6.2: *Convention for labelling the proton and neutron orbitals described by the parity and signature quantum numbers. The proton (neutron) configurations are described by small (capital) letters.*

Convention for labelling the orbitals			
Shell model	*Nilsson*	π, α	*adopted*
	Protons		
$i_{\frac{13}{2}}$	$\pi[606]\frac{13}{2}^+$	$(+,+\frac{1}{2})$	a
$i_{\frac{13}{2}}$	$\pi[606]\frac{13}{2}^+$	$(+,-\frac{1}{2})$	b
$h_{\frac{9}{2}}$	$\pi[514]\frac{7}{2}^-$	$(-,+\frac{1}{2})$	e
$h_{\frac{9}{2}}$	$\pi[514]\frac{7}{2}^-$	$(-,-\frac{1}{2})$	f
$h_{\frac{9}{2}}$	$\pi[505]\frac{9}{2}^-$	$(-,+\frac{1}{2})$	g
$h_{\frac{9}{2}}$	$\pi[505]\frac{9}{2}^-$	$(-,-\frac{1}{2})$	h
	Neutrons		
$i_{\frac{13}{2}}$	$\nu[600]\frac{1}{2}^+$	$(+,+\frac{1}{2})$	A
$i_{\frac{13}{2}}$	$\nu[600]\frac{1}{2}^+$	$(+,-\frac{1}{2})$	B
$i_{\frac{13}{2}}$	$\nu[651]\frac{3}{2}^+$	$(+,+\frac{1}{2})$	C

configuration of Band 1 in ^{197}Bi. The bottom panel of the same Figure 6.8 shows that the neutron Fermi surface is close to the low-K $\nu i_{\frac{13}{2}}[600]\frac{1}{2}$ and $\nu i_{\frac{13}{2}}[651]\frac{3}{2}$ orbitals, as well as orbitals originating from the low-j $p_{\frac{3}{2}}$ and $f_{\frac{5}{2}}$ shells. It should be noted that at frequency of $\approx$ 0.3 MeV a $(-,-\frac{1}{2})$ routhian (originating from a $h_{\frac{11}{2}}$ orbital) interacts with the h routhian. This type of interaction is expected to lead to a change of the configuration of one proton only, which would occur at $\hbar\omega = 0.3$ MeV with a gain in aligned angular momentum of $\approx 5\ \hbar$. Although the results of CSM calculations when applied to dipole bands should be taken with caution, the suggestion that the irregularity in Band 1 could be related not with a pair breaking but with a change in the proton configuration of the band, seems very interesting and worthy of further study.

6.3 Band 2 in ^{195}Bi

The spins for the levels in Band 2 of ^{195}Bi could not be determined since the de-excitation transition(s) from this band could not be found (see Chapter 5). However, we took advantage of the similarity in the behaviour of

the dynamic moments of inertia observed for Band 1 in ^{197}Bi and Band 2 in ^{195}Bi, in order to gain knowledge about the configurations upon which this Band 2 in ^{195}Bi is based. The spin as a function of γ-ray energy for Band 2 in ^{195}Bi was compared with Band 1 in ^{197}Bi and Bands 1a and 2b in ^{194}Pb [Kac02] as depicted in Figure 6.9. In order to simplify the comparison,

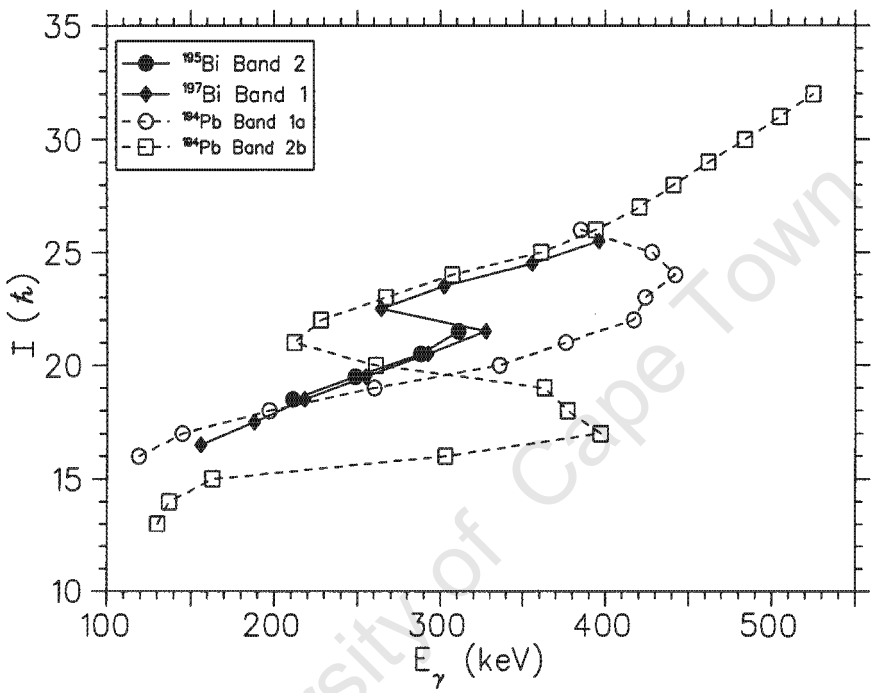

Figure 6.9: *Spin as a function of γ-ray energy for the dipole transitions of Bands 1a, 2a in ^{194}Pb [Kac02] and the new Band 2 in ^{195}Bi nuclei.*

an initial spin of $\frac{37}{2}$ $\hbar$ is assumed for Band 2 in ^{195}Bi. The slope of the curve for Band 2 in ^{195}Bi is much steeper compared to those of Bands 1a and 2b in ^{194}Pb before the backbend. However, it has the same slope as the curve for Band 1 in ^{197}Bi.

A comparison of the dynamic moments of inertia, $\Im^2$ as a function of rotational frequency, $\hbar\omega$ for Bands 1a and 2b in ^{194}Pb (below the backbend) [Kac02] and for Band 2 in ^{195}Bi were made as shown in Figure 6.10. The $\Im^2$ were calculated from the difference in spacing of the band levels, ΔE_γ, employing the formula $\Im^2 = \frac{dI}{d\omega} = \frac{1}{\Delta E_\gamma}$ (as described in Chapter 2) which is level spin independent. The $\Im^2$ observed for Band 2 in ^{195}Bi is

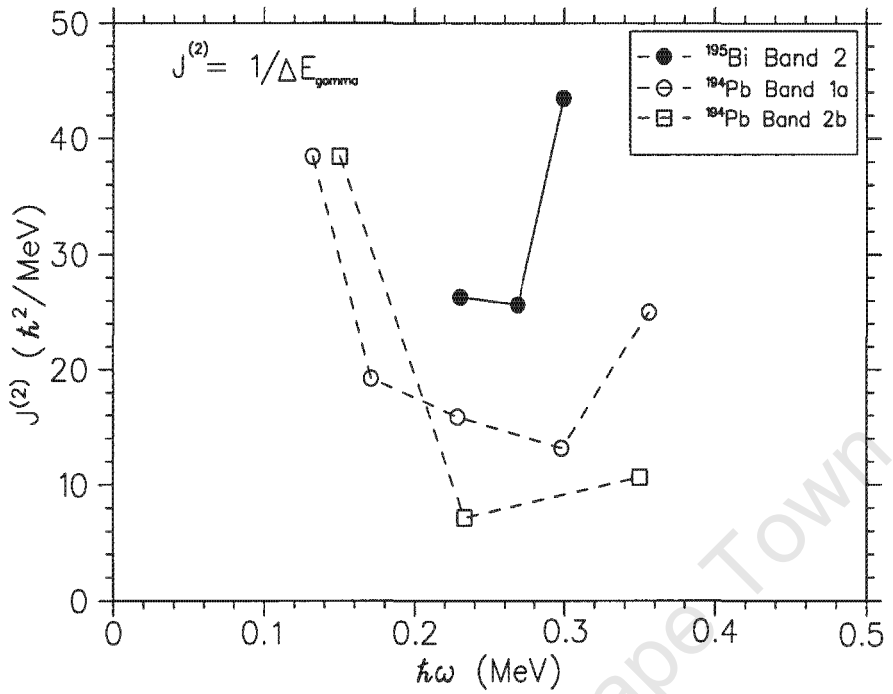

Figure 6.10: *Plots for the dynamic moment of inertia $J^{(2)}$ (denoted by $\Im^{(2)}$ in the text) for the bands in ^{195}Bi and ^{194}Pb [Kac02] nuclei as a function of the rotational frequency.*

almost twice that of Band 1a and 2a in ^{194}Pb [Kac02]. A rapid increase of the $\Im^2$ at a frequency of $\approx$ 0.3 MeV is observed for Band 2 in ^{195}Bi. Generally, such an increase in $\Im^2$ is an indicative of band crossing or breaking of a pair of nucleons. However, due to insufficient experimental data at high spin it is not possible to deduce the nature of this irregularity. However, it appears at about the same rotational frequency as the irregularity observed in Band 1 in ^{197}Bi and might thus have very similar nature. We suggest that as was the case with Band 1 in ^{197}Bi the larger values of the $\Im^2$ of Band 2 in ^{195}Bi are caused by the involvement of the intruder $\pi h_{\frac{9}{2}}[514]\frac{7}{2}^-$ orbital resulting in a proton configuration of $\pi i_{\frac{13}{2}} h^2_{\frac{9}{2}}$.

A comparison of the angular momentum along the rotational axis, I_x as a function of $\hbar\omega$ is shown on Figure 6.11 for Band 2 in ^{195}Bi and Bands 1a and 2b in ^{194}Pb [Kac02]. The plots for the bands were generated for $K = 11$ and $K = 14.5$ values in ^{194}Pb and ^{197}Bi respectively. Although the curve

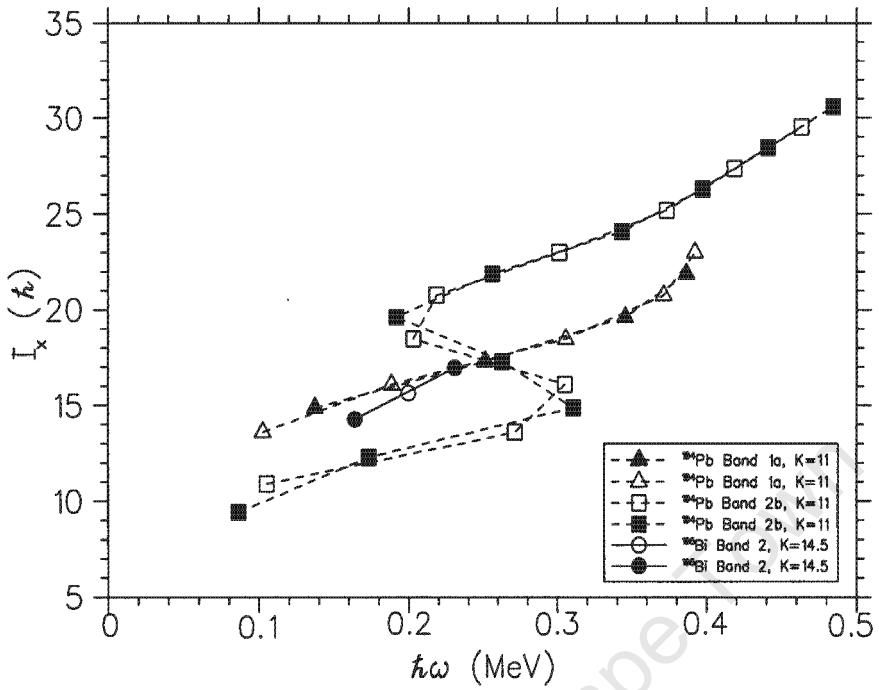

Figure 6.11: *Angular momentum, I_x along the rotational axis as a function of the rotational frequency, $\hbar\omega$ for Band 1 in ^{195}Bi and Bands 1a and 2a ^{194}Pb [Kac02]. The curves were generated for $K = 11$ and $K = 14.5$ in the case of bands in ^{194}Pb and ^{195}Bi respectively.*

for Band 2 of ^{195}Bi consists of only three points it seems that as was the case with Band 1 of ^{197}Bi its steepness is still larger than that for the bands in ^{196}Pb. This implies again that either the deformation of ^{195}Bi is different from that of ^{194}Pb or that the assumption that the collective rotation is responsible for this dipole band is not applicable.

In order to measure signature splitting for Band 2 in ^{195}Bi, the experimental routhians, é as a function of the rotational frequency, $\hbar\omega$ were plotted together with those for Bands 1a and 2b in ^{194}Pb [Kac02] as displayed in Figure 6.12. The curves for the bands in ^{195}Bi and ^{194}Pb were generated for $K = 11$ and $K = 14.5$ values respectively. The absence of signature splitting is an indication of a configuration involving high-K orbitals.

The TRS calculations were performed for the $(\pi, \alpha) = (+, +\frac{1}{2})$, configuration at a rotational frequency, $\omega = 0.283$ MeV$\hbar^{-1}$ for ^{195}Bi, in order to estimate

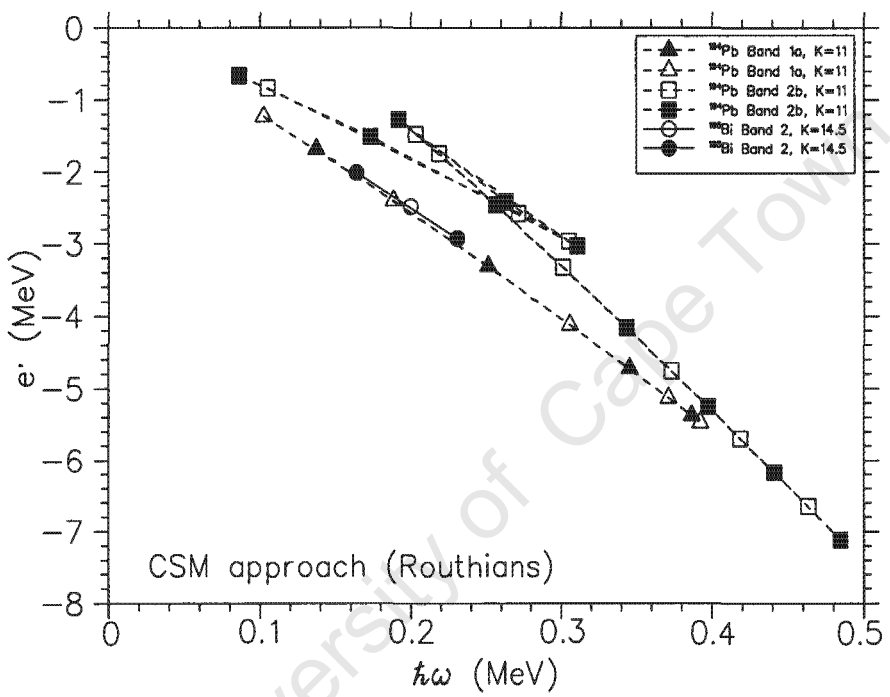

Figure 6.12: *The experimental routhians extracted from the bands in ^{195}Bi and ^{194}Pb [Kac02] nuclei as a function of the rotational frequency. The plots were generated for $K = 11$ and $K = 14.5$ values and the following Harris parameters were used as reference: $J_0 = 8\ \hbar^2/MeV$, $J_1 = 40\ \hbar^4/MeV^3$ [Hüb86, Plo93, Moo95].*

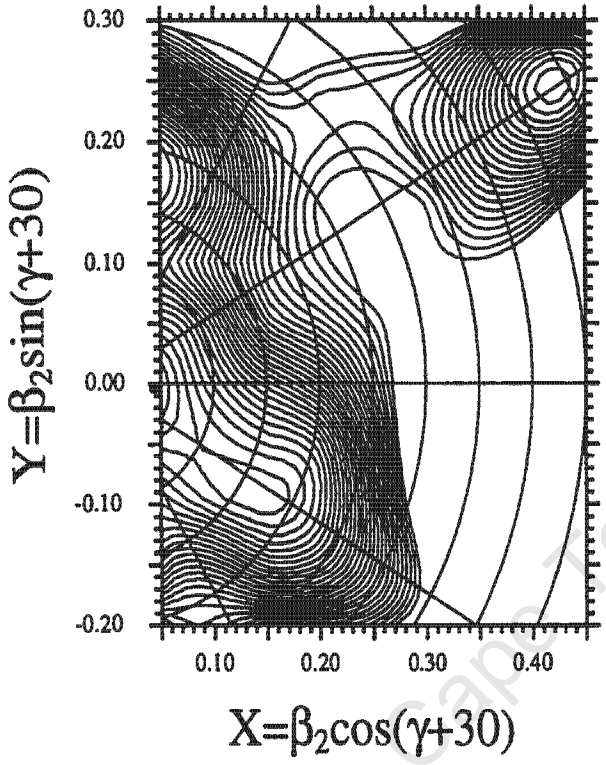

Figure 6.13: *TRS calculation for ^{195}Bi in the (β_2, γ) plane, performed at a rotational frequency of 0.283 $MeV\hbar^{-1}$ for the $(\pi, \alpha) = (+, +\frac{1}{2})$ configuration.*

the deformation corresponding to Band 2. The results for this configuration are depicted in Figure 6.13 which predicts the development of four energy minima corresponding to spherical, non-collective oblate, superdeformed and collective oblate deformation on the (β_2, γ) plane and are summarised in Table 6.3. Considering the non-collective oblate minimum (because of similar considerations as for Band 1 in ^{197}Bi) oblate deformation with $\beta_2 \approx 0.19$ is suggested to correspond to Band 2 in ^{195}Bi.

Although the spin and parity of Band 2 in ^{195}Bi were not measured and this makes it impossible to assign configuration to this band, the nearly identical γ-ray energies of this band and Band 1 in ^{197}Bi suggest that Band 2 might have the same configuration, that is $\pi i_{\frac{13}{2}} h_{\frac{9}{2}}^2 \otimes \nu i_{\frac{13}{2}}^2$.

Table 6.3: *Deformation parameters, β_2 and γ; proton, I_p and neutron, I_n spins for ^{195}Bi nucleus calculated from TRS. The values correspond to the rotational frequencies, $\hbar\omega$ tabulated for the $(\pi, \alpha) = (+, +\frac{1}{2})$ configuration.*

Shape	β_2	γ	I_p	I_n	$\hbar\omega$ *(MeV)*
Spherical	0.044	-34.0°	5.67	17.15	0.283
Non collective oblate/Triaxial	0.189	> 46.6°	16.76	0.42	0.244
	0.177	> 45.6°	13.38	6.41	0.283
	0.192	> 44.7°	14.42	7.04	0.322
Collective oblate	0.154	-64.6°	2.34	18.23	0.283
Superdeformed	0.488	0.3°	12.08	19.28	0.283

6.4 Systematics of Dipole Bands in the Bi isotopes

In previous studies the proton configuration $\pi i_{\frac{13}{2}} h_{\frac{9}{2}} s_{\frac{1}{2}}$ was involved for the bands in heavier $^{198-203}$Bi isotopes [Dag94, Cla93a]. In this work we suggested that three high-K protons, $\pi i_{\frac{13}{2}}$ and $\pi h^2_{\frac{9}{2}}$ participate in the configuration of the newly found dipole Bands 2 and 1 in ^{195}Bi and ^{197}Bi respectively. In order to investigate how the $\pi i_{\frac{13}{2}} h_{\frac{9}{2}} s_{\frac{1}{2}}$ and $\pi i_{\frac{13}{2}} h^2_{\frac{9}{2}}$ configurations compete along the Bi isotopic chain, we extracted the $\Im^{(2)}$ for the most intense bands (before the backbend) in ^{192,194,196,198}Pb [Gör01, Kac02, Sin02, Plo93], and compared them with those for the bands in ^{195,197}Bi and ^{198,199,200,202,203}Bi [Cla93a, Dag94, Zwa00], as shown in Figure 6.14. A similar behaviour of $\Im^{(2)}$ as a function of $\hbar\omega$ and a value of $\Im^{(2)} \approx 12\ \hbar^2$/MeV for $\hbar\omega > 0.2$ MeV is observed for the bands in the Pb isotopes and for Bands 1 and 5 in ^{202}Bi [Cla93a] and ^{203}Bi [Dag94] respectively. A larger $\Im^{(2)}$ value of $\approx 20\ \hbar^2$/MeV is observed for Band 5 in ^{200}Bi. A much larger value of $\Im^{(2)}$ is found for the Bands 1, 2 and 2 in ^{197}Bi, ^{195}Bi and ^{199}Bi respectively. These bands have $\Im^{(2)}$ values of $\approx 28\ \hbar^2$/MeV over the frequency range $0.22 \leq \hbar\omega \leq 0.28$ MeV, about twice as large as those for the bands in the Pb isotopes. The large value of $\Im^{(2)}$ for Band 2 in ^{199}Bi, similar to those of ^{195,197}Bi bands indicates that similar proton configuration, that is $\pi i_{\frac{13}{2}} h^2_{\frac{9}{2}}$ would be involved, as compared to the initially proposed $\pi i_{\frac{13}{2}} h_{\frac{9}{2}} s_{\frac{1}{2}}$ configuration [Dag94, Cla93a]. Thus, it looks like for the lighter Bi isotopes the $\pi i_{\frac{13}{2}} h^2_{\frac{9}{2}}$ configuration becomes yrast while for the

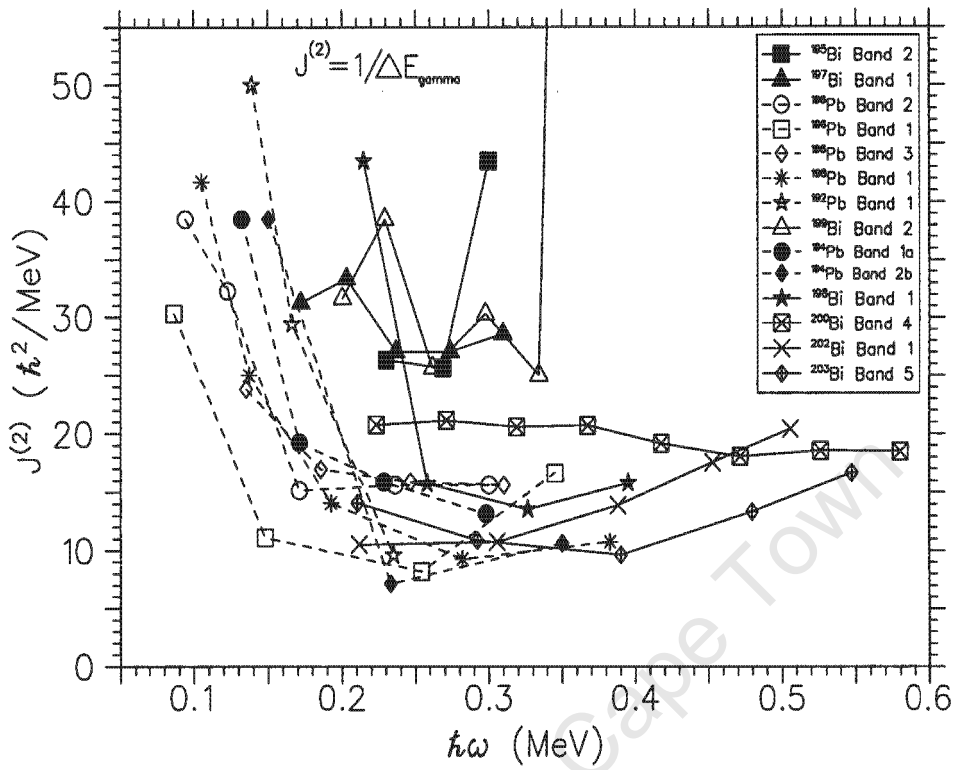

Figure 6.14: *Plots for the dynamic moment of inertia $J^{(2)}$ (denoted by $\Im^{(2)}$ in the text) as a function of the rotational frequency for the new bands in ^{195,197}Bi compared with those for known bands in ^{198,199,200,202,203}Bi [Cla93a, Dag94, Zwa00] and ^{192,194,196,198}Pb [Gör01, Kac02, Sin02, Plo93] nuclei.*

heavier ones the $\pi i_{\frac{13}{2}} h_{\frac{9}{2}} s_{\frac{1}{2}}$ configuration is the lowest.

Furthermore, we employed the TRS model in order to check whether it will be able to predict the above mentioned configuration competition in the Bi isotopic chain. The calculations were performed for A $(+,+\frac{1}{2})$ and F $(-,+\frac{1}{2})$, routhians for ^{195,197,199,201}Bi isotopes. We searched on the non-collective oblate axis for the energy minimum of the proton which would have $I_p = 11\hbar$. However, among the obtained minima for ^{199,201}Bi we could not find the one that could be unambiguously associated with the oblate shape, and $\pi i_{\frac{13}{2}} h_{\frac{9}{2}} s_{\frac{1}{2}}$ configuration with $K = 11$. Shown in Figure 6.15 are the plots for the Routhian energy, Er as a function of Bi isotopic mass predicted by TRS for the A $(+,+\frac{1}{2})$ and F $(-,+\frac{1}{2})$ routhians, and corresponding to $\pi i_{\frac{13}{2}} h_{\frac{9}{2}}^2$ and $\pi i_{\frac{13}{2}} h_{\frac{9}{2}} s_{\frac{1}{2}}$ configurations respectively. They predict well that the $\pi i_{\frac{13}{2}} h_{\frac{9}{2}}^2$

minimum shown in Figure 6.15 is more yrast than $\pi i_{\frac{13}{2}} h_{\frac{9}{2}} s_{\frac{1}{2}}$ one in ^{195,197}Bi. However, it was not possible to predict if the $\pi i_{\frac{13}{2}} h_{\frac{9}{2}} s_{\frac{1}{2}}$ configuration will become yrast for the heaviest isotopes.

We studied the behaviour of the deformation parameter, β_2 predicted by

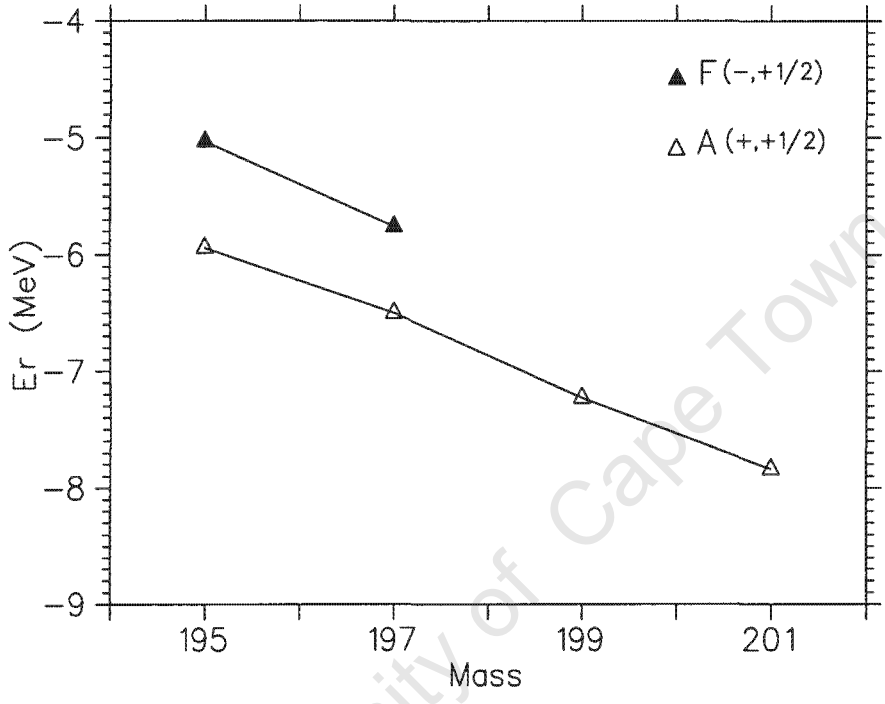

Figure 6.15: *Plots for the Routhian energy, Er as a function of Bi isotopic mass, generated from the TRS calculations performed at $\hbar\omega = 0.321$ MeV for A $(+,+\frac{1}{2})$ and F $(-,+\frac{1}{2})$ configurations corresponding to $\pi i_{\frac{13}{2}} h^2_{\frac{9}{2}}$ and $\pi i_{\frac{13}{2}} h_{\frac{9}{2}} s_{\frac{1}{2}}$ configurations respectively.*

the TRS calculations performed for the $\pi i_{\frac{13}{2}} h^2_{\frac{9}{2}}$ and $\pi i_{\frac{13}{2}} h_{\frac{9}{2}} s_{\frac{1}{2}}$ configurations in ^{195,197,199,201}Bi isotopes. These results are summarised in Table 6.4. The measured β_2 for the 11^- isomers in ^{194,196}Pb [Vyv02, Vyv02a], corresponding to $\pi i_{\frac{13}{2}} h_{\frac{9}{2}}$ configuration are also included in Table 6.4. From these results it is observed that β_2 increases with the decreasing N. This trend is consistent with the earlier predictions that the deformation of the oblate minima in the Pb isotopes increases with decreasing N [Ben89, Cla93]. Relatively large deformations are predicted for both configurations. The values are similar to the measured quadrupole deformations of the 11^- isomers in

Table 6.4: *TRS deformation parameters, β_2 for $_{83}Bi$ at rotational frequency, $\hbar\omega \approx 0.282$ MeV and the measured β_2 for the 11^- isomers in $^{194,196}Pb$ [Vyv02, Vyv02a].*

N	β_2 values		
	from TRS for $_{83}Bi$		*measured for* $_{82}Pb$
	$\pi i_{\frac{13}{2}} h^2_{\frac{9}{2}}$	$\pi i_{\frac{13}{2}} h_{\frac{9}{2}} s_{\frac{1}{2}}$	$\pi i_{\frac{13}{2}} h_{\frac{9}{2}}$
112	0.191	0.186	0.21 (4))[a]
114	0.171	0.186	0.156 (28))[b]
116	0.165	)[c]	
118	0.152	)[c]	

)[a] taken from [Vyv02].

)[b] taken from [Vyv02a].

)[c] could not find the corresponding minima.

^{194,196}Pb [Vyv02, Vyv02a] and also to the earlier predicted values of β_2 for the dipole bands in Pb [Ben89, Cla93].

The deformations predicted for ^{195,197}Bi dipole bands are much larger than those used with the TAC model for the Pb nuclei, ($\beta_2 = 0.1$). Within the TAC model, the dipole bands are described as a consequence of the shears mechanism. The particle and hole spins, initially coupled perpendicularly to each other, align towards the direction of the total angular momentum. During this re-orientation of the spins, strong M1 transitions are emitted and states with excitation energy $E - E_{bandhead} \propto I(I+1)$ are formed. This shears mechanism competes with the collective rotation of the oblate core. It has been suggested in the framework of Particle-Rotor Model (PRM), that the shears mechanism dominates only if the quadrupole deformation is $\epsilon_2 \leq 0.12$ [Mac99, Mac98]. It would be very interesting to perform TAC calculations at higher quadrupole deformation, in order to further study the nature of the dipole bands in lighter Bi isotopes.

6.5 Band 1 in ^{195}Bi

An irregular structure called Band 1 in ^{195}Bi, consists of M1 and E2 γ-ray transitions and looks like a strongly coupled rotational band built above the $(\frac{13}{2}^+)$ level. Indeed, it is known that among the lowest lying proton

orbitals in the Bi isotopes are the $\pi i_{\frac{13}{2}}$ and $\pi h_{\frac{9}{2}}$ orbitals. Low lying $(\frac{9}{2}^-)$ and $(\frac{13}{2}^+)$ levels in many Bi nuclei were associated with $\pi h_{\frac{9}{2}}$ and $\pi i_{\frac{13}{2}}$ orbitals, but always nearly spherical nuclear shape was suggested. This is the first case, when it looks like the $\pi i_{\frac{13}{2}}[606]\frac{13}{2}^+$ orbital induces a deformed nuclear shape in a Bi nucleus. Such a behaviour is not very surprising. Indeed, it is well known that the high-K $\pi i_{\frac{13}{2}}$ and $\pi h_{\frac{9}{2}}$ orbitals are deformation-driving, inducing oblate-deformed shapes in the Pb isotopes. It is also well known that the oblate deformed minimum becomes more yrast with respect to the spherical one, when lighter Pb nuclei are considered (when going away from the N = 126 closed shell). Thus, finding oblate deformation induced by the $\pi i_{\frac{13}{2}}[606]\frac{13}{2}^+$ orbital in the most neutron deficient Bi isotopes studied to date at high spins is consistent with these considerations. We therefore, tentatively assign the $\pi i_{\frac{13}{2}}[606]\frac{13}{2}^+$ configuration to Band 1 in ^{195}Bi and study if the theoretical predictions for this configuration are consistent with the experimental results.

In order to investigate the behaviour of the angular momentum, the projection of the angular momentum along the rotational axis, I_x as a function of rotational frequency, $\hbar\omega$ shown in Figure 6.16 and the aligned angular momentum, i_x as a function of rotational frequency, $\hbar\omega$ depicted in Figure 6.17 were generated for $K = 6.5$. The Harris parameters, $J_0 = 8\ \hbar^2/\text{MeV}$ and $J_1 = 40\ \hbar^4/\text{MeV}^3$ which were used for the oblate bands in the Hg isotopes [Hüb86], were used in order to produce the i_x curves represented by dashed lines. One can see that these Harris parameters are not appropriate for Band 1 in ^{195}Bi, since the obtained curves of i_x are steep. This implies that a larger deformation than that in Hg might be involved. Subsequently, we varied the above Harris parameters to $J_0 = 8\ \hbar^2/\text{MeV}$ and $J_1 = 200\ \hbar^4/\text{MeV}^3$ in order to obtain a flat curve (to estimate single-particle alignment) for i_x which were also used in order to calculate the experimental routhians.

The experimental routhians, e' as a function of the rotational frequency, $\hbar\omega$ for ^{195}Bi shown in Figure 6.18, were generated for $K = 6.5$. Signature splitting of $\approx$ 20 keV is observed for Band 1 in ^{195}Bi.

In order to compare these experimental results with the theoretical predictions for the $\pi i_{\frac{13}{2}}[606]\frac{13}{2}^+$ orbital, we first studied the nuclear deformation

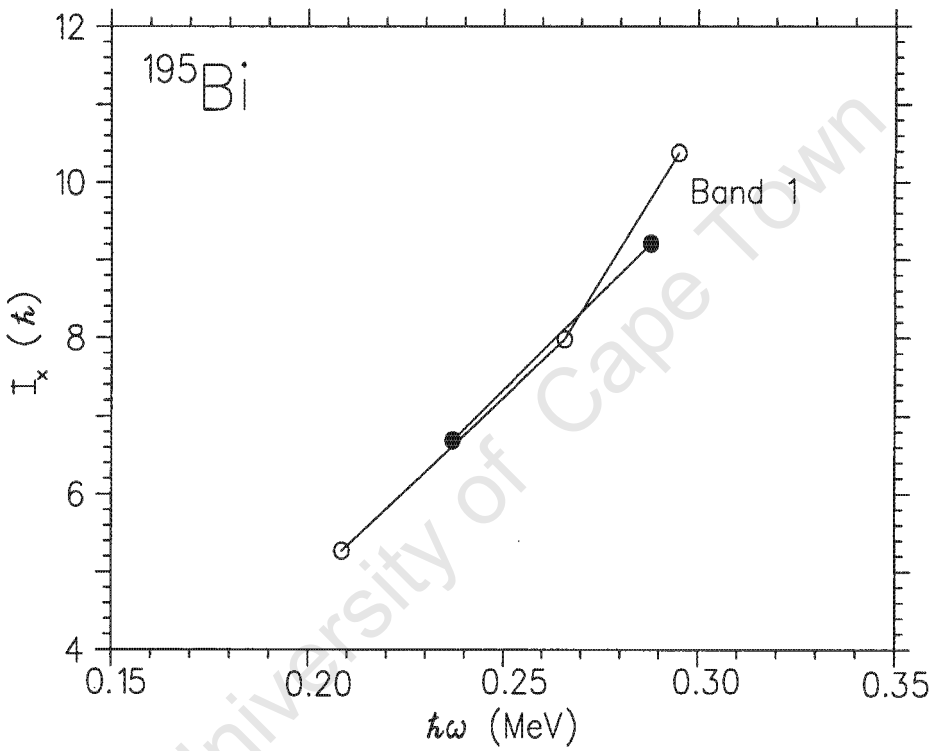

Figure 6.16: *Angular momentum, I_x along the rotational axis as a function of the rotational frequency, $\hbar\omega$ for Band 1 in ^{195}Bi. The K-value of 6.5 was used for generating the plot.*

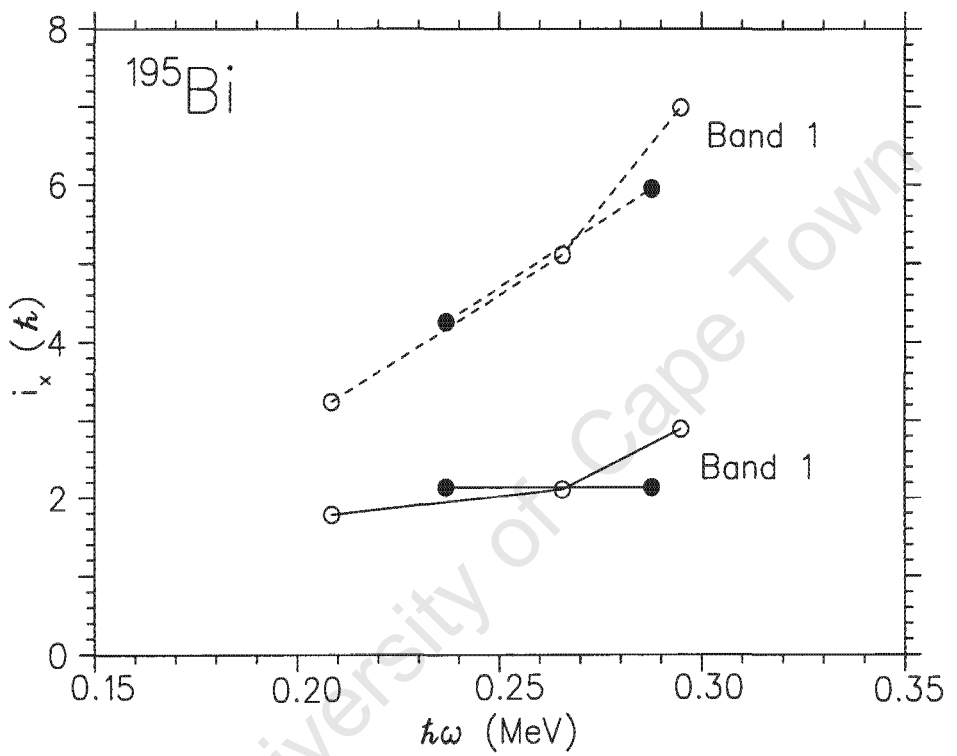

Figure 6.17: *Plot for the angular momentum alignment as a function of the rotational frequency for Band 1 in ^{195}Bi. The K-value of 6.5 and the following Harris parameters were used as reference: $J_0 = 8\ \hbar^2/MeV$; $J_1 = 40\ \hbar^4/MeV^3$ (dotted lines) [Hüb86, Plo93, Moo95] and $J_0 = 8\ \hbar^2/MeV$; $J_1 = 200\ \hbar^4/MeV^3$ (solid lines).*

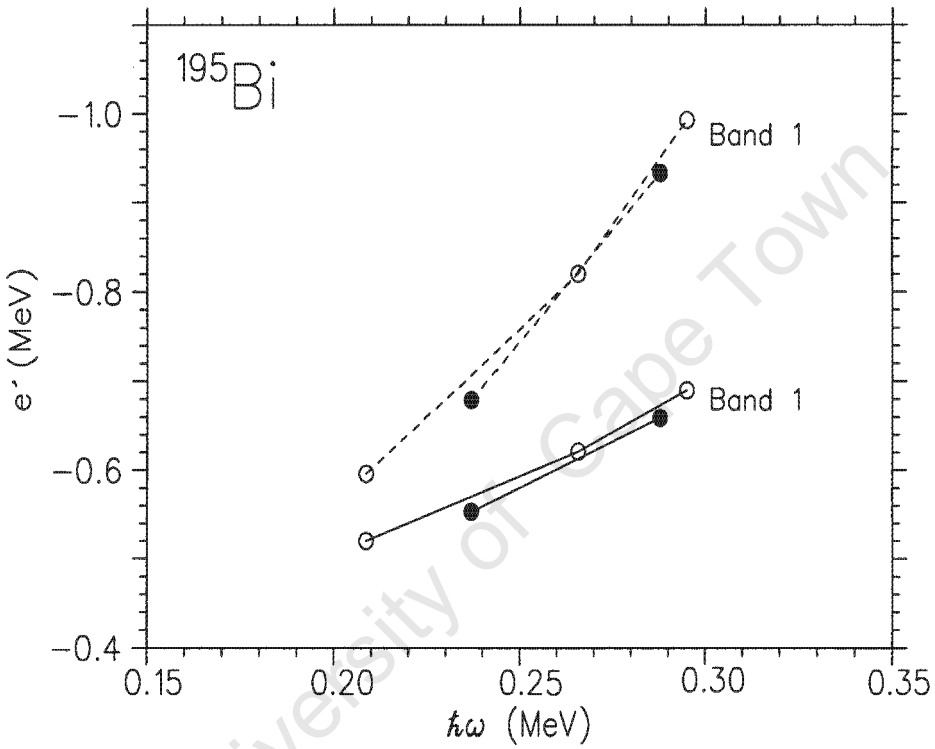

Figure 6.18: *The experimental routhians extracted from the new Band 1 in* ^{195}*Bi nucleus as a function of the rotational frequency. The K-value of 6.5 and the following Harris parameters were used as reference:* $J_0 = 8\ \hbar^2/MeV$; $J_1 = 40\ \hbar^4/MeV^3$ *(dotted lines) [Hüb86, Plo93, Moo95] and* $J_0 = 8\ \hbar^2/MeV$; $J_1 = 200\ \hbar^4/MeV^3$ *(solid lines) for generating the plots.*

that corresponds to Band 1 in ^{195}Bi. TRS calculations were performed for the $(\pi, \alpha) = (+, +\frac{1}{2})$ configuration. The results obtained for the rotational frequencies of 0.166, 0.205 and 0.127 MeV$\hbar^{-1}$ as shown in the top left, top right and bottom left panels of Figure 6.19 respectively. In each of

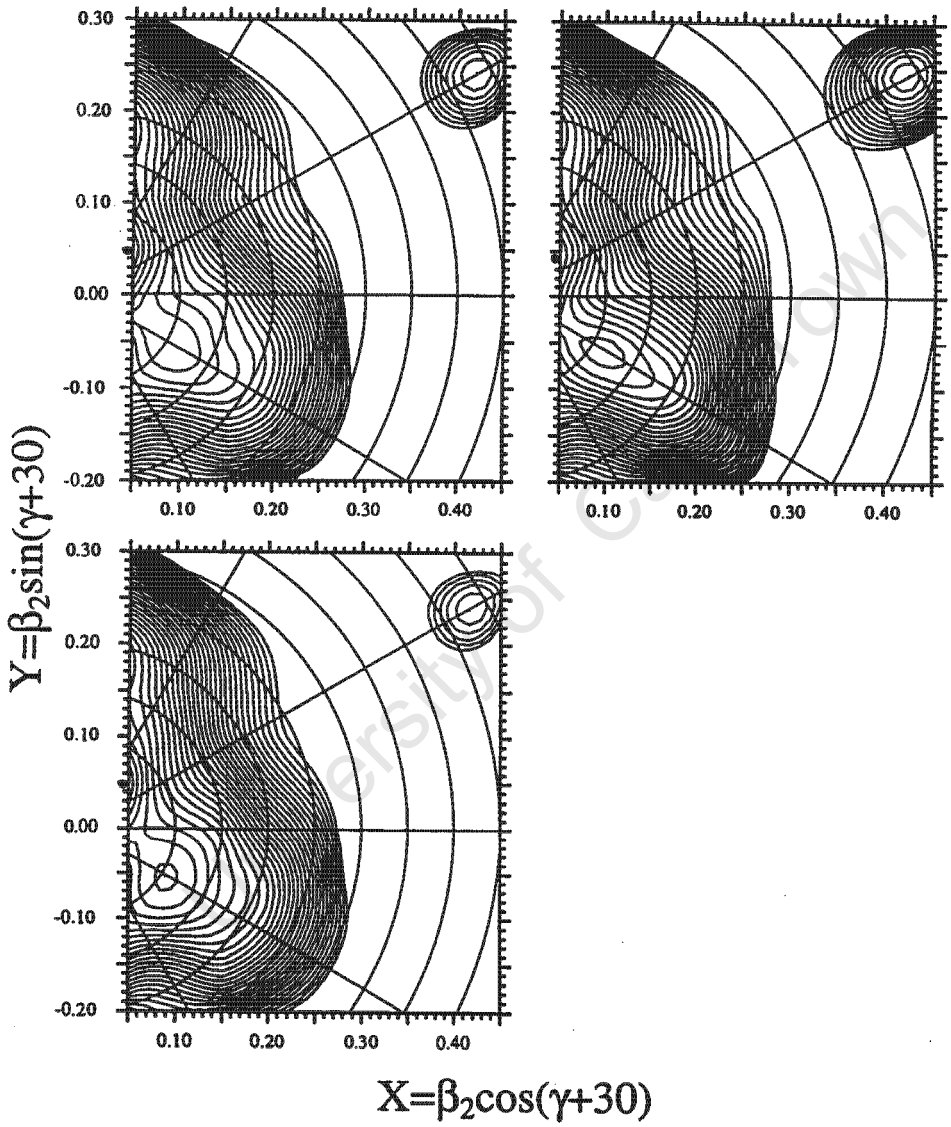

Figure 6.19: *TRS calculations for ^{195}Bi in the (β_2, γ) plane, performed at the following rotational frequencies: 0.166, 0.205 and 0.127 MeV$\hbar^{-1}$ for the top left, top right, and bottom left panels respectively. The plots are calculated for the $(\pi, \alpha) = (+, +\frac{1}{2})$, configuration.*

Table 6.6: *Convention for labelling the proton and neutron orbitals described by the parity and signature quantum numbers. The proton (neutron) configurations are described by small (capital) letters.*

Convention for labelling the orbitals			
Shell model	*Nilsson*	π, α	*adopted*
Protons			
$i_{\frac{13}{2}}$	$\pi[606]\frac{13}{2}^+$	$(+,+\frac{1}{2})$	a
$i_{\frac{13}{2}}$	$\pi[606]\frac{13}{2}^+$	$(+,-\frac{1}{2})$	b
$h_{\frac{9}{2}}$	$\pi[514]\frac{7}{2}^-$	$(-,+\frac{1}{2})$	e
$h_{\frac{9}{2}}$	$\pi[514]\frac{7}{2}^-$	$(-,-\frac{1}{2})$	f
$h_{\frac{9}{2}}$	$\pi[514]\frac{9}{2}^-$	$(-,+\frac{1}{2})$	g
$h_{\frac{9}{2}}$	$\pi[505]\frac{9}{2}^-$	$(-,-\frac{1}{2})$	h
Neutrons			
$i_{\frac{13}{2}}$	$\nu[651]\frac{3}{2}^+$	$(+,+\frac{1}{2})$	A
$i_{\frac{13}{2}}$	$\nu[651]\frac{3}{2}^+$	$(+,-\frac{1}{2})$	B
$i_{\frac{13}{2}}$	$\nu[642]\frac{5}{2}^+$	$(+,+\frac{1}{2})$	C
$i_{\frac{13}{2}}$	$\nu[642]\frac{5}{2}^+$	$(+,-\frac{1}{2})$	D
$f_{\frac{5}{2}}$	$\nu[503]\frac{5}{2}^-$	$(-,-\frac{1}{2})$	E
$f_{\frac{5}{2}}$	$\nu[503]\frac{5}{2}^-$	$(-,+\frac{1}{2})$	F

experimentally.

The bottom panel depicts that the neutron Fermi surface is close to the low-K levels of the $i_{\frac{13}{2}}$, $f_{\frac{5}{2}}$ and $p_{\frac{3}{2}}$ shells. Further support for this configuration assignment is supplied by the study of the $\frac{B(M1)}{B(E2)}$ ratios, which were calculated with the aid of the semi-classical Dönau–Frauendorf formula [Dön82, Dön87]. The reduced magnetic dipole transition probabilities for in-band transitions are given by:

$$B(M1) = \frac{3}{8\pi}\Big[(g_p - g_R)j_{p\perp} + (g_n - g_R)j_{n\perp}\Big]^2, \tag{6.1}$$

where g_R is the collective gyromagnetic factor (g-factor) for the collective rotation, g_p (g_n) for protons (neutrons). The proton and neutron g-factors are denoted by g_p and g_n respectively. The perpendicular component for the proton (neutron) to the total angular momentum, I is given by $j_{p\perp}$ ($j_{n\perp}$). In this case the $j_{p\perp}$ was calculated from the expression:

$$j_{p\perp} = K_p sin\theta - i_p cos\theta, \tag{6.2}$$

where $cos\theta = \frac{K_p}{\sqrt{j_p(j_p+1)}}$.
The expression for the $B(E2)$ is given by:

$$B(E2) = \frac{5}{16\pi} e^2 Q_0 \langle IK20|I-2K\rangle^2, \tag{6.3}$$

where Q_0 is the quadrupole moment.
In order to measure the experimental $\frac{B(M1)}{B(E2)}$ ratios for Band 1 in ^{195}Bi, the γ-ray intensities were measured from the ungated γ-γ matrix, gated on the γ-ray transitions above the E2 cross-over transitions. The following expression was used:

$$\frac{B(M1)}{B(E2)} = 0.697 \frac{E_\gamma^5(E2)}{E_\gamma^3(M1)} \frac{1}{\lambda(1+\delta^2)} \quad (\mu_N/eb)^2, \tag{6.4}$$

where E_γ is the γ-ray energy, the branching ratios, $\lambda = \frac{I_\gamma(E2)}{I_\gamma(M1)}$ and the γ-ray intensity, $I_\gamma(M1)$ ($I_\gamma(E2)$) for M1 (E2) transitions have been tabulated in Table 5.1 of Chapter 5 for ^{195}Bi. The mixing ratios, $\delta^2 = \frac{I_\gamma(I\rightarrow I-2)}{I_\gamma(I\rightarrow I-1)}$ could not be determined due to lack of angular correlation data. It was neglected because it is expected that $\delta^2 \ll 1$.

The comparison between the experimental (open squares) and theoretical (filled squares) $\frac{B(M1)}{B(E2)}$ ratios is displayed in Figure 6.21. The parameters employed for the theoretical calculation are listed in Table 6.7 while the measured $\frac{B(M1)}{B(E2)}$ ratios are tabulated in Table 5.1 of Chapter 5. The excellent

Table 6.7: *Parameters employed for the calculations.*

Parameters employed for the calculations								
g_p	g_n	i_np	j_p	K_p	g_R	I_i	I_f	β_2
1.264	0.0	2.0	6.5	6.5	0.426	6.5	15.5	-0.190

correspondence between the experimental and theoretical $\frac{B(M1)}{B(E2)}$ ratios for Band 1 gives strong support for the assigned $\pi i_{\frac{13}{2}}$ configuration. Thus, it looks like in the ^{195}Bi nucleus the high-K $i_{\frac{13}{2}}$ proton orbital is able to induce considerable oblate deformation and rotational behaviour at very low spins in a nucleus, known to be mostly spherical.

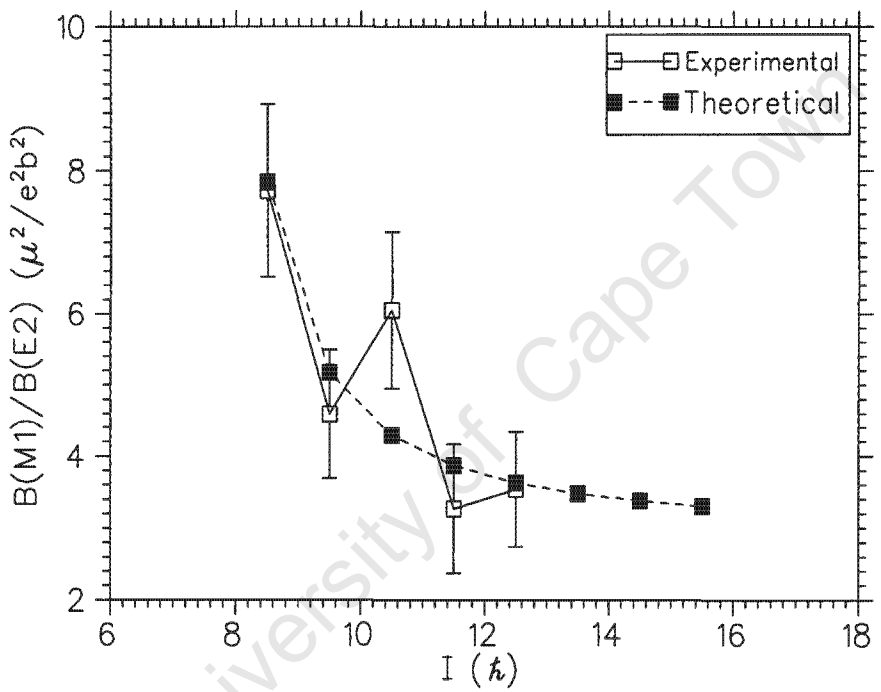

Figure 6.21: *Experimentally measured (empty squares) and theoretically calculated (filled squares)* $\frac{B(M1)}{B(E2)}$ *ratios as a function of spin, I for the new Band 1 in* ^{195}Bi.

Chapter 7

Summary and Conclusion

The work presented in this thesis is based on the study of the γ-coincidence data acquired in two experiments performed using the AFRODITE γ ray spectrometer array. High-spin states in ^{195}Bi and ^{197}Bi nuclei produced in the ^{181}Ta(^{20}Ne,6n) and ^{181}Ta(^{22}Ne,6n) reactions, were studied. The data analysis consists of analysis of the γ-γ coincidence relationship, Directional Correlation of Oriented (DCO) states measurements, linear polarisation measurements, γ intensities and Recoil Shadow Anisotropy (RSAM) lifetime measurements.

One new M1 dipole band has been discovered for each isotope. The dipole band in ^{197}Bi was linked to the low-spin states and its excitation energy, spin and parity, $\frac{37}{2}^+$, were determined. This is the first and the only dipole band in any of the Bi isotopes with known spin and parity. Several other new states were found and assigned to ^{197}Bi. The dipole band in ^{195}Bi which has similar γ-ray energies like the M1 dipole band in ^{197}Bi was not linked to the low lying states, since its decay path could not be found. Another band consisting of M1 and E2 cross-over transitions was found above the $(\frac{13}{2}^+)$ level in ^{195}Bi. This is the first observation when such a band is discovered at such a low spin, thus suggesting that shape coexistence between spherical and deformed shapes occurs at low spins in this nucleus. The analysis of ^{197}Bi data also revealed: (a) confirmation of the previously known ^{198}Bi level scheme [Zho96, Zwa00] even though no new transitions were found and (b) a sequence of four γ-ray transitions which could not be assigned

unambiguously to either ^{196}Bi, ^{197}Bi or ^{198}Bi nuclei.

The $\pi i_{\frac{13}{2}}$ configuration was assigned to Band 1 in ^{195}Bi. This is the only Bi isotope in which the $\pi i_{\frac{13}{2}}$ orbital is able to induce oblate deformation giving rise to a rotational band at low spins.

The configuration $\pi i_{\frac{13}{2}} h^2_{\frac{9}{2}} \otimes \nu i^2_{\frac{13}{2}}$ was assigned to the dipole bands in ^{195,197}Bi. This is the first time in the Bi isotopes that three high-K protons are involved in the configuration of the dipole bands.

The dipole bands we found in ^{195,197}Bi nuclei are very similar to the Pb bands interpreted within the framework of shears mechanism. The high-K protons could correspond to larger deformation. In this work we could not measure the B(M1) values. Further study of lifetime measurements would be necessary for this work.

We also studied the competition of the configurations assigned to the dipole bands in the Bi isotopes involving two and three high-K protons based on their dynamic moments of inertia. It seems that the $\pi i_{\frac{13}{2}} h_{\frac{9}{2}} s_{\frac{1}{2}}$ configuration is involved in the heavier Bi isotopes as was previously suggested [Dag94, Cla93a], while the $\pi i_{\frac{13}{2}} h^2_{\frac{9}{2}}$ configurations should be associated with the lighter Bi isotopes. Considering the predicted routhian energies from the TRS model for these proton configurations we found that the $\pi i_{\frac{13}{2}} h^2_{\frac{9}{2}}$ minimum is more yrast than $\pi i_{\frac{13}{2}} h_{\frac{9}{2}} s_{\frac{1}{2}}$ in ^{195,197}Bi, which supports the involvement of the $\pi i_{\frac{13}{2}} h^2_{\frac{9}{2}}$ configuration.

The Total Routhian Surface (TRS) model for the dipole bands in ^{195,197}Bi predicts deformation, $\beta_2 = 0.17$ much larger than that employed by the Tilted Axis Cranking (TAC) model for the Pb nuclei, ($\beta_2 = 0.1$). However, the larger deformation is in conformity with the one recently measured for the 11^- isomers in ^{194,196}Pb [Vyv02, Vyv02a] and the one earlier predicted for the dipole bands in the light Pb isotopes [Ben89, Cla93].

Considering the systematics of the dipole bands in this region, Bands 1 and 2 in ^{197}Bi and ^{195}Bi respectively, are purely shears bands. However, they have larger deformation which arises questions about the relative contribution of the collective rotation and shears mechanism for the dipole bands which need to be further studied. In contrast to these bands, Band 1 in ^{195}Bi is a collective rotational band.

References

[Ada84] H. L. Adair and E. H. Kobisk, Treatise in Heavy Ion Science, **7**, Instrumentation and Techniques, Edited by D. A. Bromley, Plenum Press, New York, (1985).

[And76] G. Andersson, S. E. Larsson, G. Leander, P. Möller, S. G. Nilsson, I. Ragnarsson, S. Åberg, R. Bengtsson, J. Dudek, B. Nerlo-Pomorski and Z. Szymański, Nucl. Phys. **A268**, 205 (1976).

[Arf85] G. Arfken, *Mathematical Methods For Physicists*, 3^{rd} Edition, Academic Press, Inc, (1985).

[Bal94] G. Baldsiefen, H. Hübel, W. Korten, D. Mehta, N. Nenoff, B. V. Thirumala Rao, P. Willsau, H. Grawe, J. Heese, H. Kluge, K. H. Maier, R. Schubart, S. Frauendorf and H. J. Maier, Nucl. Phys. **A574**, 521 (1994).

[Bal92] G. Baldsiefen, H. Hübel, F. Azaiez, C. Bourgeois, D. Hojman, A. Korichi, N. Perrin and H. Sergolle, Z. Phys. **A343**, 245 (1992).

[Bal92a] G. Baldsiefen, H. Hübel, D. Mehta, B. V. Thirumala Rao, U. Birkental, G. Fröhlingsdorf, M. Neffgen, N. Nenoff, S. C. Pancholi, N. Singh, W. Schmitz, K. Theine, P. Willsau, H. Grawe, J. Heese, H. Kluge, K. H. Maier, M. Schramm, R. Schubart and H. J. Maier, Phys. Lett. **B275**, 252 (1992).

[Bal94] G. Baldsiefen, H. Hübel, W. Korten, D. Mehta, N. Nenoff, B. V. Thirumala Rao, P. Willsau, H. Grawe, J. Heese, H. Kluge, K. H. Maier, R. Schubart, S. Frauendorf and H. J. Maier, Nucl. Phys. **A574**, 521 (1994).

[Bar57] J. Bardeen, Cooper and Schrieffer, Phys. Rev. **108**, 1178 (1957).

[Bas80] R. Bass, *Nuclear Reactions with Heavy Ions*, (Springer-Verlag), (1980).

[Bea96] C. W. Beausang and J. Simpson, J. Phys. G: Nucl. Part. Phys. **22**, 527 (1996).

[Ben93] R. Bengtsson, Nucl. Phys. **A557**, 277c (1993).

[Ben89] R. Bengtsson and W. Nazarewicz, Z. Phys. **A334**, 269 (1989).

[Boh81] A. Bohr and B. R. Mottelson, Phys. Scr. **24**, 71 (1981).

[Boh79] A. Bohr and B. R. Mottelson, Physics Today, 25 (1979).

[Boh75] A. Bohr and B. R. Mottelson, Nucl. Structure, **Vol 2**, (1975).

[Boh36] N. Bohr, Nature **137**, 344 (1936).

[Bot87] A. H. Botha, S. J Burger, Z. B. du Toit, D. Reitmann, P. J. Celliers, P. M. Cronje, H. N. Jungwirth, *Proc. 11th Int. Conf. on Cyclotrons and their Applications*, Ionics, Tokyo, 515 (1987).

[Bot87a] A. H. Botha, H. N. Jungwirth, J. J. Kritzinger, D. Reitmann, S. Schneider, *Proc. 11th Int. Conf. on Cyclotrons and their Applications*, Ionics, Tokyo, 515 (1987).

[Bur63] W. E. Burcham, *An Introduction to Nuclear Physics*, Longmans 1^{st} Publication, (1963).

[But73] P. A. Butler, P. E. Carr, L. L. Gadeken, A. N. James, P. J. Nolan, J. F. Sharpey-Schafer, P. J. Twin and D. A. Viggars, Nucl. Instr. and Meth. **108**, 497 (1973).

[Cha86] T. Chapuran, K. Dybdal, D. B. Fossan, T. Lönnroth, W. F. Piel, D. Horn and E. K.Warburton, Phys. Rev. **C33**, 130 (1986).

[Cla98] R. M. Clark and R. Wadsworth, Physics World, 25 July (1998).

[Cla98a] R. M. Clark, R. Krücken, S. J. Asztalos, J. A. Becker, B. Busse, S. Chmel, M. A. Deleplanque, R. M. Diamond, P. Fallon, D. Jenkins, K. Hauschild, I. M. Hibbert, H. Hübel, I. Y. Lee, A. O. Macchiavelli, R. W. MacLeod, G. Schmid, F. S. Stephens, U. J. van Severen, K. Vetter, R. Wadsworth and S. Wan, Phys. Lett. **B440**, 251 (1998).

[Cla97] R. M. Clark, S. J. Asztalos, G. Baldsiefen, J. A. Becker, L. Bernstein, M. A. Deleplanque, R. M. Diamond, P. Fallon, I. M. Hibbert, H. Hübel, R. Krücken, I. Y. Lee, A. O. Macchiavelli, R. W. MacLeod, G. Schmid, F. S. Stephens, K. Vetter, R. Wadsworth and Frauendorf, Phys. Rev. Lett. **78**, 1868 (1997).

[Cla96] R. M. Clark, S. Bouneau, A. N. Wilson, B. Cederwall, F. Azaiez, S. Asztalos, J. A. Becker, L. Bernstein, M. J. Brinkman, M. A. Deleplanque, I. Deloncle, R. M. Diamond, J. Duprat, P. Fallon, L. P. Farris, E. A. Henry, J. R. Hughes, W. H. Kelly, I. Y. Lee, A. O. Macchiavelli, M. G. Porquet, J. F. Sharpey-Schafer, F. S. Stephens, M. A. Stoyer and D. T. Vo, Phys. Rev. **C53**, 117 (1996).

[Cla95] R. M. Clark, S. Bouneau, F. Azaiez, S. Asztalos, J. A. Becker, B. Cederwall, M. A. Deleplanque, R. M. Diamond, J. Duprat, P. Fallon, L. P. Farris, E. A. Henry, J. R. Hughes, W. H. Kelly, I. Y. Lee, A. O. Macchiavelli, M. G. Porquet, J. F. Sharpey-Schafer, F. S. Stephens, M. A. Stoyer, D. T. Vo and A. N. Wilson, Phys. Rev. **C51**, R1052 (1995).

[Cla94] R. M. Clark, R. Wadsworth, H. R. Andrews, C. W. Beausang, M. Bergstrom, S. Clarke, E. Dragulescu, T. Drake, P. J. Dagnall, A. Galindo-Uribarri, G. Hackman, K. Hauschild, I. M. Hibbert, V. P. Janzen, P. M. Jones, R. W. MacLeod, S. M. Mullins, E. S. Paul, D. C. Radford, A. Semple, J. F. Sharpey-Schafer, J. Simpson, D. Ward and G. Zwartz, Phys. Rev. **C50**, 84 (1994).

[Cla93] R. M. Clark, R. Wadsworth, E. S. Paul, C. W. Beausang, I. Ali, A. Astier, D. M. Cullen, P. J. Dagnall, P. Fallon, M. J. Joyce,

M. Meyer, N. Redon, P. H. Regan, J. F. Sharpey-Schafer, W. Nazarewicz and R. Wyss, Nucl. Phys. **A562**, 121 (1993).

[Cla93a] R. M. Clark, R. Wadsworth, F. Azaiez, C. W. Beausang, A. M. Bruce, P. J. Dagnall, P. Fallon, P. M. Jones, M. J. Joyce, A. Korichi, E. S. Paul and J. F. Sharpey-Schafer, W. Nazarewicz, J. Phys. G: Nucl. Part. Phys. **19**, L57 (1993).

[Cla92] R. M. Clark, R. Wadsworth, E. S. Paul, C. W. Beausang, I. Ali, A. Astier, D. M. Cullen, P. J. Dagnall, P. Fallon, M. J. Joyce, M. Meyer, N. Redon, P. H. Regan, W. Nazarewicz and R. Wyss, Phys. Lett. **B275**, 247 (1992).

[Cla92a] R. M. Clark, R. Wadsworth, E. S. Paul, C. W. Beausang, I. Ali, A. Astier, D. M. Cullen, P. J. Dagnall, P. Fallon, M. J. Joyce, M. Meyer, N. Redon, P. H. Regan, J. F. Sharpey-Schafer, W. Nazarewicz and R. Wyss, Z. Phys. **A342**, 371 (1992).

[Dag94] P. J. Dagnall, C. W. Beausang, R. M. Clark, R. Wadsworth, S. Bhattacharjee, P.Fallon, P. D. Forsyth, D. B. Fossan, G. deFrance, S. J. Gale, F. Hannachi, K. Hauschild, I. M. Hibbert, H. Hübel, P. M. Jones, M. J. Joyce, A. Korichi, W. Korten, D. R. LaFosse, E. S. Paul, H. Schnare, K. Starosta, J. F. Sharpey-Schafer, P. J. Twin, P. Vaska, M. P. Waring and J. N. Wilson, J. Phys. G: Nucl. Part. Phys. **20**, 1591 (1994).

[Dag93] P. J. Dagnall, C. W. Beausang, P.Fallon, P. D. Forsyth, E. S. Paul, J. F. Sharpey-Schafer, P. J. Twin, I. Ali, D. M. Cullen, M. J. Joyce, G. Smith, R. Wadsworth, R. M. Clark, P. H. Regan, A. Astier, M. Meyer and N. Redon, J. Phys. G: Nucl. Part. Phys. **19**, 465 (1993).

[deV83] M. J. de Voigt, J. Dudek and Z. Szymański, Rev. Mod. Phys. **55** 949 (1983).

[Dia80] R. M. Diamond and F. S. Stephens, Ann. Rev. Nucl. Part. Sci. **30**, 85 (1980).

[Dön87] F. Dönau, Nucl. Phys. **A471**, 469 (1987).

[Dön82] F. Dönau and S. Frauendorf, *Proc. Conf. on High Angular Momentum Properties of Nuclei*, (Oak Ridge) ed. N. R. Johnson, (New York: Harwood Academic) 143 (1982).

[Dow00] D. Dowie and S. M. Mullins, B.Sc (Physics) Vacation Project, University of Western Cape, unpublished, December (2000).

[Dri90] M. W. Drigert, M. Piiparinen, R. V. F. Janssens, R. Holzmann, I. Ahmad, J. Borggreen, R. R. Chasman, P. J. Daly, B. K. Dichter, H. Emling, U. Garg, Z. W. Grabowski, T. L. Khoo, W. C. Ma, M. Quader, D. C. Radford and W. Trzaska, Nucl. Phys. **A515**, 466 (1990).

[Duc99] G. Duchêne, F. A. Beck, P. J. Twin, G. de France, D. Curien, L. Han, C. W. Beausang, M. A. Bentley, P. J. Nolan, J. Simpson, Nucl. Instr. and Meth. in Phys. Res. **A432**, 90 (1999).

[Duc96] L. Ducroux, A. Astier, R. Duffait, Y. Le Coz, M. Meyer, S. Perries, N. Redon, J. F. Sharpey-Schafer, A. N. Wilson, R. Lucas, V. Méot, R. Collatz, I. Deloncle, F. Hannachi, A. Lopez-Martens, M. -G. Porquet, C. Schück, F. Azaiez, S. Bouneau, C. Bourgeois, A. Korichi, N. Poffé, H. Sergolle, B. J. P. Gall, I. Hibbert and R. Wadsworth, Z. Phys. **A356**, 241 (1996).

[Dut87] Z. B. du Toit, P. J. Celliers, L. M. M. Roels, E. P. Conard, J. J. Kritzinger and S. J. Burger, *Proc. 11th Int. Conf. on Cyclotrons and their Applications*, Ionics, Tokyo, 109 (1987).

[Eji89] H. Ejiri and M. J. de Voigt, *Gamma-Ray and Electron Spectroscopy in Nuclear Physics*, Clarendon Press-Oxford, (1989).

[Eml86] H. Emling, F. Azgui, M. Däther, S. Doebereiner, H. Grein, C. Michel and H. J. Wollersheim, Nucl. Instr. and Meth. in Phys. Res. **A249**, 320 (1986).

[Fag59] L. W. Fagg and S. S. Hanna, Rev. Mod. Phys. **31**, 711 (1959).

[Fan91] B. Fant, R. J. Tanner, P. A. Butler, A. N. James, G. D. Jones, R. J. Poynter, C. A. White, K. L. Ying, D. J. G. Love, J. Simpson and K. A. Connell, J. Phys. G: Nucl. Part. Phys. **17**, 319 (1991).

[Fir96] R. B. Firestone, *Table of Isotopes*, 8^{th} Ed., Vol. 2, (John Wiley and Sons, INC, NY.), (1996).

[Fra97] S. Frauendorf, Z. Phys. **A358**, 163 (1997).

[Fra96] S. Frauendorf and Jie Meng, Z. Phys. **A356**, 263 (1996).

[Fra96a] S. Frauendorf, J. Reif and G. Winter, Nucl. Phys. **A601**, 41 (1996).

[Fra93] S. Frauendorf, Nucl. Phys. **A557**, 259c (1993).

[Gav93] A. Gavron, Computational Nuclear Physics 2, Nuclear Reactions, Springer-Verlag New York, Inc, 108 (1993).

[Gav80] A. Gavron, Phys. Rev. **C21**, 230 (1980).

[Gil95] G. Gilmore and J. Hemingway, *Practical Gamma-Ray Spectroscopy*, John Wiley & Sons Ltd, (1995).

[Gou83] C. R. Gould and N. R. Roberson, IEEE Trans. Nucl. Sci. **NS-30**, 3758 (1983).

[Gou81] C. R. Gould, L. G. Holzsweig, S. E. King, Y. C. Lau, R. V. Poore, N. R. Roberson and S. A. Wender, IEEE Trans. Nucl. Sci. **NS-28**, 3708 (1981).

[Gör01] A. Görgen, N. Nenoff, H. Hübel, G. Baldsiefen, J. A. Becker, A. P. Byrne, S. Chmel, R. M. Clark, M. A. Deleplanque, R. M. Diamond, P. Fallon, K. Hauschild, I. M. Hibbert, W. Korten, R. Krücken, I. Y. Lee, A. O. Macchiavelli, E. S. Paul, U. J. van Severen, F. S. Stephens, K. Vetter, R. Wadsworth, A. N. Wilson and J. N. Wilson, Nucl. Phys. **A683**, 108 (2001).

[Gri95] D. J. Griffiths, *Introduction to Quantum Mechanics*, Prentice Hall, Inc. (1995).

[Gro67] J. R. Grover, Phys. Rev. **157**, 832 (1967).

[Gue01] E. Gueorguieva, M. Kaci, C. Schück, A. Minkova, Ch. Vieu, J. J. Correia and J. S. Dionisio, Nucl. Instr. and Meth. in Phys. Res. **A474**, 132 (2001).

[Har80] M. Harvey, M. G. Vassanji, Nucl. Phys. **A344**, 61 (1980).

[Har65] S. M. Harris, Phys. Rev. **138**, 3B, B509 (1965).

[Häu80] O. Häusser, H. E. Mahnke, J. F. Sharpey-Schafer, M. L. Swanson, P. Taras, D. Ward, H. R. Andrews and T. K. Alexander, Phys. Rev. Lett. **44**, 132 (1980).

[Hüb86] H. Hübel, A. P. Byrne, S. Ogaza, A. E. Stuchbery, G. D. Dracoulis and Guttormsen, Nucl. Phys. **A453**, 316 (1986).

[Hug93] J. R. Hughes, Y. Liang, R. V. F. Janssens, A. Kuhnert, J. A. Becker, I. Ahmad, I. G. Bearden, M. J. Brinkman, J. Burde, M. P. Carpenter, J. A. Cizewski, P. J. Daly, M. A. Deleplanque, R. M. Diamond, J. E. Draper, C. Duyar, B. Fornal, U. Garg, Z. W. Grabowski, E. A. Henry, R. G. Henry, W. Hesselink, N. Kalantar-Nayestanaki, W. H. Kelly, T. L. Khoo, T. Lauritsen, R. H. Mayer, D. Nissius, J. R. B. Oliveira, A. J. M. Plompen, W. Reviol, E. Rubel, F. Soramel, F. S. Stephens, M. A. Stoyer, D. Vo and T. F. Wang, Phys. Rev. **C47**, R1337 (1993).

[Ing54] D. R. Inglis, Phys. Rev. **96**, 1059 (1954).

[Jen99] D. G. Jenkins, Phys. Rev. **C83**, 500 (1999).

[Jen98] D. G. Jenkins, Phys. Rev. **C58**, 2703 (1998).

[Jon95] P. M. Jones, L. Wei, F. A. Beck, P. A. Butler, T. Byrski, G. Duchêne, G. de France, F. Hannachi, G. D. Jones and B. Kharraja, Nucl. Instr. and Meth. in Phys. Res. **A362**, 556 (1995).

[Kac02] M. Kaci, M. -G. Porquet, I. Deloncle, M. Aiche, F. Azaiez, G. Bastin, C. W. Beausang, C. Bourgeois, R. M. Clark, R. Duffait, J.

Duprat, B. J. P. Gall, F. Hannachi, K. Hauschild, M. J. Joyce, A. Korichi, Y. Le Coz, M. Meyer, E. S. Paul, N. Perrin, N. Poffé, N. Redon, C. Schück, H. Sergolle, J. F. Sharpey-Schafer, J. Simpson, A. G. Smith and R. Wadsworth, Nucl. Phys. **A697**, 3 (2002).

[Ker81] A. K. Kerman, N. Onishi, Nucl. Phys. **C361**, 179 (1981).

[Kra88] K. S. Krane, *Introductory Nuclear Physics*, John Wiley and Sons, New York, (1988).

[Kra73] K. S. Krane, R. M. Steffen and R. M. Wheeler, Nuclear Data Tables, **11**, 351 (1973).

[Kuh92] A. Kuhnert, M. A. Stoyer, J. A. Becker, E. A. Henry, M. J. Brinkman, S. W. Yates, T. F. Wang, J. A. Cizewski, F. S. Stephens, M. A. Deleplanque, R. M. Diamond, A. O. Macchiavelli, J. E. Draper, F. Azaiez, W. H. Kelly and W. Korten, Phys. Rev. **C46**, 133 (1992).

[Law97] J. J. Lawrie, AUTOCAL-NEW software program on VAX, iThemba LABS, (1997).

[Lie84] R. M. Lieder, H. Jäger, A. Neskakis, T. Venkova and C. Michel, Nucl. Instr. and Meth. in Phys. Res. **220**, 363 (1984).

[Lit70] A. E. Litherland, G. T. Ewan and S. T. Lam, Canadian Journal of Phys. **48**, 2320 (1970).

[Lön86] T. Lönnroth, C. W. Beausang, D. B. Fossan, L. Hildingsson, W. F. Piel, Jr., M. A. Quader, Phys. Rev. **C33**, 1641 (1986).

[Mac99] A. O. Macchiavelli, R. M. Clark. M. A. Deleplanque, R. M. Diamond, P. Fallon, I. Y. Lee, F. S. Stephens and K. Vetter, Phys. Lett. **B450**, 1 (1999).

[Mac98] A. O. Macchiavelli, R. M. Clark. M. A. Deleplanque, R. M. Diamond, P. Fallon, I. Y. Lee, F. S. Stephens and K. Vetter, AIP. Conf. Proc. **481**, 517 (1998).

[Mac98a] A. O. Macchiavelli, R. M. Clark. P. Fallon, M. A. Deleplanque, R. M. Diamond, R. Krücken, I. Y. Lee, F. S. Stephens, S. Asztalos and K. Vetter, Phys. Rev. **C37**, R1073 (1998).

[Mar69] P. Marmier and E. Sheldon, *Physics of Nuclei and Particles*, **Vol. 1**, Academic Press Inc., (1969).

[Moo95] E. F. Moore, M. P. Carpenter, Y. Liang, R. V. F. Janssens, I. Ahmad, I. G. Bearden, P. J. Daly, M. W. Drigert, B. Fornal, U. Garg, Z. W. Grabowski, H. L. Harrington, R. G. Henry, T. L. Khoo, T. Lauritsen, R. H. Mayer, D. Nisius, W. Reviol and M. Sferrazza, Phys. Rev. **C51**, 115 (1995).

[Mor63] H. Morinaga and P. C. Gugelot, Nucl. Phys. **A46**, 210 (1963).

[Naz92] W. Nazarewicz and Z. Szymanski, Phys. Rev. **C45**, 2771 (1992).

[New98] R. T. Newman, J. J. Lawrie, B. R. S. Babu, M. S. Fetea, S. V. Förtsch, S. Naguleswaran, J. V. Pilcher, D. A. Raavé, C. Rigollet, J. F. Sharpey-Schafer, C. J. Stevens, F. D. Smit, G. F. Steyn, C. V. Wikner, D. G. Aschman, R. Beetge, R. W. Fearick, G. K. Mabala, S. Murray, D. G. Roux, W. Whittaker and N. J. Ncapayi, *Proceedings of Balkan School on Nuclear Physics, September 1-10, 1998 Baltalimani*, Istanbul-TURKEY, Balkan Physics Letters, 182 (1998).

[New74] J. O. Newton, *Nuclear Spectroscopy and Reactions*, Part C (J. Cerny, ed.), Academic Press, 185 (1974).

[Pil92] J. V. Pilcher, NAC Internal Report, National Accelerator Centre, Faure, (1992).

[Pil88] J. V. Pilcher, NAC Internal Report, National Accelerator Centre, Faure, (1988).

[Plo93] A. J. M. Plompen, M. N. Harakeh, W. H. A. Hesselink, G. van 't Hof, N. Kalantar-Nayestanaki, J. P. S. van Schagen, M. P. Carpenter, I. Ahmad, I. G. Bearden, R. V. F. Janssens, T. L.

Khoo, T. Lauritsen, Y. Liang, U. Garg, W. Reviol and D. Ye, Nucl. Phys. **A562**, 61 (1993).

[Por94] M. -G. Porquet, F. Hannachi, G. Bastin, V. Brindejonc, I. Deloncle, B. Gall, C. Schück, A. G. Smith, F. Azaiez, C. Bourgeois, J. Duprat, A. Korichi, N. Perrin, N. Poffé, H. Sergolle, A. Astier, Y. Le Coz, M. Meyer, N. Redon, J. Simpson, J. F. Sharpey-Schafer, M. J. Joyce, C. W. Beausang, R. Wadsworth and R. M. Clark, J. Phys. G: Nucl. Part. Phys. **20**, 765 (1994).

[Pro95] V. M. Prozesky, W. J. Przybylowicz, E. van Achterbergh, C. L. Churms, C. A. Pineda, K. A. Springhorn, J. V. Pilcher, C. G. Ryan, J. Kritzinger, H. Schmitt, T. Swart, Nucl. Instr. and Meth. **B104**, 36 (1995).

[Rad95] D. C. Radford, Nucl. Instr. and Meth. **A361**, 306 (1995).

[Rad95a] D. C. Radford, Nucl. Instr. and Meth. **A361**, 297 (1995).

[Rae86] A. I. M. Rae, *Quantum Mechanics*, 2^{nd} Edition Adam Hilger, (1986).

[Reu83] U. Reus and W. Westmeier, Atomic Data and Nuclear Data Tables, **Vol. 29**, No. 1, July (1983).

[Rev92] W. Reviol, M. P. Carpenter, U. Garg, R. V. F. Janssens, I. Ahmad, I. G. Bearden, Ph. Benet, P. J. Daly, M. W. Drigert, P. B. Fernandez, T. L. Khoo, E. F. Moore, S. Pilotte and D. Ye, Nucl. Phys. **A548**, 331 (1992).

[Rin80] P. Ring and P. Schuck, *The Nuclear Many-Body Problem*, Springer-Verlag, New York, (1980).

[Rou01] D. G. Roux, Ph.D Thesis, University of Cape Town, unpublished, (2001).

[Sch81] J. P. Schiffer, Italian Physical Society, *Proceedings of the International School of Physics, Enrico Fermi, Course LXXVII*, Villa Monastero, 205 (1979).

[Sch94] B. Schlitt, U. Maier, H. Friedrichs, S. Albers, I. Bauske, P. von Brentano, R. -D. Herzberg, U. Kneissl, J. Margraf, H. H. Pitz, C. Wesselborg and A. Zilges, Nucl. Instr. and Meth. in Phys. Res. **A337**, 416 (1994).

[Sch98] G. J. Schmid, A. O. Macchiavelli, S. J. Asztalos, R. M. Clark, M. A. Deleplanque, R. M. Diamond, P. Fallon, R. Kruecken, I. Y. Lee, R. W. MacLeod, F. S. Stephens and K. Vetter, Nucl. Instr. and Meth. **A417**, 95 (1998).

[Sch99] H. Schnare, R. Schwengner, S. Frauendorf, F. Dönau, L. Käubler, H. Prade, A. Jungclaus, K. P. Lieb, C. Lingk, S. Skoda, J. Eberth, G. de Angelis, A. Gadea, E. Farnea, D. R. Napoli, C. A. Ur and G. Lo Bianco, Phys. Rev. Lett. **82**, 4408 (1999).

[Sha88] J. F. Sharpey-Schafer and J. Simpson, Prog. Part. Nucl. Phys. **21**, 293 (1988).

[Shi90] Y. R. Shimizu, E. Vigezzi, R. A. Broglia, Nucl. Phys. **A509**, 80 (1990).

[Sim83] J. Simpson and P. A. Butler, Nucl. Instr. and Meth. **204**, 463 (1983).

[Sin02] A. K. Singh, N. Nenoff, D. Roßbach, A. Görgen, S. Chmel, F. Azaiez, A. Astier, D. Bazzacco, M. Belleguic, S. Bouneau, C. Bourgeois, N. Buforn, B. Cederwall, I. Deloncle, J. Domscheit, F. Hannachi, K. Hauschild, H. Hübel, A. Korichi, W. Korten, T. Kröll, Y. LeCoz, A. Lopez-Martens, R. Lucas, S. Lunardi, H. J. Maier, E. Mergel, M. Meyer, C. M. Petrache, N. Redon, P. Reiter, C. Rossi-Alvarez, G. Schönwaßer, O. Stezowski, P. G. Thirolf and A. N. Wilson, Nucl. Phys. **A707**, 3 (2002).

[Tho62] D. J. Thouless, J. G. Valatin, Nucl. Phys. **31**, 24 (1962).

[Tjø85] P. O. Tjøm, R. M. Diamond, J. C. Bacelar, E. M. Beck, M. A. Deleplanque, J. E. Draper and F. S. Stephens, Phys. Rev. Lett. **55**, 2405 (1985).

[Van86] J. J. Van Ruyven, J. Penninga, W. H. A. Hesselink, P. Van Nes, K. Allaart, E. J. Hengeveld, H. Verheul, M. J. A. De Voigt, Z. Sujkowski and J. Blomqvist, Nucl. Phys. **A449**, 579 (1986).

[Vyv02] K. Vyvey, D. Borremans, N. Coulier, R. Coussement, G. Georgiev, S. Teughels, G. Neyens, H. Hübel and D. L. Balabanski, Phys. Rev. **C65**, 024320 (2002).

[Vyv02a] K. Vyvey, S. Chmel, G. Neyens, H. Hübel, D. L. Balabanski, D. Borremans, N. Coulier, R. Coussement, G. Georgiev, N. Nenoff, S. Pancholi, D. Rossbach, R. Schwengner, S. Teughels and S. Frauendorf, Phys. Rev. Lett. **88**, 102502 (2002).

[Wad98] R. Wadsworth and R. M. Clark, AIP. Conf. Proc. **481**, 503 (1998).

[Wys02] R. Wyss, Private Communication, (2002).

[Wys90] R. Wyss, Nucl. Phys. **A511**, 324 (1990).

[Wys88] R. Wyss, J. Nyberg, A. Johnson, R. Bengtsson and W. Nazarewicz, Phys. Lett. **B215**, 15 (1988).

[Zho96] X. H. Zhou, X. F. Sun, Y. X. Gou, X. G. Lei , X. F. Chen, Z. Liu, Y. H. Zhang, H. J. Jin, and Y. X. Luo, Phys. Rev. **C54**, 2948 (1996).

[Zho96] X. H. Zhou, X. F. Sun, Y. X. Gou, X. G. Lei , X. F. Chen, Z. Liu, Y. H. Zhang, H. J. Jin, Y. X. Luo, S. X. Wen, G. J. Yuan, G. S. Li, C. X. Yang, Z. Phys. **A354**, 7 (1996).

[Zho95] X. H. Zhou, Y. Gou, X. Sun, X. Lei, X. Chen, Z. Liu, Y. Zhang, H. Jin, Y. Luo, S. X. Wen, G. J. Yuan, G. S. Li, C. X. Yang, Z. Phys. **A353**, 3 (1995).

[Zwa00] G. Zwartz, T. E. Drake, M. Cromaz, D. Ward, V. Janzen, A. Galindo-Uribarri, D. Prévost, J. Waddington and S. M. Mullins, J. Phys. G: Nucl. Part. Phys. **26**, 846 (2000).